

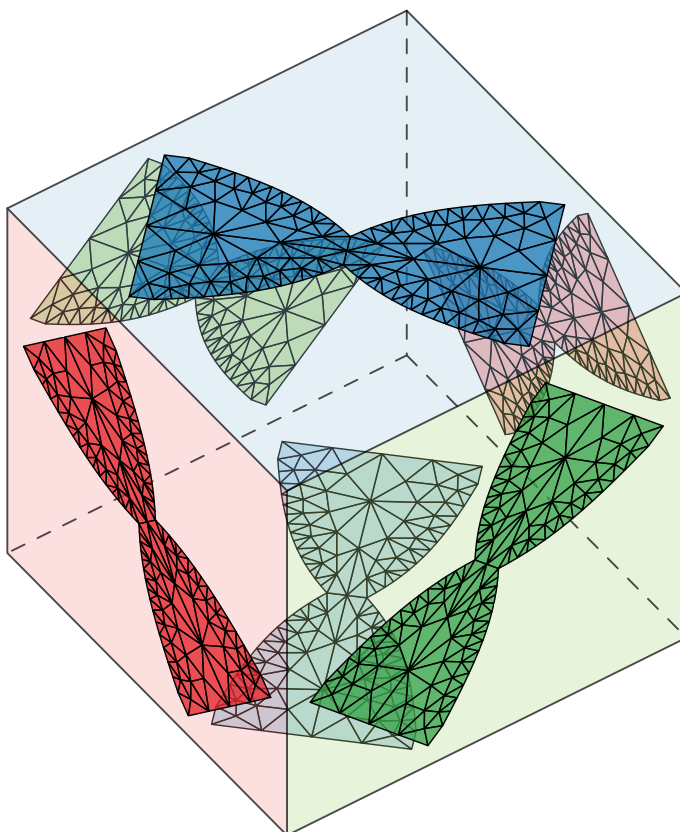


CZECH TECHNICAL UNIVERSITY IN PRAGUE
FACULTY OF ELECTRICAL ENGINEERING
DEPARTMENT OF ELECTROMAGNETIC FIELD

UTILIZATION OF SYMMETRIES IN ANTENNA MODAL ANALYSIS

Doctoral Thesis

Michal Mašek





CZECH TECHNICAL UNIVERSITY IN PRAGUE

FACULTY OF ELECTRICAL ENGINEERING
DEPARTMENT OF ELECTROMAGNETIC FIELD

Utilization of Symmetries in Antenna Modal Analysis

Doctoral Thesis

Author: Ing. Michal Mašek

Supervisor: doc. Ing. Miloslav Čapek, Ph.D.

Supervisor-Specialist: doc. Ing. Lukáš Jelínek, Ph.D.

Ph.D. program: Electrical Engineering and Information Technology – P2612

Branch of studies: Radioelectronics – 2601V010

Prague, the Czech Republic — January 2022

Symmetry – from the Greek *συμμετρία* (*symmetria*), a compound of *συν-* (*syn*) “together with; alike; at the same time”, *μέτρον* (*metron*) “measure”, and the suffix *-ία*: “agreement in dimensions, due proportion, arrangement.” Meaning the “harmonic arrangement of parts to each other or to the whole” [1, 2].



C_{6v} point group.



Declaration

“I hereby declare I have written this thesis independently and have quoted all the sources of information used in accordance with the methodological instructions on ethical principles for writing an academic thesis. Moreover, I state that this thesis has neither been submitted nor accepted for any other degree.”

In Prague, January 5, 2022

.....
Michal Mašek



Acknowledgement

Firstly, I would like to express my thanks to my supervisors—Miloslav Čapek and Lukáš Jelínek—who supported and guided me during my studies. A special thank you goes out to Miloslav for arousing my passion for $\text{L}^{\text{A}}\text{T}_{\text{E}}\text{X}$ and TikZ . I appreciate the cooperation and fruitful discussions with other colleagues from the department and the AToM development team. It was a pleasure to be a part of such great collectives, and a much appreciated acknowledgment is extended to all their members.

I am also grateful to prof. Ammann, prof. Chu, and prof. Boix for giving me the chance to visit foreign universities and spend time in their research groups.

Last but not least, a huge thank goes to my family for allowing me and supporting me in my studies and to my beloved wife Jaroslava for her never-ending support and inexpressible patience.



Abstrakt

Tato práce se zabývá uplatněním geometrických symetrií v řešení elektromagnetických úloh. Bodové symetrie — tedy symetrie, které ponechávají alespoň jeden bod prostoru nedotčený — jsou využity v rámci metody momentů aplikované na integrální rovnice pro pole a uvažující po částech konstantní bázové funkce. Klíčovou roli zastává současná bloková diagonalizace několika operátorů, která je založena na získání dále neredukovatelných (tzv. ireducibilních) reprezentací. Von Neumann-Wignerův teorém a jeho interpretace křížení průběhů vlastních čísel jsou aplikovány jako prostředek k řešení problémů vyskytujících se v modální analýze geometricky symetrických objektů. Mezi ně patří samotné rozhodování o protnutí křivek vlastních čísel či eliminace chybně interpretovaného rozdílu mezi primárním a duálním řešením v kvadratických optimalizačních problémech. Přirozená ortogonalita mezi neredukovatelnými reprezentacemi je využita k současnému vybuzení několika navzájem neovlivňujících se přenosových kanálů, což je technika uplatňovaná ve vícevstupových/vícevýstupových rádiových komunikacích. Bloková diagonalizace operátorů symetrických systémů je dále využita k redukcí výpočetního času.

Klíčová slova: Návrh antén, počítačové simulace, symetrie, teorie bodových grup, metoda momentů, modální analýza, degenerovaná vlastní čísla, konvexní optimalizace.



Abstract

The thesis focuses on the role of symmetries in computational electromagnetics. The presence of point symmetries—geometric similarities with respect to a fixed point—is studied within the realm of the method of moments, revealing the simultaneous block-diagonalization of matrix operators as the key instrument. The theory and an effective procedure to acquire this so-called irreducible representation are devised and implemented over a set of piece-wise basis functions. The von Neumann-Wigner theorem and its interpretation of avoided crossing are shown to be a remedy of problems associated with parametrized modal analysis. This includes the identification of crossings/crossing avoidances in modal tracking or an erroneous duality gap appearing in the dual formulation of quadratic programs. The orthogonality between irreducible representations is utilized to simultaneously excite independent radiation states, a method that can find its use in multiple-input multiple-output devices. Lastly, it is shown that the block-diagonal description of symmetrical systems can lead to a remarkable increase in the speed of computations.

Key Words: Antenna design, computer simulation, symmetry, point group theory, method of moments, modal analysis, degenerated eigenvalues, convex optimization.



Contents

1	Introduction	1
1.1	Organization of the Thesis	2
2	State of the Art	3
2.1	Point Group Theory	3
2.2	Modal Analysis	8
2.3	Perspective Areas of Interest	12
2.4	Thesis Objectives	17
3	Thesis Solutions	19
3.1	Publication A	19
3.2	Publication B	20
3.3	Publication C	21
3.4	Publication D	22
4	Conclusion	25
4.1	Future Work	25
A	Modal Tracking Based on Group Theory	27
A.1	Introduction	27
A.2	Background Theory	28
A.3	Practical Evaluation of Required Matrices	33
A.4	Examples	36
A.5	Discussion	42
A.6	Conclusion	45
A.A	Correction of Vertical Shifts in Symmetry-Based Tracking	46
B	Excitation of Orthogonal Radiation States	47
B.1	Introduction	47
B.2	Orthogonal States	49
B.3	Illustrative Example	52
B.4	Excitation States Based on Point Group Theory	54
B.5	Ports' Positioning	56
B.6	Conclusion	63
B.A	Matrix Operators	63

B.B	Excitation Vector	64
B.C	Symmetry-Adaptation of a Vector	65
B.D	Total Active Reflection Coefficient	67
C	Finding Optimal Total Active Reflection Coefficient and Realized Gain for Multi-port Lossy Antennas	69
C.1	Introduction	69
C.2	TARC: Full-Wave Algebraic Formulation	70
C.3	Expression of TARC in Port Quantities	72
C.4	Optimal Excitation for Minimum TARC	76
C.5	Synthesis of Optimal Feeding Placement	80
C.6	Optimal Characteristic and Tuning Impedances for Minimum TARC	83
C.7	Realized Gain	88
C.8	Conclusion	92
C.A	Fundamental Bound on Radiation Efficiency	92
D	A Role of Symmetries in Evaluation of Fundamental Bounds	95
D.1	Introduction	95
D.2	QCQP Problems	96
D.3	Illustrative Example: Problem of \mathcal{P}_1 -Type	99
D.4	Presence of Symmetries	102
D.5	Various Aspects of the Symmetry Presence	102
D.6	Discussion	115
D.7	Conclusion	119
D.A	Character Tables	119
E	Antenna Toolbox for MATLAB	123
E.1	Author's Contribution to the AToM	124
F	About the Author	125
F.1	Personal Information	125
F.2	Education	125
F.3	Work Experience	126
F.4	International Internships	126
F.5	Publications	127
F.6	Software	128
F.7	Foundation Acknowledgment	128
	Bibliography	129
	Lists	145
	List of Figures	145
	List of Tables	149
	List of Acronyms	151
	List of Symbols	153

1

Introduction

Symmetries are an integral part of our everyday lives. Not only from the atomic perspective, since every molecule has its atoms in symmetrical arrangement [3], but also from our standard view where symmetries are perceived as natural, beautiful, and harmonic [4, 5]. Humans have adapted them since prehistoric times [6–9] as the deepest harmony in our minds. Symmetries occur in ancient symbols and ornaments, in manufactured products, in architecture, art, music, and many other branches. The existence of symmetries is also observed in all fields of natural science: biology, chemistry, and, of course, physics.

Modal analysis is a widely used numerical approach decomposing linear operators representing a system. For computational purposes, a system is typically discretized and the operator is represented by a matrix. Its decomposition provides an orthogonal set of eigenvectors that diagonalize the input matrix into the diagonal matrix containing eigenvalues. Eigenmodes, represented by eigenvalues and associated eigenvectors, give profound insight into a system’s behavior. The method is often used in vibroacoustics to determine natural frequencies, damping factors and mode shapes of mechanical structures and components [10, 11]. Another branch where modal analysis is widely used is quantum mechanics: eigenvectors of the time-independent Schrödinger equation are stationary states of the quantum mechanical system and corresponding eigenvalues represent energy [12–14]. In recent decades, modal analysis became popular in antenna theory as well, especially in the form of characteristic modes [15].

Computing the eigenmodes of non-trivial planar structures has been a challenge for many mathematicians over the centuries and these efforts have intensified with the advent of computer simulations¹ [18, and references therein]. The impact of symmetries on the presence of degenerated eigenvalues was described by von Neumann and Wigner [19, English transcription: 20] and the presence of symmetries in eigenmodes was further addressed in many works across the fields of science, such as: in studding photonic crystals [21, 22]; in analyzing lasers [23] or electromagnetic resonators [24]; in designing microstrip transmission lines [25]; in parallel waveguide couplers [26]; or in waveguides using the decomposition of fields into odd and even modes [27].

¹One of the most familiar non-trivial planar shapes is the “L-shape” formed from three unit squares. In the late 1970s, Cleve Moler [16] used this shape to illustrate the power of his new computing software, nowadays known as MATLAB[®] [17]. The logo of MathWorks, Inc.—the company which developed MATLAB[®]—shows the first eigenmode of the “L” [16, 18].

Although the development of electromagnetic software used for antenna design and analysis has made tremendous progress in recent years, it is not common to utilize symmetries during a simulation save for magnetic or electric planes. This thesis aims to demonstrate that symmetries are not only associated with mirror planes and that they also offer many possibilities for improving the computational performance of numerical methods, such as method of moments (MoM) [28].

In this thesis, the presence of symmetries is used to block-diagonalize a system matrix resulting in the division of the original problem into separated subproblems which can be evaluated one by one in significantly shorter computational time. In addition to this general benefit, symmetries are used to solve specific problems frequently addressed in the past. Based on invariance of modes to symmetry operations, a classification into irreducible representations (irreps) has been developed and utilized for the deterministic and unequivocal solution of the modal tracking problem. Knowledge of mode classification can also be beneficial in convex optimization where an erroneous duality gap occurs due to the presence of symmetries. It is shown that this erroneous duality gap can be eliminated, and, thus, the optimal value can be reached by an appropriate linear combination of two degenerated modes. The native orthogonality between irreps is utilized to simultaneously excite several orthogonal radiation states for multiple-input multiple-output (MIMO) applications. The maximal number of those states and the minimal number of feeders needed to excite them is determined only from the knowledge of symmetry operations with respect to which the structure is invariant.

The thesis proves that any additional knowledge of the antenna's geometrical properties may be used to increase the precision or to reduce the computational time of a numerical evaluation. Thanks to the implementation in MoM code, these features can be utilized within a broad antenna community. The thesis provides a rigorous solution to the treatment of degenerated modes or the approach to effectively design orthogonal MIMO channels.

1.1 Organization of the Thesis

The thesis consists of two main parts.

The first part, divided into four chapters, contains a brief theoretical explanation of the problem. Chapter 2 offers an overview of the state of the art, and leads to a summary of open problems in Section 2.4, which are taken as the goals of this thesis. Chapter 3 briefly describes and refers to publications in a journal with impact factor (*IEEE Transactions on Antennas and Propagation*) and/or in the proceedings of prestigious international conferences (*EuCAP*, *IEEE AP-S/URSI*, *PIERS*), where solutions to the thesis' goals were published. The thesis is concluded in Chapter 4.

The second part, consisting of Appendices A–D, reprints the aforementioned publications. Note that the bibliographies from all reprinted publications have been merged into a sole bibliography list in the thesis. This leads to different reference numbering in the thesis and journal publications.

Appendix E describes the Antenna Toolbox for MATLAB (AToM) [29], the software package in which all results published in the thesis were computed, and the development of which the author of the thesis participated. Appendix F contains the author's résumé and a list of all publications he collaborated on as a principal author or co-author during his studies.

The theory of symmetries is an advanced branch of mathematics belonging to the theory of groups, from which only point symmetry groups are considered in this thesis. [Section 2.1](#) contains a brief extract of the theory to introduce the necessary technical background and nomenclature used in the thesis. For greater insight, the reader can refer to textbooks on the subject, *e.g.*, [30–32]. In [Section 2.2](#), modal analysis is introduced with an example of characteristic modes [15]. This section is followed by [Section 2.3](#) which describes antenna topics that can benefit from the utilization of symmetries, particularly modal tracking, the selective excitation of modes, optimization problems defined by quadratically constrained quadratic programs (QCQPs), and the fundamental bounds of symmetrical structures. The chapter closes with [Section 2.4](#) enumerating the objectives of the thesis.

2.1 Point Group Theory

The utilization of symmetries is based on point group theory [30, 31], a field of mathematics focusing on point symmetries expressed by these symmetry operations¹:

- identity: E,
- inversion: I,
- reflection by a plane: σ , typically supplemented by the subscripts “v” or “h” to distinguish between reflection by vertical (containing the principal axis²) or horizontal (perpendicular to the principal axis) planes,
- n -fold rotation (proper rotation): C_n (C_n^p when is repeated p times),
- n -fold rotoreflection (improper rotation): $S_n = C_n\sigma_h$.

The symmetry operation, represented by the symbol R , can be applied to object Ω by operation $R\Omega$, *e.g.*, vector $\mathbf{v}' = (x', y', z')^T$ in the three-dimensional cartesian coordinate system is obtained by the application of symmetry operation R on original vector $\mathbf{v} = (x, y, z)^T$ as

$$\mathbf{v} \xrightarrow{R} \mathbf{v}' : \quad \mathbf{v}' = R\mathbf{v} = \mathbf{C}(R)\mathbf{v}, \quad (2.1)$$

¹The Schoenflies notation [33] is used to denote symmetry operations and point groups.

²The standard convention considers the z -axis as the principal axis of the system and the yz -plane as the principal plane [34].


	Ω	$E\Omega$	$\sigma_v^{yz}\Omega$	$\sigma_v^{xz}\Omega$	$C_2\Omega$	G
	F	F	F	F	F	C_1
	A	A	A	A	A	C_s
	Y	Y	Y	Y	Y	C_s
	H	H	H	H	H	C_{2v}

Figure 2.1: Four symmetry operations applied to four different objects Ω : identity E , reflection by yz -plane σ_v^{yz} , reflection by xz -plane σ_v^{xz} and rotation by angle π around the z axis C_2 . Each object is invariant under a different set of symmetry operations, *i.e.*, they are classified into different point groups G .

where $\mathbf{C}(R) \in \mathbb{R}^{3 \times 3}$ is a coordinate transformation matrix representing operation R in the basis of the corresponding vector space, see Figure 2.1 for examples of symmetry operations and their application to different objects. Symmetry operations can be concatenated using (2.1) multiple times, *i.e.*,

$$\mathbf{v} \xrightarrow{R_1} \mathbf{v}' \xrightarrow{R_2} \mathbf{v}'' : \mathbf{v}'' = R_2(R_1\mathbf{v}) = R_2R_1\mathbf{v} = \mathbf{C}(R_2)\mathbf{C}(R_1)\mathbf{v}. \quad (2.2)$$

The closure of point group G [31] can be verified by constructing a multiplication table where rows and columns are labeled by the group elements and the body of the table contains the products of all the combinations of symmetry operations $R_1, R_2 \in G$. Each row and column of the multiplication table must contain each element of the group once and only once [30], see the multiplication table of point group C_{2v} in Table 2.1.

A subset of symmetry operations in G , which can create its own closed multiplication table, is called the subgroup (a point group with lower order). For example, group C_{2v} has the following subgroups: group C_2 ($G = \{E, C_2\}$) and two groups C_s ($G = \{E, \sigma_h\}$).

Depending on the list of symmetry operations under which the object Ω is invariant, the object can be categorized into one of the point groups G [30]. Objects from Figure 2.1 belong to point groups C_1 (letter³ F), C_s (letters A and Y), and C_{2v} (letter H). Notice that non-symmetric structures can also be studied via point group theory, they belong to the C_1 point group and are solely invariant under identity operation.

³The author is aware that, strictly speaking, these letters, as planar structures, should be classified into point groups C_1 (letter F), D_1 (letters A and Y), and D_2 (letter H), respectively, because reflection operations and point groups C_{nv} are connected to volumetric objects. For planar structures, rotation can be substituted by reflection, *e.g.*, $\sigma^{yz} = C_2^x$. However, at the beginning of the work, reflection operations were used in parallel with reflection planes available in commercial electromagnetic solvers. At least in the scope of the thesis, this substitution is isomorphic and does not have any impact on the presented methods and results.

Table 2.1: Multiplication table for point group C_{2v} consisting of four symmetry operations: identity, rotation by angle π and two reflections, *i.e.*, $G = \{E, C_2, \sigma_v^{xz}, \sigma_v^{yz}\}$. A rectangle is a representative example belonging to this group.

	E	C_2	σ_v^{xz}	σ_v^{yz}
E	E	C_2	σ_v^{xz}	σ_v^{yz}
C_2	C_2	E	σ_v^{yz}	σ_v^{xz}
σ_v^{xz}	σ_v^{xz}	σ_v^{yz}	E	C_2
σ_v^{yz}	σ_v^{yz}	σ_v^{xz}	C_2	E

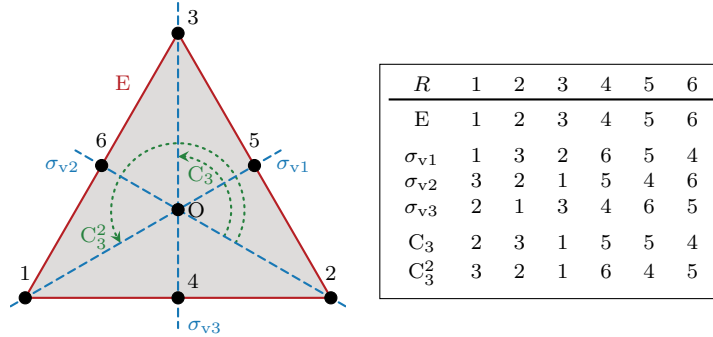


Figure 2.2: Six nodes arranged into an equilateral triangle. The structure belongs to point group C_{3v} and consists of six symmetry operations. The table shows how each node is transformed via a corresponding symmetry operation.

2.1.1 Matrix Representations

Within a complex N -dimensional vector space V , object Ω is described by vector \mathbf{V} , and symmetry operation $R \in G$ is described by a non-singular matrix $\mathbf{C}(R)$. As an example, Figure 2.2 shows six nodes arranged on an equilateral triangle, a structure belonging to point group C_{3v} . Transformations of all points via all symmetry operations $R \in G$ are shown in the right panel of the figure. Examples of the corresponding mapping matrices⁴ $\mathbf{C}(R)$, which describe how each node is transformed by symmetry operation R , are

$$\mathbf{C}(C_3) = \begin{bmatrix} 0 & 0 & 1 & 0 & 0 & 0 \\ 1 & 0 & 0 & 0 & 0 & 0 \\ 0 & 1 & 0 & 0 & 0 & 0 \\ 0 & 0 & 0 & 0 & 0 & 1 \\ 0 & 0 & 0 & 1 & 0 & 0 \\ 0 & 0 & 0 & 0 & 1 & 0 \end{bmatrix}, \quad \mathbf{C}(\sigma_{v1}) = \begin{bmatrix} 1 & 0 & 0 & 0 & 0 & 0 \\ 0 & 0 & 1 & 0 & 0 & 0 \\ 0 & 1 & 0 & 0 & 0 & 0 \\ 0 & 0 & 0 & 1 & 0 & 0 \\ 0 & 0 & 0 & 0 & 0 & 1 \\ 0 & 0 & 0 & 0 & 1 & 0 \end{bmatrix}. \quad (2.3)$$

⁴The matrices are constructed in the selected vector space. Here, each row/column represents one node of the structure, which leads to the matrices of dimension six. There are, however, other options. For example, representing each node in cartesian coordinates x, y, z would require matrices $\mathbf{C}(R)$ of dimension 18.

$$\begin{aligned}
 \mathbf{D}(E) &= \begin{pmatrix} \boxed{1} & \boxed{0} & 0 & 0 & 0 & 0 \\ 0 & \boxed{1} & 0 & 0 & 0 & 0 \\ 0 & 0 & \boxed{1} & 0 & 0 & 0 \\ 0 & 0 & 0 & \boxed{1} & 0 & 0 \\ 0 & 0 & 0 & 0 & \boxed{1} & 0 \\ 0 & 0 & 0 & 0 & 0 & \boxed{1} \end{pmatrix} & \mathbf{D}(\sigma_1) &= \begin{pmatrix} \boxed{0.73} & \boxed{-0.68} & 0 & 0 & 0 & 0 \\ \boxed{-0.68} & \boxed{-0.73} & 0 & 0 & 0 & 0 \\ 0 & 0 & \boxed{1} & 0 & 0 & 0 \\ 0 & 0 & 0 & \boxed{-0.51} & \boxed{-0.86} & 0 \\ 0 & 0 & 0 & \boxed{0.86} & \boxed{0.51} & 0 \\ 0 & 0 & 0 & 0 & 0 & \boxed{1} \end{pmatrix} \\
 \mathbf{D}(C_3) &= \begin{pmatrix} \boxed{-0.50} & \boxed{-0.87} & 0 & 0 & 0 & 0 \\ \boxed{0.87} & \boxed{-0.50} & 0 & 0 & 0 & 0 \\ 0 & 0 & \boxed{1} & 0 & 0 & 0 \\ 0 & 0 & 0 & \boxed{-0.50} & \boxed{0.87} & 0 \\ 0 & 0 & 0 & \boxed{-0.87} & \boxed{-0.50} & 0 \\ 0 & 0 & 0 & 0 & 0 & \boxed{1} \end{pmatrix} & \mathbf{D}(\sigma_2) &= \begin{pmatrix} \boxed{-0.96} & \boxed{-0.29} & 0 & 0 & 0 & 0 \\ \boxed{-0.29} & \boxed{0.96} & 0 & 0 & 0 & 0 \\ 0 & 0 & \boxed{1} & 0 & 0 & 0 \\ 0 & 0 & 0 & \boxed{1} & \boxed{-0.01} & 0 \\ 0 & 0 & 0 & \boxed{-0.01} & \boxed{-1} & 0 \\ 0 & 0 & 0 & 0 & 0 & \boxed{1} \end{pmatrix} \\
 \mathbf{D}(C_3^2) &= \begin{pmatrix} \boxed{-0.50} & \boxed{0.87} & 0 & 0 & 0 & 0 \\ \boxed{-0.87} & \boxed{-0.50} & 0 & 0 & 0 & 0 \\ 0 & 0 & \boxed{1} & 0 & 0 & 0 \\ 0 & 0 & 0 & \boxed{-0.50} & \boxed{-0.87} & 0 \\ 0 & 0 & 0 & \boxed{0.87} & \boxed{-0.50} & 0 \\ 0 & 0 & 0 & 0 & 0 & \boxed{1} \end{pmatrix} & \mathbf{D}(\sigma_3) &= \begin{pmatrix} \boxed{0.23} & \boxed{0.97} & 0 & 0 & 0 & 0 \\ \boxed{0.97} & \boxed{-0.23} & 0 & 0 & 0 & 0 \\ 0 & 0 & \boxed{1} & 0 & 0 & 0 \\ 0 & 0 & 0 & \boxed{-0.49} & \boxed{0.87} & 0 \\ 0 & 0 & 0 & \boxed{0.87} & \boxed{-0.49} & 0 \\ 0 & 0 & 0 & 0 & 0 & \boxed{1} \end{pmatrix}
 \end{aligned}$$

Figure 2.3: An example of matrix representation $\mathbf{D}(R \in G)$ of an equilateral triangle from Figure 2.2. Two presented irreps are highlighted by the colored rectangles. Decimal numbers were rounded to two digits.

The set of mapping matrices $\{\mathbf{C}(R \in G)\}$ forms a representation⁵. An infinite number of representations with the use of similarity transformation exist, however, it is convenient to use those in block-diagonalized form. Such a transformation can be done as

$$\mathbf{D}(R) = \mathbf{V}^{-1} \mathbf{C}(R) \mathbf{V} = \begin{bmatrix} \mathbf{D}_1(R) & \mathbf{0} & \cdots & \mathbf{0} \\ \mathbf{0} & \mathbf{D}_2(R) & \cdots & \mathbf{0} \\ \vdots & \vdots & \ddots & \vdots \\ \mathbf{0} & \mathbf{0} & \cdots & \mathbf{D}_Q(R) \end{bmatrix}. \quad (2.4)$$

It is not trivial to find the transformation matrix \mathbf{V} which simultaneously block-diagonalizes all matrices $\mathbf{C}(R \in G)$; see also Section 2.1.4. One possibility is to use eigenvectors of an arbitrary matrix operator of a corresponding structure belonging to point group G , arranged into matrix $\mathbf{V} = \mathbf{v}_1 \oplus \mathbf{v}_2 \oplus \cdots \oplus \mathbf{v}_N$. As an example, the matrix of Euclidean distances between all points of the equilateral triangle in Figure 2.2 was constructed, its eigenvectors were computed and arranged into matrix \mathbf{V} to express a block-diagonalized matrix representation (2.4). These matrices $\mathbf{D}(R \in G)$ are shown in Figure 2.3.

2.1.2 Reducible and Irreducible Representations

A representation of vector space V is said to be reducible if there exists a proper linear subspace V_1 of V with the property that every transformation via this representation maps every vector of V_1 back onto V_1 only [31]. A non-reducible representation is called an irreducible [31] representation (or shortly irrep). The reducibility can

⁵“A representation is a set of matrices, each of which corresponds to a symmetry operation and combines in the same way that the symmetry operators in the group combine” [3].

Table 2.2: Character table for point group C_{3v} , [30].

C_{3v}	E	$2C_3$	$3\sigma_v$
A ₁	+1	+1	+1
A ₂	+1	+1	-1
E	+2	-1	0

be easily observed from the block-diagonal form of representation (2.4). Each block $\mathbf{D}_q(R)$ (all matrices in the representation must be block-diagonalized in the same way) is a matrix representation of the irrep; see highlighted matrices of all presented irreps in Figure 2.3. Each irrep follows the same multiplication table as the original reducible representation.

It is observable from Figure 2.3 that blue blocks of size 2×2 cannot be diagonalized further and, thus, they belong to a two-dimensional irrep. The consequences of higher-dimensional irreps and modal analysis is described in detail later in Section 2.2.1.

Every point group has a limited number of irreps which may occur in $\mathbf{D}(R)$ multiple times. Irreps α are labeled by Mulliken's symbols [34] according to the dimensionality of their matrix representation $g^\alpha = \dim[\mathbf{D}^\alpha(R)]$: A and B for one-dimensional, E for two-dimensional, and T for three-dimensional irreps, respectively. If more irreps of the same label are present, additional subscripts and/or superscripts are used.

In the example displayed in Figure 2.3, a one-dimensional irrep occurs twice and a two-dimensional irrep also occurs twice. Further classification to distinguish if the same-dimensional irreps are the same, or if there are several irreps which exist with the same dimensionality, can be performed with the knowledge of its characters.

2.1.3 Characters and Character Tables

As written previously, the use of similarity transformation offers an unlimited number of matrix representations $\mathbf{D}^\alpha(R)$ of irrep α , however, all these transformations do not affect the parameter of the matrix—its trace—which is called group character $\chi^\alpha(R) = \text{trace}[\mathbf{D}^\alpha(R)]$.

Characters χ can be stored as entries of the character table where each row represents one irrep α and columns iterate over symmetry operations $R \in G$. Table 2.2 shows the character table for point group C_{3v} . Note that columns containing the same entities are arranged into so-called conjugacy classes. There are as many irreps in each point group as there are classes in it.

For the example in Figure 2.3, it can be concluded that the fourth and sixth eigenvectors belong to irrep A₁, and the remaining eigenvectors belong to irrep E, while irrep A₂ is not represented at all in this example.

2.1.4 Block-Diagonalization of the Matrix Operator

To characterize matrix operators of the system at hand, it is useful to find a similarity transformation which converts them all into diagonal form simultaneously. In general, such a basis can be found for up to two matrix operators using modal decomposition (see later in Section 2.2), but only in special cases it is possible to diagonalize three or more operators simultaneously. For symmetrical structures, the orthogonality

between irreps can be utilized to find a basis which, at least, block-diagonalize [35] all matrix operators invariant under the symmetry operations of the point group G .

To perform the block-diagonalization, a symmetry-adapted basis [31]

$$\boldsymbol{\rho}^{(\alpha,i)} = \frac{g^\alpha}{g} \sum_{R \in G} \tilde{d}_{ii}^\alpha(R) \mathbf{C}(R) \quad (2.5)$$

is used to create a projection operator $\boldsymbol{\rho}^{(\alpha,i)}$ which projects an original basis vector for any irreducible representation. In (2.5), $\tilde{\mathbf{D}} = (\mathbf{D}^{-1})^T$ stands for a contra-gradient representation, d_{ii} is an element of matrix \mathbf{D} at position ii and (α, i) [30] is typically denoted as a species.

The application of this projection operator onto arbitrary vector \mathbf{v} ,

$$\mathbf{v}^{(\alpha,i)} = \boldsymbol{\rho}^{(\alpha,i)} \mathbf{v}, \quad (2.6)$$

for a different species (α, i) provides, due to the great orthogonality theorem [30], orthogonal vectors $\mathbf{v}^{(\alpha,i)}$.

Collecting linearly-independent columns of $\boldsymbol{\rho}^{(\alpha,i)}$ into matrix $\boldsymbol{\Gamma}^{(\alpha,i)} \in \mathbb{C}^{N \times n^\alpha}$ and concatenating these matrices into matrix $\boldsymbol{\Gamma} \in \mathbb{C}^{N \times N}$ provides a similarity transformation matrix, such that

$$\hat{\mathbf{A}} = \boldsymbol{\Gamma}^T \mathbf{A} \boldsymbol{\Gamma} \quad (2.7)$$

is block-diagonal. Note that matrix $\boldsymbol{\Gamma}$ is related only to the geometry of the structure and is independent of matrix operator \mathbf{A} . Thus, the block-diagonalization can be performed for an arbitrary operator computed on the structure.

2.2 Modal Analysis

The modal analysis is a widely used concept in numerical analysis that decomposes a linear operator into a set of eigenvectors and eigenvalues [36]. Considering a matrix, the discretized form of such an operator in a selected basis [37], which can be achieved, for example, by MoM [28] or finite element method (FEM) [38], the decomposition is provided by solving a generalized eigenvalue problem (GEP) [39], *i.e.*,

$$\mathbf{A}(p) \mathbf{I}_n(p) = \lambda_n(p) \mathbf{B}(p) \mathbf{I}_n(p), \quad (2.8)$$

where \mathbf{A} and \mathbf{B} are the mentioned decomposed matrices and \mathbf{I}_n is the n -th eigenvector with the corresponding eigenvalue λ_n . The eigenvalue problems can be solved using a generalized Schur decomposition [40] or an implicitly restarted Arnoldi method [41].

Parameter p in (2.8) reminds us that input matrices \mathbf{A} , \mathbf{B} are typically dependent on some parameter, such as energy, frequency, etc. Then, the parameter-dependency of eigenvalues $\lambda_n(p)$ is often studied, see Sections 2.2.2 and 2.3.1 for a detailed description.

2.2.1 Degenerated Modes

When there are several modes with equal eigenvalue $\lambda_n(p)$, they are called “multiplied” or “degenerated”. There exist two types of degeneracies: “geometrical” and “algebraic” [42], both of which are caused by the presence of symmetries.

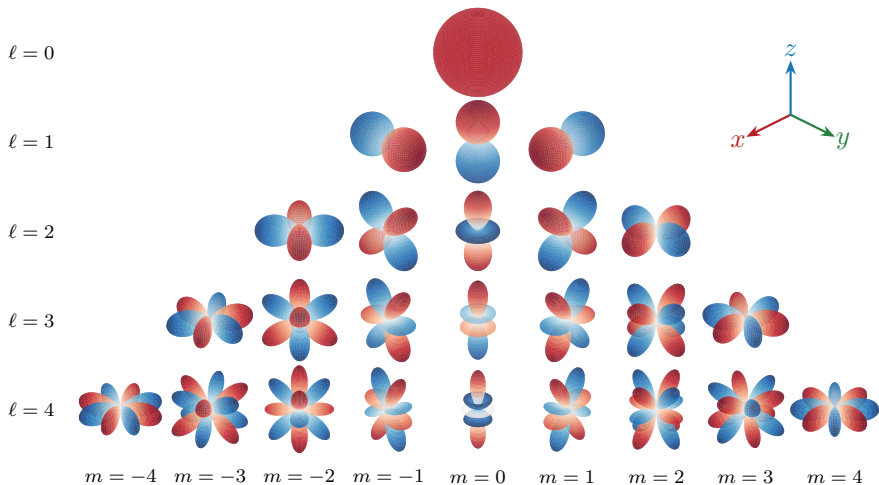


Figure 2.4: Real spherical harmonics S_ℓ^m up to degree $\ell = 4$ [44, 45]. The red colors represent positive values while the blue colors are for negative values. Each row shows geometrically degenerated modes within one irrep which has a dimensionality of $g^\alpha = 2\ell + 1$.

The geometrical degeneracy, also called systematic or essential, is related to the occurrence of higher-order irreps. Modes belonging to such irreps are degenerated over the entire range of parameter p . A typical example of a geometrical degeneracy is spherical harmonics (modes of the spherical shell), which occurs in $2\ell + 1$ degeneracies for the degree ℓ [43], see Figure 2.4.

The latter degeneracy—algebraic, also called accidental—occurs coincidentally. It just so happens that, for a specific value of parameter p , more modes with the same eigenvalue exist, however for the value $p + \Delta p$ eigenvalues differ.

The degeneracies were studied by von Neumann and Wigner in 1929 which led to a theorem [19], from which it follows that accidental degeneracies can occur only between modes from different irreps. This theorem, and the distinction between geometrical and accidental degeneracies, plays a crucial role in the solution to modal tracking, see Sections 2.3.1 and 3.1. Having degenerated modes might act as beneficial applications when one of those modes is to be selected and further utilized. Sections 2.3.3 and 3.4 are dedicated to this topic.

2.2.2 Characteristic Modes

As a very current example of modal analysis, characteristic modes (CMs) can be introduced as they have become popular within the antenna design community in recent decades. CMs were originally introduced for scattering matrices by Garbacz [46, 47], and the theory was subsequently extended and generalized for conducting bodies by Harrington and Mautz [48, 49]. CMs are acquired by the decomposition (2.8) of impedance matrix $\mathbf{Z} = \mathbf{R}_0 + j\mathbf{X}_0$ [50], specifically

$$\mathbf{X}_0 \mathbf{I}_n = \lambda_n \mathbf{R}_0 \mathbf{I}_n. \quad (2.9)$$

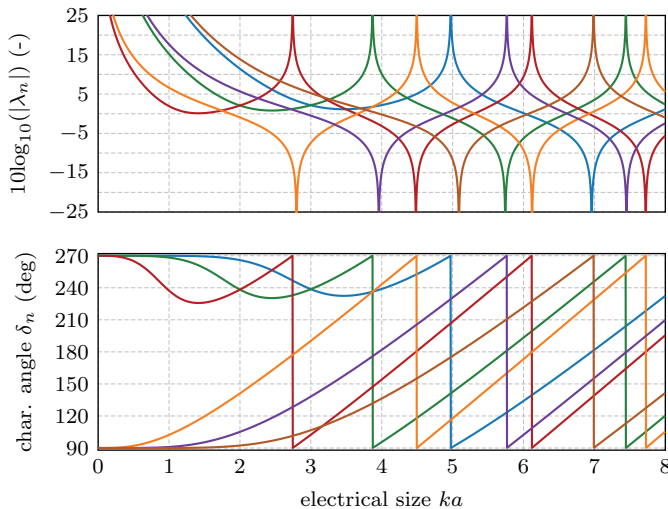


Figure 2.5: Dependency of analytically computed characteristic numbers (top panel) and characteristic angles (bottom panel) on electrical size ka of a spherical shell with radius $a = 1$ m. The first three transverse magnetic (TM) and transverse electric (TE) modes are depicted [52]. Note that each mode is geometrically degenerated (more modes have the same eigenvalue); thus, several overlapped lines exist for each mode [52].

Here, eigenvector \mathbf{I}_n , also called a characteristic vector, stands for expansion coefficients, which, in a combination of used basis functions $\boldsymbol{\psi}(\mathbf{r})$, typically Rao-Wilton-Glisson (RWG) basis functions [51], can express n -th modal current density

$$\mathbf{J}_n(\mathbf{r}) \approx \sum_{m=1}^N I_{nm} \boldsymbol{\psi}_m(\mathbf{r}). \quad (2.10)$$

Eigenvalues λ_n are called characteristic numbers and can be rewritten as a Rayleigh quotient [36]

$$\lambda_n = \frac{2\omega(W_{m,n} - W_{e,n})}{P_{\text{rad},n}} \approx \frac{\mathbf{I}_n^H \mathbf{X}_0 \mathbf{I}_n}{\mathbf{I}_n^H \mathbf{R}_0 \mathbf{I}_n} \quad (2.11)$$

with $W_{m,n}$, $W_{e,n}$, and $P_{\text{rad},n}$ representing stored magnetic energy, stored electric energy, and radiated power of the n -th mode, respectively; superscript H stands for the complex conjugate. Depending on the sign of the characteristic number, characteristic mode can be classified as

- $W_{m,n} > W_{e,n} \iff \lambda_n > 0$: mode is of inductive nature,
- $W_{m,n} < W_{e,n} \iff \lambda_n < 0$: mode is of capacitive nature,
- $W_{m,n} = W_{e,n} \iff \lambda_n = 0$: mode is in resonance.

To find the resonance of each CM, it is frequently useful to study modal behavior depending on the frequency as parameter p in (2.8), see Figure 2.5 which shows

analytically computed eigenvalues⁶ of a spherical shell [52, 53] made of a perfect electric conductor (PEC). Characteristic angles [54], shown in the bottom panel of Figure 2.5,

$$\delta_n = 180^\circ - \arctan(\lambda_n). \quad (2.12)$$

are used to rescale characteristic numbers from $\lambda_n \in (-\infty, \infty)$ to $\delta_n \in (90^\circ, 270^\circ)$.

Notice, that the eigenvalue decomposition of the impedance matrix provides an elegant overview of fundamental antenna behavior only from the knowledge of antenna geometry and the operating frequency without the necessity of setting any excitation. The total current resulting from the excitation represented by excitation vector \mathbf{V}^{inc} can be computed as a superposition of modal currents [50]

$$\mathbf{J}(\mathbf{r}) = \sum_{n=1}^{\infty} \alpha_n \mathbf{J}_n(\mathbf{r}) \quad (2.13)$$

with a complex coefficient [55]

$$\alpha_n = \frac{1}{P_{\text{rad}}} \frac{\mathbf{I}_n^H \mathbf{V}^{\text{inc}}}{1 + j\lambda_n}. \quad (2.14)$$

Figure 2.6 shows an example of modal currents on a bowtie antenna.

The consequences of symmetries and CMs were observed by Knorr in 1973 [56] where properly selected expansion functions, with respect to symmetries, were used and substituted into GEP (2.8). It has been shown that for the case of symmetrical structure, the presence of symmetries is also reflected in its eigenvectors. It was demonstrated on the body of revolution (belonging to group $C_{\infty v}$) that its characteristic modes can be classified into irreducible representations. Moreover, an approach of block-diagonalization of the impedance matrix was introduced. This operation provided the possibility of solving each block separately which significantly reduced computational time. The block-diagonalization was further developed by Tripp and Hohmann [35], who used a symmetry-adapted basis, see Section 2.1.4, for structures belonging to arbitrary point groups. Although these observations were demonstrated on CMs, they can be generalized and applied for arbitrary modal decomposition.

2.2.3 Other Decompositions

Characteristic modes are not the only modal decompositions used in electromagnetism. Eigenmodes of other matrix operators are also studied, *e.g.*:

- stored energy modes ($\mathbf{A} \equiv \mathbf{X}_e$ or $\mathbf{A} \equiv \mathbf{X}_m$, $\mathbf{B} \equiv \mathbf{E}$) [57],
- “Loop-Star” type decomposition ($\mathbf{A} \equiv \mathbf{X}_m$, $\mathbf{B} \equiv \mathbf{X}_e$) [58],
- radiation efficiency modes ($\mathbf{A} \equiv \mathbf{R}_\rho$, $\mathbf{B} \equiv \mathbf{R}_0$) [59],
- natural modes ($\mathbf{A} \equiv \mathbf{Z}$, $\mathbf{B} \equiv \mathbf{E}$) [60],
- modes of gain to the Q-factor ratio ($\mathbf{A} \equiv \mathbf{X}_0$, $\mathbf{B} \equiv \omega \mathbf{W}$) [61],
- directivity modes ($\mathbf{A} \equiv 4\pi \mathbf{U}$, $\mathbf{B} \equiv 1/2(\mathbf{R}_0 + \mathbf{R}_\rho)$) [62],

with the meaning of all matrices explained in the above mentioned references.

Modal analysis was not only studied as a full-domain problem, port-modes were published as well [55, 63].

⁶Note that obtaining such smooth curves for discretized objects, which cannot be solved analytically, is challenging and the process is described in further detail in Section 2.3.1.

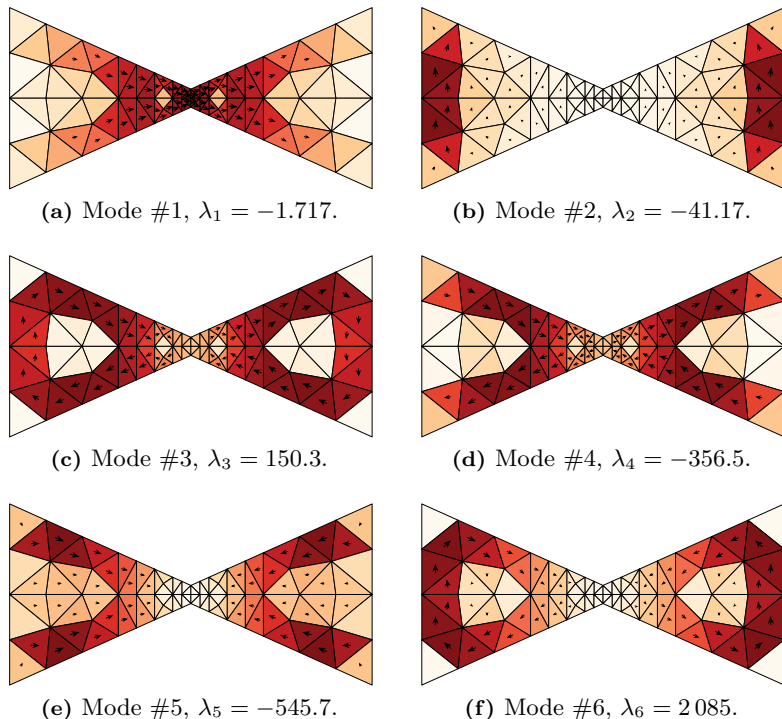


Figure 2.6: Current densities of the six most significant characteristic modes (with the lowest magnitude of characteristic number) of a bowtie antenna. The structure has electrical size $ka = 1$ and aspect ratio 2 : 1. The narrowest dimension of the bowtie is $\sqrt{5}a/50$.

2.3 Perspective Areas of Interest

This section introduces fields of computational electromagnetics where the utilization of symmetries has not been sufficiently studied yet, and it has high potential to improve or solve current problems.

2.3.1 Modal Tracking

Modal tracking is a post-processing algorithm used in cases when a modal analysis is computed for a set of matrix operators dependent on parameter p , and modes dependent on such a parameter are required as a result. CMs computed for frequency range f , which is discretized into N_f frequency samples, can serve as a representative example, and for each frequency sample, the eigenvalue problem is computed separately. Figure 2.7a shows the ten most significant modes at each frequency sample for a structure of four dipoles.

An expected result is to obtain traces of characteristic numbers, also known as

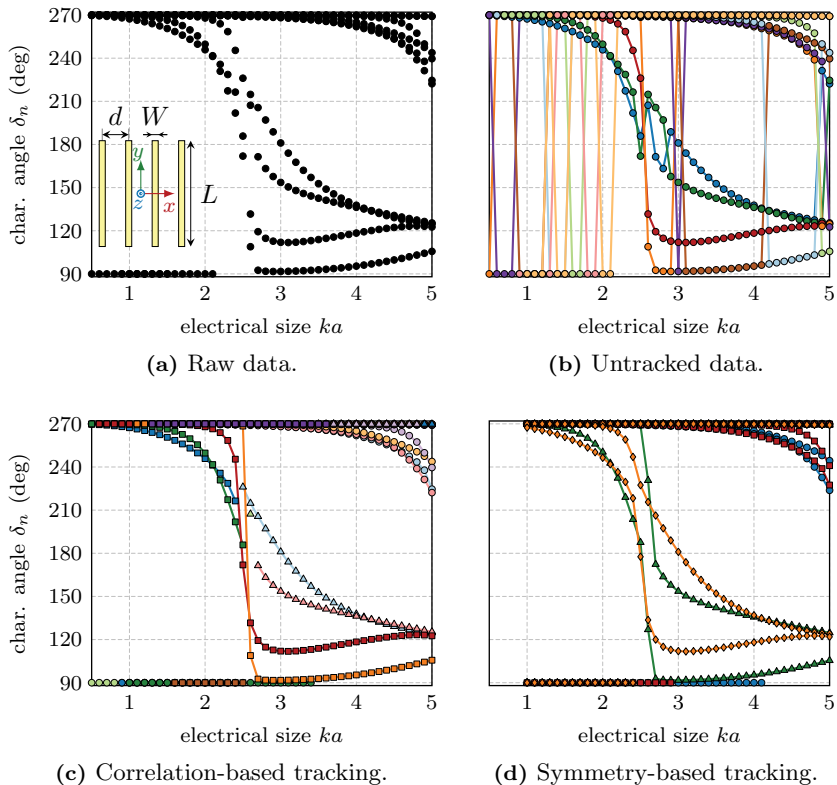


Figure 2.7: Characteristic angles of four-dipoles array ($W = L/25$, $d = L/2$). (a) Raw data, (b) untracked data, connected without any postprocessing algorithm. (c) tracked data by the correlation-based algorithm [29], (d) symmetry-based tracking—a solution described in this thesis; see more in Section 3.1.

“modal traces” or “eigen-traces” and $\lambda_n(p)$ as smooth functions over parameter p . Since the numerical methods solving the eigenvalue problem (2.8), *e.g.*, functions `eig` or `eigs` in MATLAB[®] [17], typically provide modes sorted by the magnitude of their eigenvalues, a simple connection of the n -th eigenvalue at each frequency sample does not provide the expected result, as shown in Figure 2.7b.

Correlation-based algorithms [64–70] were developed to track modes over frequency, especially for CMs solvers. These algorithms benefit from the fact that the modal current distribution changes slowly with frequency. For each eigenvector at frequency f_i , correlation coefficients with all eigenvectors at frequency f_{i+1} are computed, and, if the correlation is higher than a predefined threshold, the corresponding two eigenvectors are paired. If, however, the modal current distribution changes significantly between two frequency steps, tracking does not perform appropriately, see Figure 2.7c. Although there exist many enhancements of this algorithm (far-field patterns correlation [67], surface current correlation [68], adaptive solver

which compute additional frequency samples when the correlation is low [66, 68], estimating of eigenvalues to avoid mistakes in tracking [69], additional tracking error correction algorithm [70]), modal tracking is still not perfect.

The reaction of eigenvalues to a change of parameter(s) was studied by von Neumann and Wigner [20]. In the interest of quantum-mechanical problems, they investigated whether two modes could be degenerated between known values at two samples of the parameters. This study resulted in the von Neumann-Wigner theorem stating that “Usually two levels (modal traces) cross each other only if the corresponding eigenfunctions have different symmetries.” [71].

This theorem was adapted for tracking characteristic modes by Schab and Bernhard [72]: “Characteristic mode eigenvalue crossings are only possible between modes belonging to unique irreducible representations.”, and it can easily be applied to non-symmetrical structures as well: “Objects that have no inherent geometric symmetry (*i.e.*, a symmetry group of C_1) will have entirely non-crossing characteristic mode eigenvalues. [...] This result relaxes the need for precise modal tracking routines since non-crossing eigenvalue sets are trivial to sort.”

These conclusions open possible challenges addressed in this thesis: Can modal tracking be simplified for symmetrical structures? If the crossing is allowed only between unique irreps, how can modes be classified into them? Does it mean that correlation methods are superfluous?

2.3.2 Excitation of Characteristic Modes

The concept of CMs sparked the pursuit of exciting solely a selected mode. These efforts have occurred since the introduction of CMs [54] to the present [73–87]. However, unless N ports cannot be used to excite every unknown (basis function) separately, other modes will always be a part of the total current (2.13) with, more or less, the excitation coefficient α_n . Figure 2.8 shows the excitation coefficients of a bowtie antenna fed by a delta-gap source in its center. It can be observed that, in this example, for small electrical size ka , the excitation of only the first mode was successful; however, for $ka > 4$, the total current is going to be composed of the superposition of modes 1 and 9 with similar weights.

With the vast expansion of MIMO systems, the idea to use CMs in antenna design arose. The orthogonality between CMs is intended to be utilized for creating several orthogonal radiated states. There exist several studies utilizing this idea. To mention a few:

- several publications are focused on the excitation of orthogonal radiated patterns on a rectangular plate or mobile chassis [73–75, 77, 79, 82, 83];
- the excitation of degenerated modes on a metallic equilateral triangular-shaped antenna [76] or on a circular ring antenna [84];
- 3×3 antenna array with four modal current distributions excited at each element resulting in a 36-port antenna system [78];
- the excitation of modes on a block platform by mounting an inductive coupling exciter [81] or inverted-F antennas [87];
- a 3-port bug-like structure [85].

In some of the above-cited publications, the utilization of symmetries was indicated or studied, at least in distinguishing odd and even modes [80, 84, 85], distinguishing

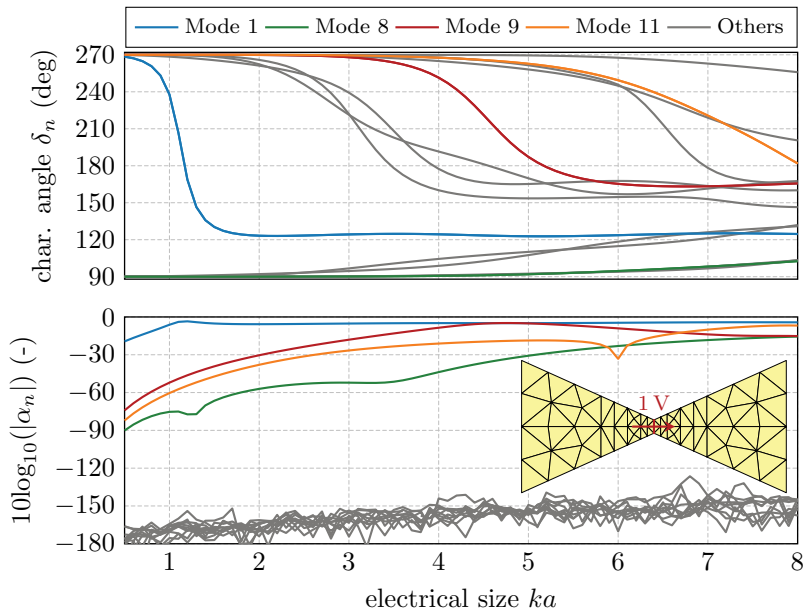


Figure 2.8: Top: Tracked characteristic modes by the correlation algorithm [29] of a bowtie antenna. Bottom: Excitation coefficients α_n for the case of exciting the antenna by a delta gap placed in the narrowest part of the antenna.

odd and even reflections along axes on a rectangular plate [79, 83], or exciting modes from four different irreps [73].

The most thorough utilization of symmetries and point group theory for the excitation of several orthogonal states was published by Peitzmeier and Manteuffel [86] who classified modes into irreps by visually inspecting symmetries present on modal current distributions. In the end, they excited six orthogonal radiated patterns on a square plate with twelve excitation slots (delta gaps). The work concludes with the statement: “the number of feasible uncorrelated antenna ports can be predicted from the number and dimensions of the irreducible representations. In other words, there is an upper bound for the number of perfectly uncorrelated antenna ports of given antenna geometry.”

The topic of modal excitation, despite the fact that a lot of work has already been published, hides many challenges which are waiting to be investigated and answered: Can CMs be classified into irreps “automatically” without the necessity of their visual inspection? Can a feasible number of orthogonal radiated patterns be predicted and what is the minimal number of feeders to excite all of them? What are the appropriate positions of these feeders?

2.3.3 Fundamental Bounds

Fundamental bounds [88–90] addresses the question raised when a device is designed: *What is the best achievable performance?* They are used to compare an existing design with its physical limits and to decide whether it is worth improving the design

further, or if it is already performing in an acceptable manner. In electromagnetism, one of the first investigations on fundamental bounds was related to the maximum directivity of a given antenna concluding that: “with the super-gain theorem, it is possible to design an aerial of arbitrarily small dimensions with a directivity as high as desired” [91]. The topic was further studied by Chu [92], who set a lower bound on the Q-factor for electrically small antennas. By expanding the field into spherical waves, he had shown that the Q-factor is inversely proportional to the third power of electric size of the smallest sphere enclosing the antenna. Among others [93–98], this work was followed by Harrington [99], who expressed Q-factor as the ratio of quadratic forms in MoM matrices. The topic of fundamental limits has become increasingly popular in recent years and has also entered the realm of optics and plasmonics [100–105].

Since many antenna quantities can be expressed as ratios of quadratic forms in the vector of current expansion coefficients, there exists a large number of works focused on finding the fundamental bounds of such parameters using QCQP [106]:

- minimizing the Q-factor [89, 107],
- maximizing antenna gain [62],
- maximizing radiation efficiency [99, 108], or
- minimizing the total active reflection coefficient (TARC) [109],

to name a few.

The solution is typically approached using Lagrange duality [106]. Modal analysis is frequently used within the process as a model order reduction technique or, since the corresponding dual problem has itself the form of a GEP, parameterized by Lagrange multipliers. In this latter case, the supremum of the dual function is a lower bound to the primal optimization problem [106] and is given by the minimum eigenvalue of the underlying eigenvalue problem.

Unfortunately, recent studies have revealed that degeneracies caused by the presence of point symmetries induce an erroneous duality gap [106], *i.e.*, the difference between the solution to the primal and dual problems. The empirical solutions showed that the combination of degenerated modes can suppress the duality gap [62, 107]. This approach is easy to apply to accidental degeneracies between two modes, but geometrically degenerated modes may introduce more options to combine.

For illustrative purposes, Figure 2.9 compares the lower bounds on the radiation Q-factor [61, 89] of various structures. The bound is compared to several realized self-resonant antennas. Note that the studied regions (a sphere, a torus, a cylinder) with continuous symmetries had to be discretized to evaluate the fundamental limits numerically. There exist two ways of how to prepare the discretization:

- to use non-symmetric mesh, *i.e.*, to treat the object as non-symmetric, in which case there cannot be degenerated modes causing an erroneous duality gap, or
- to use symmetric mesh keeping at least some symmetries of the original object, in which case a special treatment is needed to compute bounds correctly.

The latter is preferred for the remarkable speed-up in evaluating fundamental bounds.

The impact of point symmetries on fundamental bounds is studied in this thesis in detail. Namely, the following questions are answered: Can the block-diagonalization of a matrix describing a point-symmetrical structure accelerate the computational time of optimization? Can the classification of modes into irreps be beneficial in the

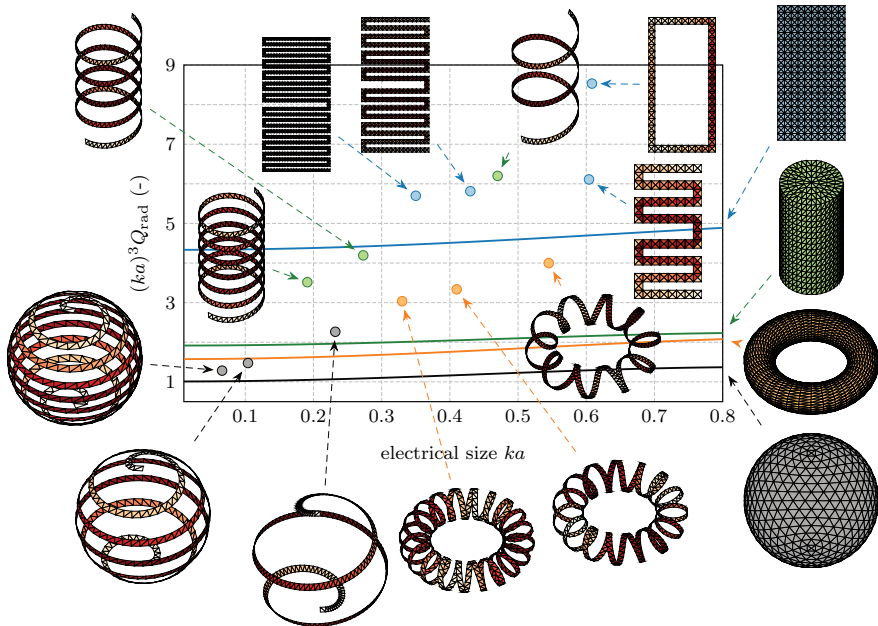


Figure 2.9: Comparison of lower bounds on radiation Q-factor [61, 89] with realized antennas. Solid lines represent bounds on various regions: a spherical shell (black), a torus (orange), a cylindrical tube (green), and a rectangular plate (blue). Markers represent the Q-factor of self-resonant antennas designed within the respective regions.

evaluation of fundamental bounds? Is it possible to determine which degenerated modes should be combined to eliminate the erroneous duality gap induced by symmetries? What is the role of the von Neumann-Wigner theorem in resolving these issues?

2.4 Thesis Objectives

The application of symmetries within electromagnetic theory offers many benefits as well as challenges. Several questions raised in the previous section have yet to be fully answered and are addressed in this thesis. The main aims are defined as follows:

1. Utilize point group theory within the MoM framework and the theory of characteristic modes.
2. Provide a deterministic solution to modal tracking.
3. Adopt symmetries to design excitation schemes on antennas to realize uncorrelated radiation states.
4. Study erroneous dual gaps occurring in QCQP problems defining the fundamental bounds on quadratic metrics on symmetrical structures.

The core of the thesis is based on four publications in *IEEE Transactions on Antennas and Propagation* covering the thesis objectives defined in [Section 2.4](#). Results from the thesis were also presented at six prestigious international conferences. The list of conference papers is enumerated in [Section F.5.2](#).

3.1 Publication A

- **M. Masek**, M. Capek, L. Jelinek, and K. Schab, “Modal Tracking Based on Group Theory,” *IEEE Transactions on Antennas and Propagation*, vol. 68, no. 2, pp. 927-937, Feb. 2020, DOI: [10.1109/TAP.2019.2943354](https://doi.org/10.1109/TAP.2019.2943354).

The basics of manipulation with symmetries within the MoM paradigm are described in this paper for surfaces represented by triangular mesh, see [Figure 3.1](#) which displays different meshes of a square plate, each of which are invariant under a different set of symmetry operations and belonging to a different point group. The paper proposes how to test invariance of objects under given symmetry operation R , how to construct mapping matrices $\mathbf{C}(R)$ and matrix representation $\mathbf{D}(R)$. Further, the classification of eigenmodes into irreps is presented, allowing us to use the von Neumann-Wigner theorem [20] which states that eigentraces can only cross (*i.e.*, accidental degeneracy occurs) if modes belong to different irreps. Eigentraces of modes belonging to the same irrep cannot cross each other. This provides a deterministic solution to modal tracking.

The construction of a symmetry-adapted basis is explained, and the benefits of block-diagonalizing a matrix operator are discussed. This block-diagonalization is then used to compute only eigenmodes from the selected irrep (species).

The paper is reprinted in [Appendix A](#).

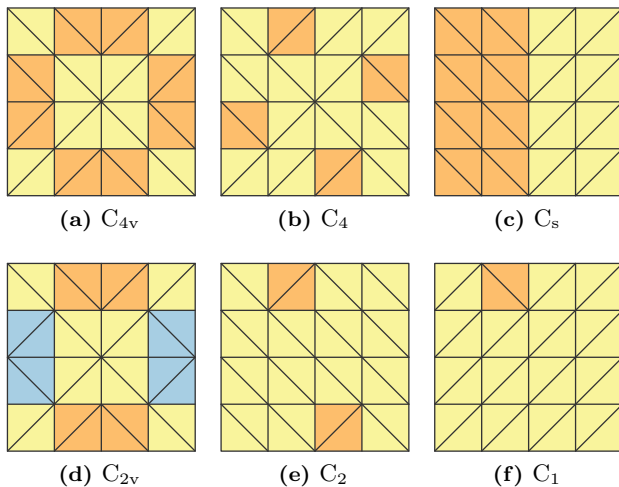


Figure 3.1: Six different meshes of a square plate. (a) Fully symmetrical mesh belonging into point group C_{4v} . (b)–(f) Not all symmetries are fulfilled, thus meshes belong only to different subgroups. Triangles highlighted by different colors point out areas of changed mesh with a significant impact on the presence/absence of some symmetry operations and, thus, the point group.

3.2 Publication B

- **M. Masek**, L. Jelinek, and M. Capek, “Excitation of Orthogonal Radiation Channels,” *IEEE Transactions on Antennas and Propagation*, vol. 69, no. 9, pp. 5365–5376, Mar. 2021, DOI: [10.1109/TAP.2021.3061161](https://doi.org/10.1109/TAP.2021.3061161).

This paper is dedicated to the question of the simultaneous excitation of several orthogonal radiation states used, for example, in MIMO applications. This is achieved by employing the orthogonality between irreps when symmetries are present.

The maximal number of realized orthogonal states is determined based on the point group to which the antenna structure belongs. The minimal number of ports required to excite all of the states is also evaluated. The (im)practicality of port placement at the reflection planes is discussed.

The procedure is illustrated, in detail, on an example showing the result of a search for the best position of ports to obtain the best average TARC over all excited orthogonal states. Thanks to the presence of symmetries, the task is reduced to find the position of the “initial” port in the region of the generator of the structure¹ and symmetry-adapted vectors (2.6) are used to acquire the solution on the entire structure. Examples of resulting far-field diagrams, each representing the desired orthogonal state, are shown in Figure 3.2.

The paper is reprinted in Appendix B.

¹The generator of the structure is its minimal part which, after the application of all symmetry operations, generates the entire structure.

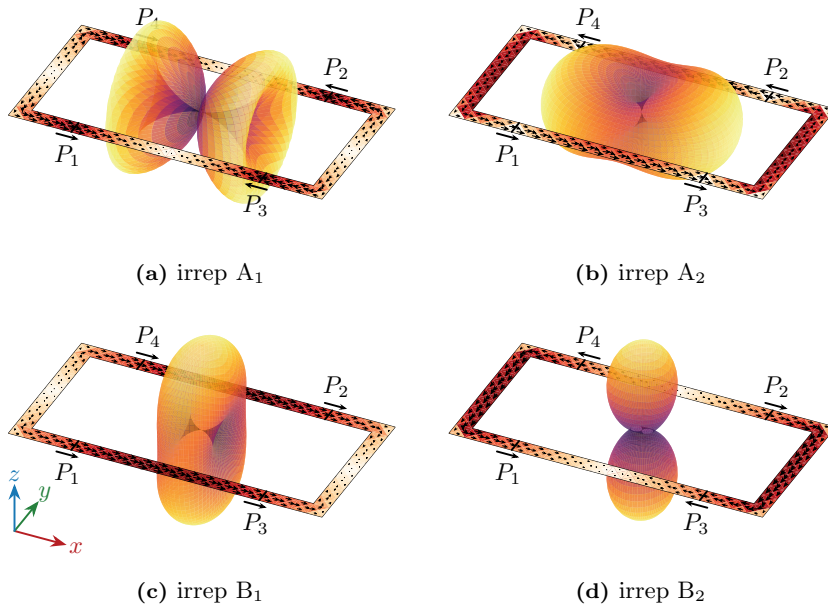


Figure 3.2: Four symmetrically placed ports were excited so as to excite currents belonging to different irreps and providing four orthogonal radiation channels on a rectangular rim.

3.3 Publication C

- M. Capek, L. Jelinek, and M. Masek, “Finding Optimal Total Active Reflection Coefficient and Realized Gain for Multiport Lossy Antennas,” *IEEE Transactions on Antennas and Propagation*, vol. 69, no. 5, pp. 2481-2493, May 2021, DOI: [10.1109/TAP.2020.3030941](https://doi.org/10.1109/TAP.2020.3030941).

The paper provides a study of antenna **TARC** and realized gain, and shows how these factors can possibly be improved. At the beginning, these antenna parameters are described using **MoM**-based quantities and are subsequently reduced to port-based expressions. Since the number of the connected ports is typically low, this formulation significantly reduces the computational time of the following optimization that follows.

TARC is evaluated for two cases: a single-port and a multi-port antenna. The latter structure is taken as an example on which the **TARC** parameter is tuned by finding the optimal excitation coefficient, the optimal port’s characteristic impedance, the best port positions, tuning admittances, and optimal matching. Some of these optimizations are described as **QCQP** problems to be solved by an eigenvalue problem, while others lead to combinatorial optimization problems solved by an exhaustive search. The optimization of realized gain is another example studied in the paper.

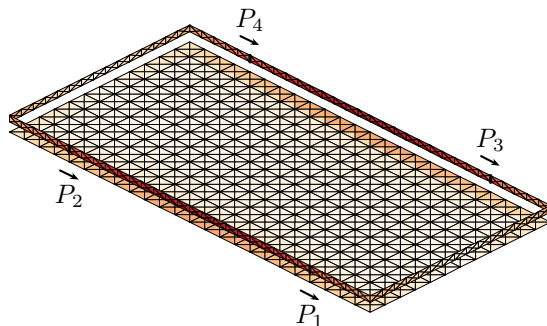


Figure 3.3: Four ports are considered at positions highlighted by black labels, and their voltage optimized to provide the best TARC. Notice that the symmetrical placement of ports, together with the symmetrical mesh of the structure, results in the same voltage for each port. The structure belongs to point group C_{2v} which has only one-dimensional irreps with characters $\chi^\alpha(R) = \pm 1$.

It can be noticed that the structure used in all examples has symmetrical mesh on the rim, but the ground plane is not symmetrical, see, for example, Figure C.4. Considering a perfectly symmetrical structure, point group theory dictates, in this case, unitary voltages with a corresponding orientation defined by the dominating irrep, see Figure 3.3. Despite the slightly asymmetrical ground plane, voltages in Figures C.13c and C.13d are, however, close to be symmetrical. Having symmetrical mesh would allow for applying the theory described in this thesis to accelerate the computations or to reduce the searched area for port's placement only to the generator of the structure.

The paper is reprinted in Appendix C.

3.4 Publication D

- M. Capek, L. Jelinek, and M. Masek, “A Role of Symmetries in Evaluation of Fundamental Bounds,” *IEEE Transactions on Antennas and Propagation*, vol. 69, no. 11, pp. 7729-7742, Nov. 2021, DOI: [10.1109/TAP.2021.3070103](https://doi.org/10.1109/TAP.2021.3070103).

This paper studies two general classes of QCQPs: those containing only quadratic terms and those which include linear terms. The paper shows, on an example of Q-factor minimization, that purely quadratic programmes for symmetrical structures suffer from an erroneous duality gap which presents itself as an accidental degeneracy in Lagrange's multipliers. Further study shows that a linear combination of the degenerated eigenmodes can eliminate this erroneous duality gap. The case where an accidental degeneracy occurs between geometrically degenerated modes is also introduced since it provides an additional degree of freedom to choose which two modes can be combined to eliminate the erroneous duality gap, see an illustrative example in Figure 3.4.

Other presented examples show the impact of the symmetrical imperfections of mesh on the presence of degeneracies, or change of basis to port-modes representation which reduces the size of the problem while the procedure remains valid. The paper concludes with a robust algorithm eliminating the erroneous duality gap.

The paper is reprinted in Appendix D.

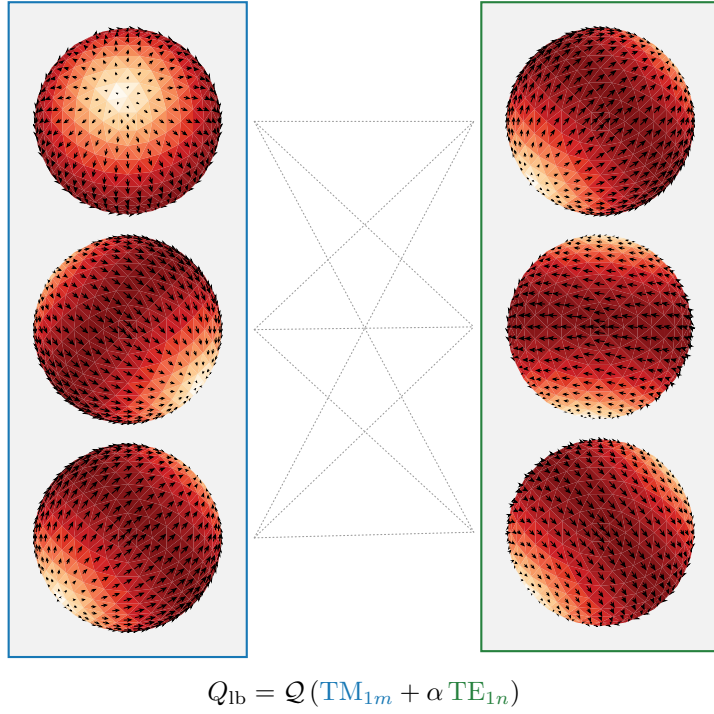


Figure 3.4: Example of linear combinations of **TM** and **TE** characteristic modes that can, in this specific case, eliminate the erroneous duality gap and reach the fundamental bound on the radiation Q-factor. Degeneracies provide an additional degree of freedom to which modes to use.

The thesis studied the utilization of point symmetries in computational electromagnetics. The mathematical formulation was based on a method of moments (MoM) framework utilizing piece-wise basis functions. Point group theory was employed, and irreducible representations of the structure were used to create a so-called symmetry-adapted basis. It was shown that this basis block-diagonalizes MoM matrix operators where each block corresponds to one irreducible representation. In such a case, both the modal decompositions and the solution to the equation system can be made block-wise resulting in a significant reduction of computation time.

The classification of eigenmodes into irreducible representations, together with the von Neumann-Wigner theorem, was used to provide a deterministic solution to modal tracking. It had been shown and verified that the accidental crossing could only appear between modes from different irreducible representations. Mixing modes from different irreducible representations was also utilized to eliminate the erroneous duality gap, which occurs in quadratically constrained quadratic program problems when geometrical degeneracies are present.

Bearing in mind a potential application in multiple-input multiple-output systems, the orthogonality between irreducible representations was utilized to simultaneously excite several orthogonal radiation states. The maximal number of excitable orthogonal states and the minimal number of feeders needed to excite them was determined solely from the knowledge of symmetry operations under which the structure is invariant.

4.1 Future Work

Besides the topics solved in this thesis, several other symmetry-related issues may be challenged in future:

- It would be interesting to generalize the presented theory by including other types of symmetries: translational and glide symmetries, which could be utilized for the analysis and synthesis of antenna arrays, waveguide filters, and other periodic structures.
- It is of interest to utilize symmetries in other numerical methods, *e.g.*, in multilevel fast multipole method [110]. It has been shown that this method, used typically for electrically large objects with an enormous number of unknowns unsuitable for MoM, can also be used to compute characteristic

modes [111, 112], and symmetries could be used to reduce the computational complexity.

- Symmetries could also be utilized to reduce the number of degrees-of-freedom in topology optimization [113] which would result in accelerated design procedure and also to designs more appealing to human eye. Alternatively, asymmetrical structures can be penalized during the shape optimization process.
- Another topic is a development of an algorithm that automatically detects all symmetry operations under which the input mesh is invariant. That would make the use of implemented algorithms easier for the user. In their current version, it is required to supply the list of symmetry operations together with the mesh.



Modal Tracking Based on Group Theory

Published as: M. Masek, M. Capek, L. Jelinek, and K. Schab, “Modal Tracking Based on Group Theory,” *IEEE Transactions on Antennas and Propagation*, vol. 68, no. 2, pp. 927-937, Feb. 2020, DOI: [10.1109/TAP.2019.2943354](https://doi.org/10.1109/TAP.2019.2943354).

Abstract—Issues in modal tracking in the presence of crossings and crossing avoidances between eigenvalue traces are solved via the theory of point groups. The von Neumann-Wigner theorem is used as a key factor in predictively determining mode behavior over arbitrary frequency ranges. The implementation and capabilities of the proposed procedure are demonstrated using characteristic mode decomposition as a motivating example. The procedure is, nevertheless, general and can be applied to an arbitrarily parametrized eigenvalue problems. A treatment of modal degeneracies is included and several examples are presented to illustrate modal tracking improvements and the immediate consequences of improper modal tracking. An approach leveraging a symmetry-adapted basis to accelerate computation is also discussed. A relationship between geometrical and physical symmetries is demonstrated on a practical example.

Index terms: Antenna theory, computer simulation, eigenvalues and eigenfunctions, electromagnetic modeling, method of moments (MoM), modal analysis.

A.1 Introduction

Modal tracking is an important part of every procedure dealing with parametrized eigenvalue problems. In antenna theory, eigenvalue problems—for example, the problem defining characteristic modes (CMs) [49]—are commonly parametrized in frequency and solved at a finite set of discrete frequency points. Therefore, tracking is required to order and associate modes across the frequency band of interest so as to obtain modal quantities which are smooth functions of frequency. A common way of dealing with modal tracking is to employ correlation between modes [64–68]. Despite the success of correlation-based tracking [52], there are, however, scenarios in which this technique fails to provide reliable results. One specific example where correlation-based tracking becomes difficult in the vicinity of accidental degeneracies or crossing avoidances [20, 114]. Point group theory [30, 32, 115] has recently been

used to provide ground truth for determining whether modal degeneracies may exist by means of the von Neumann-Wigner theorem and to show that if the object under study exhibits no symmetry, traces of the characteristic numbers, as functions of frequency, cannot cross [20, 72]. Simultaneously, it has been shown that when symmetries are present, modes can be divided into separate unique sets called irreducible representations (irreps) and that within these sets, modal crossings are limited by simple, known features of each irrep. The problem of how to detect symmetries and assign modes to irreps in the general case of multidimensional irreps encountered in bodies with non-abelian symmetry groups [30] has not been solved. Our goal in this work is to establish a robust modal tracking implementation based on the fundamental modal crossing rules discussed in [72] capable of working with non-symmetric, abelian symmetric, and non-abelian symmetric structures.

To accomplish this, a procedure for performing classification of modes is developed for surfaces having any known symmetry point group. An application for broadband characteristic mode tracking, which includes two approaches, is demonstrated. The first, an *a posteriori* approach, deals with previously calculated modes and their assignment into irreps. The second, an *a priori* approach, uses a symmetry-adapted basis to block-diagonalize the underlying operator and divide the problem into a series of smaller parts which are solved independently. Each part spans a separate eigenmode subspace corresponding to a given irrep [56]. Computation speed is remarkably accelerated in this latter approach due to the cubic dependence of computation time on the number of discretization elements. Despite the aforementioned differences, both methods divide modes into sets where traces of the eigenvalues cannot cross, automatically solving the eigenvalue crossing/crossing avoidance issue. A framework based on group theory presented in this paper is numerically implemented on Rao-Wilton-Glisson (RWG) basis functions [51] and its capabilities are demonstrated on characteristic mode decomposition [49]. It should, however, be noted that the results are applicable to other modal decompositions or alternative choices of basis functions as well.

The paper is organized as follows. Background theory is reviewed in Section A.2 where characteristic modes are introduced as an example generalized eigenvalue problem in Section A.2.1. Point group theory and modal classification into irreps is described in Section A.2.2 and the utilization of a symmetry-adapted basis to reduce the original problem is shown in Section A.2.3. Section A.3 describes a practical implementation and basic results using an illustrative example. Further examples of results are presented in Section A.4. Section A.5 is dedicated to a discussion of several related topics: the importance of modal tracking in Section A.5.1, the effective generation of a symmetry-adapted basis in Section A.5.2, the reduction of computational time of modal decomposition in Section A.5.3 and the relationship between geometrical and physical symmetries in Section A.5.4. Section A.6 concludes the paper.

A.2 Background Theory

The following sections briefly summarize the theory of characteristic modes (Section A.2.1) and point group theory (Sections A.2.2 and A.2.3). Details related to modal tracking are emphasized.

A.2.1 Characteristic Modes

Characteristic modes (CMs) [49] form a set of orthogonal solutions to a generalized eigenvalue problem (GEP) [36]

$$\mathcal{X}\mathbf{J}_n(\mathbf{r}) = \lambda_n \mathcal{R}\mathbf{J}_n(\mathbf{r}), \quad (\text{A.1})$$

in which $\mathcal{Z} = \mathcal{R} + j\mathcal{X}$ is the impedance operator [49] defined for a perfectly electrically conducting body Ω as

$$\mathcal{Z}\mathbf{J}(\mathbf{r}) = \hat{\mathbf{n}} \times \hat{\mathbf{n}} \times \mathbf{E}(\mathbf{J}(\mathbf{r})). \quad (\text{A.2})$$

In (A.2), $\mathbf{r} \in \Omega$, $\hat{\mathbf{n}}$ denotes a unit normal to surface Ω and \mathbf{E} denotes the scattered electric field produced by the electric current $\mathbf{J}(\mathbf{r})$ [116]. Each characteristic vector $\mathbf{J}_n(\mathbf{r})$ and its corresponding characteristic number λ_n define a unique eigen-solution, completely independent of excitation, as being a sole function of geometry Ω and angular frequency ω . The most appealing property of CMs is their ability to diagonalize the impedance operator (A.2) as

$$\frac{\langle \mathbf{J}_m(\mathbf{r}), \mathcal{Z}\mathbf{J}_n(\mathbf{r}) \rangle}{\langle \mathbf{J}_n(\mathbf{r}), \mathcal{R}\mathbf{J}_n(\mathbf{r}) \rangle} = (1 + j\lambda_n) \delta_{mn}, \quad (\text{A.3})$$

where $\langle \cdot, \cdot \rangle$ is the inner product

$$\langle \mathbf{A}(\mathbf{r}), \mathbf{B}(\mathbf{r}) \rangle = \int_{\Omega} \mathbf{A}^*(\mathbf{r}) \cdot \mathbf{B}(\mathbf{r}) d\mathbf{r} \quad (\text{A.4})$$

and δ_{mn} is the Kronecker delta.

The solution to (A.1) is typically approached using the method of moments (MoM) [28] which recasts the original integro-differential problem into a matrix problem, *i.e.*,

$$\mathbf{X}\mathbf{I}_n = \lambda_n \mathbf{R}\mathbf{I}_n, \quad (\text{A.5})$$

using a set of M basis functions $\{\psi_m(\mathbf{r})\}$ to approximate the current density as

$$\mathbf{J}(\mathbf{r}) \approx \sum_{m=1}^M I_m \psi_m(\mathbf{r}) \quad (\text{A.6})$$

and performing Galerkin testing [37], *i.e.*,

$$\mathbf{R} + j\mathbf{X} = [z_{mn}] = [\langle \psi_m(\mathbf{r}), \mathcal{Z}\psi_n(\mathbf{r}) \rangle]. \quad (\text{A.7})$$

Within the discretized (matrix) form, the unknowns are column vectors of expansion coefficients $\mathbf{I} \in \mathbb{C}^{M \times 1}$, see [28]. If N characteristic modes are calculated, they form a matrix $[\mathbf{I}] = [\mathbf{I}_1, \dots, \mathbf{I}_n, \dots, \mathbf{I}_N] \in \mathbb{C}^{M \times N}$ with an associated vector of eigenvalues $\boldsymbol{\lambda} = [\lambda_1, \dots, \lambda_n, \dots, \lambda_N]$. Notice that, theoretically, $[\mathbf{I}]$ is a square matrix ($M = N$), however, in practice, the number of modes is typically limited to $N \ll M$ due to numerical constraints [52].

The necessity of modal tracking arises from the fact that the GEP (A.1) is parametrized by angular frequency ω . Therefore, if (A.5) is to be solved at F unique frequency points, its solution must be evaluated at each frequency point independently. If collected together, the resulting matrix structure of the eigenvalues

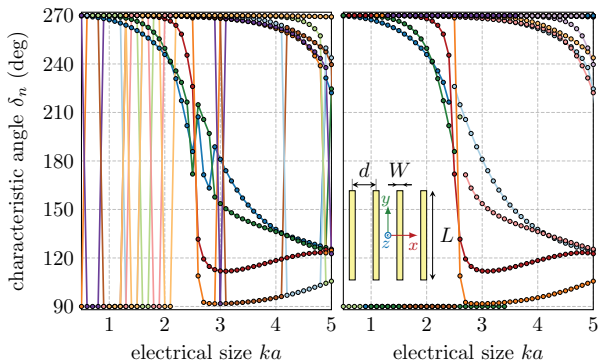


Figure A.1: Raw untracked (left) and correlation tracked (right) traces of characteristic angles. Point markers indicate computed frequency samples.

reads $[\boldsymbol{\lambda}] \in \mathbb{R}^{F \times N}$. Generally, there is no guarantee that all of the eigenvalues (and similarly for eigenvectors) in one column of $[\boldsymbol{\lambda}]$ will belong to the same mode, *i.e.*, the modal data are not properly tracked over frequency. Consequently, the frequency behavior of the individual characteristic modes cannot be effectively studied.

The effects of insufficient tracking are demonstrated in [Figure A.1](#) on a practical example of four parallel dipoles made of a perfect electric conductor (PEC) with length L , width $W = L/25$, and separation distance $d = L/2$. Frequency is scaled as electrical size ka (k is the free space wave-number and a is the radius of the smallest circumscribing sphere) and spans from $ka = 0.5$ to $ka = 5$ with $F = 46$ equidistantly distributed frequency samples. The first $N = 15$ characteristic modes were calculated in Antenna Toolbox for MATLAB (AToM) [29] using $M = 496$ RWG basis functions [51]. The left panel of [Figure A.1](#) shows untracked eigenvalue modal traces, while the right panel of the same figure shows modal eigenvalue traces tracked using correlation between two neighboring frequencies [64, 65]. The characteristic numbers λ_n are rescaled as characteristic angles δ_n , [47, 54]

$$\delta_n = 180^\circ \left(1 - \frac{1}{\pi} \arctan(\lambda_n) \right). \quad (\text{A.8})$$

The results presented in [Figure A.1](#) demonstrate the impact of modal tracking as well as some of the shortcomings of current and field correlation based tracking algorithms previously discussed in the literature [66–68]. Specifically, it is observed that tracking problems commonly occur in regions where modal eigenvalue traces cross or come very near one another. Some traces are also unpredictably stopped while new traces arise when the correlation value between modes at adjacent frequency samples do not exceed some user-defined threshold.

While the preceding discussion focused on characteristic modes, many problems in computational electromagnetics rely on the broadband solution of parametrized eigenvalue problems in the form of

$$\mathbf{A}(p) \mathbf{I}_n = \lambda_n \mathbf{B}(p) \mathbf{I}_n, \quad (\text{A.9})$$

for which the same consideration of broadband tracking must be given for the proper and consistent interpretation of results.

A.2.2 Point Group Theory and Classification of Modes

This section introduces necessary elements of the theory of symmetry point groups [30, 32, 115] as well as key results from group theory which are relevant for the symmetry classification of eigenmodes and eigenvalue tracking.

To begin, assume a surface Ω which supports a surface current density $\mathbf{J}(\mathbf{r})$. The symmetry point group G of this object is the set $G = \{R_i\}$ of all symmetry operations R (*e.g.*, identity E , n -fold rotations C_n , reflections σ , and their products) to which the object is invariant. Let the vector space V contain all possible complex current distributions $\mathbf{J}(\mathbf{r})$ on this object. The operation R maps V onto itself, *i.e.*,

$$R\mathbf{J}(\mathbf{r}) = \mathbf{T}(R)\mathbf{J}(\mathbf{T}^{-1}(R)\mathbf{r}) \in V, \quad \forall \mathbf{J}(\mathbf{r}) \in V, \quad (\text{A.10})$$

or, equivalently, the operation R transforms one current on Ω into another current on Ω . The matrix $\mathbf{T}(R)$ in (A.10) is a 3×3 coordinate transformation matrix corresponding¹ to the operation R . If a finite basis $\{\psi_m(\mathbf{r})\}$ is chosen to approximate the space V according to (A.6), and if the basis is chosen to preserve the symmetry of Ω (*i.e.*, the object Ω is represented by a mesh which preserves all symmetries of the object), then by (A.10),

$$R\psi_n(\mathbf{r}) = \sum_{m=1}^M c_{mn}(R)\psi_m(\mathbf{r}). \quad (\text{A.11})$$

Note here that R is any element of group G , and that the coefficients $c_{mn}(R)$ can be collected in a mapping matrix $\mathbf{C}(R) = [c_{mn}(R)]$. Thus, by (A.6), the effect of R on the current $\mathbf{J}(\mathbf{r})$ is realized by

$$R\mathbf{I} = \mathbf{C}(R)\mathbf{I}, \quad (\text{A.12})$$

where $R\mathbf{I}$ is the vector of expansion coefficients corresponding to $R\mathbf{J}(\mathbf{r})$. The set of mapping matrices $\{\mathbf{C}(R \in G)\}$ define a matrix representation of G . The structure and nature of these matrices is dependent of the basis chosen. Consider N current expansion vectors \mathbf{I}_n which form a modal basis. These can, *e.g.*, be CMs defined by (A.5). Equivalently, as shown in (A.11), the effect of R on a particular mode can be expressed as

$$R\mathbf{I}_n = \sum_{m=1}^N d_{mn}(R)\mathbf{I}_m, \quad (\text{A.13})$$

where the matrix $\mathbf{D}(R) = [d_{mn}(R)]$ is a matrix representation of R in the modal basis. Arranging all modal vectors \mathbf{I} and $R\mathbf{I}$ into matrices $[\mathbf{I}]$ and $\mathbf{C}(R)[\mathbf{I}]$, relation (A.13) can also be written as

$$[\mathbf{I}]\mathbf{D}(R) = \mathbf{C}(R)[\mathbf{I}]. \quad (\text{A.14})$$

For a symmetrical object, subsets of modes exclusively map onto themselves with each operation $R \in G$, [30]. This is observed, after the specific ordering of columns in the matrix $[\mathbf{I}]$, as a block diagonalization of $\mathbf{D}(R)$,

$$\begin{bmatrix} \mathbf{D}_1(R) & 0 & 0 & 0 \\ 0 & \mathbf{D}_2(R) & 0 & 0 \\ 0 & 0 & \ddots & 0 \\ 0 & 0 & 0 & \mathbf{D}_Q(R) \end{bmatrix} = [\mathbf{I}]^{-1}\mathbf{C}(R)[\mathbf{I}]. \quad (\text{A.15})$$

¹We assume that $\mathbf{J}(\mathbf{r})$ is a polar vector.

Each collection of block matrices $\{\mathbf{D}_q(R \in G)\}$, for a certain block number $q \in \{1, \dots, Q\}$, and its corresponding subset of the modal basis, is known as an irreducible representation (irrep) of the group G , [30]. The characters $\chi_q(R) = \text{tr}(\mathbf{D}_q(R))$ are commonly used to fully characterize the group G and to classify modes within irreps. Note that the block matrices of a particular irrep may be repeated multiple times along the diagonal of $\mathbf{D}(R)$, which means that separate sets of modes may belong to the same irrep but map only onto themselves. The dimension of the block matrices in an irrep is known as the dimension g^α of that irrep, where the superindex α is used throughout the paper to denote different irreps². For the rest of the paper, a particular block, *e.g.*, $\mathbf{D}_q(R)$, corresponding to an irrep α is denoted $\mathbf{D}^\alpha(R)$.

Identifying irreps, the von Neumann-Wigner theorem [20] states that modal degeneracies can only occur between modes of the same irrep up to the dimension of that irrep. Given that the difficulties in tracking characteristic modes over frequency largely stem from the accurate identification of degeneracies [114] (eigenvalue crossings), this result is of great utility and provides an analytic ground truth for verifying mode tracking algorithms. For example, this result states that two eigenvalue traces may not cross if both belong to modes within the same Abelian (one-dimensional) irrep. If a modal tracking algorithm under test outputs eigenvalue traces that do cross in spite of this, we can deduce that the modal tracking was not performed correctly. A similar situation occurs in higher-dimension irreps with continuously degenerated modes, as discussed in Section A.4.2.

A.2.3 Symmetry-Adapted Basis and Reduced Problems

The presence of symmetries is not limited to the *a posteriori* classification of modes as described above, but it can be used to produce “symmetry-adapted” eigenvalue problems that directly produce modes corresponding to a given irrep. To that point, imagine that matrices $\mathbf{D}^\alpha(R)$ are known. Then, according to [30], the left hand side of

$$\mathbf{v}^\alpha = \frac{g^\alpha}{g} \sum_{R \in G} \tilde{d}_{ii}^\alpha(R) \mathbf{C}(R) \mathbf{v}, \quad (\text{A.16})$$

is a transformed version of the arbitrary vector \mathbf{v} which is “symmetry-adapted” to the i -th degeneracy (dimension) of irrep α . Here, $\tilde{\mathbf{D}} = (\mathbf{D}^{-1})^T$ stands for a contra-gradient representation, and $g = \sum_\alpha (g^\alpha)^2$ is the order of group G . Here we assign \mathbf{v} as the columns of an $M \times M$ identity matrix, so that

$$\boldsymbol{\rho}_i^\alpha = \frac{g^\alpha}{g} \sum_{R \in G} \tilde{d}_{ii}^\alpha(R) \mathbf{C}(R) \quad (\text{A.17})$$

produces matrices $\boldsymbol{\rho}_i^\alpha$ whose columns are “symmetry-adapted” vectors. Naturally, there are only $\eta^\alpha = \text{rank}(\boldsymbol{\Gamma}_i^\alpha) \leq M$ linearly independent columns in each matrix $\boldsymbol{\rho}_i^\alpha$. Removal of the linearly dependent columns from the matrices $\boldsymbol{\rho}_i^\alpha$ produces matrices $\boldsymbol{\Gamma}_i^\alpha$ of size $M \times \eta^\alpha$ which are able to modify matrix operators of the physical system at hand so that their eigenvectors belong solely³ to an irrep α . Explicitly,

²Standard designations for irreps are used in this paper: A and B for one-dimensional irreps, E for two-dimensional irreps and T for three-dimensional irreps, see, *e.g.*, [30].

³In the case of multidimensional representation, all matrices $\boldsymbol{\Gamma}_i^\alpha$ for $i \in \{1, \dots, g^\alpha\}$ must be employed to obtain all modes belonging to an irrep α .

having a generalized eigenvalue problem (A.9), a solution subspace of eigenvectors belonging to an irrep α is found, assuming that in this irrep, due to the presence of symmetry, an eigenvector $\mathbf{I} \in \mathbb{C}^{M \times 1}$ can be composed as $\mathbf{\Gamma}_i^\alpha \widehat{\mathbf{I}}_i^\alpha$, where $\widehat{\mathbf{I}}_i^\alpha \in \mathbb{C}^{n^\alpha \times 1}$. Substituting into (A.9) and multiplying from the left by $(\mathbf{\Gamma}_i^\alpha)^\top$ results in

$$\widehat{\mathbf{A}}_i^\alpha \widehat{\mathbf{I}}_{i,n}^\alpha = \lambda_{i,n}^\alpha \widehat{\mathbf{B}}_i^\alpha \widehat{\mathbf{I}}_{i,n}^\alpha, \quad (\text{A.18})$$

where

$$\widehat{\mathbf{A}}_i^\alpha = (\mathbf{\Gamma}_i^\alpha)^\top \mathbf{A} \mathbf{\Gamma}_i^\alpha, \quad (\text{A.19})$$

$$\widehat{\mathbf{B}}_i^\alpha = (\mathbf{\Gamma}_i^\alpha)^\top \mathbf{B} \mathbf{\Gamma}_i^\alpha. \quad (\text{A.20})$$

The modes generated by the eigenvalue problem (A.18) belong solely to the irrep α .

The matrices $\mathbf{D}^\alpha (R \in G)$ must be known in order to evaluate the reduction matrices $\mathbf{\Gamma}_i^\alpha$. It is important, however, to realize that these can be obtained from any eigenvalue decomposition using (A.15) on any object with the same symmetries. This initial object can, therefore, be chosen to have a minimal number of basis functions, making the evaluation of the matrices $\mathbf{D}^\alpha (R \in G)$ computationally inexpensive.

A.3 Practical Evaluation of Required Matrices

An implementation of the methodology introduced in the previous sections is shown on a test case, depicted in Figure A.2, consisting of a triangularized domain Ω , [117], for which $N = 5$ RWG basis functions are generated. Construction of the matrices $\mathbf{C}(R)$, $\mathbf{D}(R)$, and $\mathbf{\Gamma}_i^\alpha$ is demonstrated using this simple object with symmetry group⁴ $G = \{\mathbf{E}, \sigma_v^{yz}, \sigma_v^{xz}, C_2^z\}$.

A.3.1 Construction of Matrices $\mathbf{C}(R)$

A necessary step to classify modes according to their symmetry properties is to construct mapping matrices $\mathbf{C}(R \in G)$. Here we assume that each basis function is mapped onto exactly one basis function under each symmetry operation within the symmetry group of the system. Under this assumption, the behavior of symmetry operation R is tested individually by (A.10) for all doublets of basis functions as

$$\gamma_m(R) = n : \boldsymbol{\psi}_n(\mathbf{r}) = s_m(R) \mathbf{T}(R) \boldsymbol{\psi}_m(\mathbf{T}^{-1}(R) \mathbf{r}), \quad (\text{A.21})$$

where the vector $\boldsymbol{\gamma}(R)$ contains an integer n at each position m so that the basis functions $\boldsymbol{\psi}_m$ and $\boldsymbol{\psi}_n$ map onto one another by the operation $\mathbf{T}(R)$ with a sign $s_m = \pm 1$. The vectors $\boldsymbol{\gamma}(R)$ and $\mathbf{s}(R)$ are constructed for all symmetry operations $R \in G$.

With all vectors $\boldsymbol{\gamma}(R \in G)$ and $\mathbf{s}(R \in G)$ known, the orthonormal mapping matrices $\mathbf{C}(R \in G) = [c_{mn}(R)]$, see (A.11) and (A.12), are constructed as

$$c_{mn}(R) = \begin{cases} s_m(R) & \text{if } n = \gamma_m(R), \\ 0 & \text{otherwise.} \end{cases} \quad (\text{A.22})$$

A particular example of this procedure is shown in Figure A.2, including the vectors $\boldsymbol{\gamma}(R)$ and $\mathbf{s}(R)$, and the resulting matrices $\mathbf{C}(R \in G)$. Note that the trivial results associated with the identity operator \mathbf{E} are omitted.

⁴It is supposed that the set of operations G is known for a given structure.

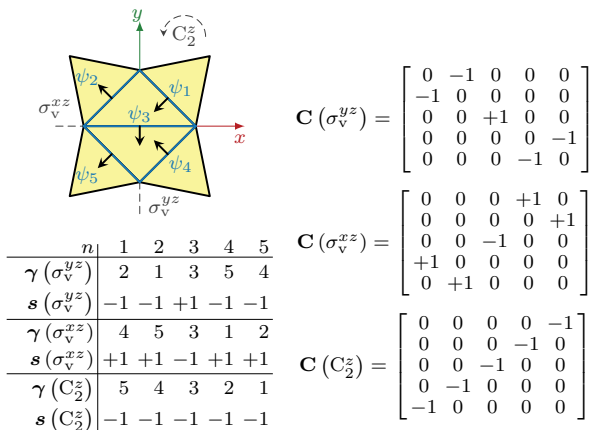


Figure A.2: An illustration of a simple symmetric structure with depicted RWG basis functions $\{\psi_n(\mathbf{r})\}$. The structure belongs to point group C_{2v} [30] with symmetry operations $G = \{E, \sigma_v^{yz}, \sigma_v^{xz}, C_2^z\}$. Vectors $\gamma(R \in G)$, $\mathbf{s}(R \in G)$, and matrices $\mathbf{C}(R \in G)$ are shown. The matrix $\mathbf{C}(E)$ is an identity matrix and is omitted.

A.3.2 Construction of Matrices $\mathbf{D}(R)$

The next step is the evaluation of matrices $\mathbf{D}(R)$ using (A.15). To do so, the impedance matrix \mathbf{Z} is computed and CMs are found by (A.5). The resulting modal basis and corresponding matrices $\mathbf{D}(R)$ are depicted in Figure A.3 (the identity matrix for identity operation E is omitted). In this case, the diagonal blocks in (A.15) are of size 1×1 which is a signature of the abelian nature of the C_{2v} symmetry group [30].

Collecting the unique traces from the on-diagonal block matrices (here directly from diagonal entries) gives the character table. Notice that the trace record corresponding to the B_2 irrep is repeated twice indicating that there are two modes in the matrix $[\mathbf{I}]$ belonging to the B_2 irrep (the first and the fifth).

It is important to realize that diagonal blocks of the matrices $\mathbf{D}(R)$ and their corresponding traces are a property of given symmetry. Therefore, once calculated, they can be reused for all structures of the same point group.

A.3.3 Construction of Symmetry-Adapted Basis Γ^α

The final step is the construction of symmetry-adapted bases which are used for the block-diagonalization of the eigenvalue problem. The matrices ρ_i^α are generated from (A.17) and only

$$M = \sum_{\alpha} g^{\alpha} \eta^{\alpha}, \quad (\text{A.23})$$

linearly independent columns are kept in matrices Γ_i^α , as depicted in Figure A.4. For a given discretization, the symmetry-adapted bases Γ_i^α are utilizable either to compress an arbitrary eigenvalue problem as in (A.18) in order to find solutions

$$\mathbf{I} = \begin{bmatrix} 1 & -1 & -1 & 1 & -1 \\ -1 & 1 & -1 & 1 & 1 \\ -a & 0 & 0 & 0 & -b \\ -1 & -1 & 1 & 1 & 1 \\ 1 & 1 & 1 & 1 & -1 \end{bmatrix}$$

$$\mathbf{D}(\sigma_v^{yz}) = \begin{bmatrix} +1 & 0 & 0 & 0 & 0 \\ 0 & +1 & 0 & 0 & 0 \\ 0 & 0 & -1 & 0 & 0 \\ 0 & 0 & 0 & -1 & 0 \\ 0 & 0 & 0 & 0 & +1 \end{bmatrix}$$

C_{2v}	E	σ_v^{yz}	σ_v^{xz}	C_2^z
A ₁	+1	+1	+1	+1
A ₂	+1	-1	-1	+1
B ₁	+1	-1	+1	-1
B ₂	+1	+1	-1	-1

$$\mathbf{D}(\sigma_v^{xz}) = \begin{bmatrix} -1 & 0 & 0 & 0 & 0 \\ 0 & +1 & 0 & 0 & 0 \\ 0 & 0 & -1 & 0 & 0 \\ 0 & 0 & 0 & +1 & 0 \\ 0 & 0 & 0 & 0 & -1 \end{bmatrix}$$

$$\mathbf{D}(C_2^z) = \begin{bmatrix} -1 & 0 & 0 & 0 & 0 \\ 0 & +1 & 0 & 0 & 0 \\ 0 & 0 & +1 & 0 & 0 \\ 0 & 0 & 0 & -1 & 0 \\ 0 & 0 & 0 & 0 & -1 \end{bmatrix}$$

Figure A.3: Eigenvectors \mathbf{I} computed by (A.5) at $ka = 0.5$ and corresponding matrices \mathbf{D} ($R \in G$) are shown for the structure depicted in Figure A.2. Each vector is normalized resulting in $a = 1.764$ and $b = 1.616$. Association of modes with particular irreps is performed by comparing the traces of submatrices within matrices \mathbf{D} (in this case simply the values on the diagonal of matrices \mathbf{D}) and values in character table. This association is highlighted by colored squares. Here $\{\alpha\} = \{B_2, A_1, A_2, B_1, B_2\}$.

$$\rho^{A_1} = \frac{1}{4} \begin{bmatrix} 1 & -1 & 0 & 1 & -1 \\ -1 & 1 & 0 & -1 & 1 \\ 0 & 0 & 0 & 0 & 0 \\ 1 & -1 & 0 & 1 & -1 \\ -1 & 1 & 0 & -1 & 1 \end{bmatrix} \quad \rho^{B_1} = \frac{1}{4} \begin{bmatrix} 1 & 1 & 0 & 1 & 1 \\ 1 & 1 & 0 & 1 & 1 \\ 0 & 0 & 0 & 0 & 0 \\ 1 & 1 & 0 & 1 & 1 \\ 1 & 1 & 0 & 1 & 1 \end{bmatrix}$$

$$\Gamma^{A_1} = \frac{1}{4} [1 \ -1 \ 0 \ 1 \ -1]^T \quad \Gamma^{B_1} = \frac{1}{4} [1 \ 1 \ 0 \ 1 \ 1]^T$$

$$\rho^{A_2} = \frac{1}{4} \begin{bmatrix} 1 & 1 & 0 & -1 & -1 \\ 1 & 1 & 0 & -1 & -1 \\ 0 & 0 & 0 & 0 & 0 \\ -1 & -1 & 0 & 1 & 1 \\ -1 & -1 & 0 & 1 & 1 \end{bmatrix} \quad \rho^{B_2} = \frac{1}{4} \begin{bmatrix} 1 & -1 & 0 & -1 & 1 \\ -1 & 1 & 0 & 1 & -1 \\ 0 & 0 & 4 & 0 & 0 \\ -1 & 1 & 0 & 1 & -1 \\ 1 & -1 & 0 & -1 & 1 \end{bmatrix}$$

$$\Gamma^{A_2} = \frac{1}{4} [1 \ 1 \ 0 \ -1 \ -1]^T \quad \Gamma^{B_2} = \frac{1}{4} [1 \ -1 \ 0 \ -1 \ 1]^T$$

Figure A.4: Matrices ρ^α and symmetry-adapted basis Γ^α for each irrep of the structure in Figure A.2.

within a given irrep only, or to establish a current solutions fulfilling the constraints imposed by symmetries of a given irrep, *i.e.*, $\mathbf{I}_i^\alpha = \Gamma_i^\alpha \hat{\mathbf{I}}$.

A.4 Examples

Using the implementation techniques described in [Section A.3](#), here we give practical examples of the mode tracking framework developed in [Section A.2](#). The methodology is presented on examples of increasing complexity, namely:

1. four dipoles (simple abelian, [Section A.4.1](#)),
2. an equilateral triangle (the simplest non-abelian, [Section A.4.2](#)),
3. a cubic array (complex non-abelian, [Section A.4.3](#)),
4. a radiator above a ground plane ([Section A.4.4](#)).

Throughout this section the eigenvalues have only been sorted according to their values. Potential vertical shifts in the modal spectrum, which are caused by an abrupt appearance or disappearance of a mode, have been treated according to [Section A.A](#).

A.4.1 Example 1: Four Dipoles

Characteristic modes of a rectangular array of four dipoles treated in [Figure A.1](#) are evaluated in this section. The geometry and meshing of the array are described in [Section A.2.1](#). The point symmetry group of this object is identical to that of [Figure A.2](#), *i.e.*, $G = \{E, \sigma_v^{yz}, \sigma_v^{xz}, C_2^z\}$. The point group is abelian with four irreps, see character table in [Figure A.3](#), therefore, only non-degenerate modes exist in each irrep. From the point of view of [Section A.2.3](#), the symmetry-adapted eigenvalue problems ([A.18](#)) give non-degenerated modes.

Tracked modes for this structure are shown in [Figure A.5](#). The top figure shows results from correlation-based tracking while in the bottom figure, each color corresponds to one irrep (to a given α in ([A.18](#))) and modes within the irrep were tracked using the symmetry-based algorithm proposed in this paper. Note that the correlation-based algorithm has problem with proper connections of traces of characteristic angles near $ka \approx 2.6$ and that some modes are connected incorrectly (red, orange and light green lines in top figure). These issues are not present in the symmetry-based tracking. It can be observed that tracks are crossed only between modes from different irreps, *i.e.*, modal crossings and modal crossing avoidances are no longer an issue. It is also important to stress that this simple procedure is less computationally expensive than correlation based tracking, see [Section A.5.3](#), and yields correct results irrespective of the spacing parameter d . On the contrary, the correlation algorithm performs poorly for decreasing d and/or increasing number of dipoles.

Examples of eigencurrents of characteristic modes from each irrep are depicted in [Table A.1](#).

A.4.2 Example 2: Equilateral Triangle

The equilateral triangle with side length ℓ was chosen as the simplest example of a non-abelian symmetric structure. Equilateral triangles have the point symmetry group C_{3v} which possesses two one-dimensional and one two-dimensional irreps, see [Table A.2](#) for its character table. According to group theory [30], the modes belonging to this two-dimensional irrep E exist in degenerated pairs with identical eigenvalues at all frequencies. Thus, there are two eigenvalue problems ([A.18](#))

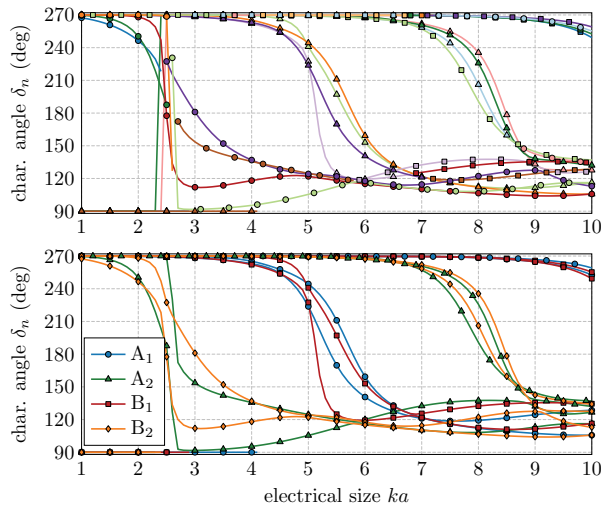


Figure A.5: Tracked characteristic angles of the four-dipole array treated in Figure A.1. Four modes of (A.18) with the smallest eigenvalue have been computed for every irrep of the corresponding symmetry point group. The collection of all these modes and their tracking via a correlation-based algorithm is shown in the top panel. The bottom panel shows sorted characteristic angles when each irrep was solved separately via the procedure described in this paper. Markers on every fifth frequency sample are depicted for clarity. Animation of this figure is available in [118].

Table A.1: Current distribution of the first two modes of each irrep of the four-dipole array. Only directions of currents on each dipole is depicted, different amplitudes are not considered.

irrep	ka	\mathbf{I}_1	λ_1	\mathbf{I}_2	λ_2
A_2	2.8	↓ ↓ ↑ ↑	0.293	↑ ↓ ↓ ↓	30.9
B_2	2.8	↑ ↑ ↑ ↑	-0.313	↑ ↓ ↓ ↑	2.15
A_1	5.6	↑ ↑ ↑ ↑ ↓ ↓ ↓ ↓	-0.375	↓ ↓ ↓ ↓ ↑ ↑ ↓ ↑	0.332
B_1	5.6	↑ ↑ ↓ ↓ ↓ ↓ ↑ ↑	-0.119	↑ ↓ ↓ ↓ ↓ ↓ ↓ ↑	1.60

for $\alpha = E$, each of them giving one member of the completely degenerated modal pair. It is worth noting that the separation into the degenerated pair (the form of matrix Γ_i^α) is independent of frequency, *i.e.*, modal tracking is possible even within this pair.

Despite the aforementioned degeneracy, the treatment of modal crossings can be performed in exactly the same manner as for abelian point groups. The result of this procedure is depicted in Figure A.6 where the lines belonging to irrep E are twice degenerated. Examples of eigencurrents of characteristic modes from each irrep are depicted in Figure A.7.

Table A.2: Character table for point group C_{3v} , [30].

C_{3v}	E	$2C_3$	$3\sigma_v$
A_1	+1	+1	+1
A_2	+1	+1	-1
E	+2	-1	0

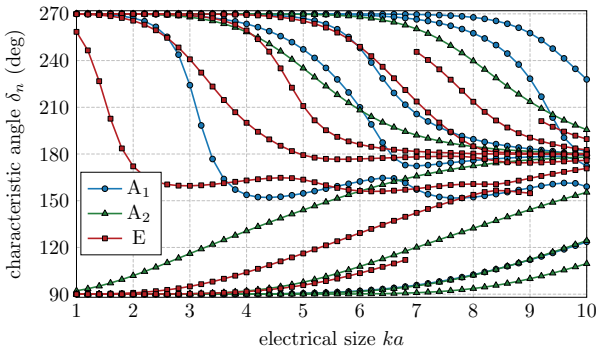


Figure A.6: Tracked characteristic angles of an equilateral triangle. Only the six lowest eigenvalue modes are computed. Notice, the set of the most significant modes changes with frequency which leads to truncation and appearance of modes, see [Section A.A](#). Each color represents one irrep. Red lines with square markers, which correspond to irrep E, are twice degenerated. Animation of this figure is available in [118].

Table A.3: Character table for point group T_d , [30].

T_d	E	$8C_3$	$3C_2$	$6S_4$	$6\sigma_d$
A_1	+1	+1	+1	+1	+1
A_2	+1	+1	+1	-1	-1
E	+2	-1	+2	0	0
T_1	+3	0	-1	+1	-1
T_2	+3	0	-1	-1	+1

A.4.3 Example 3: A Cubic Array

As a complex example, we examine the 3D cubic array of bowtie antennas depicted in [Figure A.8](#). The point symmetry group of this object is T_d with character table shown in [Table A.3](#). Modes of this structure exhibit three-dimensional irreps and an intricate modal spectrum which is shown in [Figure A.9](#) and [Figure A.10](#).

The complexity of the modal spectrum is enormous, with many modal crossings and crossing avoidances, see [Figure A.9](#). Yet, the framework developed in this paper properly deals with all of them via a straightforward tracking procedure, see [Figures A.9](#) and [A.10](#).

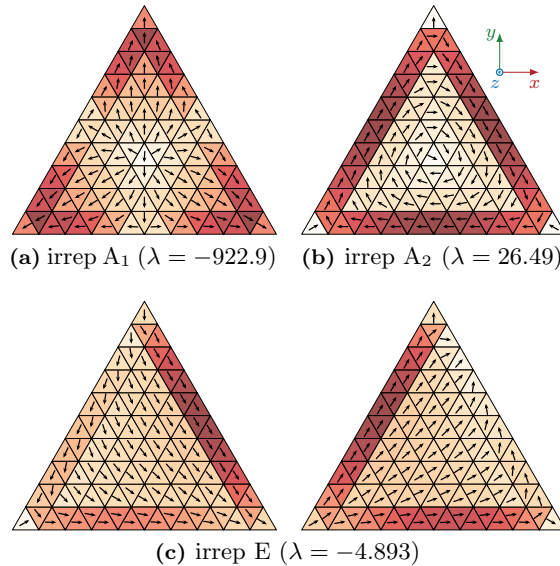


Figure A.7: First characteristic modes of each irreducible representation of equilateral triangle at electrical size $ka = 1$.

Table A.4: Character table of point group C_s (first three columns) [30] and characterization of modes and physical symmetries with respect to the modes belonging to irreps A' and A'' .

C_s	E	σ_h	solution	physical symmetry (GND)
A'	+1	+1	even ($\uparrow\uparrow$)	PMC
A''	+1	-1	odd ($\uparrow\downarrow$)	PEC

A.4.4 Characteristic Modes of a Radiator Above a Ground Plane

The procedure presented in this paper can advantageously be applied to scenarios where an antenna is placed over a **PEC** ground plane, see [Figure A.11a](#), and only the characteristic modes of the antenna are needed. This task is often approximated by replacing the ground plane with an image of the antenna [119], see [Figure A.11b](#). In such a case, only the odd modes have to be extracted, since the even modes are not valid solutions to the original problem depicted in [Figure A.11a](#).

The same task can be solved via point group theory. The arrangement in [Figure A.11a](#) is, in fact, equivalent to the one depicted in [Figure A.11c](#), *i.e.*, the presence of a physical symmetry can be replaced by the C_s symmetry group, see [Table A.4](#) for its character table. The symmetry operator σ_h splits the spectrum of modes into two irreps, A' and A'' . Irrep A' contains only even modes, *i.e.*, those corresponding to the presence of PMC, while irrep A'' contains all the remaining (odd) modes, *i.e.*, those corresponding to the presence of PEC.

To gather all antenna modes over the **PEC** symmetry plane, the symmetry-

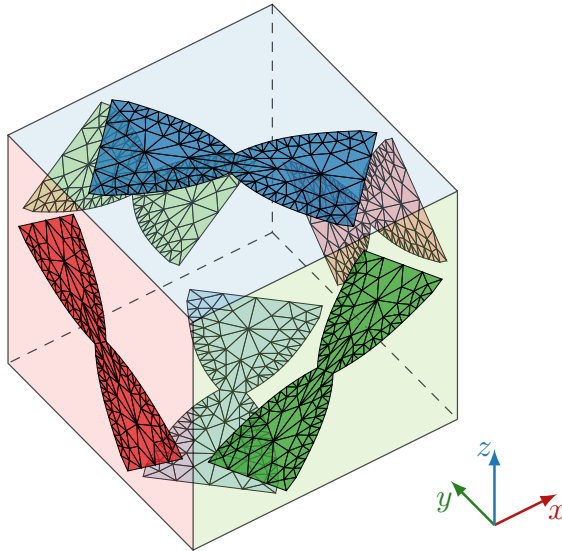


Figure A.8: Six bowtie antennas arranged to a cubic array belonging to the T_d point symmetry group.

adapted basis $\Gamma^{A''}$ is constructed and the impedance matrix \mathbf{Z} describing the original problem is reduced as

$$\widehat{\mathbf{Z}}^{A''} = \left(\Gamma^{A''}\right)^T \mathbf{Z} \Gamma^{A''} \quad (\text{A.24})$$

and substituted into (A.18) with a particular choice of $\widehat{\mathbf{A}}_i^\alpha = \text{Im}\{\widehat{\mathbf{Z}}^{A''}\}$ and $\widehat{\mathbf{B}}_i^\alpha = \text{Re}\{\widehat{\mathbf{Z}}^{A''}\}$ respectively. A favorable aspect of this procedure is a remarkable speed-up as compared to the evaluation of the problem from Figure A.11b. Notice that the same effect can be achieved via the incorporation of PEC or perfect magnetic conductor (PMC) boundary conditions directly into the Green's function of the problem [120]. With this modified Green's function, the system matrix within the MoM framework will attain exactly the same form as in (A.24).

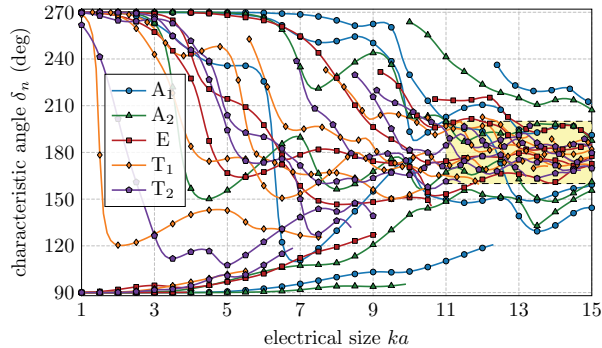


Figure A.9: Tracked characteristic angles of a cubic array depicted in Figure A.8. Four modes with the lowest eigenvalue (not counting degeneracies) are shown for every irrep. Lines corresponding to irrep E, are twice degenerated, lines corresponding to irreps T₁ and T₂ are three times degenerated. The highlighted area is enlarged in Figure A.10. Only every fifth marker is depicted for clarity. Animation of this figure is available in [118].

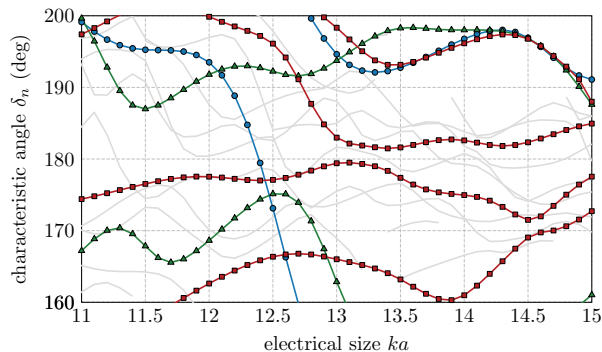


Figure A.10: Enlarged area from Figure A.9. The traces depicted by the same color cannot cross as they belong to the same irrep. Modes of irreps T₁ and T₂ are plotted in gray color for clarity.

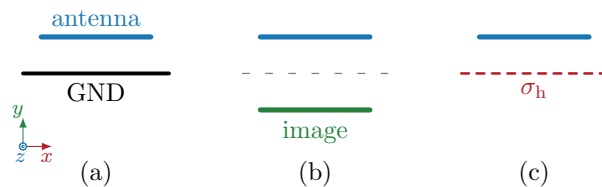


Figure A.11: (a) Original arrangement of an antenna motif above ground plane GND, (b) removal of the ground plane via image theory, and (c) point group C_s with symmetry operator σ_h (for the character table, see Table A.4).

A.5 Discussion

Point group theory establishes a solid theoretical background for the thorough discussion of several questions related to modal decomposition and mode tracking in general. Some recurring questions in this area (yet-to-be fully answered) are discussed in the following section from the perspective of point group theory.

A.5.1 On the Physical Importance of Modal Tracking

This section addresses the question of whether modal tracking is or is not needed. Central to this discussion is the comparison of modal interpretations in the time and time-harmonic (frequency) domains.

A.5.1.1 Tracking in the Time-Harmonic Domain

An interesting dilemma associated with modal tracking is depicted in [Figure A.12](#). Both panels show very similar situations consisting of two dipoles placed in parallel. The dipoles in the left panel have exactly the same lengths ℓ . The dipoles in the right panel have lengths ℓ and $\ell + \Delta\ell$. Although the electromagnetic behavior of both structures must be very similar (especially as $\Delta\ell \rightarrow 0$), one can immediately notice qualitatively different results arising from symmetry-based mode tracking. The dipoles with the same lengths are symmetrical, with the two plotted modal traces belonging to different irreps, and there we observe the expected eigenvalue trace crossing. The second setup (right panel) is not symmetrical, only the identity operation E exists (point group C_1), and therefore all characteristic modes belong to the same irrep so no modal traces can cross (as dictated by the von Neumann-Wigner theorem).

Owing to the arbitrarily small alteration which may affect this discrete change in behavior, we may be led to the conclusion that no physical phenomenon should depend on whether the eigenvalues as functions of frequency cross or not. It should be sufficient to interpret modal data independently at each frequency⁵. Such a conclusion is correct if modes at a single frequency are desired or if summation formulas such as [\[49\]](#)

$$\mathbf{I}(\omega) = \sum_n a_n(\omega) \mathbf{I}_n(\omega) \quad (\text{A.25})$$

are used. If so, mode ordering is irrelevant. A different situation arises when one wants to perform [\(A.25\)](#) in the time domain or to study the impulse response of a single mode, *i.e.*, $\mathcal{F}^{-1}\{a_n(\omega) \mathbf{I}_n(\omega)\}$, where \mathcal{F}^{-1} denotes an inverse Fourier's transform. In such a case, it must be stated that the solution presented in [Figure A.12](#) is the only correct solution⁶ for both arrangements irrespective of how close in appearance (how small $\Delta\ell$ is) the structures are to each other.

A.5.1.2 Modal Currents in the Time Domain

This subsection shows a simple example of the influence of improper modal tracking on time domain modal characteristics. As an example, two dipoles from the left

⁵This argument has already been raised by R. Mittra during the IEEE AP Symposium in 2016.

⁶If improperly tracked, the spectrum is discontinuous which leads to unphysical time-domain artifacts with violation of causality being a notable example.

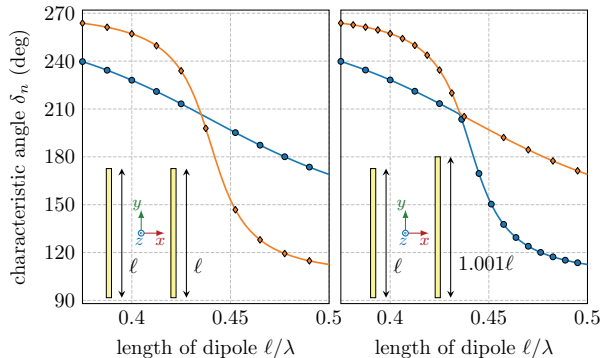


Figure A.12: The first odd and even characteristic modes in the vicinity of their resonance. In the left panel, the dipoles have the same length, in the right panel the lengths are slightly different.

panel of Figure A.12 are used. The two most significant modes at first resonance were computed for electrical sizes ranging from $ka = 0.04$ to $ka = 16$ in $F = 400$ frequency samples. Dipoles were afterwards fed in their centers by two delta gap sources of the same orientation and amplitude across the entire frequency sweep. Modal contributions to the total time domain current at the source have been evaluated with an FFT algorithm after interpolation to 2^{17} frequency points of a double-sided spectrum and using a Blackman-Nuttall Window [121]. Prior to the FFT evaluation, eigencurrents were aligned at subsequent frequency samples. This has to be made because the direction of the eigencurrent is arbitrary with respect to (A.5). The results for properly tracked and improperly tracked modes are depicted in Figure A.13. As previously argued, these data demonstrate how proper tracking ensures meaningful time domain responses of the individual modes.

A.5.2 Effective Generation of Symmetry-Adapted Bases

It is advantageous to use the *a priori* tracking described in Section A.2.3 and Section A.4 owing to its straightforward implementation and capability of reducing the computational burden of the eigenvalue decomposition as shown by (A.27). However, to accomplish this, the symmetry-adapted bases $\mathbf{\Gamma}_i^\alpha$ must first be constructed. Consequently, one “pilot” eigenvalue decomposition (A.9) is needed to evaluate the $\mathbf{D}(R)$ matrices. One straightforward option is to take $\mathbf{A} \equiv \mathbf{X}$ and $\mathbf{B} \equiv \mathbf{\Psi}$, where [61]

$$\mathbf{\Psi} = [\langle \psi_m(\mathbf{r}), \psi_n(\mathbf{r}) \rangle]. \quad (\text{A.26})$$

As compared to the immediate choice of characteristic mode basis (\mathbf{X}, \mathbf{R}) , the modes generated by $(\mathbf{X}, \mathbf{\Psi})$ have better numerical dynamics.

A.5.3 Reduction of Computational Time With *A Priori* Tracking

Utilization of *a priori* tracking makes it possible to significantly accelerate modal decomposition. Assuming $M \gg 1$ discretization elements, the speed-up, expressed

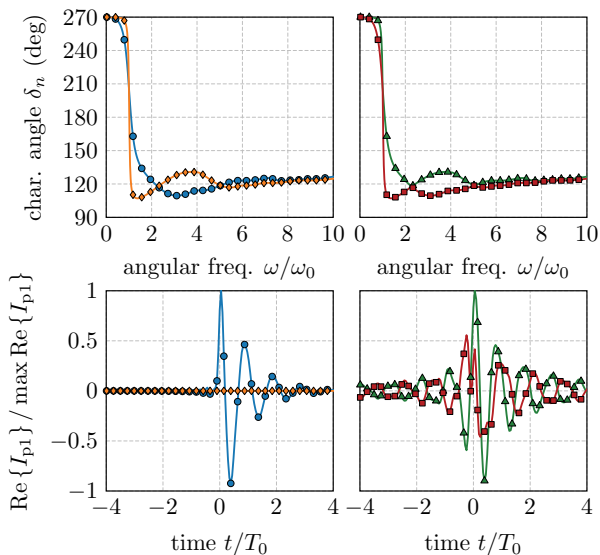


Figure A.13: The influence of improper modal tracking on time domain characteristics. The left column represents modal tracking according to this paper. The right column represents improper tracking. Time domain responses show modal contributions of the two modes to the total current flowing through delta gaps feeding the structure.

Table A.5: Reduction of computational time of characteristic mode decomposition for the *a priori* tracking scheme. It is assumed that generalized Schur decomposition (QZ algorithm) is applied [40].

G	T_{pg}/T	G	T_{pg}/T
C_1	1	C_{2v}	$1/2^4$
C_s	$1/2^3$	T_d	0.013

as a ratio between computational time T_{pg} needed to evaluate all reduced problems (A.18) and computational time T needed to evaluate the original problem (A.5), is expressed as

$$\frac{T_{\text{pg}}}{T} \propto \sum_{\alpha} \frac{g^{\alpha} N^{\alpha}}{N} \left(\frac{\eta^{\alpha}}{M} \right)^2, \quad (\text{A.27})$$

where N^{α} is the number of modes in one degeneration of irrep α , *i.e.*, $N = \sum_{\alpha} g^{\alpha} N^{\alpha}$. The relation between η^{α} and M is mentioned in (A.23). Note that $g^{\alpha} N^{\alpha} \leq N$, $\eta^{\alpha} \leq M$. Typical speed-ups for symmetry groups treated in this paper are depicted in Table A.5.

Table A.6: A physical realization of irreps generated by the C_{2v} point group.

C_{2v}	plane yz	plane xz
A_1	PMC	PMC
A_2	PEC	PEC
B_1	PEC	PMC
B_2	PMC	PEC

A.5.4 Relationship between Geometrical and Physical Symmetries

With respect to the theory developed in this paper and the example in [Section A.4.4](#), it is interesting to point out that the correspondence between geometrical mirror symmetries and physical symmetries generated by [PEC](#) and [PMC](#) planes is general. Specifically, in the case of a polar vector, such as electric current density $\mathbf{J}(\mathbf{r})$, the introduction of a [PMC](#) plane is identical to a reflection plane, while the introduction of a [PEC](#) plane is identical to a mirror plane with odd parity (a reflection plus change of a sign). In the case of pseudovectors, such as magnetic current density \mathbf{M} , the roles of the [PEC](#) and [PMC](#) planes are interchanged. This means that in the case of abelian reflection groups (groups in which all operations can be generated as combinations of reflections), such as C_{2v} , there exists a “physical” equivalent of every irrep which is generated by the [PEC](#) and [PMC](#) planes.

Let us take the C_{2v} point symmetry group with $G = \{E, \sigma_v^{yz}, \sigma_v^{xz}, C_2^z = \sigma_v^{xz}\sigma_v^{yz}\}$ as an example. Characters of this group, see [Figure A.3](#), can be interpreted as follows. A character with value $+1$ means that the representative current density is invariant with respect to a given set of reflections, *i.e.*, the mirror planes can be substituted by [PMCs](#). A character with value -1 means that the sign of the representative current must be inverted if the current is to stay invariant, *i.e.*, such mirror planes can be substituted by [PECs](#). Using the aforementioned rules, a character table from [Figure A.3](#) can be converted into [Table A.6](#), from which reduced simulations and calculations may be derived. This physical representation produces exactly the same modes as those generated by reduced eigenvalue problems ([A.18](#)) of the corresponding irreps.

A.6 Conclusion

A general framework utilizing point group theory for an arbitrarily parametrized eigenvalue problem was presented. A process uniquely classifying modes into irreducible representation was described. This classification method is independent of mesh density and requires only that the selected mesh and basis functions accurately represent the symmetry of the underlying structure. Applying the von Neumann-Wigner theorem on these irreducible representations conclusively decides when traces of eigenvalues can or cannot cross and, thus, the problem of crossing and crossing avoidance is solved. An important consequence is that eigenvalue traces of modes belonging to a non-symmetric object can never cross. An understanding and treatment of degenerated modes was also provided.

Two approaches, *a priori* and *a posteriori*, were shown and their performances were demonstrated on characteristic mode decomposition. Examples of varying complexity confirmed the validity and robustness of the proposed method. The *a priori* method was shown to considerably reduce computational time with respect to the standard eigenvalue solution.

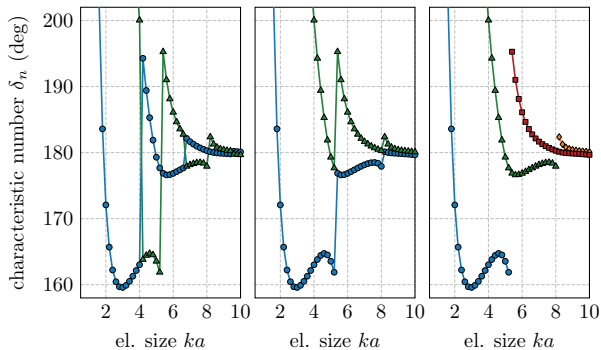


Figure A.14: Two most significant modes at every frequency sample of irrep $\alpha = E$ of an equilateral triangle. The left panel shows raw unsorted data, the middle panel shows eigenvalues sorted with respect to their eigenvalues, and, finally the right panel shows data after the removal of vertical shifts.

Future efforts may extend the presented method to include translational symmetries. The devised framework might be utilized for the design of non-correlated feeding networks and for handling degeneracies when seeking sets of optimal currents. Advanced topics, such as chirality and its role in modal formalism, might also be rigorously addressed.

The robust detection of symmetries for arbitrary objects would allow for a fully automated implementation of the proposed procedure.

A.A Correction of Vertical Shifts in Symmetry-Based Tracking

Under the assumption that all modes of the structure are available, the procedure described in this paper can track them flawlessly. In practice, however, we deal with a fixed (and usually small) number of the most significant (*e.g.*, smallest eigenvalue magnitude) modes, *i.e.*, $N \ll M$. Such a modal set naturally changes with frequency and, at specific frequencies, the appearance of a new mode and disappearance of an old mode occurs. When the tracking framework presented in this paper is used on this modal set, a global vertical shift of modal tracks (in a modal index) shows up every time a mode appears or disappears, see middle panel of [Figure A.14](#).

When frequency discretization is dense enough, the detection of the aforementioned shifts and their remedy can be based on the continuity of modal tracks, which is, in this paper, evaluated by

$$\kappa(\lambda_n^i) = \frac{2\lambda_n^i - \lambda_n^{i+1} - \lambda_n^{i-1}}{2 \max\{|\lambda_n^i|, |\lambda_n^{i+1}|, |\lambda_n^{i-1}|\}}, \quad (\text{A.28})$$

where i is a frequency index. A value of $\kappa = 0.5$ is used as a detection threshold. After detecting a vertical shift, modal indices are globally shifted in order to minimize the value of κ . The result of this procedure is shown in the right panel of [Figure A.14](#) and throughout [Section A.4](#).

Published as: M. Masek, L. Jelinek, and M. Capek, “Excitation of Orthogonal Radiation Channels,” *IEEE Transactions on Antennas and Propagation*, vol. 69, no. 9, pp. 5365–5376, Mar. 2021, DOI: [10.1109/TAP.2021.3061161](https://doi.org/10.1109/TAP.2021.3061161).

Abstract—A technique of designing antenna excitation realizing orthogonal states is presented. It is shown that a symmetric antenna geometry is required in order to achieve orthogonality with respect to all physical quantities. A maximal number of achievable orthogonal states and a minimal number of ports required to excite them are rigorously determined from the knowledge of an antenna’s symmetries. The number of states and number of ports are summarized for commonly used point groups (a rectangle, a square, etc.). The theory is applied to an example of a rectangular rim where the positions of ports providing the best total active reflection coefficient, an important metric in multi-port systems, are determined. The described technique can easily be implemented in existing solvers based on integral equations.

Index terms: Antenna theory, computer simulation, eigenvalues and eigenfunctions, electromagnetic modeling, method of moments, modal analysis.

B.1 Introduction

The ever-growing requirements on data throughput capacity [122] and simultaneous full occupancy of the radio spectrum has led to many novel concepts in recent decades [123]. One of the most successful techniques is the multiple-input multiple-output (MIMO) method [124, 125] heavily utilized in modern communication devices [126, 127]. When considering MIMO spatial multiplexing, spatial correlation has a strong impact on ergodic channel capacity [128], therefore, low mutual coupling between the states generated by individual antennas is required [129, 130].

In this paper, free-space channel capacity is increased by considering spatial multiplexing realized by orthogonal electromagnetic field states excited by a multi-port radiator [131–133]. This assumes that orthogonal states are a good starting position for realistic channels where stochastic effects cannot be neglected. Instead of an array of transmitters [134], the orthogonality is provided by a general multiport

antenna system. This approach addresses the question of how many orthogonal states can, in principle, be induced by a radiating system of a given geometry and how many localized ports are needed to excite them separately.

Previous research on this topic utilized characteristic modes [49, 135] which provide orthogonal states in far field. Unfortunately, as shown by the long history of attempts within the characteristic mode community [63, 74, 77, 82, 83, 136–141], this task is nearly impossible to accomplish, as entire-domain functions defined over arbitrarily shaped bodies cannot be selectively excited by discrete ports [142].

Many other methods exist to characterize and approach the maximal capacity, for both a special case of spherical geometry [143, 144] and for arbitrarily shaped antennas [145–147]. The number of degrees of freedom represented by electromagnetic field states were studied on an information theory level as well [148–150]. As with the characteristic modes approach, in all these cases the optimal coefficients do not prescribe any particular excitation of a selected or optimized antenna designs. This issue was solved in [151] utilizing a singular value decomposition of excitation coefficients represented in spherical wave expansion and in [109] by employing a port-mode basis [55]. The orthogonal radiation patterns are excited, however, the schemes are not orthogonal with respect to other physical operators, leading to unpleasant effects, such as non-zero mutual reactances [152].

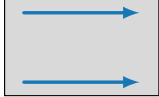
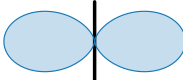
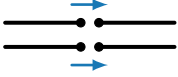

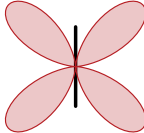
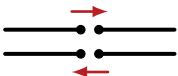
The situation changes dramatically for a structure invariant under certain symmetry operations, including rotation, reflection, or inversion. Certain symmetry operations were utilized in [131] and [153], however, a general approach can be reached only by applying point group theory [30] which allows modes computed by arbitrary modal decomposition to be classified into several irreducible representations (irreps) which are orthogonal to each other. Spherical harmonics [43] of a different order are a notable example of such an orthogonal set of states. A known property of physical states selected arbitrarily from two different irreps is that all mutual metrics are identically zero [114]. This useful property has already been utilized for the block-diagonalization of the bodies of a revolution matrix [56] and further study reveals interesting properties regarding the simultaneous excitation of perfectly isolated states [79, 154]. An additional benefit is that selective excitation is possible since the antenna excitation vectors may follow the irreducible representations of the underlying structure [155].

The key instrument employed in this work is the group theory-based construction of a symmetry-adapted basis [30] and block-diagonalization of the operators. This methodology leads to a fully automated design, without the necessity of a visual inspection or manual manipulation of the data [86]. The upper bound on the number of orthogonal states and the lower bound on the number of ports are rigorously derived only from the knowledge of symmetries. It is observed that the later number is significantly lower than the number of ports utilized in practice [83]. The placement of a given number of ports maximizing a selected antenna metric is investigated through combinatorial optimization [156] over vector adapted bases.

The entire design procedure can easily be incorporated into a simple algorithm, thus opening possibilities to analyze MIMO antennas automatically. All findings are demonstrated on a set of canonical geometries. The figure of merit classifying the performance of MIMO radiating systems is the total active reflection coefficient (TARC) [157], however, all the presented material is general and valid for all operators and all metrics.

The paper is structured as follows. The theory is developed in Section B.2, primarily based on point group theory and eigenvalue decomposition. The basic consequences are demonstrated on an example in Section B.3. Section B.4 addresses

Table B.1: Three examples of system states \mathbf{q}_m and associated operators \mathcal{A} preserving orthogonality in the sense of (B.3). The algebraic representation of states \mathbf{Q}_m , and operators \mathbf{A} , is expressed in a basis $\{\psi_n(\mathbf{r})\}$, see Section B.A for details. All quantities depicted in the table are subsequently introduced throughout the paper.

current densities characteristic modes [49]	far fields far-field patterns [158]	excitation port modes [159]
		
		
$\mathbf{q}_m = \mathbf{J}_m(\mathbf{r})$ $\mathcal{A}_1 = \mathcal{X}_0, \mathcal{A}_2 = \mathcal{R}_0$	$\mathbf{q}_m = \mathbf{F}_m(\vartheta, \varphi)$ $\mathcal{A} = \mathcal{R}_0 = \text{Re}\{\mathcal{Z}_0\}$	$\mathbf{q}_m = \mathbf{E}_m^i(\mathbf{r})$ $\mathcal{A} = y = z^{-1}$
$\mathbf{Q}_m = \mathbf{I}_m$ $\mathbf{A}_1 = \mathbf{X}_0, \mathbf{A}_2 = \mathbf{R}_0$	$\mathbf{Q}_m = \mathbf{I}_m$ $\mathbf{A} = \mathbf{R}_0 = \text{Re}\{\mathbf{Z}_0\}$	$\mathbf{Q}_m = \mathbf{v}_m$ $\mathbf{A} = \mathbf{P}^H \mathbf{Z}^{-1} \mathbf{P}$

the important questions of how many orthogonal states are available and how many ports are needed to excite them independently. The optimal placement of a given number of ports is then solved in Section B.5 via an exhaustive search. The paper is concluded in Section B.6.

B.2 Orthogonal States

Let us assume antenna metric p defined via quadratic form

$$p(\mathbf{q}_m, \mathbf{q}_n) = \langle \mathbf{q}_m, \mathcal{A}(\mathbf{q}_n) \rangle, \quad (\text{B.1})$$

where \mathbf{q}_m and \mathbf{q}_n are states of the system (*e.g.*, modal current densities, modal far fields, or excitation states, see Table B.1), \mathcal{A} is a linear complex operator, see Section B.A for representative examples, and $\langle \cdot, \cdot \rangle$ denotes the inner product

$$\langle \mathbf{a}(\mathbf{r}), \mathbf{b}(\mathbf{r}) \rangle = \int_{\Omega} \mathbf{a}^*(\mathbf{r}) \cdot \mathbf{b}(\mathbf{r}) dV, \quad (\text{B.2})$$

where $\mathbf{a}(\mathbf{r})$ and $\mathbf{b}(\mathbf{r})$ are generic vector fields supported in region Ω , $\mathbf{r} \in \Omega$. For the purpose of this paper, orthogonality of states is further defined as

$$p(\mathbf{q}_m \in \mathcal{S}_i, \mathbf{q}_n \in \mathcal{S}_j) = \zeta_{ijmn} \delta_{ij}, \quad (\text{B.3})$$

where $\{\mathcal{S}_i\}$ are disjoint sets of states \mathbf{q} , ζ are normalization constants and δ_{ij} is a Kronecker delta.

In order to obtain a numerically tractable problem, procedures such as the method of moments (MoM) [28] or finite element method (FEM) [38] are commonly employed,

recasting states \mathbf{q} , operators \mathcal{A} , and sets S into column vectors \mathbf{Q} , matrices \mathbf{A} [39], and linear vector spaces S , respectively, see Table B.1 and Section B.A. Within such a paradigm, the orthogonality (B.3) can be written as

$$\mathbf{Q}_m^H \mathbf{A} \mathbf{Q}_n = 0 : \quad \mathbf{Q}_m \in S_i, \quad \mathbf{Q}_n \in S_j, \quad (\text{B.4})$$

which means that matrix \mathbf{A} is block-diagonalized in the basis generated by these states.

Difficulties in finding orthogonal sets of vectors strongly depend on the number of operators $\{\mathbf{A}_i\}$ with respect to which relation (B.4) must simultaneously be satisfied. In the case of a sole operator $\{\mathbf{A}\}$ or two operators $\{\mathbf{A}_1, \mathbf{A}_2\}$, the solution to a standard $\mathbf{A}\mathbf{Q} = \lambda\mathbf{Q}$ or a generalized $\mathbf{A}_1\mathbf{Q} = \lambda\mathbf{A}_2\mathbf{Q}$ eigenvalue problem gives vectors which diagonalize the underlying operators [36]. The well-known example is the characteristic modes decomposition [49] defined as

$$\mathbf{X}_0 \mathbf{I}_m = \lambda_m \mathbf{R}_0 \mathbf{I}_m, \quad (\text{B.5})$$

where \mathbf{I}_m are the characteristic modes, λ_m are the characteristic numbers, and $\mathbf{Z}_0 = \mathbf{R}_0 + j\mathbf{X}_0$ is the vacuum impedance matrix defined in Section B.A. Multiplying (B.5) from the left by the n th characteristic mode \mathbf{I}_n and considering unitary radiated power of each mode, we see that matrices \mathbf{X}_0 and \mathbf{R}_0 are diagonalized,

$$\frac{1}{2} \mathbf{I}_n^H \mathbf{X}_0 \mathbf{I}_m = \lambda_n \delta_{mn}, \quad (\text{B.6})$$

$$\frac{1}{2} \mathbf{I}_n^H \mathbf{R}_0 \mathbf{I}_m = \delta_{mn}, \quad (\text{B.7})$$

generating orthogonality in reactive and radiated power, respectively. In the case of three or more operators, simultaneous diagonalization is possible only under special conditions (*e.g.*, mutually commuting matrices). For example, choosing a third matrix $\mathbf{W} = \omega \partial \mathbf{X}_0 / \partial \omega$, [160], it is realized that

$$\frac{1}{2} \mathbf{I}_n^H \mathbf{W} \mathbf{I}_m = w_{mn} \neq w_{mn} \delta_{mn}, \quad (\text{B.8})$$

i.e., characteristic modes, in general, only diagonalize matrices \mathbf{X}_0 and \mathbf{R}_0 . However, when point symmetries are present, at least simultaneous block-diagonalization can be reached and, as explained in the following sections, orthogonal states with respect to all operators describing the physical behaviour of the underlying structure can be easily established.

B.2.1 Orthogonal States Based on Point Symmetries

In the case of symmetrical objects (see examples of symmetry operations in Figure B.1 and sketches of several point groups in Figure B.2), point group theory [30] shows that physical states of the system can be uniquely divided into disjoint sets called species. For each such set, a rectangular matrix $\mathbf{\Gamma}^{(\alpha, i)}$ can be constructed so that

$$\widehat{\mathbf{A}}^{(\alpha, i)} = \left(\mathbf{\Gamma}^{(\alpha, i)} \right)^T \mathbf{A} \mathbf{\Gamma}^{(\alpha, i)} \quad (\text{B.9})$$

is a single block of a block-diagonalized matrix $\widehat{\mathbf{A}} = \mathbf{\Gamma}^T \mathbf{A} \mathbf{\Gamma}$ with matrix $\mathbf{\Gamma}$ accumulating all blocks $\mathbf{\Gamma}^{(\alpha, i)}$ side by side. Indices α and i form species (α, i) , with α denoting

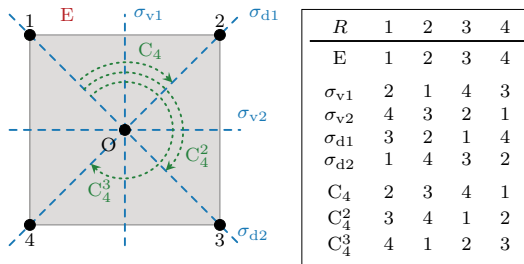


Figure B.1: An example of symmetry operations—a square. This structure belongs to point group C_{4v} [30] and has eight symmetry operations: identity E, four reflections σ and three rotations C. The table shows how each node is transformed via each symmetry operation.

selected irreducible representation (irrep) and $i(\alpha) \in \{1, \dots, g^{(\alpha)}\}$ counting along a dimension of the selected irrep [30]. The rectangular matrix $\mathbf{\Gamma}^{(\alpha,i)}$ will be called a symmetry-adapted basis and its construction within the MoM paradigm is detailed in [161].

Let us recall once again the characteristic modes (B.5) and their lack of orthogonality with respect to stored energy (B.8). Possessing a symmetrical structure and considering block-diagonalization (B.9) of matrices \mathbf{R}_0 , \mathbf{X}_0 , and \mathbf{W} , the characteristic modes

$$\mathbf{I}_m^{(\alpha,i)} = \mathbf{\Gamma}^{(\alpha,i)} \widehat{\mathbf{I}}_m^{(\alpha,i)} \quad (\text{B.10})$$

with

$$\widehat{\mathbf{X}}_0^{(\alpha,i)} \widehat{\mathbf{I}}_m^{(\alpha,i)} = \lambda_m \widehat{\mathbf{I}}_m^{(\alpha,i)} \widehat{\mathbf{R}}_0^{(\alpha,i)}, \quad (\text{B.11})$$

belong exclusively to species (α, i) [161]. In such case, the relation (B.8) changes to

$$\frac{1}{2} \left(\mathbf{I}_n^{(\alpha,i)} \right)^H \mathbf{W} \mathbf{I}_m^{(\beta,j)} = w_{mn} \delta_{\alpha\beta} \delta_{ij}, \quad (\text{B.12})$$

which means that the characteristic modes from different irreps ($\alpha \neq \beta$), or from the same irrep but different dimension ($i \neq j$), are orthogonal with respect to stored energy as well. This statement can be generalized to all operators resulting from a MoM paradigm, see examples in Section B.A or in [61].

The relation (B.9) states that columns of matrices $\mathbf{\Gamma}^{(\alpha,i)}$ form vector spaces S in (B.4), consequently the columns of $\mathbf{\Gamma}^{(\alpha,i)}$ can be desired vectors \mathbf{Q} . In such a case, the orthogonality (B.4) holds simultaneously for all operators $\{\mathbf{A}_i\}$ describing the physical behavior of the underlying structure whenever two vectors belong to different species.

Notice that the utilization of symmetries induces the pattern diversity, see the second column of Table B.1, and allows to create several orthogonal states, which are not affected by, and does not have the influence on, used multiplexing technique, thus, for example, time or code diversity can be applied at each orthogonal state to further increase the capacity of the system.

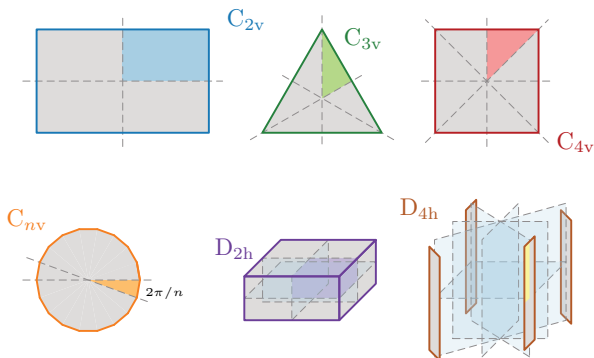


Figure B.2: Examples of various point groups. Colored regions show generator of the structure, *i.e.*, the minimal part of the object from which the entire structure can be constructed via symmetry operations.

B.3 Illustrative Example

This section demonstrates the usefulness of the point group-based block diagonalization (B.9) to obtain orthogonal states.

The design procedure is illustrated on the example of a rectangular plate of dimensions $2L \times L$ and of electrical size $ka \approx 10.19$ (k abbreviates a free-space wavenumber and a denotes the radius of the smallest sphere circumscribing the plate), which was used in [83] to construct orthogonal states via the selective excitation of characteristic modes (CMs). The CMs in [83] were visually separated into four “groups” (using the nomenclature of [83]), and voltage sources (ports) were associated with each such group so as to provide maximum excitation of the dominant CM of each group. In order to independently control four sets of modes, eight voltage sources (delta gaps) were used. The structure and positions of voltage sources used in [83] are shown in Figure B.3. Unit voltages were considered with polarity determined by the second column of Table B.2.

The point group theoretical treatment introduced in Section B.2.1 offers a different solution to the same problem. The underlying object has four point symmetries (identity, rotation of π around z -axis and two reflections via xz and yz planes) and belongs to the C_{2v} point group (see Figure B.2) which possess four one-dimensional irreps [30]. The number of distinct species¹ introduced in Section B.2.1 is four, each being connected to a distinct matrix $\Gamma^{(\alpha,1)}$. Within a standard notation [30], these irreps are listed in the third column of Table B.2.

As mentioned in Section B.2.1, any columns of matrices $\Gamma^{(\alpha,1)}$ [161] can be used as excitation vectors $\mathbf{V}^{(\alpha,1)}$, see Section B.B, to enforce orthogonality. To minimize the number of voltage sources used, it is advantageous to select those columns which have non-zero elements at the same positions across all species. In the specific case of Figure B.3, matrices $\Gamma^{(\alpha,1)}$ also contain columns with only four non-zero entries (*i.e.*, with four voltage sources) at positions corresponding to ports 1–4 shown in Figure B.3 in blue. Orientations of connected unit voltage sources are shown in

¹Only one-dimensional irreps exist in this case, *i.e.*, dimensionality of each irrep α is $g^{(\alpha)} = 1$.

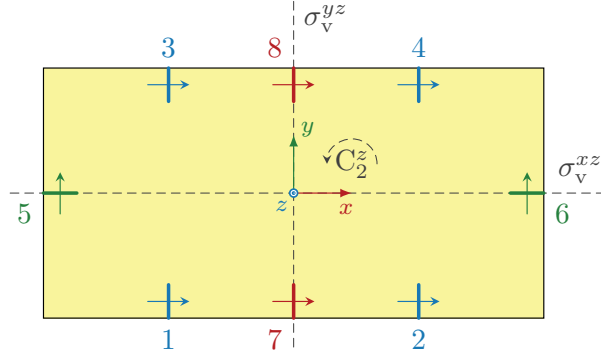


Figure B.3: Port locations on a rectangular plate. Reprinted from [83, Fig. 5]. Arrows show the orientation of the voltage sources.

Table B.2: Orthogonal excitation states for a plate from Figure B.3. The second column is a solution found in [83, Table IV]. Numbers refer to the voltage source in Figure B.3 and superscripts + and - denote its orientation with respect to the directions in Figure B.3. The third column denotes irreps designation in the notation of point group theory [30]. The last column shows a solution via the only four voltage sources described in this paper.

Set	Ports [83, Table IV]	irrep α	Four ports
S_1	$1^+, 2^-, 3^+, 4^-$	A_1	$1^+, 2^-, 3^+, 4^-$
S_2	$5^+, 6^+$	B_1	$1^+, 2^-, 3^-, 4^+$
S_3	$7^+, 8^+$	B_2	$1^+, 2^+, 3^+, 4^+$
S_4	$7^+, 8^-$	A_2	$1^+, 2^+, 3^-, 4^-$

the last column of Table B.2. This means that the eight ports used in [83] are not necessary to provide four orthogonal states.

This example introduces a series of questions of fundamental importance for multiport and multimode devices:

- Q1) How many orthogonal states, with respect to all physical operators N_s , can be found for a structure belonging to a specific point group?
- Q2) What is the lowest number of ports N_p that ensures a given number of orthogonal states?
- Q3) Where should ports be placed to maximize the performance of a device, with respect to a given physical metric, to maintain the orthogonality of states?

These questions are addressed throughout the paper using point group theory revealing important aspects of the symmetry-based design of orthogonal states.

B.4 Excitation States Based on Point Group Theory

Referring to [161, eq. (16)], symmetry-adapted excitation vectors can be constructed as

$$\mathbf{V}^{(\alpha,i)}(\xi) = \frac{g^{(\alpha)}}{g} \sum_{R \in G} \tilde{d}_{ii}^{(\alpha)}(R) \mathbf{C}(R) \mathbf{V}(\xi), \quad (\text{B.13})$$

which is a linear map from excitation vector $\mathbf{V}(\xi) \in \mathbb{C}^{N_u \times 1}$ (see Section B.B) onto a symmetry-adapted excitation vector $\mathbf{V}^{(\alpha,i)}(\xi) \in \mathbb{C}^{N_u \times 1}$ that satisfies

$$\left(\mathbf{V}^{(\alpha,i)}(\xi)\right)^H \mathbf{A} \mathbf{V}^{(\beta,j)}(\xi) = \zeta_{\alpha\beta ij} \delta_{\alpha\beta} \delta_{ij} \quad (\text{B.14})$$

for an arbitrary operator $\mathbf{A} \in \mathbb{C}^{N_u \times N_u}$ with N_u being number of unknowns (number of basis functions). The mapping (B.13) is characterized by the point group of structure $G = \{R\}$ consisting of symmetry operations R , dimensionality $g^{(\alpha)} = \dim \mathbf{D}^{(\alpha)}$ of irrep α , the order of the point group $g = \sum_{\alpha} \left(g^{(\alpha)}\right)^2$, mapping matrix $\mathbf{C}(R)$ and irreducible matrix representation $\mathbf{D}^{(\alpha)} = \left[d_{ij}^{(\alpha)}\right]$ with $\tilde{\mathbf{D}} = \left(\mathbf{D}^{-1}\right)^T$, see [30] and [161, Sec. II-C] for more details. The application of (B.13) and the exact meaning of all variables used is illustrated in an example in Section B.C.

Throughout the paper, excitation vector $\mathbf{V}(\xi)$ represents an arbitrarily shaped port (*e.g.*, delta-gap, coaxial probe, etc.) that lies entirely in the generator of the structure, see highlighted areas in Figure B.2, and variable ξ is used to code the position of this port. As an example, assume that port No. 1 in Figure B.3 is a delta-gap port represented by excitation vector $\mathbf{V}(1)$. Notice that it is placed in one of the quadrants, which are the generators of the structure. Each summand of (B.13) maps (changing orientation, position and amplitude) this port on its symmetry positions 2, 3, 4, creating symmetry-adapted excitation vector $\mathbf{V}^{(\alpha,i)}(1)$ for a particular species (α, i) .

The first two questions from Section B.3 can be answered by inspecting (B.13):

1. The maximum number of orthogonal states, N_s , (orthogonal with respect to all physical operators) is equal to the number of species of the given point group, *i.e.*, to the number of vectors $\mathbf{V}^{(\alpha,i)}(\xi)$ generated by (B.13) for a given set of ports in the generator of the structure, which is $N_s = \sum_{\alpha} g^{(\alpha)}$. In other words, for a given distribution of ports in the generator of the structure, described by vector $\mathbf{V}(\xi)$, there exist N_s ways of how to symmetry-adapt this vector within the given point group. Each symmetry-adaptation creates an orthogonal excitation vector $\mathbf{V}^{(\alpha,i)}(\xi)$.
2. The minimum number of ports, N_p , needed to distinguish all orthogonal states mentioned above is equal to the number of symmetry operations in point group G since each summand of (B.13) maps initial excitation vector $\mathbf{V}(\xi)$ onto a new position and there are as many summands as symmetry operations. See detailed example in Section B.C. It is assumed that each mapping is unique, otherwise not all orthogonal states are reached—this possibility is discussed later in Section B.4.1.

Table B.3 summarizes the number of maximal reachable orthogonal states and number of ports required for it for the known point symmetry groups.

Table B.3: Maximum number of symmetry-based orthogonal states N_s / minimal number of ports N_p needed to excite all of them for a given point group. Selected point groups are shown in [Figure B.2](#). A Schoenflies notation [30] is used for point groups naming.

n	2	3	4	5	6	7	8
C_n	2/2	3/3	4/4	5/5	6/6	7/7	8/8
C_{nv}	4/4	4/6	6/8	6/10	8/12	8/14	10/16
C_{nh}	4/4	6/6	8/8	10/10	12/12	14/14	16/16
D_n	4/4	4/6	6/8	6/10	8/12	8/14	10/16
D_{nh}	8/8	8/12	12/16	12/20	16/24	16/28	20/32
D_{nd}	6/8	8/12	10/16	12/20	14/24	16/28	18/32
S_n	2/2		4/4		6/6		8/8
	T	T _h	T _d	O	O _h	I	I _h
	6/12	12/24	10/24	10/24	20/48	16/60	32/120

Table B.4: A symmetry-adapted delta gap number five from [Figure B.3](#).

$R \setminus \alpha$	A ₁	A ₂	B ₁	B ₂
E	5 ⁺	5 ⁺	5 ⁺	5 ⁺
σ_v^{xz}	5 ⁻	5 ⁺	5 ⁻	5 ⁺
σ_v^{yz}	6 ⁺	6 ⁻	6 ⁻	6 ⁺
C_2^z	6 ⁻	6 ⁻	6 ⁺	6 ⁺

When combined together, the answers to Q1 and Q2 show how orthogonal states can be efficiently established for a given point group. On the other hand, this procedure does not ensure that all states lead to the same/optimal value of the selected antenna metric. This calls for a reply to question Q3 which is addressed in [Section B.5](#).

B.4.1 Port Placed in the Reflection Plane

Formula (B.13) suggests that a problematic design appears when the port corresponding to excitation vector $\mathbf{V}(\xi)$ lies at the boundary of the generator of the structure [30], *e.g.*, at the reflection plane. In this case, the port generally breaks the symmetry of the structure making the process of symmetry adaptation invalid. To give an example, imagine that a delta-gap port is placed at position $\xi = 5$ in [Figure B.3](#). The reflection σ_v^{xz} and identity operation E project this port onto itself but with different polarity. This collision is demonstrated in [Table B.4](#). In this case, only states belonging to irreps A₂ and B₂ are realizable. More than four ports would be needed to establish four states.

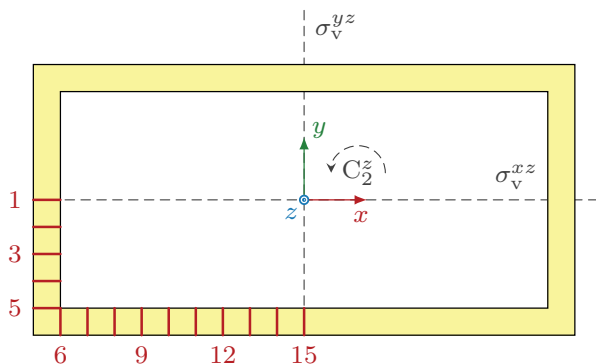


Figure B.4: The structure of the rectangular rim. Possible placements of ports ξ in the generator of the structure are highlighted in red.

B.5 Ports' Positioning

In order to answer the third question from [Section B.3](#)—*Where should ports be placed to maximize the performance of a device, with respect to a given physical metric, to maintain the orthogonality of states?*—it is necessary to take into account the particular requirements on the performance of the device. An example of investigating port positions to optimize the [TARC](#) of an antenna is used to demonstrate the sequence of steps to resolve this question. Instead of the rectangular plate shown in [Figure B.3](#), a rectangular rim of dimensions $2L \times L$ and width $L/10$ is considered, see the object in [Figure B.4](#). The geometry of the rim belongs to the same point group as the plate but allows for the placement of discrete ports [\[162\]](#) at an arbitrary position without creating undesired short circuits.

B.5.1 Total Active Reflection Coefficient

The total active reflection coefficient [\[157\]](#), which is defined as

$$t = \sqrt{1 - \frac{P_{\text{rad}}}{P_{\text{in}}}}, \quad (\text{B.15})$$

is used as a performance metric, where P_{rad} stands for radiated power and P_{in} stands for incident power. Within the [MoM](#) framework, [\(B.15\)](#) can be reformulated as

$$t(\mathbf{v}) = \sqrt{1 - \frac{4Z_0 \mathbf{v}^H \mathbf{P}^H \mathbf{Y}^H \mathbf{R}_0 \mathbf{Y} \mathbf{P} \mathbf{v}}{\mathbf{v}^H \mathbf{k}^H \mathbf{k} \mathbf{v}}}, \quad (\text{B.16})$$

where

$$\mathbf{k} = \mathbf{e} + Z_0 \mathbf{y}. \quad (\text{B.17})$$

Here, \mathbf{e} is the identity matrix, $Z_0 = 50 \Omega$ is the characteristic impedance of all transmission lines connected to the ports, $\mathbf{Y} = \mathbf{Z}^{-1} \in \mathbb{C}^{N_u \times N_u}$ is an admittance matrix, \mathbf{R}_0 is the radiation part of the impedance matrix, and $\mathbf{y} \in \mathbb{C}^{N_p \times N_p}$ is the admittance matrix seen by N_p connected ports. Each port is represented by one

column of matrix \mathbf{P} and port voltages are all accumulated in vector \mathbf{v} . Matrix \mathbf{P} is therefore of size $N_u \times N_p$ and the excitation vector is given by $\mathbf{V} = \mathbf{P}\mathbf{v}$, see [Appendices B.A](#), [B.B](#) and [B.D](#) for detailed derivations.

B.5.2 Optimization Problem

The problem of [TARC](#) minimization with additional constraints on N_m orthogonal states is defined as to find port excitation vectors $\{\mathbf{v}_m\}$, $m \in \{1, \dots, N_m\}$ and port configuration \mathbf{P} such as to fulfill

$$\begin{aligned} & \underset{\{\mathbf{P}, \mathbf{v}_m\}}{\text{minimize}} && t_{\text{RMS}} \\ & \text{subject to} && \mathbf{v}_m^H \mathbf{P}^H \mathbf{A}_1 \mathbf{P} \mathbf{v}_n = 0, \quad m \neq n, \\ & && \vdots = \vdots \\ & && \mathbf{v}_m^H \mathbf{P}^H \mathbf{A}_{N_k} \mathbf{P} \mathbf{v}_n = 0, \quad m \neq n, \end{aligned} \quad (\text{B.18})$$

where the root mean square ([RMS](#)) metric based on [\(B.16\)](#) is adopted

$$t_{\text{RMS}} = \sqrt{\frac{1}{N_m N_f} \sum_{m=1}^{N_m} \sum_{f=1}^{N_f} t^2(\mathbf{v}_m, \omega_f)} \quad (\text{B.19})$$

to measure the overall performance over N_f frequency samples ω_f and over multiple states. Matrices \mathbf{A}_k , $k \in \{1, \dots, N_k\}$, in the constraints above are placeholders for matrix operators from, *e.g.*, [Section B.A](#). These constraints enforce simultaneous orthogonality with respect to all operators describing the physical system at hand, *e.g.*, with respect to far fields ($\mathbf{A}_k = \mathbf{Y}^H \mathbf{R}_0 \mathbf{Y}$), current densities ($\mathbf{A}_k = \mathbf{Y}^H \mathbf{Y}$), excitation vectors (\mathbf{A}_k is the identity matrix), or energy stored by the states ($\mathbf{A}_k = \mathbf{Y}^H \mathbf{W} \mathbf{Y}$).

In light of the discussion in [Section B.2](#), the simultaneous realization of all $N_k > 2$ constraints in [\(B.18\)](#) is only possible on symmetric structures and only when excitation vectors $\mathbf{V}_m = \mathbf{P}\mathbf{v}_m$ are given by [\(B.13\)](#), *i.e.*, $\mathbf{V}_m = \mathbf{V}^{(\alpha, i)} = \mathbf{P}\mathbf{v}^{(\alpha, i)}$. This imposes specific requirements on port matrix \mathbf{P} and port voltages $\mathbf{v}^{(\alpha, i)}$.

First, ports represented by columns of port matrix \mathbf{P} have to be symmetrically distributed on the structure. This is achieved by placing a port (a single column of matrix \mathbf{P}) at arbitrary position ξ in the generator of the structure and then by replication of this port by the application of symmetry operations $R \in G$ (column of matrix P is transformed by mapping matrices $\mathbf{C}(R)$). Each replication results in a new port, *i.e.*, new column² of port matrix \mathbf{P} .

Second, port excitation vector \mathbf{v} is constructed so that only ports placed in the region of the generator of the structure are excited (others are kept at zero voltage) and the symmetry-adaptation [\(B.13\)](#) of vector $\mathbf{V}(\xi) = \mathbf{P}\mathbf{v}$ is processed. Here and further, ξ represents a particular position in the generator of the structure, see possible placements in [Figure B.4](#).

Lastly, port voltages $\mathbf{v}^{(\alpha, i)}$ for species (α, i) are acquired from excitation vector $\mathbf{V}^{(\alpha, i)}$ as

$$\mathbf{v}^{(\alpha, i)} = \left(\mathbf{P}^H \mathbf{P} \right)^{-1} \mathbf{P}^H \mathbf{V}^{(\alpha, i)}, \quad (\text{B.20})$$

see [\(B.48\)](#) in [Section B.D](#).

²Note, that one of the symmetry operations is an identity which represents the original port in the generator of the structure and the corresponding column of matrix \mathbf{P} should be omitted.

Being now equipped with symmetry-adapted excitation vectors $\mathbf{V}^{(\alpha,i)} = \mathbf{P}\mathbf{v}^{(\alpha,i)}$, constraints of (B.18) are automatically fulfilled irrespective of their number. The variables remaining for optimization (B.18) are therefore positions ξ of ports in the generator of the structure and their amplitudes. In a simplified case, when only one port exists in the generator of the structure, its amplitude is of no relevance and the only optimized variable is position ξ , *i.e.*, the optimization problem (B.18) reduces to

$$\underset{\xi}{\text{minimize}} \quad t_{\text{RMS}}. \quad (\text{B.21})$$

In order to give a simple set of instructions for the procedure above, the TARC minimization with fully orthogonal states iteratively performs:

1. Pick a position ξ .
2. Create a port matrix \mathbf{P} , see (B.47) in Section B.D.
3. Construct vector \mathbf{v} exciting only the ports in the generator of the structure.
4. Perform symmetry-adaptation (B.13) of the vector $\mathbf{V} = \mathbf{P}\mathbf{v}$ into all species (α, i) .
5. Get $\mathbf{v}^{(\alpha,i)}$ via (B.20) for each species.
6. Calculate TARC $t(\mathbf{v}^{(\alpha,i)})$ for all species (B.16).
7. Evaluate the fitness function t_{RMS} via (B.19).

B.5.3 Single-Frequency Analysis

The optimization of the port's placement in the generator of the structure (B.21) computed at the single frequency sample ($N_f = 1$) is analyzed in this section. The selected frequency corresponds to the antenna's electrical size $ka = 10.19$. The low number of tested positions and the possibility to precalculate all matrix operators \mathbf{A} enables the use of an extensive search to evaluate (B.16) for each tested position ξ depicted by the red color in Figure B.4.

The results are presented in Figure B.5. As mentioned in Section B.4.1, positions $\xi = 1$ and $\xi = 15$ are not able to excite all four orthogonal states since they are placed at the reflection plane. All other positions ξ result in a total of four symmetrically placed ports providing four orthogonal states.

Bars in Figure B.5 show TARC values (B.16) computed for each of the four species $(\alpha, 1)$, $\alpha \in \{A_1, A_2, B_1, B_2\}$. The values t_{RMS} are represented by the black vertical lines. The optimal port position ξ in the generator of the structure is declared as the one with the lowest value of t_{RMS} , *i.e.*, position $\xi = 14$.

Radiated patterns were computed and plotted as two-dimensional cuts in Figure B.6 to confirm the orthogonality of the designed excitation vectors $\mathbf{V}^{(\alpha,i)}(\xi)$. One can see that these patterns are similar to spherical harmonics which are orthogonal [43]. To reduce the complexity of radiation patterns in Figure B.6, radiation patterns were computed at $ka = 1$, bearing in mind that the orthogonality between states is frequency independent.

B.5.4 Frequency Range Analysis

Multiport antenna systems typically operate in a wide frequency range. However, evaluating (B.21) at each frequency, as was done in the previous section, does not

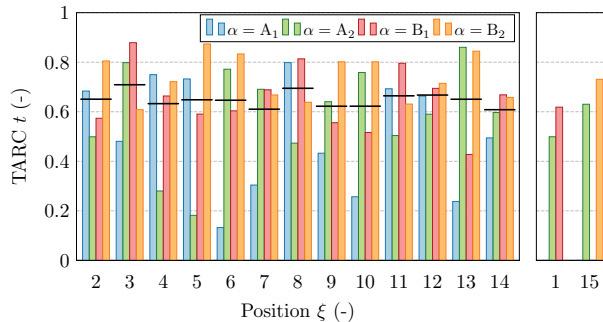


Figure B.5: TARC values of four orthogonal states ($\alpha, 1$) for the rectangular rim from Figure B.4 evaluated for different positions of port in the generator of the structure ξ at $ka = 10.19$. Black lines denote RMS values t_{RMS} . The states are named according to irreducible representations, see Table B.4.

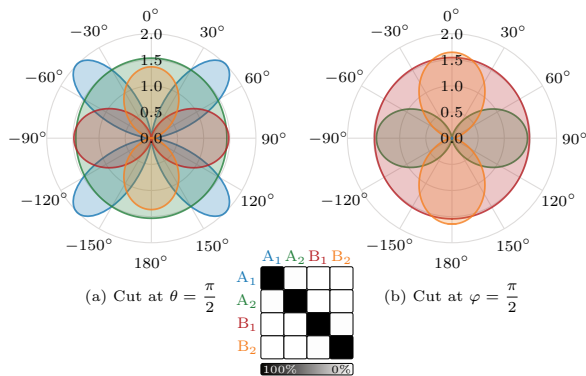


Figure B.6: Far-field cuts with polarization along direction $\hat{\varphi}$ computed at $ka = 1$ for excitation vectors $\mathbf{V}^{(\alpha, i)}$ for $\xi = 7$. Radiation patterns are orthogonal which is confirmed by the envelope correlation coefficient [163] depicted in the table. The naming convention adapted for the states is the same as in Figure B.5 and in Table B.4.

provide a unique best position ξ , see Figure B.7, where $N_f = 116$ frequency samples in the range corresponding to the antenna's electrical size $ka \in (0.5, 12)$ was used.

The unique solution is accomplished by evaluating the RMS value of TARC (B.19) over the frequency range in which the best position minimizing (B.21) is $\xi = 7$, see Figure B.8. The realized TARC for this optimal position over the whole frequency band is shown in Figure B.9. It can be observed that there is no frequency where all four states radiate well, which results from their different current distributions. However, minimizing (B.21), by counting all frequencies of the selected band, provides a solution in which average TARC over all channels is the best.

The values in Figure B.8 are not so different and, in fact, are unsatisfactory. This

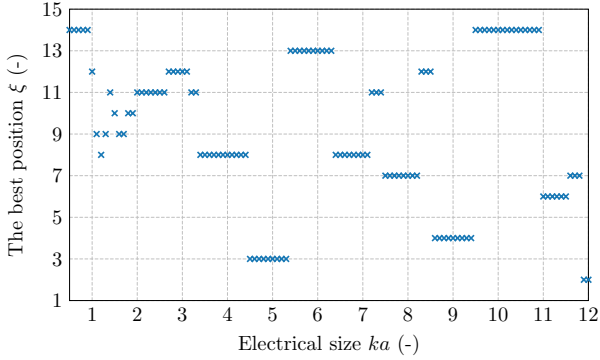


Figure B.7: The best position of the port in the generator of the structure ξ with respect to **TARC** value t_{RMS} evaluated at each frequency sample.

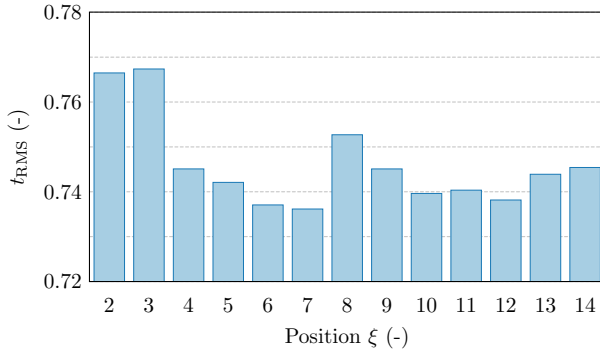


Figure B.8: **TARC** values evaluated by (B.19) for different positions ξ of the sole ($N_\xi = 1$) feeder which was symmetry-adapted.

is caused by the wide frequency range used and by employing the connected transmission lines of characteristic impedance $Z_0 = 50 \Omega$, which is not an optimal value for the chosen structure. Optimization of the impedance matching would demand a topological change of the antenna structure (keeping the necessary symmetries) which is beyond the scope of this paper.

B.5.5 More Ports Placed in the Generator of the Structure

The previous subsections assumed the existence of a sole port placed in the generator of the structure which was symmetry-adapted. Nevertheless, a higher number of ports might give better radiation properties. In the case of $N_\xi > 1$ ports placed in the generator of the structure, in addition to all statements in [Section B.5.2](#), the complex amplitudes connected to the ports also have significance.

As port excitation vector \mathbf{v} is constructed so that only ports placed in the generator of structure are excited (*i.e.*, there is N_ξ nonzero values) and because

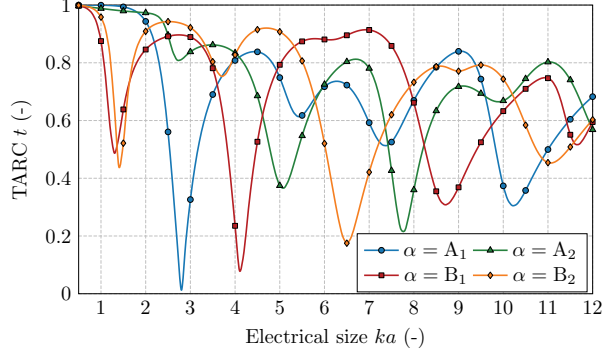


Figure B.9: TARC values of four orthogonal states $(\alpha, 1)$ for a rectangular rim depicted in Figure B.4, the best position $\xi = 7$ is considered.

the symmetry-adaptation process (B.13) transforms these N_ξ nonzero values to N_p nonzero values in vector $\mathbf{v}^{(\alpha,i)}$, the symmetry-adapted vector can also be expressed as

$$\mathbf{v}^{(\alpha,i)} = \mathbf{p}^{(\alpha,i)} \boldsymbol{\kappa}^{(\alpha,i)}, \quad (\text{B.22})$$

where $\mathbf{p} \in \mathbb{R}^{N_p \times N_\xi}$ is a port-indexing matrix (each column in \mathbf{p} corresponds to one exclusively excited port in the generator of the structure) and vector $\boldsymbol{\kappa}$ of size $N_\xi \times 1$ contains only voltages of ports placed in the generator of the structure.

Substituting (B.22) into (B.16) leads to

$$t^{(\alpha,i)}(\boldsymbol{\kappa}^{(\alpha,i)}) = \sqrt{1 - \frac{(\boldsymbol{\kappa}^{(\alpha,i)})^H \mathbf{A}^{(\alpha,i)} \boldsymbol{\kappa}^{(\alpha,i)}}{(\boldsymbol{\kappa}^{(\alpha,i)})^H \mathbf{B}^{(\alpha,i)} \boldsymbol{\kappa}^{(\alpha,i)}}}, \quad (\text{B.23})$$

where

$$\mathbf{A}^{(\alpha,i)} = 4Z_0 \left(\mathbf{Y} \mathbf{P} \mathbf{p}^{(\alpha,i)} \right)^H \mathbf{R}_0 \mathbf{Y} \mathbf{P} \mathbf{p}^{(\alpha,i)} \in \mathbb{C}^{N_\xi \times N_\xi} \quad (\text{B.24})$$

and

$$\mathbf{B}^{(\alpha,i)} = \left(\mathbf{k} \mathbf{p}^{(\alpha,i)} \right)^H \mathbf{k} \mathbf{p}^{(\alpha,i)} \in \mathbb{C}^{N_\xi \times N_\xi}. \quad (\text{B.25})$$

In order to minimize (B.23), a generalized eigenvalue problem

$$\mathbf{A}^{(\alpha,i)} \boldsymbol{\kappa}_p^{(\alpha,i)} = \lambda_p^{(\alpha,i)} \mathbf{B}^{(\alpha,i)} \boldsymbol{\kappa}_p^{(\alpha,i)} \quad (\text{B.26})$$

is solved and an eigenvector minimizing (B.23), *i.e.*, one corresponding to the highest eigenvalue $\lambda_p^{(\alpha,i)}$, is chosen. This solution provides the best achievable TARC for a given species (α, i) , the value of which is

$$t_{\text{bound}}^{(\alpha,i)} = \sqrt{1 - \max(\lambda_p^{(\alpha,i)})}. \quad (\text{B.27})$$

In the case of more ports placed in the generator of the structure, the process described in this section must be used in every step of optimization (B.21), *i.e.*, vectors $\boldsymbol{\kappa}^{(\alpha,i)}$ must be evaluated for each choice of ξ .

Table B.5: The best values of RMS of TARC for various excitation strategies on a rectangular rim depicted in Figure B.4.

Solution	N_ξ	$\{\xi_p\}$	N_p	t_{RMS}
Best 1	1	14	4	0.608
Best 2	2	10, 11	8	0.400
Best 3	3	11, 12, 13	12	0.317
Table B.2, column 2	3	1, 10, 15	8	0.587

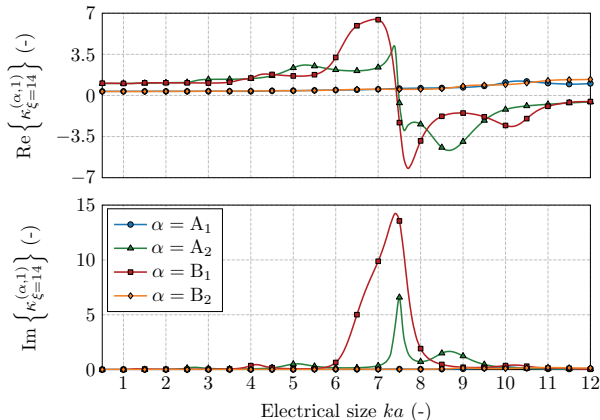


Figure B.10: Voltage amplitudes $\kappa^{(\alpha,1)}$ for a configuration with a combination of $N_\xi = 2$ positions at $\xi \in \{12, 14\}$. The voltage impressed to the port at position $\xi = 12$ is normalized to one volt.

B.5.6 Analysis with More Ports in the Generator of the Structure

The optimal placement of two and three ports, $N_\xi = \{2, 3\}$, in the generator of the structure is studied in this section. The same metallic rim as in Section B.5.3 operating at $ka = 10.19$ is used and the method from Section B.5.5 is applied, see Table B.5 for the results. It can be observed that the involvement of more ports significantly decreases the RMS of TARC across the states. This is because the optimal current density reaching minimal TARC is better approximated with more excitation ports.

Table B.5 shows results for a port configuration adopted from [83] which was discussed in Section B.3. This configuration uses $N_\xi = 3$ ports placed in the generator of the structure and $N_p = 8$ ports. Nevertheless, Table B.5 reveals that better results may be obtained when the symmetry-adapted basis described in this paper is utilized.

The frequency range analysis from Section B.5.4 was repeated for the combination of $N_\xi = 2$ ports placed in the generator of the structure. Ports at positions $\xi \in \{12, 14\}$ provide the lowest RMS (B.19) $t_{\text{RMS}} = 0.605$. However, the solution with a combination of more positions $\{\xi_k\}$ requires optimized port voltage amplitudes κ (B.22) which vary over frequency, see Figure B.10. Figure B.11 shows realized TARC values reached by this configuration. The radiation efficiency is significantly improved as compared to the previous solution shown in Figure B.9.

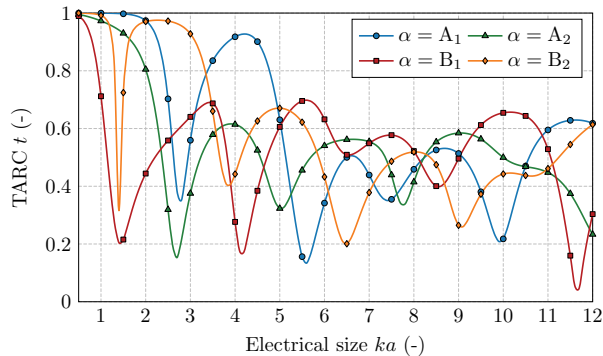


Figure B.11: TARC values of four orthogonal states ($\alpha, 1$) for the rectangular rim depicted in Figure B.4 and a combination of $N_\xi = 2$ positions at $\xi \in \{12, 14\}$.

B.6 Conclusion

The presence of symmetries was utilized via point group theory to describe a procedure that determines where to place ports on an antenna to achieve orthogonal states with respect to any radiation metric, such as radiation and total efficiency, antenna gain, or Q-factor.

The methodology can play an essential role in the design of MIMO antennas when a few ports can orthogonalize several states (*e.g.*, four ports on a rectangular structure generate four orthogonal states, eight ports on a square structure generate six orthogonal states, etc.). The maximal number of orthogonal states and the minimal number of ports needed to excite all of them is determined only from the knowledge of the point group to which the given geometry belongs. Due to the symmetries, the procedure of ports' placement can be accelerated by the reduction of the section where the port placed in the region of the generator of the structure can be placed and subsequently “symmetry-adapted” to the proper positions at the entire structure. It was also demonstrated that port positions intersecting reflection planes should not be used since they do not allow the excitation of all states.

A proper placement of ports was illustrated by an example—with a single frequency and frequency range analysis—featuring a simultaneous minimization of total active reflection coefficient across the realized orthogonal states. Leaving aside the final matching optimization, it has been clearly presented how symmetries can be utilized in the design of a multi-port antenna.

B.A Matrix Operators

Many antenna metrics are expressible as quadratic forms over time-harmonic current density $\mathbf{J}(\mathbf{r})$, [61, 158], which is represented in a suitable basis $\{\boldsymbol{\psi}_n(\mathbf{r})\}$ as

$$\mathbf{J}(\mathbf{r}) \approx \sum_{n=1}^{N_{\text{in}}} I_n \boldsymbol{\psi}_n(\mathbf{r}) \quad (\text{B.28})$$

with N_u being the number of basis functions. The metric p is then given as

$$p = \langle \mathbf{J}, \mathcal{A}\mathbf{J} \rangle \approx \mathbf{I}^H [\langle \boldsymbol{\psi}_m(\mathbf{r}), \mathcal{A}\boldsymbol{\psi}_m(\mathbf{r}) \rangle] \mathbf{I} = \mathbf{I}^H \mathbf{A} \mathbf{I}. \quad (\text{B.29})$$

For example, the complex power balance [164] for radiator Ω made of a good conductor reads

$$P_{\text{rad}} + P_L + 2j\omega (W_m - W_e) \approx \frac{1}{2} \mathbf{I}^H (\mathbf{Z}_0 + \mathbf{R}_\rho) \mathbf{I}, \quad (\text{B.30})$$

where the vacuum impedance matrix $\mathbf{Z}_0 = \mathbf{R}_0 + j\mathbf{X}_0$ is defined element-wise as

$$Z_{0,mn} = -j\omega\mu_0 \int_{\Omega} \int_{\Omega} \boldsymbol{\psi}_m(\mathbf{r}) \cdot \mathbf{G}(\mathbf{r}, \mathbf{r}') \cdot \boldsymbol{\psi}_n(\mathbf{r}') \, dS \, dS', \quad (\text{B.31})$$

with ω being angular frequency, μ_0 being vacuum permeability, and \mathbf{G} being free-space dyadic Green's function [165]. Ohmic losses P_L are represented via matrix \mathbf{R}_ρ which, under thin-sheet approximation [166], is defined element-wise as [61]

$$R_{\rho,mn} = \int_{\Omega} \rho(\mathbf{r}) \boldsymbol{\psi}_m(\mathbf{r}) \cdot \boldsymbol{\psi}_n(\mathbf{r}) \, dS, \quad (\text{B.32})$$

where ρ is surface resistivity [166]. Another notable operator [167, 168]

$$\mathbf{W} = \omega \frac{\partial \mathbf{X}_0}{\partial \omega} \quad (\text{B.33})$$

gives energy stored in the near-field on a device, thus determining the bandwidth potential of a radiator [169].

B.B Excitation Vector

The excitation of obstacle Ω is realized by an incident electric field intensity $\mathbf{E}^i(\mathbf{r})$ represented element-wise in a basis (B.28) as

$$V_n = \int_{\Omega} \boldsymbol{\psi}_n(\mathbf{r}) \cdot \mathbf{E}^i(\mathbf{r}) \, dS, \quad (\text{B.34})$$

with $\mathbf{V} = [V_n]$ called the excitation vector. Incident field $\mathbf{E}^i(\mathbf{r})$ can be non-zero everywhere (then the vector \mathbf{V} generally contains non-zero entries everywhere, *e.g.*, a plane wave), or in a limited region only (then vector \mathbf{V} is sparse, *e.g.*, a delta-gap generator or a coaxial probe).

Considering electric field integral equation [28] in algebraic representation (B.28), current solution \mathbf{I} to a problem of given excitation \mathbf{V} reads

$$\mathbf{Z}\mathbf{I} = \mathbf{V}, \quad (\text{B.35})$$

where $\mathbf{Z} = \mathbf{Z}_0 + \mathbf{R}_\rho$ is the system (impedance) matrix.

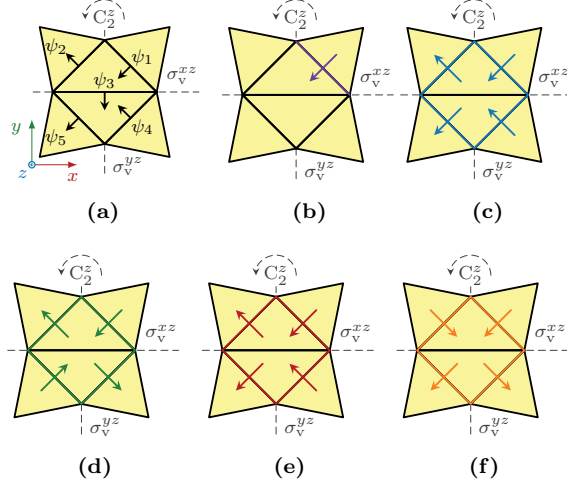


Figure B.12: (a) Five basis functions and their orientation on a star structure. (b) An excitation vector $\mathbf{V}(1) = [1, 0, 0, 0, 0]^T$ was symmetry-adapted by (B.13) to four irreps: (c) $\alpha = A_1$, (d) $\alpha = A_2$, (e) $\alpha = B_1$, (f) $\alpha = B_2$.

B.C Symmetry-Adaptation of a Vector

The process of symmetry-adaptation of a vector (B.13) is illustrated and explained in the example of a simple structure consisting of five RWG [51] basis functions, see Figure B.12a. The delta-gap ports are connected directly to the basis functions, *i.e.*, ports' positions ξ are identical to the numbering of basis functions. This structure belongs to the same point group C_{2v} as the rectangular plate introduced in Section B.3 and is thus invariant to the same four symmetry operations: identity (E), rotation by π around z axis (C_2^z) and two reflections by xz and yz planes ($\sigma_v^{xz}, \sigma_v^{yz}$). The point group C_{2v} consists of four irreps $\alpha \in \{A_1, A_2, B_1, B_2\}$, with dimensionality $g^{(\alpha)} = 1$ for each irrep α .

Mapping matrix $\mathbf{C}(R)$, for each symmetry operation R , is constructed so as to interlink pairs of basis functions which are mapped onto each other (respecting their orientation) via a given symmetry operation. Mapping matrices for the star structure from Figure B.12a read

$$\mathbf{C}(E) = \text{diag}([+1, +1, +1, +1, +1]), \quad (\text{B.36})$$

$$\mathbf{C}(C_2^z) = \begin{bmatrix} 0 & 0 & 0 & 0 & -1 \\ 0 & 0 & 0 & -1 & 0 \\ 0 & 0 & -1 & 0 & 0 \\ 0 & -1 & 0 & 0 & 0 \\ -1 & 0 & 0 & 0 & 0 \end{bmatrix}, \quad (\text{B.37})$$

Table B.6: Character table for point group C_{2v} [30], a rectangular plate and the star structure belong to.

C_{2v}	E	C_2^z	σ_v^{xz}	σ_v^{yz}
A_1	+1	+1	+1	+1
A_2	+1	+1	-1	-1
B_1	+1	-1	+1	-1
B_2	+1	-1	-1	+1

$$\mathbf{C}(\sigma_v^{xz}) = \begin{bmatrix} 0 & 0 & 0 & +1 & 0 \\ 0 & 0 & 0 & 0 & +1 \\ 0 & 0 & -1 & 0 & 0 \\ +1 & 0 & 0 & 0 & 0 \\ 0 & +1 & 0 & 0 & 0 \end{bmatrix}, \quad (\text{B.38})$$

$$\mathbf{C}(\sigma_v^{yz}) = \begin{bmatrix} 0 & -1 & 0 & 0 & 0 \\ -1 & 0 & 0 & 0 & 0 \\ 0 & 0 & +1 & 0 & 0 \\ 0 & 0 & 0 & 0 & -1 \\ 0 & 0 & 0 & -1 & 0 \end{bmatrix}. \quad (\text{B.39})$$

A general framework of how to obtain irreducible matrix representations $\mathbf{D}^{(\alpha)}(R)$ is described in [161, Sec. II.B]. However, for one-dimensional irreps, the matrices $\mathbf{D}^{(\alpha)}(R)$ can be obtained directly from the character table, see the character table for the C_{2v} point group in Table B.6. These character tables are known [30] and unique for all point groups. For each irrep α (row) and each symmetry operation (column) the entry in the character table, called ‘‘a character’’, is $\chi^{(\alpha)}(R) = \text{trace}(\mathbf{D}^{(\alpha)}(R))$. Since the dimensionality of all irreps of the point group C_{2v} is one ($g^{(\alpha)} = 1$ for each irrep α), values in the character table are equal to the irreducible matrix representations $\mathbf{D}^{(\alpha)}(R)$ (matrices of size 1×1).

The position of the initial port ξ can be freely chosen within the generator of the structure. Let us pick the position at $\xi = 1$ and construct an excitation vector $\mathbf{V}(1) = [1, 0, 0, 0, 0]^T$, see Figure B.12b.

Once matrices $\mathbf{C}(R)$ and $\mathbf{D}^{(\alpha)}(R)$ are known, a symmetry-adaptation of the excitation vector $\mathbf{V}(1)$ into a given species (α, i) can be processed. The equation (B.13) can be read as: An initial port recorded in $\mathbf{V}(\xi)$ is mapped onto its ‘‘doublet’’ under symmetry operation R via mapping matrix $\mathbf{C}(R)$ while multiplying by a proper value from matrix $\mathbf{D}^{(\alpha)}(R)$ (in this case only values ± 1) adds and provides a orthogonality property to the final symmetry-adapted vector $\mathbf{V}^{(\alpha, i)}$:

$$\mathbf{V}^{(A_1, 1)} = [+1, -1, 0, +1, -1]^T, \quad (\text{B.40})$$

$$\mathbf{V}^{(A_2, 1)} = [+1, +1, 0, -1, -1]^T, \quad (\text{B.41})$$

$$\mathbf{V}^{(B_1, 1)} = [+1, +1, 0, +1, +1]^T, \quad (\text{B.42})$$

$$\mathbf{V}^{(B_2, 1)} = [+1, -1, 0, -1, +1]^T. \quad (\text{B.43})$$

These solutions are shown in Figures B.12c–f. The normalization $g^{(\alpha)}/g = 1/4$ is intentionally omitted for each of solutions.

B.D Total Active Reflection Coefficient

In order to derive (B.16), incident power P_{in} is written using incident power waves $\mathbf{a} \in \mathbb{C}^{P \times 1}$ at antenna ports [170] as

$$P_{\text{in}} = \frac{1}{2} \mathbf{a}^H \mathbf{a} \quad (\text{B.44})$$

and the radiated power is written as [28]

$$P_{\text{rad}} = \frac{1}{2} \mathbf{I}^H \mathbf{R}_0 \mathbf{I}, \quad (\text{B.45})$$

where $\mathbf{R}_0 \in \mathbb{R}^{N_u \times N_u}$ is a radiation part of impedance matrix $\mathbf{Z} \in \mathbb{C}^{N_u \times N_u}$ and $\mathbf{I} \in \mathbb{C}^{N_u \times 1}$ is a vector of expansion coefficients within the MoM solution to the electric field integral equation (EFIE) [28], see Section B.A. Using (B.35) it holds that

$$P_{\text{rad}} = \frac{1}{2} \mathbf{V}^H \mathbf{Y}^H \mathbf{R}_0 \mathbf{Y} \mathbf{V}. \quad (\text{B.46})$$

Assume an antenna fed by ports connected to transmission lines of real characteristic impedance Z_0 . Within the MoM paradigm [28], the excitation vector is

$$\mathbf{V} = \mathbf{P} \mathbf{v}, \quad (\text{B.47})$$

where \mathbf{v} are port voltages and matrix $\mathbf{P} \in \mathbb{R}^{N_u \times N_p}$ is a matrix the columns of which are the representations of separate ports. Notice that

$$\mathbf{v} = \left(\mathbf{P}^H \mathbf{P} \right)^{-1} \mathbf{P}^H \mathbf{V}. \quad (\text{B.48})$$

The incident power waves can be expressed as [170]

$$\mathbf{a} = \frac{1}{2\sqrt{Z_0}} (\mathbf{e} + Z_0 \mathbf{y}) \mathbf{v}, \quad (\text{B.49})$$

where \mathbf{e} is an identity matrix and \mathbf{y} is the admittance matrix [170] for port-like quantities.

Substituting (B.46), (B.47) and (B.49) into (B.15) results in (B.16). More details about TARC for multi-port lossy antennas can be found in [109].



Finding Optimal Total Active Reflection Coefficient and Realized Gain for Multi-port Lossy Antennas

Published as: M. Capek, L. Jelinek, and M. Masek, “Finding Optimal Total Active Reflection Coefficient and Realized Gain for Multiport Lossy Antennas,” *IEEE Transactions on Antennas and Propagation*, vol. 69, no. 5, pp. 2481-2493, May 2021, DOI: [10.1109/TAP.2020.3030941](https://doi.org/10.1109/TAP.2020.3030941).

Abstract—A numerically effective description of the total active reflection coefficient and realized gain are studied for multi-port antennas. Material losses are fully considered. The description is based on operators represented in an entire-domain port-mode basis, *i.e.*, on matrices with favorably small dimensions. Optimal performance is investigated and conditions on optimal excitation and matching are derived. The solution to the combinatorial problem of optimal ports’ placement and optimal feeding synthesis is also accomplished. Four examples of various complexity are numerically studied, demonstrating the advantages of the proposed method. The final formulas can easily be implemented in existing electromagnetic simulators using integral equation solver.

Index terms: Antenna theory, MIMO, electromagnetic modeling, method of moments, eigenvalues and eigenfunctions, optimization.

C.1 Introduction

With increasing interest in multi-port and multiple-input multiple-output (MIMO) systems, see, *e.g.*, [132, 133, 137, 171–173], a new set of figure of merits were needed to judge their performance. Among the few available choices, the total active reflection coefficient (TARC) [157, 174, 175] became widely used, due mainly to its straightforward definition and experimental accessibility. Considering a given excitation, it reads “the square root of the available power generated by all excitations minus radiated power, divided by available power” [157].

The TARC was successfully utilized for practical antenna design, covering wide range of MIMO applications [176–179]. Improvement of large-scale end-fire antenna arrays matching with simultaneous pattern synthesis was achieved via convex opti-

mization in [180]. The optimal performance on TARC in a loss-less scenario using scattering matrix was studied in [133].

Numerical evaluations of TARC typically neglect ohmic losses (relating TARC to matching efficiency only), assuming that vanishing TARC implies the acceptance of all incident power by the antenna and radiation of it into far field [181]. This assumption is, nevertheless, not true when ohmic losses are present and it may be a source of significant discrepancies between simulation and measurement [182]. In order to remedy this issue and provide simple, yet precise TARC evaluation, a new formulation has been devised in this paper (relating TARC to the total efficiency). Unlike other procedures relying on equivalent circuits [175, 182], the presented approach is of full-wave nature, *i.e.*, there are many discrete ports which can be freely distributed across arbitrarily shaped scatterer, optionally made of lossy and inhomogeneous material. Another notable feature is that characteristic impedance can be separately prescribed for each port.

The presented derivations make use of port modes [28, 159], which compress the large algebraic system (typically thousands times thousands) describing the antenna into port-related matrix operators of rank given by the number of ports (typically not more than tens by tens). Due to this property, the evaluation of antenna metrics is numerically inexpensive and allows for optimal design. Particularly, assuming a given shape, materials, operational frequency, number of ports and matching topology, this manuscript introduces methodology, how to determine where the ports have to be placed, what is the best combination of excitation voltages and what are the optimal matching impedances to reach the best attainable values of TARC and realized gain. The understanding provided by the method also updates the knowledge about optimal excitation of antenna arrays [135, 159, 183–185].

This paper is structured as follows. TARC is briefly reviewed and expressed in operator form in Section C.2, and reformulated in port modes in Section C.3. The fundamental bounds on TARC performance are derived in Section C.4. To demonstrate the usefulness of the novel formula and its capability of determining optimal performance of a multi-port antenna, the optimal placement of feeding ports is shown in Section C.5 and optimal characteristic impedances are found in Section C.6. The realized gain and its fundamental bound are treated in Section C.7. The paper is concluded in Section C.8. All relevant sections are accompanied with numerical examples demonstrating flexibility of the method.

C.2 TARC: Full-Wave Algebraic Formulation

Considering a multi-port antenna as depicted in Figure C.1, the total active reflection coefficient (TARC) is defined as [157]

$$\Gamma^t = \sqrt{1 - \frac{P_{\text{rad}}}{P_{\text{in}}}}, \quad (\text{C.1})$$

where P_{rad} is the power radiated by the antenna and P_{in} is the incident (available) power. The incident power is most easily evaluated as

$$P_{\text{in}} = \frac{1}{2} \mathbf{a}^H \mathbf{a}, \quad (\text{C.2})$$

where $\mathbf{a} \in \mathbb{C}^{P \times 1}$ is a vector of incident power waves [170] with P being the number of ports and superscript H denoting the Hermitian conjugate.

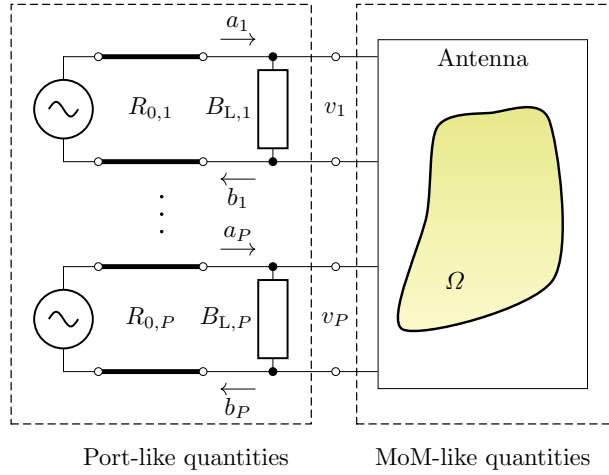


Figure C.1: Multi-port antenna system, consisting of scatterer Ω and P ports connected to transmission lines of characteristic impedance $R_{0,p}$. All ports might optionally be tuned by a lumped susceptance $B_{L,p}$. The variable connecting circuitry on the left and the full-wave model on the right are port voltages accumulated in vector \mathbf{v} .

In the case of a loss-less antenna, the radiated power can be evaluated as

$$P_{\text{rad}} = \frac{1}{2} (\mathbf{a}^H \mathbf{a} - \mathbf{b}^H \mathbf{b}), \quad (\text{C.3})$$

where $\mathbf{b} \in \mathbb{C}^{P \times 1}$ is the vector of reflected power waves. For a lossy antenna, this is no longer valid. In a general case, the radiated power must be evaluated as [28]

$$P_{\text{rad}} = \frac{1}{2} \mathbf{I}^H \mathbf{R}_{\Omega} \mathbf{I}, \quad (\text{C.4})$$

where $\mathbf{R}_{\Omega} \in \mathbb{R}^{N \times N}$ is the radiation part of the impedance matrix [28]

$$\mathbf{Z} = \mathbf{R}_{\Omega} + \mathbf{R}_{\rho} + j\mathbf{X}_{\Omega}, \quad (\text{C.5})$$

and $\mathbf{I} \in \mathbb{C}^{N \times 1}$ is a vector of expansion coefficients within a method of moments (MoM) solution [28] to surface current density

$$\mathbf{J}(\mathbf{r}) \approx \sum_{n=1}^N I_n \psi_n(\mathbf{r}) \quad (\text{C.6})$$

with $\{\psi_n\}$ being a properly chosen set of basis functions [37]. The power dissipated in ohmic losses¹ is correspondingly evaluated as

$$P_{\text{lost}} = \frac{1}{2} \mathbf{I}^H \mathbf{R}_{\rho} \mathbf{I}, \quad (\text{C.7})$$

¹If volumetric method of moments is used, matrix \mathbf{X}_{ρ} would have to be added to (C.5) to account for the presence of dielectric bodies. The rest of the formulation remains untouched.

where matrix $\mathbf{R}_\rho \in \mathbb{R}^{N \times N}$ is calculated for a surface resistivity model as described in [61, App. C]. The procedure of how to evaluate current \mathbf{I} with connected lumped susceptances $\{B_{L,p}\}$ is described in the following section.

The substitution of (C.2) and (C.4) into (C.1) is, in principle, enough to evaluate TARC, nevertheless, such a prescription is unpleasant when mixing port-based (\mathbf{a} , \mathbf{b}) and MoM-based (\mathbf{I}) quantities. This form, as an example, does not allow for evaluating optimal performance [61, 107, 158], which will be derived later. In order to overcome this difficulty, the TARC formula will now be recast into a form which solely contains port quantities.

C.3 Expression of TARC in Port Quantities

In order to rewrite TARC in terms of port-related quantities, *i.e.*, matrices and vectors of size P , the excitation vector \mathbf{V} and current vector \mathbf{I} must be related to port voltages \mathbf{v} and port currents \mathbf{i} .

In the first step, excitation vector \mathbf{V} from the MoM description of the antenna

$$\mathbf{I} = \mathbf{Y}\mathbf{V}, \quad (\text{C.8})$$

with $\mathbf{Y} = \mathbf{Z}^{-1} \in \mathbb{C}^{N \times N}$ being admittance matrix, is related to port voltages $\mathbf{v} \in \mathbb{C}^{P \times 1}$ via

$$\mathbf{V} = \mathbf{D}\mathbf{C}\mathbf{v}, \quad (\text{C.9})$$

where port positions are defined by an indexing matrix $\mathbf{C} \in \{0, 1\}^{N \times P}$,

$$C_{np} = \begin{cases} 1 & p\text{-th port is placed at } n\text{-th position,} \\ 0 & \text{otherwise,} \end{cases} \quad (\text{C.10})$$

i.e., $\mathbf{C}^H\mathbf{C} = \mathbf{1} \in \mathbb{R}^{P \times P}$. Since the basis functions (C.5) may or may not have dimensions, diagonal normalization matrix $\mathbf{D} \in \mathbb{R}^{N \times N}$ is defined elementwise as

$$D_{nn} = \xi_n \quad (\text{C.11})$$

to ensure that the port-based quantities such as impedances, voltages and currents have dimensions of Ohms, Volts and Amperes. For example, for dimensionless basis functions, such as Rao-Wilton-Glisson (RWG) [51], the normalization variable would typically be the basis function's edge length l_n , *i.e.*, $\xi_n = l_n$. Analogously to the port voltage \mathbf{v} , port current \mathbf{i} is defined via

$$\mathbf{i} = \mathbf{C}^H\mathbf{D}^H\mathbf{I}. \quad (\text{C.12})$$

Substituting (C.8) and, subsequently, (C.9) into (C.12) gives port admittance matrix \mathbf{y}

$$\mathbf{i} = \mathbf{y}\mathbf{v}, \quad (\text{C.13})$$

where

$$\mathbf{y} = \mathbf{C}^H\mathbf{D}^H\mathbf{Y}\mathbf{D}\mathbf{C}. \quad (\text{C.14})$$

Note that complex power [116] is strictly conserved between port-like and MoM-like quantities, *i.e.*, $\mathbf{i}^H\mathbf{v} = \mathbf{I}^H\mathbf{V}$.

The next step is the evaluation of the radiated power (C.4) using port voltages. This can be done thanks to the relation

$$\mathbf{I}^H \mathbf{M} \mathbf{I} = \mathbf{v}^H \mathbf{n} \mathbf{v}, \quad (\text{C.15})$$

with

$$\mathbf{n} = \mathbf{C}^H \mathbf{D}^H \mathbf{Y}^H \mathbf{M} \mathbf{Y} \mathbf{D} \mathbf{C}, \quad (\text{C.16})$$

which is valid for any matrix \mathbf{M} and results from substituting (C.8) and (C.9) into the left-hand side of (C.15). A particularly important example of this relation is the substitution $\mathbf{M} = \mathbf{R}_\Omega$ which gives rise to relation

$$P_{\text{rad}} = \frac{1}{2} \mathbf{I}^H \mathbf{R}_\Omega \mathbf{I} = \frac{1}{2} \mathbf{v}^H \mathbf{g}_\Omega \mathbf{v}, \quad (\text{C.17})$$

with $\mathbf{g}_\Omega = \mathbf{C}^H \mathbf{D}^H \mathbf{Y}^H \mathbf{R}_\Omega \mathbf{Y} \mathbf{D} \mathbf{C}$ and analogously for ohmic losses to

$$P_{\text{lost}} = \frac{1}{2} \mathbf{I}^H \mathbf{R}_\rho \mathbf{I} = \frac{1}{2} \mathbf{v}^H \mathbf{g}_\rho \mathbf{v}. \quad (\text{C.18})$$

The last step is the connection of power waves \mathbf{a}, \mathbf{b} , which exist in lossless feeding transmission lines of characteristic impedance $R_{0,p}$, see Figure C.1, with port voltages, *i.e.*,

$$\mathbf{a} = \frac{1}{2} (\mathbf{\Lambda}^{-1} \mathbf{v} + \mathbf{\Lambda} \mathbf{i}) = \frac{1}{2} (\mathbf{1} + \mathbf{\Lambda} (\mathbf{y} + \mathbf{y}_L) \mathbf{\Lambda}) \mathbf{\Lambda}^{-1} \mathbf{v} = \mathbf{k}_i \mathbf{v}, \quad (\text{C.19})$$

$$\mathbf{b} = \frac{1}{2} (\mathbf{\Lambda}^{-1} \mathbf{v} - \mathbf{\Lambda} \mathbf{i}) = \frac{1}{2} (\mathbf{1} - \mathbf{\Lambda} (\mathbf{y} + \mathbf{y}_L) \mathbf{\Lambda}) \mathbf{\Lambda}^{-1} \mathbf{v} = \mathbf{k}_r \mathbf{v}, \quad (\text{C.20})$$

where [170]

$$\Lambda_{pp} = \sqrt{R_{0,p}} \quad (\text{C.21})$$

and where admittances $jB_{L,p}$ were accumulated at the diagonal of matrix \mathbf{y}_L .

The final expression for TARC used throughout this paper reads

$$\Gamma^t = \sqrt{1 - \frac{\mathbf{v}^H \mathbf{g}_\Omega \mathbf{v}}{\mathbf{v}^H \mathbf{k}_i^H \mathbf{k}_i \mathbf{v}}} = \sqrt{1 - \frac{\mathbf{a}^H \mathbf{k}_i^{-H} \mathbf{g}_\Omega \mathbf{k}_i^{-1} \mathbf{a}}{\mathbf{a}^H \mathbf{a}}}. \quad (\text{C.22})$$

The formulas (C.17), (C.18), and (C.22) can, in principle, be evaluated in contemporary electromagnetic simulators as well. Nevertheless, the port-mode matrix formulation (C.16) seems to not be implemented yet. For this reason, the ohmic losses extraction is conventionally done via far field integration which is a time-consuming task. The procedure (C.16) is not only computationally more efficient but also more general. Any quantity based on matrix operator, *e.g.*, stored energy matrix [107], can be transformed. In this last case, only integration of near field, a computationally challenging operation, can circumvent the usage of (C.16).

C.3.1 Example: Evaluation of TARC (Single-port Antenna)

Let us start with a simple single-port radiator, a thin-strip dipole made of copper ($\sigma_{\text{Cu}} = 5.96 \cdot 10^7 \text{ Sm}^{-1}$) with length ℓ and width $\ell/100$. The frequency range used for the study is $ka \in [1/2, 10]$, where k is the wavenumber in vacuum and a is a radius of the smallest sphere circumscribing the antenna. TARC is evaluated with the

APPENDIX C. FINDING OPTIMAL TOTAL ACTIVE REFLECTION
COEFFICIENT AND REALIZED GAIN FOR MULTI-PORT LOSSY ANTENNAS

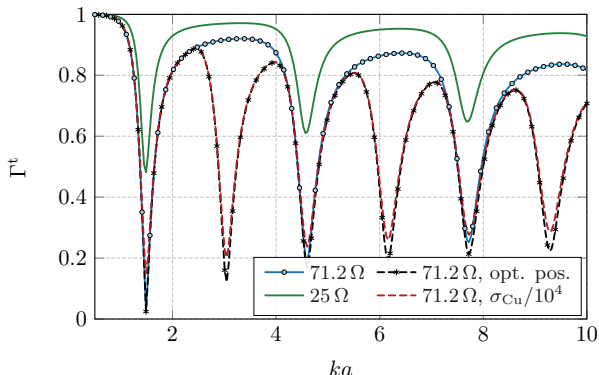


Figure C.2: TARC for a thin-strip dipole of length ℓ and width $\ell/100$. Various characteristic impedances $R_{0,1}$ and surface resistivities were used. The dashed lines present the cases of the optimal delta gap placement at each frequency ka . The solid curves assume the delta gap in the geometrical center of the dipole.

delta-gap feeding [162] covering the entire width of the dipole. All the operators were evaluated in Antenna Toolbox for MATLAB (AToM) [29] which utilizes RWG basis functions [51]. Two distinct values of transmission line characteristic impedance are studied, $R_{0,1} = 71.2 \Omega$ (the input impedance of the dipole at its first resonance) and $R_{0,1} = 25 \Omega$, see Figure C.2. There are no tuning lumped elements, $\mathbf{y}_L = \mathbf{0}$. Since the dipole is a single-port antenna, the specific excitation voltage plays no role in the evaluation of (C.22) and can be freely set to $v_1 = 1 \text{ V}$. This makes it possible to effectively find an optimal placement of the port along the dipole depending on the electrical size ka . Matrices \mathbf{g}_Ω and \mathbf{k}_i , corresponding to a port at n -th edge, are denoted as $g_{\Omega,n}$ and $k_{i,n}$ (they are scalars in this single-port case). Consequently, the minimal TARC, with respect to the optimal placement of the port, can be found via elementwise division

$$\min_n \{ \Gamma_n^t \} = \max_n \left\{ \frac{g_{\Omega,n}}{|k_{i,n}|^2} \right\} \quad (\text{C.23})$$

for all tested positions. The position for minimum TARC is shown in Figure C.3 with the corresponding TARC shown in Figure C.2.

The last study reveals that the dipole antenna is relatively immune to ohmic losses since the reduction of the conductivity by four orders in magnitude causes only a mild drop in performance. It is worth noting that, as far as the ohmic losses are negligible, TARC can be zeroed by a proper choice of tuning susceptance and characteristic resistance. This possibility is studied later on in Section C.6 for multi-port antennas.

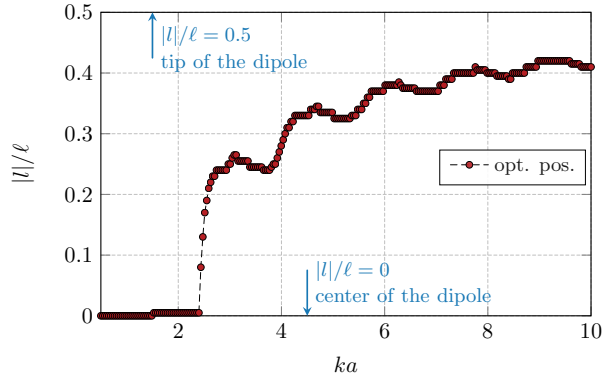


Figure C.3: Optimal placement of a delta-gap feeder along the thin-strip dipole made of copper. The placement is shown in relative length $|l|/\ell$ from the middle of the dipole. The vertical scale represents the position of the basis function to be fed at each electrical size ka . The corresponding TARC is depicted by the black dashed line in Figure C.2.

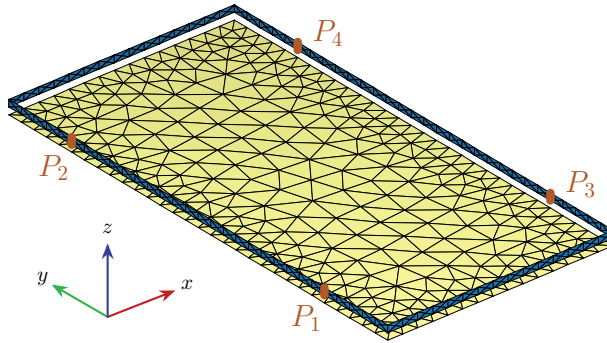


Figure C.4: A metallic rim with parasitic ground plane with four possible ports, denoted P_p , $p \in \{1, \dots, 4\}$. Both the rim and the ground plane are made of copper. The ports are placed at a distance of $\ell/5$ from the ends of the longer side.

C.3.2 Example: Evaluation of TARC (Multi-port Antenna)

The second example, to be studied in the rest of the paper, is a four-port metallic rim placed above a ground plane, both of which are made of copper ($\sigma_{\text{Cu}} = 5.96 \cdot 10^7 \text{ Sm}^{-1}$), see Figure C.4. The dimensions of the structure are: length $\ell = 150 \text{ mm}$, width $\ell/2$, height of the strip $3\ell/200$, and the elevation of the rim above the ground plane $3\ell/200$. The rim is discretized by a uniform mesh grid consisting of 450 basis functions. The ground plane is discretized by a Delaunay triangulation [117] with 798 basis functions, *i.e.*, the total number of degrees of freedom is $N = 1248$. Notice here that the example serves mainly as a demonstration of a new designing framework for the effective evaluation and optimization of TARC. We have no intention of designing and optimizing a realistic system.

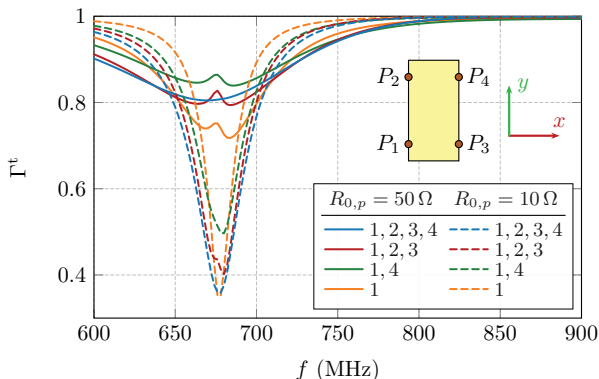


Figure C.5: TARC for the metallic rim with parasitic ground plane, depicted in Figure C.4. The characteristic impedance $50\ \Omega$ and $10\ \Omega$ were used for all enabled ports. Four various combination of ports with unit voltage excitation were studied.

We start the investigation with the fixed placement of the ports, denoted as P_p , $p \in \{1, \dots, 4\}$, see Figure C.4, and with unit excitation $v_p = 1\text{ V}$ at all ports (the impressed electric field intensity points in y direction for all ports) and with equal characteristic impedances $R_{0,p}$.

TARC for two different impedances $R_{0,p}$ and a varying number of uniformly excited ports is depicted in Figure C.5. No lumped susceptances were used for simplicity, $B_{L,p} = 0$. Some observations may already be made. In general, utilizing more ports does not automatically result in a lower value of TARC. Considering the fixed body of an antenna, optimal TARC is a complicated function of the characteristic impedances, matching, excitation, and ports' placement. The optimality of TARC with respect to all these parameters is studied in the following sections.

C.4 Optimal Excitation for Minimum TARC

Let us first consider that characteristic impedances $R_{0,p}$ and matching susceptances $B_{L,p}$ are fixed. In such scenario, TARC (C.22) is, for a fixed geometry, solely a function of voltage vector \mathbf{v} and its minimization takes the form of the maximization of the total efficiency η_{tot} since

$$\eta_{\text{tot}} = \eta_{\text{rad}}\eta_{\text{match}} = 1 - (\Gamma^t)^2 = \frac{\mathbf{v}^H \mathbf{g}_\Omega \mathbf{v}}{\mathbf{v}^H \mathbf{k}_i^H \mathbf{k}_i \mathbf{v}}, \quad (\text{C.24})$$

where the radiation and matching efficiencies are defined as [164]

$$\eta_{\text{rad}} = \frac{P_{\text{rad}}}{P_{\text{rad}} + P_{\text{lost}}}, \quad (\text{C.25})$$

and

$$\eta_{\text{match}} = \frac{P_{\text{rad}} + P_{\text{lost}}}{P_{\text{in}}}. \quad (\text{C.26})$$

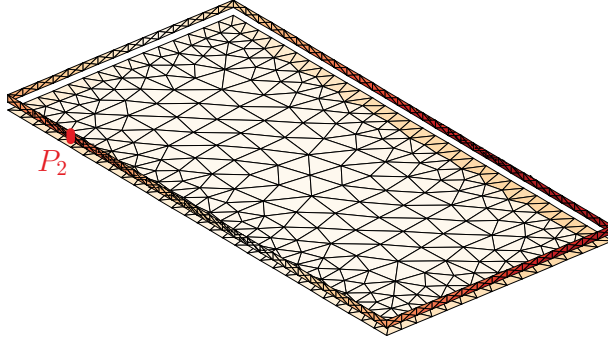


Figure C.6: Current density (absolute value) of a port-mode excited at 500 MHz by a unit voltage impressed at port P_2 . For the set of ports depicted in Figure C.4, the excitation scheme reads $\mathbf{v} = [0 \ 1 \ 0 \ 0]^H$.

Rigorously, the optimization problem for the maximal total efficiency (minimum TARC) reads

$$\begin{aligned} & \text{maximize} && \mathbf{v}^H \mathbf{g}_\Omega \mathbf{v} \\ & \text{subject to} && \mathbf{v}^H \mathbf{k}_i^H \mathbf{k}_i \mathbf{v} = 1, \end{aligned} \quad (\text{C.27})$$

which is a quadratically constrained quadratic program [106] solved by taking the largest eigenvalue η_1

$$\max_{\mathbf{v}} \{\eta_{\text{tot}}\} = \min_{\mathbf{v}} \{\Gamma^t\} = \max_i \{\eta_i\} = \eta_1 \quad (\text{C.28})$$

of the generalized eigenvalue problem

$$\mathbf{g}_\Omega \mathbf{v}_i = \eta_i \mathbf{k}_i^H \mathbf{k}_i \mathbf{v}_i. \quad (\text{C.29})$$

Eigenvector \mathbf{v}_1 , corresponding to the largest eigenvalue, represents the optimal terminal voltages. The optimal vector of incident power waves can be evaluated from the optimal port voltage as $\mathbf{a}_1 = \mathbf{k}_i \mathbf{v}_1$, see (C.19).

Optimal vector \mathbf{v}_1 attains an interesting interpretation when relations (C.8), (C.9) are combined into

$$\mathbf{I} = \mathbf{YDCv} = \sum_p \mathbf{I}_p v_p, \quad (\text{C.30})$$

where $\mathbf{I}_p = \mathbf{Y}_p D_p$ denotes that the normalized column of matrix \mathbf{Y} connected to the p th port, the so-called ‘‘port mode’’ [159]. Within the full-wave solution to the antenna problem, optimal port voltages \mathbf{v}_1 thus excite a specific combination of port modes. An example of a port mode excited by port P_2 is depicted in Figure C.6.

C.4.1 Example: Optimal Excitation of Multi-port Antenna

Continuing with the example of the rim above a ground plane from Section C.3.2, the optimal excitation voltages for 4, 3, and 2 ports with $R_{0,p} = 50 \Omega$ and 3 ports with $R_{0,p} = 10 \Omega$ are evaluated using (C.29), see Figure C.7. The ports have the same configuration as in Figure C.5. For the sake of convenience, corresponding

APPENDIX C. FINDING OPTIMAL TOTAL ACTIVE REFLECTION
COEFFICIENT AND REALIZED GAIN FOR MULTI-PORT LOSSY ANTENNAS

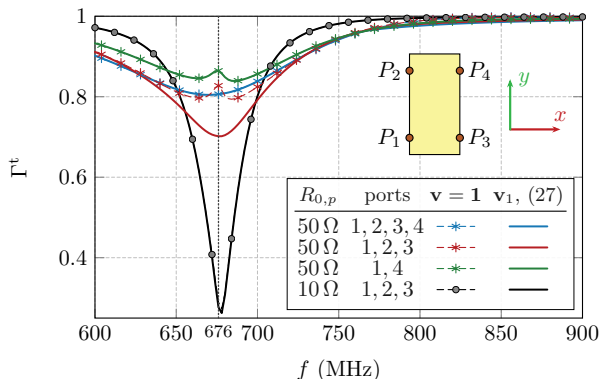


Figure C.7: Comparison of TARC for optimal excitation (solid lines) and uniform excitation (dashed lines). The characteristic impedance $R_{0,p} = 50 \Omega$ was used for 4, 3, and 2 ports enabled, and $R_{0,p} = 10 \Omega$ for 3 ports. The configuration of ports is shown in the inset.

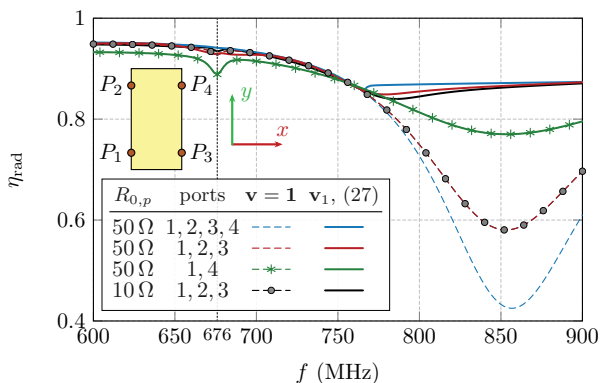


Figure C.8: Comparison of radiation efficiency for optimal excitation (solid lines) and uniform excitation (dashed lines). The setting is identical as in Figure C.7.

results for unit voltages from Figure C.5 are directly included as dashed lines to evaluate the effect of optimal excitation. Radiation efficiency η_{rad} , defined in (C.25), is depicted in Figure C.8 for the same setup. The radiation efficiency for uniform excitation is depicted by dashed marked lines.

It is seen that there is no improvement in TARC and radiation efficiency for four and two ports in the frequency range between 600 MHz and 770 MHz. This is a property of a specific placement of ports, which is very close to a point-symmetric configuration. If the symmetry was perfect, the solution to the eigenvalue problem (C.29) would belong to one of the irreducible representations (irrep) [72]. The dominant solution in this frequency would belong to the irrep with unit voltages. The irrep is changed around 770 MHz and non-uniform excitation found via (C.29) improves the performance. This is most visible for radiation efficiency with 4 ports connected (blue lines, Figure C.8). The corresponding optimal voltages and switch

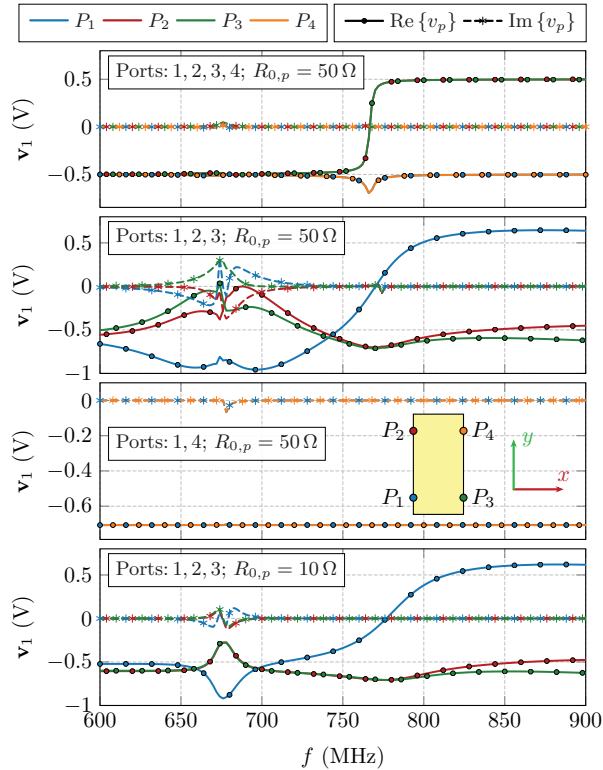


Figure C.9: Optimal excitation for configurations from Figures C.7 and C.8.

of irrep [161] is depicted in the top pane of Figure C.9 which shows the optimal voltages for all the discussed scenarios.

Considering different characteristic impedances $R_{0,p}$, the lower value $R_{0,p} = 10 \Omega$ leads to significantly better performance which is expected as the radiation resistance of the antenna is low. This observation addresses the question of optimal characteristic impedance. Figure C.10 shows TARC for all four configuration of ports, both for unit (dashed) and optimal (solid) excitation depending on the value of characteristic impedance $R_{0,p}$ for frequency $f = 676$ MHz (highlighted by vertical dashed line in Figures C.7 and C.8). The best performance is found for four ports with $R_{0,p} \approx 5 \Omega$ (blue line), *i.e.*, for relatively low characteristic impedance. A slightly higher TARC is realizable with only three ports and $R_{0,p} \approx 10 \Omega$ (red line). The latter option represents a practical and more appealing choice.

Thanks to the symmetrical arrangement for 2 and 4 port setups, the values of TARC for unit and optimal excitation coincide, which once again shows that the optimal excitation belongs to the irrep. with an in-phase constant eigenvector, *i.e.*, all delta gaps have the same amplitude at $f = 676$ MHz, see Figure C.9, the top and second from the top panes. This observation underlines the need for further understanding of group theory and its role in solutions of integral

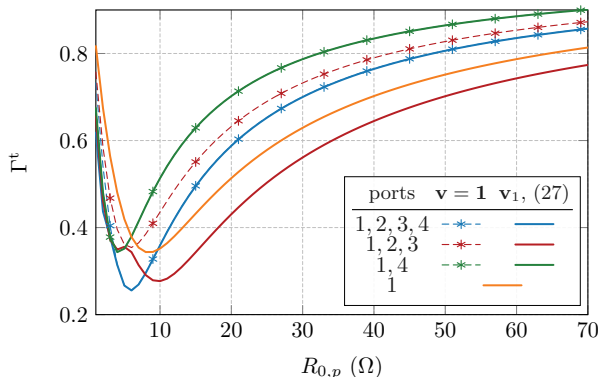


Figure C.10: Comparison of TARC for optimal excitation (solid lines) and uniform excitation (dashed marked lines) depending on the value of characteristic impedance $R_{0,p}$. TARC is evaluated at frequency $f = 676$ MHz.

equations [72, 161, 186].

It is seen that the fixed placement of ports specified by the designer significantly affects the overall performance of the antenna. Therefore, the next step is to investigate the optimal placement of the ports with simultaneous determination of their optimal excitation.

C.5 Synthesis of Optimal Feeding Placement

The maximal total efficiency (minimal TARC) given by the solution to (C.29) is a function of number P and position \mathbf{C} of the ports, terminal impedances $R_{0,p}$ and tuning reactances $jB_{L,p}$. Considering a fixed number of ports P , constant terminal impedance $R_{0,p} = R_0$, and a given tuning susceptance $jB_{L,p} = jB_L$ for all ports, the only remaining variable is the optimal placement of the ports. This task is a feeding synthesis, defined as

$$\begin{aligned} & \text{maximize} && \eta_1 \\ & \text{subject to} && \text{trace}(\mathbf{C}^T \mathbf{C}) = P, \end{aligned} \quad (\text{C.31})$$

which is a combinatorial optimization problem solved by an exhaustive search (feasible only for small, though realistic, number of potential positions) or advanced optimization tools [187]. The number of combinations is

$$\mathcal{C}(N, P) \equiv \binom{N}{P} = \frac{N!}{(N-P)!P!}, \quad (\text{C.32})$$

where, in practice, P is a small number, and N being the number of potential positions to be tested. In order to truncate the solution space, only subregions with preferred positions of the ports might be specified (see the example below).

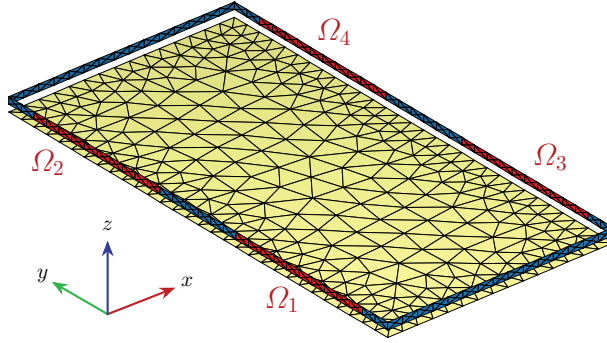


Figure C.11: The same metallic rim and parasitic ground plane as in Figure C.4 with the regions for optimal ports' placement (red color). It is assumed that there is one or no port in each region, which always consists of 11 possible positions.

From the computational point of view, the matrices

$$\widehat{\mathbf{G}}_{\Omega} = \mathbf{D}^{\text{H}} \mathbf{Y}^{\text{H}} \mathbf{R}_{\Omega} \mathbf{Y} \mathbf{D} \quad (\text{C.33})$$

$$\widehat{\mathbf{K}}_i = \frac{1}{2\sqrt{R_0}} \left(\mathbf{1} + R_0 \mathbf{D}^{\text{H}} \mathbf{Y} \mathbf{D} \right) \quad (\text{C.34})$$

can be precalculated at the beginning of the optimization procedure leaving only computationally cheap indexing operations

$$\mathbf{g}_{\Omega} = \mathbf{C}^{\text{H}} \widehat{\mathbf{G}}_{\Omega} \mathbf{C} \quad (\text{C.35})$$

$$\mathbf{k}_i = \mathbf{C}^{\text{H}} \widehat{\mathbf{K}}_i \mathbf{C} \quad (\text{C.36})$$

and dominant eigenvalue evaluation in (C.29) to be performed for every combination.

C.5.1 Example: Optimal Placement of Feeding Ports

The optimal placement of ports is investigated for a rim with the ground plane introduced in the previous sections. In order to imagine how complex the problem of the feeding synthesis is, assume first that all positions on the rim are suitable for accommodating delta gap feeding. The number of combinations is, in this case, $2^{90} \sim 1.24 \cdot 10^{27}$. Such an enormous number of combinations is reduced to $2^{44} \sim 1.76 \cdot 10^{14}$ by assuming only subregions, as depicted in Figure C.11. The number of subregions for port placement is set to four, and it is assumed that in each subregion, denoted as Ω_i , $i \in \{1, \dots, 4\}$, contains not more than one port (no port is also an available option). With these restrictions, the number of solutions drops to 20735. As a final reduction step, only unique arrangements are kept². This leads to only 5291 combinations which have to be investigated.

²There are combinations which represent the same arrangement of ports, only mirrored or rotated. This is a consequence of the symmetry of the rim, which belongs to the C_{2v} group [30]. These identical solutions can be found and truncated by application of symmetry operations which define a given group.

APPENDIX C. FINDING OPTIMAL TOTAL ACTIVE REFLECTION
COEFFICIENT AND REALIZED GAIN FOR MULTI-PORT LOSSY ANTENNAS

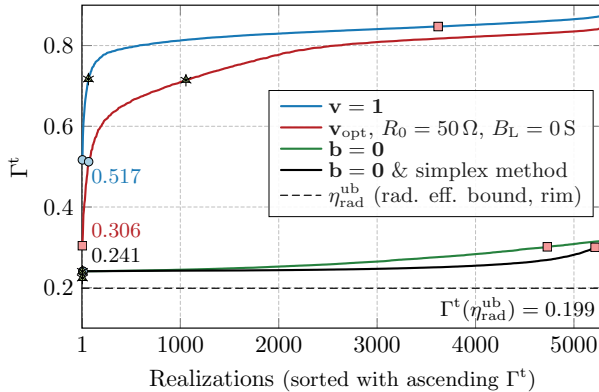


Figure C.12: Results of the feeding synthesis (solution to combinatorial optimization problem) for various approaches of TARC minimization. The meaning of all curves is explained in detail in the text of Section C.5.1. The best realization for each curve is shown in Figure C.13 and highlighted by the marker. Other markers of the same shape show what is the performance of that combination of ports if another approach is utilized. For example, the best solution for the red curve performs relatively poorly for evaluations corresponding to the green and black curves. The dashed line indicates the fundamental bound on radiation efficiency (perfect matching is assumed), see Section C.A.

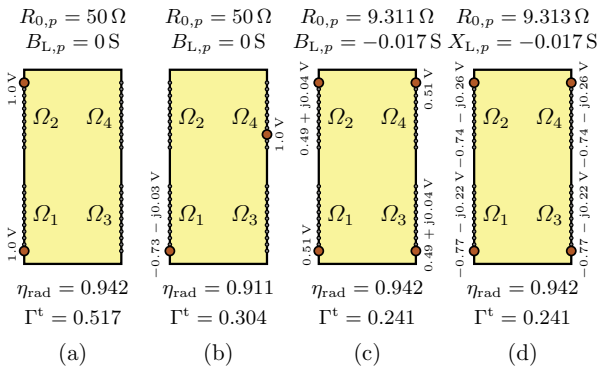


Figure C.13: An overview of the optimal placement of the ports and their performance in TARC and radiation efficiency. Various approaches found in this paper are utilized. The optimal placement defined in (C.31) was found via an exhaustive search for all four cases: (a) uniform excitation, $\mathbf{v} = \mathbf{1}$, (b) optimum excitation \mathbf{v}_1 solved by (C.29), fixed value of $R_{0,p}$ and $B_{L,p}$, (c) optimum excitation \mathbf{v}_i , $R_{0,p}$, and $B_{L,i}$ for $\mathbf{b} = \mathbf{0}$ solved by (C.39), (d) subsequent simplex optimization of (C.29) after solving (C.39). The solutions (a)–(d) correspond to the best realizations in Figure C.12 on the very left.

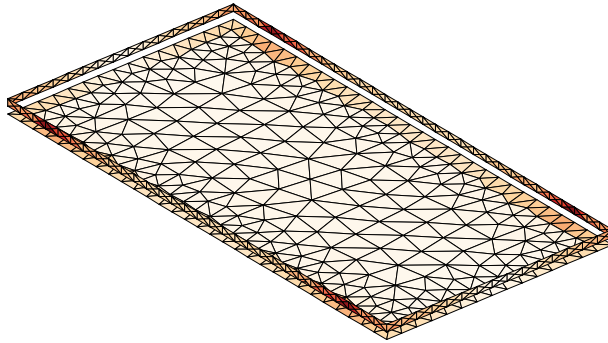


Figure C.14: Current density (absolute value) associated with the fundamental bound on radiation efficiency at frequency $f = 676$ MHz for copper cladding, $\sigma = \sigma_{\text{Cu}}$, under the condition that only the current on the rim is controllable, see Section C.A for its evaluation. It is obvious that the placement of the ports from Figure C.13d correlates well with the maxima of the optimal current density.

Various approaches presented in this paper were applied to evaluate and optimize TARC for each aforementioned combination, see Figure C.12. The first approach is an application of unit voltages on all ports within the selected combination which is represented by the blue line in Figure C.12. It is seen that the overall performance in TARC is poor and the best combination, depicted in Figure C.13a, reaches $\Gamma^t = 0.517$. A modest improvement is realized by solving (C.29) for $R_{0,p} = 50 \Omega$ and $B_{L,p} = 0 \text{ S}$ which results in the realization depicted in Figure C.13b reaching $\Gamma^t = 0.308$, see the red line in Figure C.12. The utilization of optimal feeding improves the performance, however, a further decrease in TARC is limited by the proper choice of circuit components. This is also indicated by an evaluation of the upper bound on radiation efficiency if the currents located on the rim are fully controllable and no tuning circuitry is involved, see Section C.A. The value of the upper bound at $f = 676$ MHz is $\eta_{\text{rad}}^{\text{up}} = 0.96$. Assuming perfect matching, $\eta_{\text{match}} = 1$, the corresponding TARC would be $\Gamma^t = 0.199$, as indicated by the dashed black line in Figure C.12. The optimal current is depicted in Figure C.14 and the location of the current maxima justifies the choice for regions where the ports might be located, cf. Figure C.11. The next step, represented by the remaining curves, is to optimize the characteristic impedance of connected transmission lines and tuning susceptance.

C.6 Optimal Characteristic and Tuning Impedances for Minimum TARC

For lossless antennas, the condition of perfect matching reads

$$\Gamma^t = 0 \quad \Rightarrow \quad \mathbf{b} = \mathbf{0} \quad (\text{C.37})$$

which, after substitution from (C.20), gives

$$(\mathbf{y} + \mathbf{y}_L) \mathbf{v} = (\mathbf{\Lambda} \mathbf{\Lambda})^{-1} \mathbf{v}. \quad (\text{C.38})$$

For a given excitation vector \mathbf{v} it is, therefore, always possible to find appropriate characteristic impedances and tuning susceptances to achieve perfect matching. Such solution might, however, lead to non-physical elements such as negative real part of characteristic impedance and furthermore assumes that all transmission lines are allowed to have different impedances. A more realistic scenario assumes that characteristic impedances of connected transmission lines are all identical $(\mathbf{A}\mathbf{A})^{-1} = R_{0L}^{-1}\mathbf{1}$ and so are the tuning admittances $\mathbf{y}_L = jB_L\mathbf{1}$. Then the relation (C.38) becomes an eigenvalue problem

$$\mathbf{y}\mathbf{v}_i = (R_{0L,i}^{-1} - jB_{L,i})\mathbf{v}_i. \quad (\text{C.39})$$

with P solutions distinguished by index i . The real part of the eigenvalues gives the reciprocal characteristic impedances (strictly positive), while the imaginary part gives the tuning susceptances which, together, constitute the generalization of the matching condition for a single-port antenna [164]. It can be checked that for a single-port antenna the 1×1 eigenvalue problem immediately gives $B_{L,1} = -B_{in}$ and $R_{0,1} = 1/G_{in}$, where $Y_{in} = G_{in} + jB_{in} = y$ is the input impedance of an antenna.

Considering no, or negligible, ohmic losses, combining (C.38) with iteratively solved (C.31) delivers optimal port placement, optimal voltage excitation, optimal sets of tuning susceptances and characteristic resistances. The only remaining task is to select, from all the available combinations of the ports' placement, the configuration which best fits the manufacturing and matching constraints. If none of the combinations is acceptable, the only other possibility is to change the shape of the antenna.

C.6.1 Example: Optimal Matching

The procedure from the previous section is utilized to further optimize TARC performance of the metallic rim. The formula (C.39) is evaluated for all combinations of ports introduced in Section C.5.1. For all solutions found, the optimal excitation and circuit parameters were used to evaluate true TARC value via (C.24). The results are shown in Figure C.12, as illustrated by the green curve. A significant improvement is observed for all port combinations. The best solution offers $\Gamma^t = 0.241$, and its realization is shown in Figure C.13c. Notice that TARC is not zeroed since the antenna is lossy and the assumption of zero loss from the previous section is not fulfilled. In a lossy case, the lowest TARC value is indicated by the fundamental bound on radiation efficiency in Figure C.12.

As a final step, each solution to (C.39) was taken as an initial guess and entered the local optimization (simplex method) of (C.29) with B_L and R_0 being two real variables³. This final optimum is, for each port combination, shown as the black curve in Figure C.12. Only mild improvement, as compared to the direct solution to (C.39), is observed. This indicates that the majority of the solutions were already very close to the minimum. This is confirmed by a parametric sweep of B_L and R_0 for the globally best combination, represented by a star mark on the black curve in Figure C.12 and by its realization in Figure C.13d. The parameters, B_L and R_0 , were swept in a broad range around their optima and the optimal excitation with corresponding TARC were evaluated by (C.29). The values are shown in Figure C.15, where the solution to (C.39) and its further optimization via (C.29) lie close to each other, cf., Figures C.13c and C.13d. It can be seen from Figure C.15 that TARC, for

³In general, the optimized function is not convex in these variables and care must be taken to find globally optimal solution. In low-loss cases, the global optimum lies in the vicinity of perfectly matched setup and a local optimization is justified.

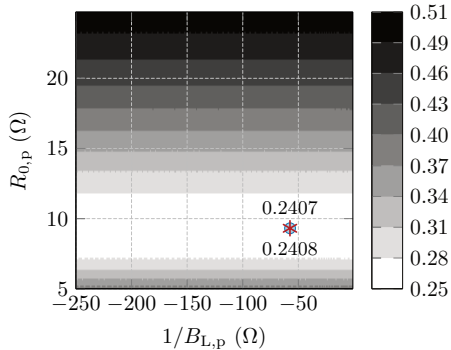


Figure C.15: TARC as a function of characteristic impedance R_0 and tuning susceptance B_L . The realization with the lowest TARC, *i.e.*, the one depicted in Figure C.13d, is studied. The marks stand for the solution found by (C.38) (circle mark, $\Gamma^t = 0.2408$) and for the solution found by (C.38) with subsequent fine-tuning via simplex method [188] of (C.29) (cross mark, $\Gamma^t = 0.2407$).

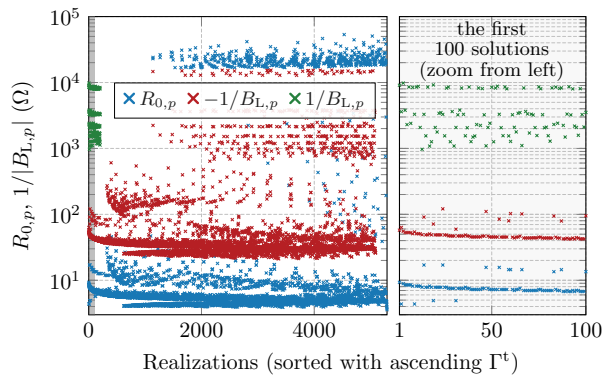


Figure C.16: The values of characteristic impedances and tuning elements required to reach TARC performance from Figure C.12, black curve. The realizations are arranged in the same order as realizations for the “ $\mathbf{b} = \mathbf{0}$, simplex method” curve in Figure C.12. A detail of the first 100 realizations with best performance in TARC are on the right. The elements with negative susceptance are highlighted by red cross marks, while those with positive susceptance are in green.

this particular setting (structure, frequency, material, port placement), is relatively insensitive to variations in connected susceptance. Conversely, the precise realization of characteristic impedance is crucial to secure low TARC.

Since the particular choice of parameters $B_{L,p}$ and $R_{0,p}$ is encumbered with some external constraints (manufacturing, availability of the components, etc.), the resulting optimal parameters of $B_{L,p}$ and $R_{0,p}$ for all combinations of ports are shown in Figure C.16. Their ordering is the same as for the data set in Figure C.12 represented by the black curve, *i.e.*, for the solution to (C.39) with subsequent local

APPENDIX C. FINDING OPTIMAL TOTAL ACTIVE REFLECTION
COEFFICIENT AND REALIZED GAIN FOR MULTI-PORT LOSSY ANTENNAS

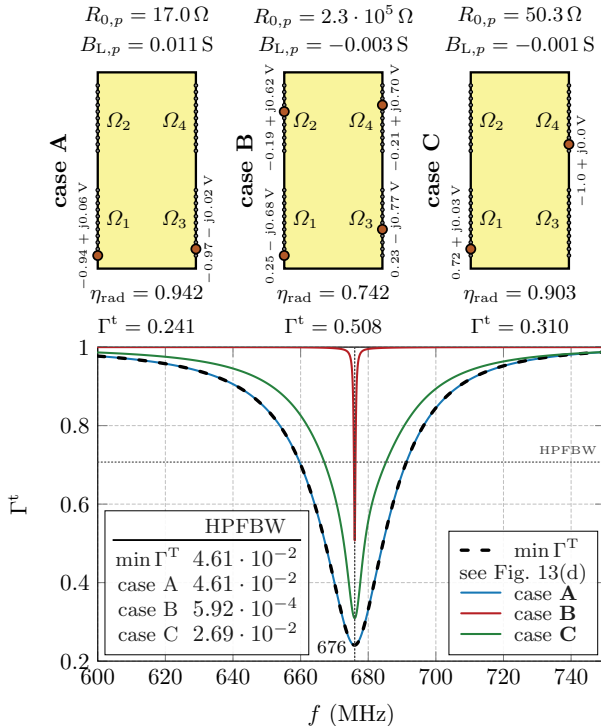


Figure C.17: Results of TARC Γ^t for several realizations from Figure C.15. The matching and excitation scheme for the minimal value of TARC reached at the frequency 676 MHz (black dashed line) is depicted in Figure C.13d. The matching and excitation schemes for cases A, B, and C are depicted in top row of the figure. The case A was chosen because of its TARC value is almost the same as for the optimal solution and the value of the resistance $R_{0,p}$ is approximately doubled. The case B was chosen because of its extremely high value of resistance $R_{0,p}$. Finally, the case C was chosen because of the closeness of its resistance $R_{0,p} = 50.3 \Omega$ to 50Ω . The level of half-power fractional bandwidth (HPFBW) is highlighted by the horizontal dotted black line with the values shown in the inset of the figure.

optimization via (C.29). One can notice that positive susceptances (capacitors) are available only for a few solutions on the left. The characteristic impedances rarely overcome 20Ω for this particular structure.

Figures C.12 and C.16 suggest that there is a great variety of port placements reaching almost the same TARC value. Particularly, the first 3000 solutions from Figure C.12 differ in TARC value by less than 2.5%. Their corresponding matching parameters shown in Figure C.16, however, differ considerably (ordering in both figures is the same) and with them the TARC bandwidth, see Figure C.17, which can be a parameter of the final choice.

To confirm the superb performance of the solution from Figure C.13d, the fundamental bound on radiation efficiency was calculated for this particular combination

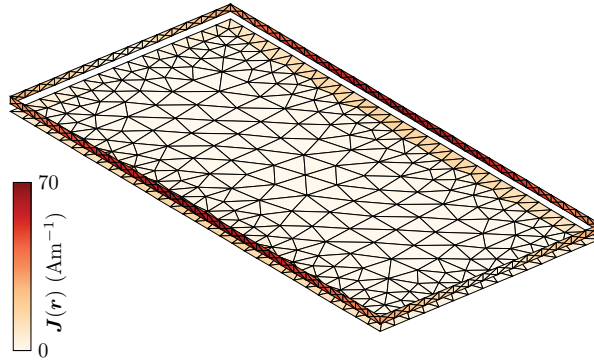


Figure C.18: Current density (absolute value) induced by the feeding scheme from Figure C.13d, $f = 676$ MHz.

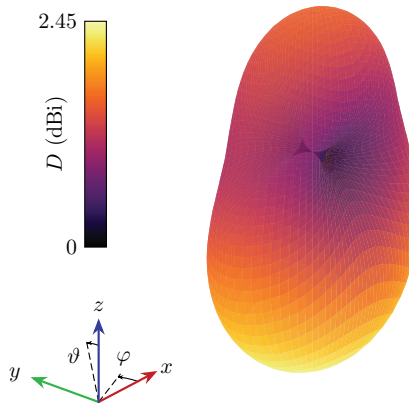


Figure C.19: Radiation pattern generated by a current from Figure C.18. The highest directivity in the broadside direction is $D = 2.37$ dBi.

of ports. The value of the upper bound $\eta_{\text{rad}}^{\text{up}} = 0.942$ is equal to the radiation efficiency realized by the ports and circuitry from Figure C.13d, *i.e.*, there is no reflected power thanks to the solution to (C.39) and the radiation efficiency reaches the fundamental bound. The current density and radiation pattern for the best solution is depicted in Figure C.18 and Figure C.19, respectively. In other words, there is no room for further improvement of the performance other than changing the shape of the antenna or adding additional ports.

This example demonstrated that there is a simple and straightforward technique to find an optimal placement of ports, their optimal excitation, and optimal parameters of a matching circuit which, for a fixed antenna body, prescribed losses and frequency, gives the lowest possible value of TARC.

C.7 Realized Gain

Antenna directivity [164] is defined here as [61]

$$D(\hat{\mathbf{e}}, \hat{\mathbf{r}}) = \frac{4\pi}{Z_0} \frac{\mathbf{I}^H \mathbf{F}^H \mathbf{F} \mathbf{I}}{\mathbf{I}^H \mathbf{R}_\Omega \mathbf{I}} = \frac{4\pi}{Z_0} \frac{\mathbf{v}^H \mathbf{f}^H \mathbf{f} \mathbf{v}}{\mathbf{v}^H \mathbf{g}_\Omega \mathbf{v}}, \quad (\text{C.40})$$

where $F(\hat{\mathbf{e}}, \hat{\mathbf{r}}) = \mathbf{F}(\hat{\mathbf{e}}, \hat{\mathbf{r}}) \mathbf{I}$ is the electric far field in polarization $\hat{\mathbf{e}}$ and direction $\hat{\mathbf{r}}$, Z_0 is the impedance of free space, and $\mathbf{f} = \mathbf{F}(\hat{\mathbf{e}}, \hat{\mathbf{r}}) \mathbf{YDC}$ is port representation of far-field, see [61, App. D] for details. Putting TARC Γ^t and antenna directivity D together gives a realized gain (sometimes called absolute gain [164]):

$$G^t = \left(1 - (\Gamma^t)^2\right) D = \frac{4\pi}{Z_0} \frac{\mathbf{v}^H \mathbf{f}^H \mathbf{f} \mathbf{v}}{\mathbf{v}^H \mathbf{k}_i^H \mathbf{k}_i \mathbf{v}} = \frac{4\pi}{Z_0} \frac{|\mathbf{f} \mathbf{v}|^2}{|\mathbf{k}_i \mathbf{v}|^2}. \quad (\text{C.41})$$

The optimization problem for maximal realized gain reads

$$\begin{aligned} & \text{maximize} && \mathbf{v}^H \mathbf{f}^H \mathbf{f} \mathbf{v} \\ & \text{subject to} && \mathbf{v}^H \mathbf{k}_i^H \mathbf{k}_i \mathbf{v} = \frac{Z_0}{4\pi}, \end{aligned} \quad (\text{C.42})$$

and is solved by a generalized eigenvalue problem

$$\mathbf{f}^H \mathbf{f} \mathbf{v}_i = \gamma_i \frac{Z_0}{4\pi} \mathbf{k}_i^H \mathbf{k}_i \mathbf{v}_i. \quad (\text{C.43})$$

Since the LHS of (C.43) contains a rank-1 operator, the dominant eigenvector is known analytically as

$$\mathbf{v}_1 \propto \left(\mathbf{k}_i^H \mathbf{k}_i\right)^{-1} \mathbf{f}^H \quad (\text{C.44})$$

and which, when substituted into the Rayleigh quotient of (C.43), gives a maximal realized gain

$$G_{\text{up}}^t = \gamma_1 = \frac{4\pi}{Z_0} |\mathbf{f} \mathbf{k}_i^{-1}|^2. \quad (\text{C.45})$$

The maximal realized gain is a function of ports' placement, tuning susceptances, and characteristic impedances (through the matrix \mathbf{k}_i). For additional optimization of ports' placement, see Section C.5 with η_1 being changed to γ_1 in (C.29). From the computational point of view, the matrix inversion has to be iteratively solved in (C.45) instead of the determination of the dominant eigenpair in (C.28) or (C.38).

C.7.1 Example: Optimal Excitation for Maximal Realized Gain

The four-element dipole antenna array operating at $f = 1$ GHz was chosen as a simple and instructive example. The thin-strip dipoles are of resonant length ($\ell = \lambda/2$), their width is $\ell/100$, and they are made of copper ($\sigma_{\text{Cu}} = 5.96 \cdot 10^7 \text{ Sm}^{-1}$). Each dipole has a delta gap feeding in its center.

Two arrangements are studied:

1. an uniform array with separation distance $d = \lambda/2$,
2. a non-uniform array, $d = \{\lambda/20, \lambda/10, \lambda/4\}$.

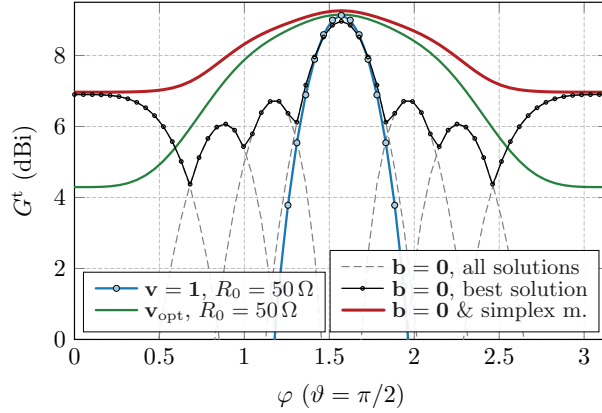


Figure C.20: Results of the feeding synthesis (solution to the optimization problem for angle φ) for various approaches of realized gain maximization. The uniform array of four metallic dipoles, separated by distance $d = \lambda/2$ is considered. The meaning of all curves is explained in details in Section C.7.1. The blue line stands for unit feeding, $\mathbf{v} = \mathbf{1}$. The curve denoted as \mathbf{v}_{opt} (green solid) was evaluated by (C.45). The black curves are individual solutions to (C.39) (thin dashed) with their maximum envelope highlighted by the solid black line. The final solution is represented by the solid red line, which was found by solving (C.39) with subsequent simplex optimization of (C.45).

Dipoles are, in both cases, parallel to the z -axis, the delta gap feeders are placed in a $z = 0$ plane, and both arrays are centered at the origin of the coordinate system. The dominant polarization $\hat{\mathbf{e}} = \hat{\boldsymbol{\nu}}$ is investigated in the $\vartheta = \pi/2$, $\varphi = [0, \pi]$ half-cut, *i.e.*, from the end-fire direction ($\varphi = 0$, to $+x$ direction), through the broad-side direction ($\varphi = 0$, to $+y$ direction), and ending with the end-fire direction ($\varphi = \pi$, to $-x$ direction).

The uniform array is treated first. The realized gain G^t is depicted in Figure C.20 for various excitation schemes. The first scheme uses unit amplitudes at all ports which is favorable in the broad-side direction, but performs poorly for other directions [164]. When the excitation is found by (C.45) (tuning circuitry fixed at $R_0 = 50 \Omega$ and $B_L = 0\text{S}$) for each direction φ , performance is improved for all studied directions except for the broad-side direction, where the unit excitation is already optimal. Still, relatively poor performance is observed in the end-fire direction, the reason being the fixed matching circuitry. The dependence on the characteristic impedance R_0 is shown in Figure C.21 for a broad-side direction where it is seen that performance close to the optimum occurs in the relatively broad range of R_0 , with the maximum being reached around $R_0 \approx 64 \Omega$ (highlighted by the vertical dashed line). Major improvements are thus expected from the reactive matching via elements B_L . This is accomplished by solving (C.39) with a subsequent simplex optimization of (C.45).

The four solutions to (C.39) are depicted by black dashed lines with the maximum envelope highlighted by the black solid line. All these solutions were subsequently considered as the starting point for a simplex optimization method which tried to locally maximize (C.45). Similarly as in the previous section, this technique is capable

APPENDIX C. FINDING OPTIMAL TOTAL ACTIVE REFLECTION
COEFFICIENT AND REALIZED GAIN FOR MULTI-PORT LOSSY ANTENNAS

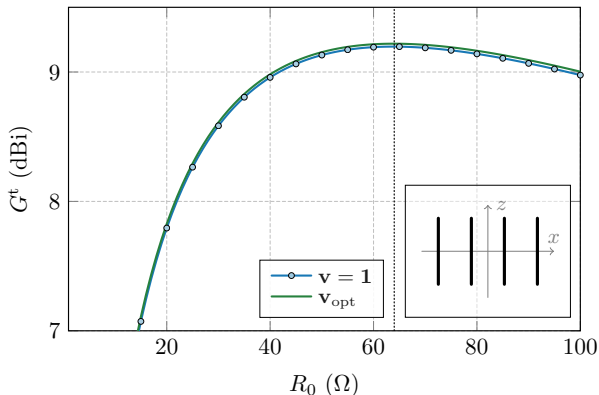


Figure C.21: Sensitivity of the realized gain G^t in the broad-side direction ($\varphi = \pi/2$, $\vartheta = \pi/2$) to the value of characteristic impedance R_0 . The meaning of the curves is the same as in the Figure C.20. The inset shows the uniform array studied in this example.

of delivering excellent results, represented here by the red solid line, which dominates the performance in realized gain G^t for all investigated directions. The associated optimal excitation of all four ports is shown in Figure C.22. Notice the in-phased constant voltages for the broad-side direction and, conversely, the alternating polarity of the voltages for the end-fire direction (*i.e.*, $v_i \sim \exp\{-j\pi i\}$, $i \in \{1, \dots, 4\}$). The end-fire setup closely follows the phase progression opposite the electric distance between the radiators ($kd = \pi$) as recommended by textbooks [164].

As anticipated from the array theory [189], the ability to radiate well to a given direction changes with separation distance d between individual array elements. This is the case of the second array considered, for which the elements are nonuniformly spaced, separated by relatively short distance. The performance of such an array is shown in Figure C.23 with the same meaning of all curves as in Figure C.20. The highest realized gain G^t is reached in end-fire directions, preferably in the $+x$ direction. The best solution to (C.39) is, in this case, very close to the solution refined by subsequent simplex optimization.

The two examples of thin-wire metallic arrays demonstrated effectiveness and insight gain by the utilization of the port mode-based definition and optimization of realized gain. Notice that the same analysis can be done for an arbitrarily large array or multi-port antenna possibly made of inhomogeneous and lossy materials.

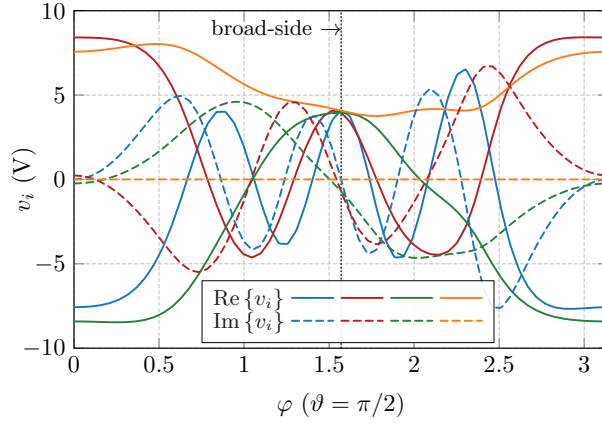


Figure C.22: The optimal excitation of the uniform metallic dipole array with separation distance $d = \lambda/2$. Different colors represent real (solid) and imaginary (dashed) parts of the voltage v_i impressed at the i -th port. Optimal excitation with optimal circuit parameters R_0 and B_L (not shown) was found for each direction φ via the solution to (C.39) and the subsequent simplex optimization of (C.45). Their realization led to the optimal performance indicated by the red curve in Figure C.20.

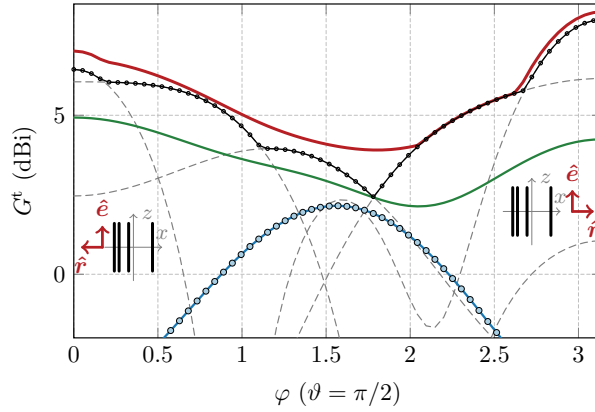


Figure C.23: Results of the feeding synthesis (solution to the optimization problem for angle φ) for various approaches of realized gain minimization. The nonuniform array of four metallic dipoles, separated by distance $d = \{\lambda/20, \lambda/10, \lambda/4\}$ is considered. The meaning of all curves is the same as in Figure C.20.

C.8 Conclusion

The total active reflection coefficient (**TARC**) and realized gain were reformulated in terms of source current density and terminal voltages. This enabled the evaluation of these antenna metrics in full-wave fashion, taking into account ohmic losses of realistic metals and the particular shape(s) of radiator(s). There are no restrictions on homogeneity of materials. Since both figure of merits are defined in terms of quadratic forms, the presented formulation allows not only for the easy evaluation of **TARC** and realized gain, but also for the determination of optimal voltages, optimal placement of the ports, or determination of optimal terminal impedances and optimal matching.

Within this formulation, the full method of moments solution has to be evaluated only once and, while the admittance matrix is obtained, only computationally cheap indexation has to be performed to sweep the position of the ports. All resulting eigenvalue problems contain only small matrices and, in the case of realized gain, the optimal excitation for its maximization was even found analytically, being a sole function of ports' placement and characteristic and matching impedances.

The fast evaluation and subsequent optimization makes it possible to solve the combinatorial feeding synthesis problem for all practically reasonable configurations of ports with an exhaustive search. As a side-product, the optimal excitation and optimal circuitry is delivered. The designer then has full access to all possible solutions, their performance, and a list of all circuit elements needed. When performance is not sufficient, the only resolution required is a change of supporting geometry or the addition of extra ports.

The method was demonstrated on a simple dipole, a multi-port **MIMO** antenna, and uniform and nonuniform arrays. The presented results confirm the usefulness of the method for multi-port antenna systems with the advantage of having the possibility of including/excluding ohmic losses from the evaluation of **TARC** to make the results comparable with practical measurements.

Further research is needed to study other multi-port metrics as a cross-correlation coefficient or the ability to excite multiple states simultaneously and to define and optimize these quantities in the same way as shown in this paper. An interesting extension would be to combine this work with a selective excitation of orthogonal radiation patterns and to determine conditions for optimal performance. Establishing a connection to characteristic port modes can reveal a link between their selective excitation and optimality in **TARC** and realized gain. Another research direction is optimality within the frequency band. Finally, since both this work and the topology sensitivity approach [190] shares the admittance matrix as the only variable needed to perform either feeding of topology synthesis, the possibilities of how to merge these two treatments of important antenna problems will be studied as an ultimate goal of antenna synthesis.

C.A Fundamental Bound on Radiation Efficiency

The fundamental bound on radiation efficiency (C.25) is expressed here in terms of the port modes associated with a controllable [107] subregion $\Omega_C \subseteq \Omega$, represented by a particular indexing matrix **C**.

The procedure starts with the introduction of the dissipation factor δ_{rad} [191]

$$\eta_{\text{rad}} = \frac{1}{1 + \delta_{\text{rad}}}, \quad (\text{C.46})$$

which has a favorable scaling $\delta_{\text{rad}} \in [0, \infty]$, for details see [192]. In order to accommodate the requirement on a controllable subregion Ω_C , the procedure from [61] is applied to a port mode representation of the radiated and lost power, (C.17) and (C.18), as

$$\begin{aligned} & \text{minimize} && \mathbf{v}^H \mathbf{g}_\rho \mathbf{v} \\ & \text{subject to} && \mathbf{v}^H \mathbf{g}_\Omega \mathbf{v} = 1, \end{aligned} \tag{C.47}$$

which is readily solved by an eigenvalue problem

$$\mathbf{g}_\rho \mathbf{v}_i = \delta_i \mathbf{g}_\Omega \mathbf{v}_i. \tag{C.48}$$

The unknowns \mathbf{v} in (C.47) and (C.48) are the expansion coefficients of the ports modes (C.30) associated with a controllable region Ω_C , *i.e.*, the matrix \mathbf{C} , defined in (C.10), has non-zero entries only for indices p belonging to the edges that coincide with ports. Taking the smallest eigenvalue of (C.48)

$$\delta_{\text{rad}}^{\text{lb}} = \min_i \{\delta_i\} \tag{C.49}$$

and substituting it back into (C.46) yields the upper bound on radiation efficiency $\eta_{\text{rad}}^{\text{ub}}$ for a given subregion Ω_C . The eigenvector of (C.48) corresponding to the smallest eigenvalue represents the optimal feeding.

As compared to the current density-based bounds, see, *e.g.*, [61, 192], which are typically not reachable since full control of current is required, the bound (C.49) is realizable by impressing the corresponding voltage \mathbf{v}_i to selected ports. This implies that (C.49) is always sub-optimal with respect to the current-based bounds. Realistic antenna designs with a fixed placement of ports, such as those proposed in [193], should rather be compared with (C.49) than with fundamental current density-based bounds [61].

Published as: M. Capek, L. Jelinek, and M. Masek, “A Role of Symmetries in Evaluation of Fundamental Bounds,” *IEEE Transactions on Antennas and Propagation*, vol. 69, no. 11, pp. 7729-7742, Nov. 2021, DOI: [10.1109/TAP.2021.3070103](https://doi.org/10.1109/TAP.2021.3070103).

Abstract—A problem of the erroneous duality gap caused by the presence of symmetries is solved in this paper utilizing point group theory. The optimization problems are first divided into two classes based on their predisposition to suffer from this deficiency. Then, the classical problem of Q-factor minimization is shown in an example where the erroneous duality gap is eliminated by combining solutions from orthogonal sub-spaces. Validity of this treatment is demonstrated in a series of subsequent examples of increasing complexity spanning the wide variety of optimization problems, namely minimum Q-factor, maximum antenna gain, minimum total active reflection coefficient, or maximum radiation efficiency with self-resonant constraint. They involve problems with algebraic and geometric multiplicities of the eigenmodes, and are completed by an example introducing the selective modification of modal currents falling into one of the symmetry-conformal sub-spaces. The entire treatment is accompanied with a discussion of finite numerical precision, and mesh grid imperfections and their influence on the results. Finally, the robust and unified algorithm is proposed and discussed, including advanced topics such as the uniqueness of the optimal solutions, dependence on the number of constraints, or an interpretation of the qualitative difference between the two classes of the optimization problems.

Index terms: Antenna theory, electromagnetic modeling, method of moments, eigenvalues and eigenfunctions, optimization.

D.1 Introduction

Fundamental bounds expressed in terms of source quantities [158, 194] have shown their versatility and usefulness for a wide range of applications in antenna theory, microwaves, and optics. They delimit the performance of theoretically feasible structures which help to judge the performance of existent designs [195] and, in a few cases, lead to the conclusion that existing designs have already reached the

bounds [89]. Additionally, given that the bounds are far from the actual performance of the devices became the driving force to search for better designs [196]. However, despite recent success and a straightforward implementation, the problem with the presence of geometry symmetries remained open [62, 107, 158].

Under certain conditions, discussed in detail in this paper, a large class of optimization problems experience difficulties when symmetries are present. Although the problem is of a technical nature, it has a serious impact on the validity of the results since the degeneracy of eigenvalues introduces a duality gap, *i.e.*, the difference between dual and primal solutions [106]. This duality gap is manifested by the fact that the current solution for a primal was not constructed correctly. The known empirical solutions to this issue utilize an *ad hoc* combination of the degenerated eigenvectors [62, 107]. This approach is difficult to apply inside a general solver dealing with a large class of problems and structures of arbitrary geometry. The main difficulty, however, arises with structures of higher-order geometry degeneracies where the choice of modes to be combined is non-trivial. Since the shapes exhibiting symmetries are often used as initial designs, and since it is expected that the field of fundamental bounds will expand into a plethora of yet unsolved problems and researchers may face the problem again, a comprehensive and general treatment of this issue is of considerable importance.

The proposed solution adheres to point group theory, namely, the von Neumann-Wigner theorem [20] is applied to a spectrum of eigenvalue traces given by the stationary points of the optimization problem. Consequently, the conditions under which the problem arises are discussed including how the problem is always connected to an underlying (parameterized) eigenvalue problem introducing an erroneous duality gap. A simple procedure showing how to detect when the problem occurs and how to close the erroneous duality gap is given. The proposed recipe can also treat cases of realistic mesh grids, *i.e.*, those not perfectly respecting the symmetry groups of the original object. The procedure was thoroughly tested on many canonical objects, such as a rectangular plate, square plate, metallic rim with ground plane, in-parallel placed and crossed dipoles, spherical shell, etc.

The paper is organized as follows. The situation is thoroughly analyzed in Section D.2. It is realized that the erroneous duality gap occurs only when the eigenvalue solution is required, *i.e.*, for quadratically constrained quadratic programs (QCQPs) without linear terms. When the linear terms are present, this ambiguity vanishes as the solution does not use eigenvalue decomposition. The illustrative example of the erroneous duality gap is introduced in Section D.3 and in Section D.4 with the help of point group theory. In Section D.5, some examples are explicitly treated, showing where and how the symmetries appeared and what is their influence on the problem. The properties of the method are discussed in Section D.6. The uniqueness of the results (current density, port voltages, etc.) is investigated in light of the knowledge gained from the symmetry treatment. It is shown, that the presence of symmetries may introduce additional degrees of freedom for the optimization and it is specified where it is so. The paper is concluded in Section D.7.

D.2 QCQP Problems

The evaluation of the source quantity-based fundamental bounds starts with a statement of the optimization problem. Two problems, denoted as \mathcal{P}_1 and \mathcal{P}_2 , are shown below to distinguish when the problem with symmetries may (\mathcal{P}_1) or may not (\mathcal{P}_2) arise. After establishing the Lagrangians, the optimization problems are solved via dual formulation [106] the solution to which are subsequently interpreted with respect to point group theory.

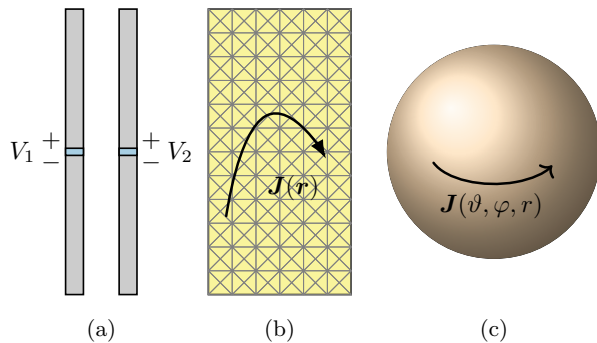


Figure D.1: Various source quantities \mathbf{x} to be optimized. (a) Port voltage, $\mathbf{x} = \mathbf{V}$, of two in-parallel placed dipoles. The arrangement embodies a C_s symmetry group, see Section D.A and [30]. (b) Current density, $\mathbf{x} = \mathbf{I}$, on a rectangular plate belonging to a C_{2v} group, see Section D.A and [30]. (c) Current density, $\mathbf{x} = \boldsymbol{\alpha}$ on a spherical shell expanded in spherical harmonics. The spherical shell belongs to the $O(3)$ symmetry group [30].

D.2.1 Optimization Problem \mathcal{P}_1

Let us start with QCQP problem \mathcal{P}_1 containing only quadratic terms

$$\begin{aligned} & \text{minimize} && \mathbf{x}^H \mathbf{A} \mathbf{x} \\ & \text{subject to} && \mathbf{x}^H \mathbf{B} \mathbf{x} = 1 \\ & && \mathbf{x}^H \mathbf{C} \mathbf{x} = 0, \end{aligned} \quad (\text{D.1})$$

where \mathbf{x} is the optimized quantity, *e.g.*, current density or port voltages in the source region, see Figure D.1, and \mathbf{A} , \mathbf{B} , and \mathbf{C} , are integro-differential operators represented in a basis defined by either piece-wise or entire-domain basis functions $\{\psi_n\}$, [37]. It is assumed that the algebraic properties of the operators are compatible with the problem to be solved, *e.g.*, $\mathbf{B} \succ \mathbf{0}$ and \mathbf{C} being generally indefinite (the true physical meaning of these operators is given later on).

The Lagrangian of the problem \mathcal{P}_1 is

$$\mathcal{L}_1(\lambda_i, \mathbf{x}) = \mathbf{x}^H \mathbf{H}(\lambda_i) \mathbf{x} + \lambda_1 \quad (\text{D.2})$$

with its derivative

$$\frac{\partial \mathcal{L}_1(\lambda_i, \mathbf{x})}{\partial \mathbf{x}^H} = \mathbf{H}(\lambda_i) \mathbf{x}, \quad (\text{D.3})$$

where $\mathbf{H}(\lambda_i) = \partial^2 \mathcal{L}_1 / \partial \mathbf{x}^H \partial \mathbf{x} = \mathbf{A} - \lambda_1 \mathbf{B} - \lambda_2 \mathbf{C}$ is the Hessian matrix [188]. The stationary points $\tilde{\mathbf{x}}$ are solutions to

$$\frac{\partial \mathcal{L}_1(\lambda_i, \mathbf{x})}{\partial \mathbf{x}^H} = \mathbf{0}, \quad (\text{D.4})$$

or explicitly to

$$\mathbf{A} \tilde{\mathbf{x}} - \lambda_2 \mathbf{C} \tilde{\mathbf{x}} = \lambda_1 \mathbf{B} \tilde{\mathbf{x}}. \quad (\text{D.5})$$

D.2.2 Optimization Problem \mathcal{P}_2

For the sake of completeness, the second optimization problem \mathcal{P}_2 is defined as

$$\begin{aligned} & \text{minimize} && \mathbf{x}^H \mathbf{A} \mathbf{x} \\ & \text{subject to} && \mathbf{x}^H \mathbf{B} \mathbf{x} = 1 \\ & && \mathbf{x}^H \mathbf{C} \mathbf{x} = \text{Re} \{ \mathbf{x}^H \mathbf{c} \}, \end{aligned} \quad (\text{D.6})$$

i.e., the second constraint contains a linear term in \mathbf{x} with \mathbf{c} being known column vector. Analogous to (D.2), the Lagrangian reads

$$\mathcal{L}_2(\lambda_i, \mathbf{x}) = \mathbf{x}^H \mathbf{H}(\lambda_i) \mathbf{x} + \lambda_2 \text{Re} \{ \mathbf{x}^H \mathbf{c} \} + \lambda_1 \quad (\text{D.7})$$

The derivative of the Lagrangian is

$$\frac{\mathcal{L}_2(\lambda_i, \mathbf{x})}{\partial \mathbf{x}^H} = \mathbf{H}(\lambda_i) \mathbf{x} + \frac{\lambda_1}{2} \mathbf{c}. \quad (\text{D.8})$$

The stationary points $\tilde{\mathbf{x}}$ are

$$\tilde{\mathbf{x}} = -\frac{\lambda_1}{2} \mathbf{H}^{-1}(\lambda_i) \mathbf{c}, \quad (\text{D.9})$$

with the demand that $\mathbf{H}(\lambda_i) \succ \mathbf{0}$.

D.2.3 Solution to Dual Problems

Primal problems \mathcal{P}_1 and \mathcal{P}_2 with stationary points (D.5) and (D.9) are generally non-convex and are often approached using dual function [106] defined as

$$d_p(\lambda_i) = \inf_{\tilde{\mathbf{x}}} \{ \mathcal{L}_p(\lambda_i, \tilde{\mathbf{x}}) \}, \quad (\text{D.10})$$

where $p = \{1, 2\}$. The supremum of the dual function

$$d_p^* = \sup_{\lambda_i} \{ d_p(\lambda_i) \}, \quad (\text{D.11})$$

is a lower bound to the primal optimization problem [106], the solution to which is here denoted as p^* . Since the dual function is convex [106], the solution to (D.11) can easily be found. Algebraic techniques reducing the computational burden behind the optimization of this type of problem are presented in [59].

Generally, the duality gap $g^* \geq 0$,

$$g^* = p^* - d^* \quad (\text{D.12})$$

exists, nevertheless, problems involving the minimum Q-factor [107], maximum antenna gain [62], maximum radiation efficiency [99, 108], minimum total active reflection coefficient (TARC) [109], and their mutual trade-offs [192], were shown to have no duality gap. Hence, to simplify the exposition, and without loss of generality, it is assumed for the rest of the paper that there is no duality gap g^* , *i.e.*, $p^* = d^*$ for both problems \mathcal{P}_1 and \mathcal{P}_2 .

The typical workflow solving problem \mathcal{P}_1 consists of an iterative evaluation of the generalized eigenvalue problem (D.5), taking the dominant eigenvalue λ_1 and setting the multiplier λ_2 so that λ_1 is maximized. On the contrary, the treatment of problem \mathcal{P}_2 requires a repetitive solution to the system of linear equations. This is an important distinction between problems \mathcal{P}_1 and \mathcal{P}_2 : *issues with symmetries may occur in problem \mathcal{P}_1 while they cannot appear for problems of type \mathcal{P}_2 .*

D.3 Illustrative Example: Problem of \mathcal{P}_1 -Type

Let us demonstrate the effect of symmetries on a practical example of Q-factor minimization with a constraint on the self-resonance of the current, specifically

$$\begin{aligned} & \text{minimize} && \mathbf{I}^H \mathbf{W} \mathbf{I} \\ & \text{subject to} && \mathbf{I}^H \mathbf{R}_0 \mathbf{I} = \frac{1}{2} \\ & && \mathbf{I}^H \mathbf{X}_0 \mathbf{I} = 0, \end{aligned} \tag{D.13}$$

where $\mathbf{W} = \mathbf{A} = \omega \partial \mathbf{X}_0 / \partial \omega$, $\mathbf{R}_0 = \mathbf{B}$, and $\mathbf{X}_0 = \mathbf{C}$ from (D.1), *i.e.*, the problem of the minimum Q-factor falls into a class of \mathcal{P}_1 problems, and $\mathbf{Z}_0 = \mathbf{R}_0 + j \mathbf{X}_0$ is the impedance matrix for a scatterer made of a perfect electric conductor (PEC), see [59] for the exact definition of all the matrix operators. The basis functions used are Rao-Wilton-Glisson (RWG) functions [51] and the optimization variable $\mathbf{x} = \mathbf{I}$ represents the surface current density as

$$\mathbf{J}(\mathbf{r}) \approx \sum_n I_n \boldsymbol{\psi}_n(\mathbf{r}). \tag{D.14}$$

All the operators were evaluated in the Antenna Toolbox for MATLAB (AToM) package [29].

This problem has a long history starting with a seminal work of Chu [92] and has fully been described and solved in [107]. The solution to the dual problem (D.11) reads

$$d^* = \max_{\lambda_2} \min_m \lambda_{1,m} \tag{D.15}$$

with the eigenvalues $\lambda_{1,m}$ defined by

$$\frac{1}{2} (\mathbf{W} - \lambda_2 \mathbf{X}_0) \mathbf{I}_m = \lambda_{1,m} \mathbf{R}_0 \mathbf{I}_m, \tag{D.16}$$

cf., (D.5).

The definition of the Q-factor [197] can be rewritten as [107]

$$Q(\mathbf{I}) = \frac{\max \{ \mathbf{I}^H \mathbf{X}_m \mathbf{I}, \mathbf{I}^H \mathbf{X}_e \mathbf{I} \}}{\mathbf{I}^H \mathbf{R}_0 \mathbf{I}}, \tag{D.17}$$

where

$$\mathbf{X}_m = \frac{1}{2} (\mathbf{W} + \mathbf{X}_0), \tag{D.18a}$$

$$\mathbf{X}_e = \frac{1}{2} (\mathbf{W} - \mathbf{X}_0). \tag{D.18b}$$

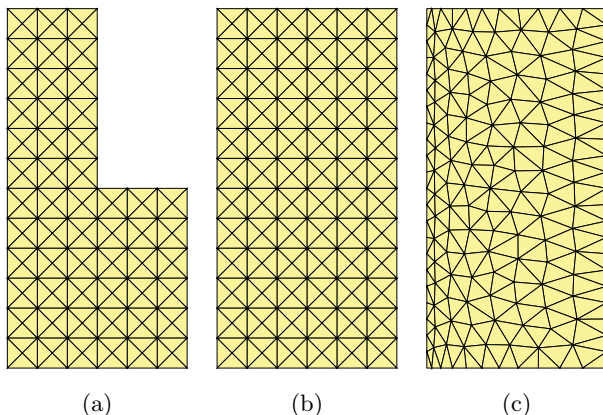


Figure D.2: Shapes and their discretization utilized to solve the optimization problem (D.13). (a) L-shape plate of dimensions $\ell \times \ell/2$ with cutoff of size $\ell/2 \times \ell/4$ discretized via Delaunay triangulation with a pixelized pattern consisting of 216 triangles and 306 basis functions. (b) The rectangular plate of dimensions $\ell \times \ell/2$ with a mesh grid respecting the symmetries of the object consisting of 288 triangles and 414 basis functions. (c) Same as (b) with a non-symmetrical mesh grid intentionally made an-isotropic, consisting of 274 triangles and 378 basis functions. The electrical size is, in all cases, $ka = 1/2$, where k is the wave-number and a is the radius of the smallest sphere circumscribing the structure. All structures are made of PEC and the numerical quadrature of the third order [198] in AToM [29] is utilized to gather the matrix operators.

The formula (D.17) is valid for arbitrary current \mathbf{I} and can be used as a useful check of the duality gap $g = Q(\lambda_2^*) - d^*$, where $Q(\lambda_2^*)$ is a Q-factor evaluated via (D.17) with current \mathbf{I}_1 ($m = 1$) found by (D.16) at $\lambda_2 = \lambda_2^*$. When no duality gap occurs, we have

$$Q^* = Q(\mathbf{I}_{\text{opt}}) = d^*. \quad (\text{D.19})$$

A solution to (D.15) is found here for two different shapes: an L-shape plate and a rectangular plate with a perfectly symmetric mesh grid, see Figure D.2b. The effects of the non-regular mesh grid, depicted in Figure D.2c are studied as well. The dual function and its maximum d^* at λ_2^* is shown in Figure D.3 with subfigures (a)–(c) corresponding to those of Figure D.2. Due to the large numerical dynamics in the bottom panes, the vicinity of the dual solutions are zoomed in the top panes of Figure D.3 with the traces for the actual value of Q-factor (D.17) added.

The non-symmetrical case (a) causes no problems and $Q^* = d^*$ for λ_2^* , *i.e.*, there is no duality gap. On the other hand, case (b) seemingly embodies a duality gap $g = Q(\lambda_2^*) - d^*$. This “erroneous” duality gap is caused by the eigenvalue crossing (two eigensolutions to (D.16) are degenerate at λ_2^*). Neither of the degenerated eigenmodes satisfy the last constraint of (D.13), which is manifested by the immediate increase in the value of corresponding Q-factor $Q(\mathbf{I}_m)$. It is shown later on that the degenerate solutions to (D.16) must properly be combined to satisfy this last constraint (to secure the self-resonance of the optimal current) and to close the gap. The last case (c) has no duality gap thanks to the slightly non-symmetrical mesh grid.

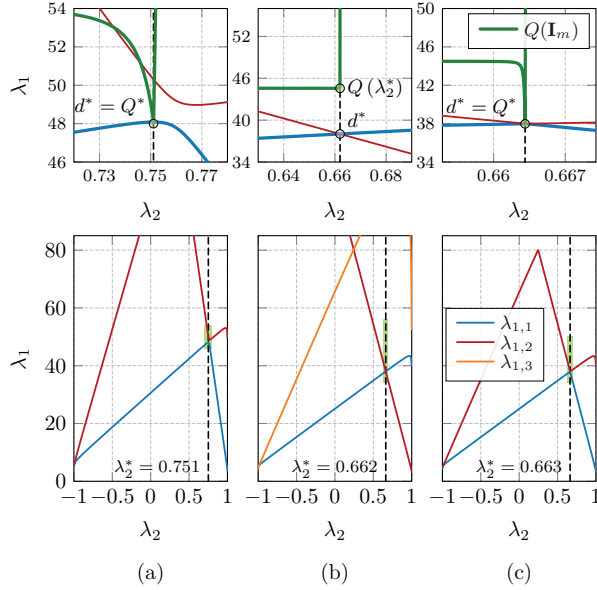


Figure D.3: Eigenvalues (Lagrange’s multipliers) λ_1 from (D.16) as functions of Lagrange’s multiplier λ_2 (bottom panes) and the corresponding Q-factors (D.17) (top panes, the green solid curves). The top panes show details in the vicinity of the optimal value of the multiplier λ_2^* . The two lowest eigenvalues $\lambda_{1,m}$ are depicted. For case (b), the lowest eigenvalue from B_2 (the blue line), A_2 (the red line), and B_1 (the orange line) irreducible representations [30] are shown (to be discussed in the next section). The structures depicted in Figure D.2 are employed with the physical setting described in the caption of Figure D.2.

This introductory example raises a series of questions:

1. When can problems with symmetries be expected?
2. How can the problem be detected?
3. How can the erroneous duality gap g caused by the presence of symmetries be fixed?
4. How can the robustness of the treatment for a numerical evaluation be improved?

These questions are addressed in the following text after a brief review of the elements of point group theory.

D.4 Presence of Symmetries

Point group theory¹ constitutes the framework, both for the theoretical understanding and practical treatment of the issues related to symmetries.

Let us assume an object Ω invariant to a set of point symmetries (*e.g.*, rotation, reflection, etc.). Imagine further that object Ω is discretized and basis functions $\{\psi_n(\mathbf{r})\}$ are applied. It can be shown [30] that any operator, say \mathbf{A} , represented in a basis $\{\psi_n(\mathbf{r})\}$ and preserving the symmetries, can be block-diagonalized as

$$\hat{\mathbf{A}} = \mathbf{\Gamma}^T \mathbf{A} \mathbf{\Gamma} = \begin{bmatrix} \mathbf{A}_1 & \cdots & \mathbf{0} \\ \vdots & \ddots & \vdots \\ \mathbf{0} & \cdots & \mathbf{A}_G \end{bmatrix}, \quad (\text{D.20})$$

where matrix $\mathbf{\Gamma}$ is called a symmetry-adapted basis [30] and its construction for piece-wise basis functions is shown, *e.g.*, in [161]. Each block \mathbf{A}_g in (D.20) belongs to a unique irreducible representation of the point group [30], briefly denoted hereinafter as “irreps”, see Section D.A for some notable examples relevant to this work.

An important consequence of relation (D.20) is that the eigenvalue decomposition of operator \mathbf{A} on a symmetrical structure is also separable into irreps, *i.e.*, each eigenvector belongs to a particular irrep and eigenvectors from different irreps are orthogonal to each other even with respect to any operator. A central observation pertaining to the spectrum of the operator $\hat{\mathbf{A}}$, attributed to von Neumann and Wigner [20], then states that if operator \mathbf{A} is dependent on a certain parameter, such as frequency or Lagrange’s multiplier, see (D.16), the traces of eigenvalues (abbreviated in this paper as “eigenvalues”) belonging to the same irreps cannot cross each other [114, 161]. Applying this theorem to Figure D.3b, the blue and red traces must belong to modes from different irreps, as only traces of modes from different irreps can cross². Applying this theorem to Figure D.3a, no problems with degeneracies occur, since no symmetries are present, *i.e.*, all modes belong to only one irrep, see Table D.3 of Section D.A. In this case, therefore, there should be no crossing of eigenvalues.

D.5 Various Aspects of the Symmetry Presence

Several problems of various complexity are solved and interpreted in this section in terms of point group theory. The necessity of combining two modes from different irreps to remove the erroneous duality gap is shown in Section D.5.1. When geometry multiplicities appear, more than one solution exists and modes can freely be combined as shown in Section D.5.2. The study of how an imperfect mesh grid affects the symmetry treatment is conducted in Section D.5.3. Since the mesh grid is often made from rectangular or triangular elements, not all objects are perfectly represented, *e.g.*, a spherical shell with triangular discretization elements [52]. The subsequent example in Section D.5.4 shows that the theory introduced in this paper is generally valid for the arbitrary representation of the unknown (source) quantities, *cf.*, Figure D.1, by employing port-mode representation [159] to minimize the TARC [109, 157]

¹Only the crucial parts essential for this work are reviewed here. The reader is referred to, *e.g.*, [30] and references therein for a comprehensive explanation.

²Modes from different irreps have no physical interaction which is the reason for allowed crossing of their traces.

of the metallic rim. The spectrum of the spherical shell is evaluated analytically and compared with the numerical solution in [Section D.5.5](#). The last example in [Section D.5.6](#) deals with an academic, yet highly relevant, technique manipulating the eigenvalue traces of the isolated irrep.

D.5.1 Algebraic Multiplicity of Eigenvalues (Rectangular Plate)

The erroneous duality gap shown in [Section D.3](#) for a rectangular plate, see [Figure D.2b](#) and the results in [Figure D.3b](#), is eliminated here by the proper combination of degenerate eigenvectors.

The optimization problem [\(D.13\)](#) is solved with [\(D.16\)](#) by separately utilizing [\(D.20\)](#) for irreps B_2 and A_2 , *i.e.*, two traces with a crossing at $\lambda_2^* = 0.662$ in [Figure D.3b](#). At the crossing point, the corresponding eigenvectors can be linearly combined without a change of dual function value $g^* = \lambda_1(\lambda_2^*)$. Taking dominant modes from irreps as $\mathbf{I}_a \in B_2$, $\mathbf{I}_b \in A_2$, see [Figure D.4](#), we get

$$\mathbf{I}_{\text{opt}} = \mathbf{I}_a + \alpha \mathbf{I}_b. \quad (\text{D.21})$$

The erroneous duality gap in [Figure D.3b](#), top pane, is a manifestation of the constraint's violation in [\(D.13\)](#). Therefore, constant α is found to fulfill

$$\mathbf{I}_{\text{opt}}^H \mathbf{X}_0 \mathbf{I}_{\text{opt}} = 0. \quad (\text{D.22})$$

Since modes \mathbf{I}_a and \mathbf{I}_b belong to different irreps, we have $\mathbf{I}_a^H \mathbf{X}_0 \mathbf{I}_b = 0$, and

$$\alpha = \sqrt{-\frac{\mathbf{I}_a^H \mathbf{X}_0 \mathbf{I}_a}{\mathbf{I}_b^H \mathbf{X}_0 \mathbf{I}_b}} e^{j\varphi} \quad (\text{D.23})$$

with $\varphi \in [0, 2\pi)$ and the assumption that the square root is real. Except of nonphysical cases when the underlying mesh grid does not support inductive modes, this is always the case as for capacitive/inductive current \mathbf{I}_a we have to choose inductive/capacitive current \mathbf{I}_b so that the reactive powers have opposite sign. Combining the degenerated modes with [\(D.21\)](#), [\(D.23\)](#), we get the optimal current, see [Figure D.4c](#), fulfilling all constraints and $d^* = Q^*$.

Notice that the mixing coefficient α has the same form as in [\[160\]](#), where two dominant characteristic modes (capacitive and inductive) were combined to get a minimum Q-factor.

D.5.2 Geometry Multiplicity of Eigenvalues (Square Plate)

This example attempts to highlight the difference between a degeneracy across irreps (the previous section) and the higher dimension of a single irrep, a situation where the symmetries introduce additional degrees of freedom (this section).

Let us consider a setting depicted in [Figure D.5](#) which shows a square plate made of a perfectly conducting material, discretized with a symmetric mesh grid, and centered with respect to the coordinate system. Antenna gain G in a direction $\hat{\mathbf{r}}$ and polarization $\hat{\mathbf{e}}$ for a self-resonant current is to be maximized as

$$\begin{aligned} & \text{minimize} && -\mathbf{I}^H \mathbf{U}(\hat{\mathbf{e}}, \hat{\mathbf{r}}) \mathbf{I} \\ & \text{subject to} && \mathbf{I}^H (\mathbf{R}_0 + \mathbf{R}_\rho) \mathbf{I} = 1 \\ & && \mathbf{I}^H \mathbf{X}_0 \mathbf{I} = 0, \end{aligned} \quad (\text{D.24})$$

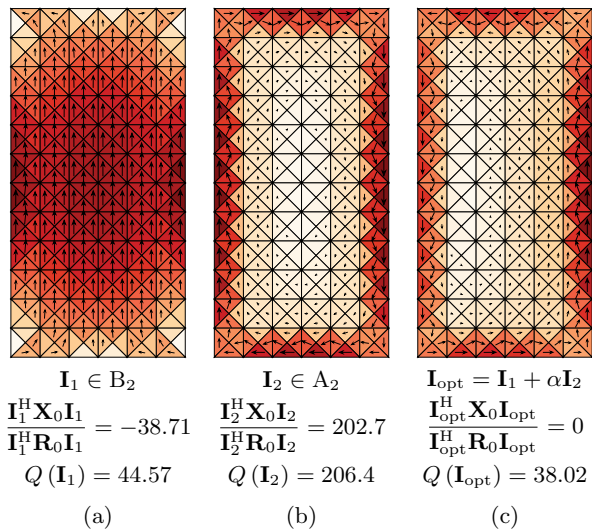


Figure D.4: Current densities associated with the first two modes of the eigenvalue problem (D.16) evaluated for the rectangular shape depicted in Figure D.2b at $\lambda_2 = \lambda_2^*$, cf. Figure D.3b. The right subfigure shows the correct combination to eliminate the erroneous duality gap depicted in the top pane of Figure D.3b. Subfigure (a) shows a capacitive mode belonging to irrep B_2 (the blue line in Figure D.3b) with Q-factor $Q(\mathbf{I}_1) = 44.57$. Subfigure (b) shows an inductive mode belonging to irrep A_2 (the red line in Figure D.3b) with Q-factor $Q(\mathbf{I}_2) = 206.4$. Finally, subfigure (c) shows the combination of currents from subfigures (a) and (b) with the mixing coefficient $\alpha = 4.232$. The resulting current \mathbf{I}_{opt} is self-resonant and $Q(\mathbf{I}_{\text{opt}}) = Q^* = d^*$.

where \mathbf{U} is a radiation intensity matrix with low-rank representation [61]

$$\mathbf{U}(\hat{\mathbf{e}}, \hat{\mathbf{r}}) = \mathbf{F}^H(\hat{\mathbf{e}}, \hat{\mathbf{r}}) \mathbf{F}(\hat{\mathbf{e}}, \hat{\mathbf{r}}), \quad (\text{D.25})$$

where $\mathbf{F}(\hat{\mathbf{e}}, \hat{\mathbf{r}}) = [\mathbf{F}_{\hat{\boldsymbol{\phi}}}^T(\hat{\mathbf{r}}) \quad \mathbf{F}_{\hat{\boldsymbol{\varphi}}}^T(\hat{\mathbf{r}})]^T$ and \mathbf{R}_ρ is a material matrix defined in [61]. The optimization problem (D.24) is solved according to the procedure from Section D.2.1 by combining constraints as proposed in [62]. The solution reads

$$G^* = d^* = -4\pi \max_{\nu} \min_m \lambda_{1,m}, \quad (\text{D.26})$$

where

$$-\mathbf{U} \mathbf{I}_m = \lambda_{1,m} (\mathbf{R}_0 + \mathbf{R}_\rho - \nu \mathbf{X}_0) \mathbf{I}_m \quad (\text{D.27})$$

with $\nu = -\lambda_2/\lambda_{1,m} \in [\nu_{\min}, \nu_{\max}]$ being picked so that the matrix on the right-hand side of (D.27) is positive definite [62]. A further acceleration of the formula (D.27) is possible, see [62] for details.

The optimization problem (D.24) differs from (D.13) in two respects. First, matrix \mathbf{U} has rank 2, which means that only two eigenvalues from (D.27) differ from zero. Second, matrix \mathbf{U} explicitly depends on the observation coordinate,

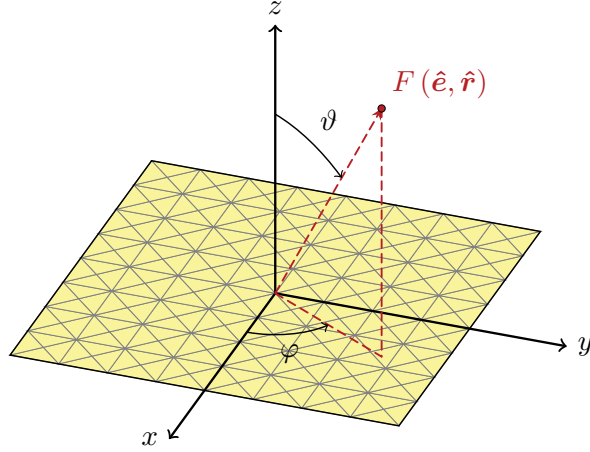


Figure D.5: Optimization setting and coordinate system used for the optimization of maximal antenna gain with a self-resonant constraint. Symbol $F(\hat{\mathbf{e}}, \hat{\mathbf{r}})$ denotes an electric far field in $\hat{\mathbf{r}}$ direction and of polarization $\hat{\mathbf{e}}$.

which also must be taken into account when considering the symmetries of the problem. Notice that for a general observation coordinate $\hat{\mathbf{r}}$, the physical problem is not symmetric although the antenna geometry is.

For the purpose of this example, let us assume that the direction for radiation intensity maximization has been set to $\hat{\mathbf{r}} = \hat{\mathbf{z}}$ and that the electrical size is $ka = 1/2$. The material parameters were set to be equivalent to copper at frequency $f = 1$ GHz. No restrictions were imposed on polarization $\hat{\mathbf{e}}$ meaning that the solution can equally be formed by polarization pointing into $\hat{\boldsymbol{\vartheta}}$ and $\hat{\boldsymbol{\varphi}}$ directions (or their combination). With these settings and the mesh grid from Figure D.5, the optimization problem complies with symmetries of the C_{4v} point group, see Table D.6 in Section D.A.

The solution to (D.27) is depicted in Figure D.6 with an immediate observation of twice degenerated eigentraces. These traces belong to irrep E (the only two-dimensional irrep of point group C_{4v}). Since there is no other eigentrace crossing these two at ν^* (all other eigenvalues are zero), there is no need to combine modes to fulfill the third constraint as in Section D.5.1. Instead, both solutions are valid on their own. They are geometry multiplicities, because for $\hat{\mathbf{r}} = \hat{\mathbf{z}}$ the two rank-one matrices $\mathbf{F}_{\hat{\boldsymbol{\vartheta}}}$ and $\mathbf{F}_{\hat{\boldsymbol{\varphi}}}$ forming operator \mathbf{U} are linearly dependent

$$\mathbf{F}_{\hat{\boldsymbol{\varphi}}} = \mathbf{F}_{\hat{\boldsymbol{\vartheta}}} \mathbf{C}_4, \quad (\text{D.28})$$

where $\mathbf{C}_4 \in \mathbb{R}^{N \times N}$ is the (unitary) rotation matrix by angle $\varphi = \pi/2$ around $\hat{\mathbf{z}}$ axis, $\mathbf{C}_4^H \mathbf{C}_4 = \mathbf{1}$, represented in basis $\{\boldsymbol{\psi}_n(\mathbf{r})\}$, therefore,

$$\mathbf{F} = \begin{bmatrix} \mathbf{F}_{\hat{\boldsymbol{\vartheta}}} \\ \mathbf{F}_{\hat{\boldsymbol{\vartheta}}} \mathbf{C}_4 \end{bmatrix} \quad (\text{D.29})$$

yields twice degenerated eigenvalue λ_1 in (D.27) since according to (D.25)

$$\mathbf{F}^H \mathbf{F} = \mathbf{F}_{\hat{\boldsymbol{\vartheta}}}^H \mathbf{F}_{\hat{\boldsymbol{\vartheta}}} + \mathbf{C}_4^H \mathbf{F}_{\hat{\boldsymbol{\vartheta}}}^H \mathbf{F}_{\hat{\boldsymbol{\vartheta}}} \mathbf{C}_4. \quad (\text{D.30})$$

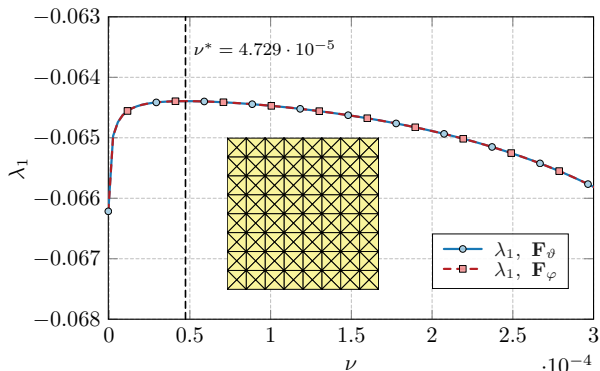


Figure D.6: Solution to the dual problem (D.27) for a rectangular plate of electrical size $ka = 1/2$ made of lossy material equivalent to copper at 1 GHz. The observation direction is $\hat{\mathbf{r}} = \hat{\mathbf{z}}$. The inset shows the mesh grid utilized for the optimization. The optimum value of Lagrange’s multiplier $\nu^* = 4.729 \cdot 10^{-5}$ is highlighted by the dashed black line. The two depicted eigentraces belong to irrep E, see Table D.6 in Section D.A, and are twice degenerated for all values of ν .

Adapting the knowledge gained in this section on an example of minimal Q-factor optimization from the previous section with a shape from, *e.g.*, the C_{4v} point group (a square plate), a problem originates where two modes out of three degeneracies have to be combined as (D.21) to fulfil the third constraint (D.22). In such a case, these two modes have to be from different irreps, specifically $\mathbf{I}_a \in \mathcal{I}_A$, $\mathbf{I}_b \in \mathcal{I}_B$, $A \neq B$ so that

$$\text{sign} \left\{ \mathbf{I}_a^H \mathbf{X}_0 \mathbf{I}_a \right\} = -\text{sign} \left\{ \mathbf{I}_b^H \mathbf{X}_0 \mathbf{I}_b \right\}, \quad (\text{D.31})$$

otherwise the erroneous duality gap cannot be eliminated.

D.5.3 Imperfections of the Mesh Grid

The understanding gained in the previous sections will be exploited here on an example of mesh grid imperfectness, where the point group rules are obscured by fact that all computations are made with finite numerical precision.

Two structures of different point groups are assumed, a square plate (C_{4v}) and a rectangular plate (C_{2v}). The optimization of the Q-factor introduced in Section D.4 and solved in Section D.5.1 is considered. The discretization grids are made of square pixels, see the insets on the left of Figure D.7, or compressed both horizontally and vertically, see the insets on the right of Figure D.7. Assuming that the mesh grid lies in the $x - y$ plane with the bottom-left corner at the origin, the compression is provided via transformation

$$\left[\frac{x}{L_x}, \frac{y}{L_y} \right] \rightarrow \left[\left(\frac{x}{L_x} \right)^\xi, \left(\frac{y}{L_y} \right)^\xi \right], \quad (\text{D.32})$$

applied on every grid node, where L_x, L_y are side lengths of the square or rectangle and $\xi \in (1, \infty)$.

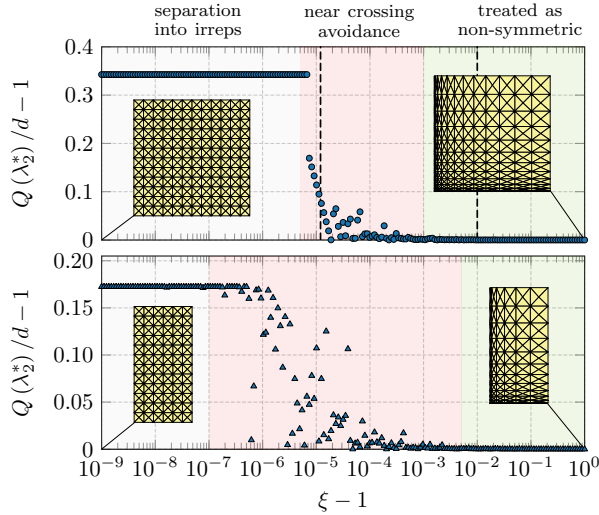


Figure D.7: Study of an erroneous duality gap expressed in terms of $Q(\lambda_2^*)/d-1$ for an optimization of self-resonant Q-factor. Two symmetric objects are considered, a square plate (C_{4v} point group, top pane) and a rectangular plate (C_{2v} points group, bottom pane). The parameter ξ distorts the mesh grid both in horizontal and in vertical directions, see the insets. The point group theory with separation into irreps applies for the negligible distortions, see left parts of the panes, highlighted by the gray background. For significant distortions, the structures behave as non-symmetric and no duality gap appears, see the right parts of the panes, highlighted by the green color. The most problematic part is the transition between symmetric and non-symmetric cases, see the intermediate parts of the panes, highlighted by the red color. The dashed black lines corresponds to subfigures (b) and (c) in Figure D.8.

The smooth distortion of the symmetric mesh grid enables an evolution of an erroneous duality gap to be seen, depicted as a normalized quantity in Figure D.7. For $\xi = 1$, the mesh grids preserve the symmetry of the object and an erroneous duality gap exists, see the left part of Figure D.7 highlighted by the gray background color. The error given by the difference between the primal and dual solution attains 34% for the square plate and about 17% for the rectangular plate, respectively. For a reasonable large value of ξ , say $\xi > 1 + 10^{-2}$, the non-symmetry of the grid is significant enough that no special treatment is required (duality gap is zero), see the right part of Figure D.7, highlighted by the green background color. The most challenging cases lie between these two regions, highlighted by the red background color in Figure D.7, and often occur in practice due to rounding errors and other numerical imperfections. This region deserves further attention because the symmetry treatments from the previous sections have to be properly adapted.

The dual solution to the example of the square plate and Q-factor minimization, depicted in Figure D.7, top pane, is repeated in Figure D.8. The close vicinity around λ_2^* point is studied for $\xi = \{1, 1 + 10^{-5}, 1 + 10^{-2}\}$, *i.e.*, for three various representatives of different regions in Figure D.7. It is seen that crossings of

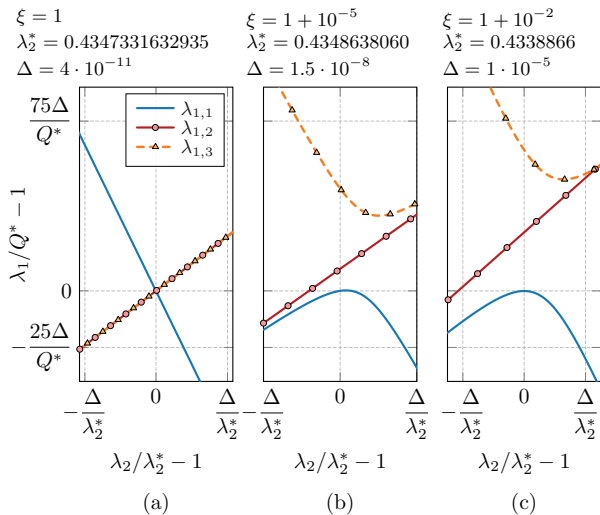


Figure D.8: Investigation of the close vicinity of the eigenvalue crossing/crossing avoidances for three particular cases from Figure D.7, top pane (the square plate). From left to right, they are evaluated for (a) $\xi = 1$ (symmetric mesh grid), (b) $\xi = 1 + 10^{-1}$ (slightly non-symmetrical mesh grid), and (c) $\xi = 1 + 10^{-2}$ (non-symmetric mesh grid). Due to the enormous sensitivity of the numerical precision, the high-order quadrature rule was applied to evaluate the matrix operators.

eigenvalues for the symmetric case evolves into the crossing avoidance scenario initially described in [20] (English transcription) and recalled in [114]. A problematic case appears in Figure D.8b where the values of λ_1 for λ_2^* are very close to each other, in this particular case they are the same up to six significant digits, yet not separated into irreps. The assumption $\mathbf{I}_a^H \mathbf{C} \mathbf{I}_b = 0$ secured by (D.20) is, therefore, not valid anymore and one has to solve (D.22) via (D.21) using

$$|\alpha|^2 + 2 \frac{\operatorname{Re} \{ \alpha \mathbf{I}_a^H \mathbf{X}_0 \mathbf{I}_b \}}{\mathbf{I}_b^H \mathbf{X}_0 \mathbf{I}_b} + \frac{\mathbf{I}_a^H \mathbf{X}_0 \mathbf{I}_a}{\mathbf{I}_b^H \mathbf{X}_0 \mathbf{I}_b} = 0. \quad (\text{D.33})$$

Formula (D.33) is a generalization of (D.23) for slightly non-symmetrical structures or for perturbed non-symmetrical mesh grids of symmetric structures. The only difference is the selection of suitable modes \mathbf{I}_a and \mathbf{I}_b to be combined. This fact is discussed further on the algorithmic level in the next section. Notice that the scenario shown in Figure D.8c contains one eigenvalue (the blue curve) which is significantly separated from the others to represent the true solution to the problem on its own.

The study in this section suggests that one may avoid issues related to the symmetries when non-symmetrical mesh grids are utilized, therefore, the symmetries within the operators are broken. However, as revealed by Figure D.7, the threshold over which the mesh can be considered non-symmetrical enough to disable the erroneous duality gap is not sharp and cannot be used for general treatment of this problem.

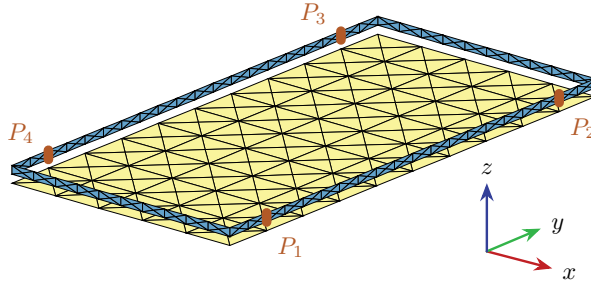


Figure D.9: A metallic rim with parasitic ground plane with four discrete ports, denoted P_1, \dots, P_4 . Both the rim and the ground plane are made of copper. The ports are placed at the distance $\ell/5$ from the ends of the longer side.

D.5.4 Change of Basis (TARC of a Lossy Metallic Rim)

It is shown in this example that the presence of symmetries strongly affects the physics even when the basis (D.14) is changed, *i.e.*, the operators are represented in another basis, which is still compatible with the point group of the studied object. A prominent example of this behaviour is a port modes representation [159], which advantageously reduces the size of the problem. Another advantage is that since the unknowns are the terminal voltages, *cf.*, Figure D.1b, the optimal solution is directly realizable.

A metallic rim placed over parasitic ground plane is shown in Figure D.9. The size of the ground plane is $150 \text{ mm} \times 75 \text{ mm}$, the height of the rim is 2.5 mm and the height over the ground plane is 2.5 mm (the dimensions are adjusted to be equivalent to a smart phone chassis). The material of the chassis is copper. The discretization grid was generated to accommodate the C_{2v} point group. The total active reflection coefficient (TARC), [157], as defined for port mode quantities in [109] is to be optimized. The degrees of freedom are the terminal voltages, the characteristic impedance of the transmission line $R_{0,i}$ and the matching susceptances $B_{L,i}$, see [109] for the detailed optimization procedure.

The position of the ports is specified in Figure D.9, with the polarization of the delta gaps pointing towards $+\hat{y}$ direction. Port admittance matrix \mathbf{y} is of 4×4 size and complies with the symmetries of the C_{2v} point group. The port voltages and admittances ($R_{0,i}^{-1} - jB_{L,i}$) enforcing simultaneously zero reflections on all ports are obtained as solutions to an eigenvalue problem [109]

$$\mathbf{y}\mathbf{v}_i = (R_{0,i}^{-1} - jB_{L,i})\mathbf{v}_i \quad (\text{D.34})$$

and are depicted in Table D.1 one by one as belonging to different irreps. When properly normalized, they evoke the character table for the C_{2v} point group, see Table D.5 in Section D.A. If port P_1 is taken as the initial port, port P_3 is identified as its rotation by π , port P_2 as reflection through xz plane, and port P_4 as reflection through yz plane. Knowing this, the voltage solutions can be assigned to the irreps they represent.

The initial values of matching B_L and loading R_0 given by (D.34) can further be optimized as described in [109]. TARC values Γ^t for all excitation schemes are summarized in the last column of Table D.1, concluding that the feeding scheme \mathbf{v}_3 ,

Table D.1: Summary of TARC optimization for rectangular metallic rim with a parasitic ground plane for symmetry placement of four ports.

	P_1	P_2	P_3	P_4	irrep	$1/B_L$	R_0	Γ^t
\mathbf{v}_1	+1	+1	+1	+1	A_1	451.3	24800	0.3064
\mathbf{v}_2	+1	-1	+1	-1	A_2	-313.8	156700	0.4212
\mathbf{v}_3	+1	+1	-1	-1	B_1	28.64	98.52	0.2374
\mathbf{v}_4	+1	-1	-1	+1	B_2	21.23	149.7	0.3302

i.e., with the voltage orientation along the loop formed by the rim, gives the minimum TARC. This excitation scheme belongs to the B_1 irrep and dominates up to frequency $f \approx 750$ MHz. Around that frequency the best performing irrep switches to another one.

One notable implication of the symmetries is that the voltage schemes from Table D.5 are identical in amplitude which simplifies the feeding circuitry, see [186] for a detailed study.

The conclusions drawn in this section, *i.e.*, that the effects of the symmetries remain the same with a proper change of basis, apply for many practical applications. For example, the entire domain basis of characteristic modes [49] suffers from the necessity of eigentrace tracking [114, 161]. On the other hand, proper use of symmetries introduces additional degrees of freedom, *e.g.*, for MIMO antenna design [86, 199]. Another notable example involves reduction with the Schur complement [107].

D.5.5 Analytically Solvable Problem (A Spherical Shell)

The next optimization problem is solved analytically. A minimal dissipation factor δ [99] is found with the optimal current being self-resonant [196]. A spherical shell of radius a and electrical size ka is considered. Explicitly, the optimization problem reads [192, 196]

$$\begin{aligned} & \text{minimize} && P_{\text{lost}} \\ & \text{subject to} && P_{\text{rad}} = 1 \\ & && P_{\text{react}} = 0, \end{aligned} \tag{D.35}$$

where the value of lost power P_{lost} , radiated power P_{rad} , and reactive power $P_{\text{react}} = 2\omega(W_m - W_e)$ is given by quadratic forms as before. The optimal dissipation factor is evaluated as $\delta = P_{\text{lost}}/P_{\text{rad}}$ [99].

Let us start with a proper representation of the operators, here, in an entire domain basis of regular spherical waves $\mathbf{u}_p(k\mathbf{r})$ [200]

$$\mathbf{J}(\mathbf{r}) = \sum_p \alpha_p \mathbf{u}_p(k\mathbf{r}). \tag{D.36}$$

The operators are given element-wise as

$$R_{0,pq} = \langle \mathbf{u}_p, \mathcal{R}_0(\mathbf{u}_q) \rangle = Z_0 k \int_{\Omega} \int_{\Omega'} U_{pq} \frac{\sin(kR)}{4\pi R} dV dV', \tag{D.37}$$

with

$$U_{pq} = \mathbf{u}_p^*(k\mathbf{r}) \cdot \mathbf{u}_q(k\mathbf{r}') - \frac{1}{k^2} \nabla \cdot \mathbf{u}_p^*(k\mathbf{r}) \nabla' \cdot \mathbf{u}_q(k\mathbf{r}'), \tag{D.38}$$

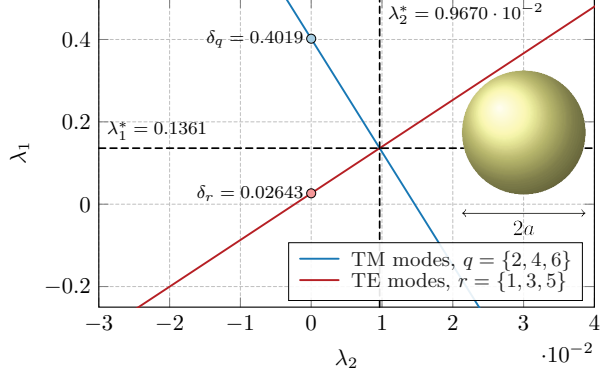


Figure D.10: Eigenvalue (Lagrange’s multipliers) λ_1 from (D.41) as functions of Lagrange’s multiplier λ_2 . The transverse magnetic (TM) modes are presented by the red eigentraces (since the characteristic number is negative, $\lambda_q < 0$, the curves are increasing). The transverse electric (TE) modes are represented by the blue eigentraces (since $\lambda_r > 0$). Both curves are three times degenerated (in correspondence with the geometrical multiplicity of dominant TM and TE modes).

$\mathbf{R}_0 = [R_{0,pq}]$, and similarly for \mathbf{X}_0 and \mathbf{R}_ρ , see [61], where $\mathbf{u}_p(kr)$ is a regular spherical wave with the multi-index

$$p = 2(l^2 + l - 1 + (-1)^s m) + \tau, \quad (\text{D.39})$$

where $l = \{0, 1, \dots, L\}$ denotes the order of spherical harmonics, $m = \{-l, \dots, l\}$, $s = \{0, 1\}$ denotes the parity and $\tau = \{1, 2\}$ denotes the used radial profile, consult [53, 200] for details, Z_0 is impedance of a vacuum, k is wavenumber, and $R = |\mathbf{r} - \mathbf{r}'|$. Importantly, the choice of spherical waves for spherical object leads to diagonal matrices \mathbf{R}_ρ , \mathbf{R}_0 , and \mathbf{X}_0 . Consequently, the eigenvalue problem (D.5) for the problem (D.35) reads

$$(\mathbf{R}_\rho - \lambda_2 \mathbf{X}_0) \boldsymbol{\alpha} = \lambda_1 \mathbf{R}_0 \boldsymbol{\alpha} \quad (\text{D.40})$$

which can further be separated into individual equations for each spherical wave

$$\frac{R_{\rho p}}{R_{0p}} - \lambda_2 \frac{X_{0p}}{R_{0p}} = \delta_p - \lambda_2 \lambda_p = \lambda_{1p}, \quad (\text{D.41})$$

where δ_p is the dissipation factor [191], and λ_p is a characteristic number³, both being evaluated for dominant spherical waves in [201]. Since the dissipation factors δ_p are positive and characteristic numbers λ_p are indefinite, (D.41) generates straight lines increasing (decreasing) with multiplier λ_2 for capacitive, $\lambda_p < 0$ (inductive, $\lambda_p > 0$) modes, see Figure D.10.

To solve the dual problem (D.11), two modes, say the q th and the r th spherical waves, have to be chosen so that their traces intersect with the lowest value of λ_1 .

³Spherical harmonics are the characteristic modes of a spherical shell [52].

This task is accomplished by taking the dominant **TM** and **TE** modes, $q \in \{2, 4, 6\}$ and $r \in \{1, 3, 5\}$, respectively, with

$$\lambda_2^* = \frac{\delta_r - \delta_q}{\lambda_r - \lambda_q}. \quad (\text{D.42})$$

Substituting (D.42) into (D.41) for $p = q$ or $p = r$ yields $\lambda_1^* = \delta^*$, see Figure D.10. The solution (D.42), however, does not secure the fulfilment of the self-resonant constraint. This constraint is met by utilizing the linear combination of modes (six modes are degenerated at $\lambda_2 = \lambda_2^*$)

$$\mathbf{J}(\mathbf{r}) = \sum_q \alpha_q \mathbf{u}_q(\mathbf{r}) + \alpha \sum_r \alpha_r \mathbf{u}_r(\mathbf{r}) = \mathbf{J}_e + \alpha \mathbf{J}_m, \quad (\text{D.43})$$

where [201]

$$\alpha = \sqrt{-\frac{\langle \mathbf{J}_e, \mathcal{X}_0(\mathbf{J}_e) \rangle}{\langle \mathbf{J}_m, \mathcal{X}_0(\mathbf{J}_m) \rangle}} e^{j\varphi}, \quad (\text{D.44})$$

cf., (D.23). Both dominant **TM** and **TE** spherical waves are three-times geometrically degenerated. Therefore, the α_q and α_r parameters are free to choose.

D.5.6 Manipulation With Isolated Eigentraces (Non-Foster Matching Elements)

Recapitulate first that, when symmetries are present, the eigentrace crossings appear and it might be required to combine two (or more) eigenvectors. Dealing with higher-dimensional point groups, more possibilities exist thanks to the geometry degeneracies. The question of whether it is possible to manipulate eigenvalue traces so that more than two traces cross each other and form an additional degree of freedom to constitute an optimal solution is answered in this example. This question goes back to the very first example of Q-factor optimization from Section D.3 and Section D.5.1.

Let us consider a hypothetical scenario of a passive structure tuned by frequency independent reactances (causing no increase in stored energy). The structure is a **PEC** rectangular rim of dimensions $\ell \times \ell/2$, see the inset of Figure D.11b, and of electrical size $ka = 1$. Without tuning reactances, the solution to the minimal Q-factor is approached via (D.16), the eigenvalues of which are shown in Figure D.11a. Let us select the first mode of B_1 irrep, depicted by the orange curve in Figure D.11a, and let us find reactance tuning such that this orange trace crosses the other two as depicted in Figure D.11b. Notice that the traces $\lambda_{1,1}(\lambda_2), \lambda_{1,2}(\lambda_2)$ were untouched. In order to manipulate only with traces of irrep B_1 , the reactance matrix of the rim is modified (by the inclusion of frequency independent tuning reactances) as

$$\tilde{\mathbf{X}}_0 = \mathbf{X}_0 + \mathbf{\Gamma}_{B_1} \hat{\mathbf{X}}_L \mathbf{\Gamma}_{B_1}^T, \quad (\text{D.45})$$

where

$$\hat{\mathbf{X}}_L = \begin{bmatrix} X_{L,1} & \cdots & 0 \\ \vdots & \ddots & \vdots \\ 0 & \cdots & X_{L,N} \end{bmatrix} \quad (\text{D.46})$$

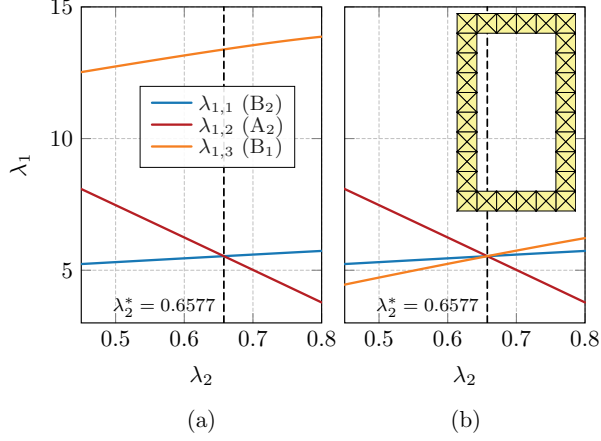


Figure D.11: Solution to the eigenvalue problem (D.16) for a rectangular rim of electrical size $ka = 1$, see the inset. (a) The solution to the original problem (D.16). (b) The solution to the modified problem (D.47) with reactance matrix $\tilde{\mathbf{X}}_0$ defined so as to manipulate B₁ irrep only. The irreducible representations of the modes are specified in the legend.

is a matrix of tuning coefficients. Notice that matrices $\mathbf{\Gamma}_{B_1}$ of the symmetry adapted basis belonging to irrep B₁ were used in the opposite direction than in relation (D.20). This composition guarantees that, irrespective of the matrix $\hat{\mathbf{X}}_L$, only properties of $\tilde{\mathbf{X}}_0$ attached to irrep B₁ will be modified.

The use of reactance matrix (D.45) in (D.16) instead of matrix \mathbf{X}_0 generates the eigenvalue problem

$$\frac{1}{2} \left(\mathbf{W} - \lambda_2 \tilde{\mathbf{X}}_0 \right) \mathbf{I}_m = \lambda_{1,m} \mathbf{R}_0 \mathbf{I}_m, \quad (\text{D.47})$$

the results of which are shown in Figure D.12 for the optimal Lagrange's multiplier $\lambda_2 = \lambda_2^* \approx 0.6577$ and for a single non-zero parameter $X_{L,i} = X_L$. Notice that particular index i of a selected tuning parameter is free to choose and is a function of basis functions ordering.

Orthogonal properties of symmetry adapted bases belonging to different irreps (D.20) can further be employed to simplify and speed up the evaluation of Figure D.12. It has already been mentioned that (D.45) cannot change eigentraces belonging to irreps different than B₁. The blue and red traces in Figure D.12 are therefore independent of the tuning parameter and there is no need to recalculate them (they attain the same value as in Figure D.11). To that point, relation (D.47) is left multiplied by $\mathbf{\Gamma}_{B_1}^T$ and $\mathbf{I}_m = \mathbf{\Gamma}_{B_1} \hat{\mathbf{I}}_m$ is substituted which leads to

$$\frac{1}{2} \left(\hat{\mathbf{W}}_{B_1} - \lambda_2^* \hat{\mathbf{X}}_{0,B_1} - \lambda_2^* \hat{\mathbf{X}}_L \right) \hat{\mathbf{I}}_{B_1} = \lambda_{1,m} \hat{\mathbf{R}}_{0,B_1} \hat{\mathbf{I}}_{B_1}. \quad (\text{D.48})$$

Eigenvalue problem (D.48) generates only those eigensolutions that belong to irrep B₁ (orange eigentrace in Figure D.12).

It is seen in Figure D.11b that three eigentraces are crossing each other at λ_2^* . That means that at least two solutions compliant with (D.21) are possible. These

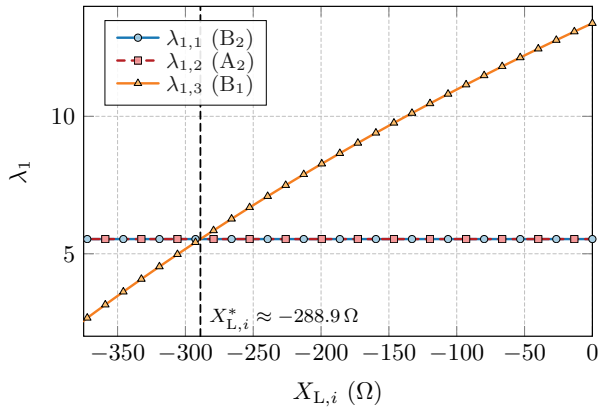


Figure D.12: Dependence of the dominant eigenvalues $\lambda_{1,1}$, $\lambda_{1,2}$, and $\lambda_{1,3}$, from irreps B_2 , A_2 , and B_1 , respectively, *cf.*, Figure D.11, on the tuning parameter $X_{L,i}$. The matrix $\tilde{\mathbf{X}}_L$ from (D.46) is full of zeros, except of the 16-th position, $i = 16$, on the diagonal.

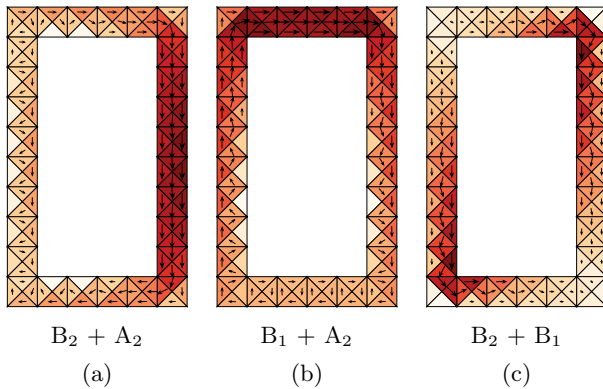


Figure D.13: Three combinations (D.21) of modes generated by (D.47). Due to the additionally introduced degeneracy in Figure D.11, not one, but three solutions are possible. The two new solutions are depicted in subfigures (b) and (c).

solutions are depicted in Figure D.13 in terms of the resulting surface currents. Case (a) is the classical solution known for C_{2v} combining B_2 and A_2 irreps, *cf.*, Figure D.4c. Case (b) in Figure D.13 is similar to case (a) in shape, but the maximum current density appears on the shorter side. This is possible thanks to added reactive matching elements which effectively elongate the side. Seen in this context, cases (a) and (b) are close to two geometrically degenerated solutions, normally appearing on the square rim (C_{4v} point group). Finally, combining solely B irreps results in case (c).

In order to reduce the Q-factor in the third irrep, an existence of frequency inde-

pendent reactance with no energy accumulation was assumed, which is unphysical. A physically more acceptable possibility would be to manipulate the first two modes (from irrep A_2, B_2) so they become equal to the third mode. This will increase the Q-factor value, but the gained benefit may be the equality of three eigenvalues (more degrees of freedom). Another possibility is a selective manipulation with a specific sub-set of characteristic modes. The same attempt was already undertaken with geometry manipulations, preserving the symmetries [79], with selective excitation [136], or with reactive tuning [138]). With the technique introduced above, one characteristic mode from each irrep can be modified so they all have the same eigenvalue at arbitrary ka . This is possible with simple reactive matching and the procedure above offers a simple recipe of how to do it.

D.6 Discussion

The determination of fundamental bounds in the presence of symmetries raised several interesting points to be discussed in this section.

D.6.1 Robust Algorithm To Eliminate Erroneous Duality Gaps

The procedure capable of dealing with all possible scenarios related to the presence of symmetries is depicted in Figure D.14. Its robustness was tested against various examples, involving both crossing (mesh grid preserving the symmetries) and near crossing avoidance (slightly unsymmetrical mesh grids), and including shapes from all point groups depicted in Table D.2.

The workflow is as follows. It is assumed that the problems belonging to class \mathcal{P}_1 are solved with a dedicated solver (the steps 1 and 2 in Figure D.14). While the optimal multiplier λ_2^* is found (step 3), identify multiplicity $|\mathcal{M}|$ of eigenvalue λ_1 (step 4), consider that they may vary up to relative error ϵ thanks to numerical errors and mesh imperfections. According to $|\mathcal{M}|$ decide whether the eigenmodes have to be combined (step 5). Notice that the decision shall not be based on constraint fulfilment as a true duality gap might exist. When degeneracies do not appear, follow standard procedure (steps 6 and 7), *i.e.*, determine the value of primal problem p^* (or verify that constraints are fulfilled). When the necessity of mode combination is detected, a special routine replacing step 6 is called for (steps 6A–6D). First evaluate projections for a matrix generating one of the constraints (step 6A, matrix \mathbf{C}_I). Identify block-diagonal matrices within \mathbf{C}_I and assign them with different irreps (step 6B). Pick one mode from two different irreps, if not possible, pick two modes arbitrarily (step 6C) and find a value of parameter α (step 6D).

When geometric multiplicities described in Section D.5.2 are present, it happens that more modes appear in sets \mathcal{I}_A and \mathcal{I}_B . In such a case, the currents \mathbf{I}_a and \mathbf{I}_b can be formed by arbitrary linear combination of modes from corresponding sets. This gives an additional degree of freedom in forming optimal currents \mathbf{I}_{opt} , reaching the same value of the optimized metric, but exhibiting different properties with respect to metrics not involved in the optimization. As an example, geometric multiplicities in the optimization problem (D.13) can be used to generate optimal currents of the same Q-factor, but different radiation diagrams.

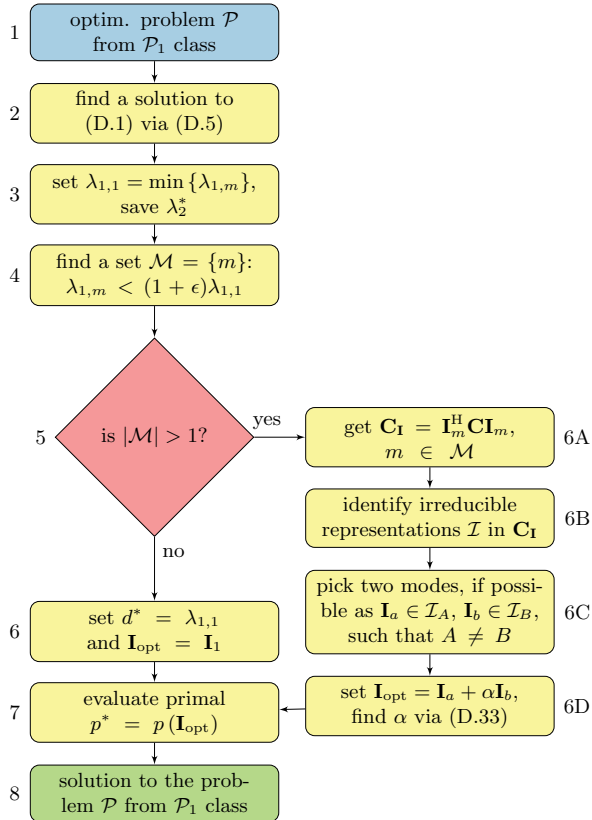


Figure D.14: Flowchart of a general algorithm dealing with degenerated eigenvalues. It is valid for an arbitrary optimization problem of type \mathcal{P}_1 (only quadratic constraints) and can deal with the imperfections of the mesh grid, as described in Section D.5.3, cf. Figure D.7. In case of geometrical degeneracies within one irrep, see Section D.5.2, one particular solution is found.

D.6.2 Distinction Between \mathcal{P}_1 -type and \mathcal{P}_2 -type Problems

We have seen that the presence of symmetries has serious consequences for the correct evaluation of problems from class \mathcal{P}_1 , defined by (D.1). Conversely, problems from class \mathcal{P}_2 , defined by (D.6), remain untouched. The reason is the presence of a linear term in the constraints which is typically a consequence of a prescribed or, in other words, uncontrollable field quantity. A good example is a prescription for complex power balance, heavily utilized in [59],

$$\mathbf{I}^H \mathbf{Z} \mathbf{I} = \mathbf{I}^H \mathbf{V}, \quad (\text{D.49})$$

where \mathbf{V} is a vector of excitation coefficients of the incident electric field intensity. Analogous to (D.49) all the linear terms with a current as the unknown couple the optimized quantity to the (external) field. This type of constraint makes the bounds sharper since it connects the optimized quantities and their excitation together.

D.6.3 Uniqueness of the Optimal Solution

The explicit solution to problems \mathcal{P}_1 and \mathcal{P}_2 enlighten the uniqueness of the solutions. In order to simplify the discussion, let us assume that matrices \mathbf{A} and \mathbf{C} in (D.1) and (D.6) have full rank, all the matrices are fixed, and the optimized quantity is properly representable in a basis (D.14), *i.e.*, the basis is chosen so that it respects the nature of the optimized problem.

The solution to problem \mathcal{P}_2 is unique. The solution to non-symmetric problem \mathcal{P}_1 is non-unique only with respect to the phase of the optimal current. For problem \mathcal{P}_1 with algebraic multiplicities, as shown in Section D.5.1, there is only one value of mixing coefficient $|\alpha|$, and only the phase of the mixed current may be chosen arbitrarily. Finally, when geometrical multiplicities occur, as shown in Section D.5.2, the optimal current further contains an arbitrary linear combination of geometrically degenerated eigenmodes, see Table D.2.

The uniqueness of the optimal currents \mathbf{I}_{opt} generating fundamental bounds implies that these bounds are not feasible except for the rare case in which the region used for the optimization, Ω , is already an optimal solution to the shape synthesis problem. Moreover, the excitation used has to be in accordance with the optimal current found, *i.e.*,


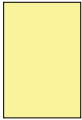
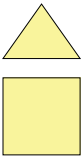
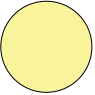
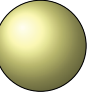
$$\mathbf{V} = \mathbf{Z} \mathbf{I}_{\text{opt}}. \quad (\text{D.50})$$

If this is not the case, and once the initial shape Ω has to be perturbed to meet the condition (D.50), see, *e.g.*, [190], the removals of the degrees of freedom immediately cause the deterioration of the fundamental bounds, which consequently indicates that the original bound was not feasible.

D.6.4 More Than Two Constraints

The existence of a duality gap is not a function of symmetries. Furthermore, the number of constraints and the number of degeneracies are not related in any way. Irrespective of the number of constraints, and considering that there is no duality gap g^* , the “erroneous” duality gap introduced by the presence of symmetries is always eliminated by the proper choice of just one constant, α . This statement is explained as follows.

Table D.2: Maximum number of degenerated eigenvalues depending on the point group of an object (no accidental crossing assumed). Symbols A and B represent the dimensions of two irreps of the highest dimensions within the point group. Only the dominant modes are considered.

					
point group	C_1	C_s, C_{2v}	C_{4v}, C_3	$O(2)$	$O(3)$
max degen. λ_1	$1 + 0$	$1 + 1$	$2 + 1$	$2 + 1$	$3 + 3$

Let us consider a problem from class \mathcal{P}_1 with multiple constraints leading to the formula for the stationary points \mathbf{I} in a form

$$\mathbf{A}\mathbf{I} - \lambda_2\mathbf{C}\mathbf{I} - \lambda_3\mathbf{D}\mathbf{I} + \dots = \lambda_1\mathbf{B}\mathbf{I}. \quad (\text{D.51})$$

The dual problem is solved by determining the set of optimal multipliers $\{\lambda_1^*, \lambda_2^*, \lambda_3^*, \dots\}$, see step 3 in Figure D.14. When degeneracies are detected (step 5 in Figure D.14), a combination of modes from different irreps has to be used (steps 6A–6D in Figure D.14), introducing an additional degree of freedom, parameter α . Notice that the values of the multipliers, $\{\lambda_1^*, \lambda_2^*, \lambda_3^*, \dots\}$, are not changed by combining degenerated modal currents. Since we know from the beginning that the problem has no duality gap, *i.e.*, the solution to the primal problem is equal to the solution of the dual problem, we know that all the constraints

$$\begin{aligned} \mathbf{I}_1^H \mathbf{B} \mathbf{I}_1 + |\alpha|^2 \mathbf{I}_2^H \mathbf{B} \mathbf{I}_2 &= 0 \\ \mathbf{I}_1^H \mathbf{C} \mathbf{I}_1 + |\alpha|^2 \mathbf{I}_2^H \mathbf{C} \mathbf{I}_2 &= 1 \\ \mathbf{I}_1^H \mathbf{D} \mathbf{I}_1 + |\alpha|^2 \mathbf{I}_2^H \mathbf{D} \mathbf{I}_2 &= d \\ \vdots &= \vdots \end{aligned} \quad (\text{D.52})$$

can be fulfilled by properly setting just one parameter α . This means that we can pick only one of the constraints (D.52) and determine the proper value of the parameter α .

The multi-objective optimization problems of fundamental bounds, see, *e.g.*, [59, 62, 192, 202] are often formulated with additional constraints (D.52) representing additional objectives. Such formulations therefore suffer from the erroneous duality gap issues once they fit into the \mathcal{P}_1 class.

D.6.5 Reduction of Computational Complexity

A useful side-product of (D.20) is the possibility to compute eigenvalue decomposition of each block (irrep) separately which leads to the acceleration of the optimization. The ratio S between computation time of generalized eigenvalue decomposition utilizing symmetries and computational time of a standard decomposition is obtained by analyzing eigenvalue decomposition of (D.20).

In order to present only the most salient features, it is assumed that that one eigenvalue is to be found within each irrep. The potential speed-up in such case is

$$S \propto \frac{1}{cN^q} \sum_{g=1}^G N_g^q, \quad (\text{D.53})$$

where G is the number of irreps, see (D.20), $N_g = \dim(\mathbf{A}_g)$, q indicates asymptotic complexity of used eigenvalue algorithm, and c indicates how many times the algorithm has been used, *e.g.*, $q \approx 2$ and $c = G$ for implicitly restarted Arnoldi method [41], and $q \approx 3$ and $c = 1$ for generalized Schur decomposition [40].

In order to provide a specific example, the C_{2v} group used in this paper is considered for evaluation of speed-up S . The dominant solution in each of the four one-dimensional irreps is demanded, and the number of modes in each irrep is the same, $N_g = N/4$. Relation (D.53) is simplified to

$$S \propto \frac{4}{cN^q} \left(\frac{N}{4}\right)^q = \frac{1}{4^2} = \frac{1}{16} \quad (\text{D.54})$$

both for implicitly restarted Arnoldi method and for generalized Schur decomposition.

An extreme case is shown in [56] for a body of revolution, where the system of basis functions forms a reducible system so that inverse of the resulting matrix is directly possible.

D.7 Conclusion

It has been shown that one entire class of optimization problems generating fundamental bounds in electromagnetism is encumbered with potential issues induced by symmetries. When no linear constraints are present, care must be taken with the investigation of the primal solution. This applies to structures with an imperfect discretization mesh grid as well, where the elimination of an erroneous duality gap might be even more problematic since the separation into irreducible representations is not possible.

A heuristic, yet general and point group theory-based technique to remove the erroneous duality gap has been presented and tested for various examples of varying complexity. The formula was tested for all canonical bodies (rectangular and square plates, a triangular shape, a spherical shell, etc.).

This work helps to understand the role of symmetries in establishing source quantity-based bounds. The challenges related to the presence of symmetries, when properly treated, introduce additional degrees of freedom. All conclusions apply not only to optimal, yet abstract and usually non-realizable, currents but also to optimal port mode excitation and other feasible representations of integro-differential operators, both for their surface and volumetric formulations.

D.A Character Tables

This appendix lists character tables of point groups used in the paper. Each table also contains symmetry operations available for the group (those are grouped into conjugacy classes and enumerated in the first row of the table) and the corresponding irreps (enumerated in the first column of the table). The table entries consist of group

characters (numbers of the table) and denote the traces of the matrix representations for a corresponding class and irrep. The number of irreps corresponds to the number of classes [30], all rows and columns of the character table are orthogonal. The symmetry operations used in Tables D.3–D.6 are: E: the identical operation, σ_t : a reflection (t is a placeholder for a specific type of reflection), $C_n(u)$: a rotation by $2\pi/n$ around u axis, σ_{uv} a reflection through plane uv .

The character corresponding to identity operation E indicates the dimension of the irrep and the geometric multiplicity of the eigenvalues within that irrep. For example, current solutions falling into the E irrep of C_{4v} group are twice degenerated, see Table D.6. This applies to the solutions of the problem (D.27) in Section D.5.2, see Figure D.6.

Non-symmetric objects belong to point group C_1 , see Table D.3. Objects with one reflection plane, often classified as having odd and even solutions, belong to point group C_s , see Table D.4. The remaining two groups mentioned here are C_{2v} (*e.g.*, rectangular plate) in Table D.5 and C_{4v} (*e.g.*, square plate) in Table D.6.

Table D.3: Character table for point group C_1 , a non-symmetric object belonging to.

C_1	E
A	+1

Table D.4: Character table for point group C_s , a non-symmetric object over ground plane belonging to.

C_s	E	σ_h
A'	+1	+1
A''	+1	-1

Table D.5: Character table for point group C_{2v} , a rectangular plate belongs to.

C_{2v}	E	$C_2(z)$	σ_{xz}	σ_{yz}
A_1	+1	+1	+1	+1
A_2	+1	+1	-1	-1
B_1	+1	-1	+1	-1
B_2	+1	-1	-1	+1

Table D.6: Character table for point group C_{4v} , a square plate belongs to.

C_{4v}	E	$2C_4(z)$	$C_2(z)$	$2\sigma_v$	$2\sigma_d$
A_1	+1	+1	+1	+1	+1
A_2	+1	+1	+1	-1	-1
B_1	+1	-1	+1	+1	-1
B_2	+1	-1	+1	-1	+1
E	+2	0	-2	0	0

E

Antenna Toolbox for MATLAB

The Antenna Toolbox for MATLAB (AToM) [29], as the name reveals, is a tool for solving antenna and scattering problems entirely written in MATLAB[®]. The development team from universities in Prague and Brno began collaborating under support by Technology Agency of the Czech Republic in September 2014 and continues to expand the toolbox with new functionalities. The graphical user interface (GUI) is user-friendly and the semi-open architecture allows users to access low-level functions. The fundamental AToM idea behind its success is “Source concept”—a generalized approach used to effectively evaluate and optimize antenna parameters using only antenna geometry and source currents.



The toolbox allows users to design arbitrary geometries made of wires or arbitrarily shaped highly conducting surfaces in the AToM DesignViewer, where also feeding is set up. All dimensions and most model settings can be parametrized via AToM Workspace. The discretization of the structure can be obtained by applying Delaunay triangulation [203] with the possibility of locally customizing the density function or to utilize symmetry planes. The session made in GUI is recorded in AToM History, from where it can be exported to the executable script.

The core of AToM is based on the method of moments (MoM) and the solution to the electric field integral equation [165]. In the newest version, the impedance matrix evaluation and the solution to $\mathbf{I} = \mathbf{Z}^{-1}\mathbf{V}$ can also be evaluated on the graphics processing unit which reduces computational time significantly. Computed current densities can be used to evaluate many antenna parameters, such as input impedance, radiation pattern, Q-factor, stored energy, etc.; matrix operators needed for the computation of these parameters are available. For a modal analysis of arbitrary operators, AToM also contains a generalized eigenvalue problem solver with an advanced adaptive tracking algorithm. The Results Browser allows the visualization of computed quantities.

In addition to the main functionality on hand in GUI, AToM offers many advanced functions accessible from the command window (*e.g.*, functions related to the point group theory). Moreover, several add-ons are available: functions for fundamental bounds or topology optimization, a generator of strip mesh from the curve definition, an add-on for export to TikZ, or a package with volumetric MoM, etc.

Table E.1 shows selected statistics about the AToM project. Figure E.1 maps the spread of AToM around the World.

Table E.1: Statistics of *AToM* valid up to December 1, 2021.

Files	2 511
Classes	216
Functions	4 326
Lines of code	207 982
– of which are comments	20 249
Add-ons	9
Free-version downloads	518
Full-version purchases	6

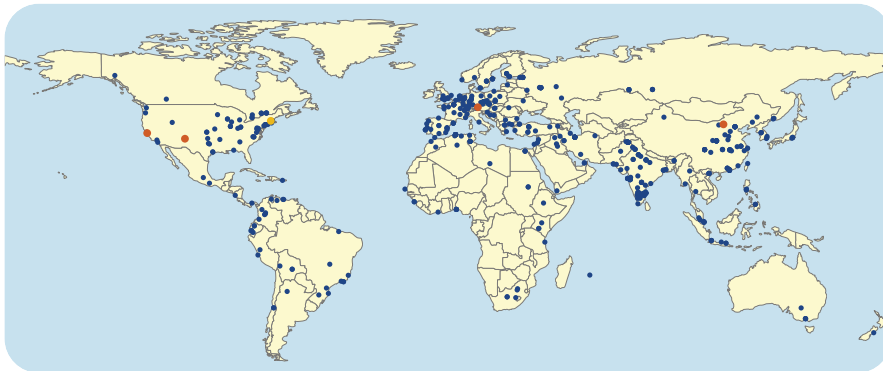


Figure E.1: Blue points represent locations (obtained from IP addresses) where the free version of *AToM* was downloaded. Orange/yellow dots point to locations where a full version of *AToM* was/is being purchased. Data updated on December 1, 2021.

E.1 Author’s Contribution to the *AToM*

“I joined the development team in October 2015. My primary responsibility was to design and create a solver for a parametrized generalized eigenvalue problem. It is mainly intended to compute characteristic modes with *AToM*’s *MoM*, but the decomposition of arbitrary input matrices are supported as well. The tracking algorithm contains several types of correlation computations or adaptive algorithms which can insert additional frequency samples at places where the tracking fails. Results from the modal solver were published and compared to commercial software [204] and were benchmarked with in-house solutions used at other universities [205]. The solution from the modal solver was used as the reference in this thesis.

Further, also for the purposes of this thesis, I implemented a set of functions handling symmetries and point groups. It includes testing mesh invariance under a given set of symmetry operations, constructing mapping matrices $\mathbf{C}(R)$, computing matrix representations $\mathbf{D}(R)$, classification modes into irreducible representation, and creating symmetry-adapted basis $\mathbf{\Gamma}^{(\alpha,i)}$.”

Visit <http://antennatoolbox.com> for more details.



About the Author

F.1 Personal Information

Name: Michal Mašek

Date of birth: October 26, 1990

Address: Tachovská 85, 323 00, Pilsen, the Czech Republic

Telephone: + 420 606 844 676

E-mail: [michal.masek@{fel.cvut.cz; antennatoolbox.com; esi-group.com}](mailto:michal.masek@fel.cvut.cz)

Personal webpage: michal-masek.cz

F.2 Education

Czech Technical University in Prague

Department of Electromagnetic Field

Faculty of Electrical Engineering

Technická 2, 166 27, Prague 6

Czech Republic

- | | |
|--------|---|
| since | Doctoral studies |
| 9/2015 | Dissertation topic: Utilization of symmetries in antenna modal analysis |
| 9/2013 | Master studies |
| – | Program studied: Wireless communication |
| 6/2015 | Specialization: RF technology |
| | Thesis topic: Field in real coaxial cable |
| 9/2010 | Bachelor studies |
| – | Program studied: Telecommunication technologies |
| 6/2013 | Thesis topic: Coaxial cable |

F.3 Work Experience

- since 2/2019 **Technical consultant** MECAS ESI s.r.o., Pilsen
Simulations in CEM One and process development in Visual-Process; L2 support for CEM One. Maintenance, development services, and technical support for Visual Antenna. Participation in the project *Virtual Prototyping and Validation of Electromagnetic Systems* – developing Visual EMBuild, an extension tool for CEM One.
- 11/2018 **Researcher** CTU in Prague
– Participation in the project *Virtual Prototyping and Validation of Electromagnetic Systems* – implementation of multilayered Green’s function.
11/2021
- 10/2015 **Researcher** CTU in Prague
– Developing the toolbox for antenna design and simulations in Matlab
12/2017 under the project *Tools for synthesis of antennas and sensors*. Responsible for the characteristic modes solver.
More information at antennatoolbox.com.

F.4 International Internships

- Aug 2019 **University of Seville, Spain**
– Dept. of Electronics and Electromagnetism
Oct 2019 prof. Rafael Rodríguez Boix – 3-week stay
Implementation of efficient method of moment codes for the analysis of multilayered structures (including electromagnetic scattering and antenna problems) with special emphasis on the computation of multilayered Green’s functions for mixed potential integral equations.
- Aug 2016 **University of Illinois at Urbana-Champaign, United States**
– Dept. of Electrical and Computer Engineering
Nov 2016 prof. Weng Cho Chew – 3-month stay
Using a Multi-level Fast Multipole Algorithm for computing characteristic modes of electrically large objects.
- Jan 2016 **Dublin Institute of Technology, Ireland**
Antenna & HF Research Centre
prof. Max Ammann – 2-week stay
Design and manufacturing of a circle-polarized patch antenna with coplanar waveguide feeding for Wi-Fi band.

F.5 Publications

Unless explicitly noted, the authorship is divided equally among the listed authors.

F.5.1 Journal Papers with Impact Factor Related to the Thesis

- [1] M. Capek, L. Jelinek, and **M. Masek**, “A Role of Symmetries in Evaluation of Fundamental Bounds,” *IEEE Transactions on Antennas and Propagation*, vol. 69, no. 11, pp. 7729-7742, Nov. 2021, DOI: [10.1109/TAP.2021.3070103](https://doi.org/10.1109/TAP.2021.3070103).
- [2] **M. Masek**, L. Jelinek, and M. Capek, “Excitation of Orthogonal Radiation Channels,” *IEEE Transactions on Antennas and Propagation*, vol. 69, no. 9, pp. 5365-5376, Mar. 2021, DOI: [10.1109/TAP.2021.3061161](https://doi.org/10.1109/TAP.2021.3061161).
- [3] M. Capek, L. Jelinek, and **M. Masek**, “Finding Optimal Total Active Reflection Coefficient and Realized Gain for Multiport Lossy Antennas,” *IEEE Transactions on Antennas and Propagation*, vol. 69, no. 5, pp. 2481-2493, May 2021, DOI: [10.1109/TAP.2020.3030941](https://doi.org/10.1109/TAP.2020.3030941).
- [4] **M. Masek**, M. Capek, L. Jelinek, and K. Schab, “Modal Tracking Based on Group Theory,” *IEEE Transactions on Antennas and Propagation*, vol. 68, no. 2, pp. 927-937, Feb. 2020, DOI: [10.1109/TAP.2019.2943354](https://doi.org/10.1109/TAP.2019.2943354).

F.5.2 Conference Papers Related to the Thesis

- [1] M. Capek, L. Jelinek, and **M. Masek** “Fundamental Bounds for Multi-Port Antennas,” *the 15th European Conference on Antennas and Propagation (EuCAP)*, Dusseldorf, Germany, 2021.
- [2] **M. Masek**, M. Capek, and L. Jelinek, “Feeding Positions Providing the Lowest TARC of Uncorrelated Channels,” *the 14th European Conference on Antennas and Propagation (EuCAP)*, Copenhagen, Denmark, 2020.
- [3] **M. Masek**, M. Capek, L. Jelinek, and K. Schab, “Utilization of Symmetries in Method of Moments,” *IEEE International Symposium on Antennas and Propagation (APS)*, Atlanta, Georgia, USA, 2019.
- [4] **M. Masek**, M. Capek, and L. Jelinek, “Utilization of Symmetries for MIMO Systems,” *Progress in Electromagnetic Research Symposium (PIERS)*, Rome, Italy, 2019.
- [5] **M. Masek**, M. Capek, L. Jelinek, and K. Schab, “Modal Crossing Treatment Using Group Theory,” *the 13th European Conference on Antennas and Propagation (EuCAP)*, Krakow, Poland, 2019.
- [6] **M. Masek**, M. Capek, and L. Jelinek, “Modal Tracking Based on Group Theory,” *the 12th European Conference on Antennas and Propagation (EuCAP)*, London, United Kingdom, 2018.

F.5.3 Journal Papers with Impact Factor not Related to the Thesis

- [1] M. Capek, P. Hazdra, **M. Masek**, and V. Losenicky, “Analytical Representation of Characteristic Mode Decomposition,” *IEEE Transactions on Antennas and Propagation*, vol. 65, no. 2, pp. 713-720, Feb. 2017. DOI: [10.1109/TAP.2016.2632725](https://doi.org/10.1109/TAP.2016.2632725)

- [2] P. Hazdra, M. Capek, **M. Masek**, and T. Lonsky, “An Introduction to the Source Concept for Antennas,” *Radioengineering*, vol. 25, no. 1, pp. 12-17, Apr. 2016. DOI: [10.13164/re.2016.0012](https://doi.org/10.13164/re.2016.0012)

F.5.4 Conference Papers not Related to the Thesis

- [1] P. Kadlec, M. Capek, J. Rymus, M. Marek, M. Stumpf, L. Jelinek, **M. Masek**, and P. Kotalik: “Design of a Linear Antenna Array: Variable Number of Dimensions Approach,” *Radioelektronika*, Czech Republic, 2020.
- [2] **M. Masek**, J. Rymus, P. Hazdra, and M. Capek, “Implementation of the Theory of Characteristic Modes into Antenna Modeling Tools and Their Benchmarking,” *the 8th Microwave and Radar Week*, Poznan, Poland, 2018.
- [3] Y. Chen, K. Schab, M. Capek, **M. Masek**, B. K. Lau, H. Aliakbariabar, Y. Haykir, Q. Wu, W. Strydom, N. Peitzmeier, M. Jovovic, S. Genovesi, and F. A. Dicandia, “Benchmark Problem Definition and Cross-Validation for Characteristic Mode Solvers,” *the 12th European Conference on Antennas and Propagation (EuCAP)*, London, United Kingdom, 2018.
- [4] M. Capek, P. Hazdra, V. Adler, P. Kadlec, V. Sedenka, M. Marek, **M. Masek**, V. Losenicky, M. Strambach, M. Mazanek, and J. Rymus, “AToM: A Versatile MATLAB Tool for Antenna Synthesis,” *the 12th European Conference on Antennas and Propagation (EuCAP)*, London, United Kingdom, 2018.
- [5] **M. Masek**, M. Capek, P. Hazdra, Q. I. Dai, and W. C. Chew, “Characteristic Modes of Electrically Small Antennas in the Presence of Electrically Large Platforms,” *Progress in Electromagnetic Research Symposium (PIERS)*, St. Petersburg, Russia, 2017.
- [6] M. Capek, **M. Masek**, and P. Hazdra, “Some numerical aspects of characteristic mode decomposition,” *the 10th European Conference on Antennas and Propagation (EuCAP)*, Davos, Switzerland, 2016.

F.6 Software

- [1] M. Capek, V. Adler, P. Kadlec, V. Sedenka, **M. Masek**, V. Losenicky, M. Strambach, and P. Hazdra: AToM - Antenna Toolbox for MATLAB, [Software] 2017, <http://antennatoolbox.com>.

F.7 Foundation Acknowledgment

The following projects supported the author’s research:

- SGS19/168/OHK3/3T/13 – Electromagnetic structures and waves
- GA19-06049S – Fundamental Bounds on Electromagnetic Radiation and Scattering Phenomena and Associated Realizable Subforms
- TA04010457 – Tools for the synthesis of antennas and sensors
- SGS16/226/OHK3/3T/13 – Investigation of high frequency electromagnetic structures
- GJ15-10280Y – Source Concept of Electrically Small Antenna Synthesis



Bibliography

- [1] R. S. P. Beekes, *Etymological Dictionary of Greek*. Leiden Boston: Brill, 2010.
- [2] Unknown Author, *Collins' Etymological Dictionary*. Forgotten Books, 2017.
- [3] B. Pfennig, *Principles of Inorganic Chemistry*. Hoboken, New Jersey: Wiley, 2015.
- [4] A. Zee, *Fearful Symmetry: The Search for Beauty in Modern Physics*. Princeton, N.J: Princeton University Press, 2007.
- [5] L. M. Lederman and C. T. Hill, *Symmetry and the Beautiful Universe*. Amherst, N.Y: Prometheus, 2008.
- [6] D. Hodgson, "The first appearance of symmetry in the human lineage: Where perception meets art," *Symmetry*, vol. 3, no. 1, pp. 37–53, 2011. [Online]. Available: <https://www.mdpi.com/2073-8994/3/1/37>
- [7] J. Ward, *The Principles of Ornament*. Charles Scribner's Sons, New York, 1896, project Gutenberg. [Online]. Available: <https://www.gutenberg.org/ebooks/60034>
- [8] S. V. Jablan, *Symmetry, Ornament and Modularity*. World Scientific, 2002.
- [9] K. Mainzer, *Symmetry and Complexity: The Spirit and Beauty of Nonlinear Science*. World Scientific, 2005.
- [10] H. S. Tsou and L. A. Bergman, *Dynamics and Control of Distributed Systems*. Cambridge University Press, 1998.
- [11] A. Brandt, *Noise and Vibration Analysis: Signal Analysis and Experimental Procedures*, 1st ed. Wiley, 2011.
- [12] L. D. Landau and L. M. Lifshitz, *Quantum Mechanics: Vol. 3 Nonrelativistic Theory*, 3rd ed. Butterworth-Heinemann, 1981.
- [13] C. Cohen-Tannoudji, B. Diu, and F. Laloe, *Quantum Mechanics (2 vol. set)*, 1st ed. Wiley, 1992.
- [14] B. M. Walter Greiner, *Quantum mechanics: Symmetries*, 2nd ed. Springer, 1994.

- [15] Y. Chen and C.-F. Wang, *Characteristic Modes: Theory and Applications In Antenna Engineering*. Wiley, 2015.
- [16] T. Haigh, “Cleve Moler: Mathematical software pioneer and creator of Matlab,” *IEEE Annals of the History of Computing*, vol. 30, no. 1, pp. 87–91, Jan.–March 2008.
- [17] (2018) The MATLAB. The MathWorks. [Online]. Available: www.mathworks.com
- [18] L. N. Trefethen and T. Betcke, “Computed eigenmodes of planar regions,” 2005, Manchester Institute for Mathematical Sciences, MMIS EPrint: 2006.367. [Online]. Available: <http://eprints.maths.manchester.ac.uk/594/>
- [19] J. von Neumann and E. P. Wigner, “Über das verhalten von eigenwerten bei adiabatischen prozessen,” *Physicalische Zeitschrift*, vol. 30, pp. 467–470, Sept. 1929.
- [20] J. von Neumann and E. Wigner, *On the Behaviour of Eigenvalues in Adiabatic Processes*. Singapore: World Scientific, 2000.
- [21] J. D. Joannopoulos, S. G. Johnson, J. N. Winn, and R. D. Meade, *Photonic Crystals: Molding the Flow of Light*, 2nd ed. Princeton University Press, 2008.
- [22] K. Sakoda, *Optical Properties of Photonic Crystals*. Springer, Berlin, Heidelberg, 2001.
- [23] D. E. McCumber, “Eigenmodes of a symmetric cylindrical confocal laser resonator and their perturbation by output-coupling apertures,” *The Bell System Technical Journal*, vol. 44, no. 2, pp. 333–363, Feb. 1965.
- [24] S. Gladyshev, K. Frizyuk, and A. Bogdanov, “Symmetry analysis and multipole classification of eigenmodes in electromagnetic resonators for engineering their optical properties,” *Physical Review B*, vol. 102, pp. 075 103/1–075 103/12, Aug. 2020.
- [25] J. Naqui, *Symmetry Properties in Transmission Lines Loaded with Electrically Small Resonators: Circuit Modeling and Applications*, 1st ed., ser. Springer Theses. Springer International Publishing, 2016.
- [26] A. Weierholt, A. Mickelson, and S. Neegard, “Eigenmode analysis of symmetric parallel waveguide couplers,” *IEEE Journal of Quantum Electronics*, vol. 23, no. 10, pp. 1689–1700, Oct. 1987.
- [27] S. F. Mahmoud, *Electromagnetic Waveguides: Theory and Applications*, ser. IET electromagnetic waves series 32. P. Peregrinus Ltd. on behalf of the Institution of Electrical Engineers, 1991.
- [28] R. F. Harrington, *Field Computation by Moment Methods*. Piscataway, New Jersey, United States: Wiley – IEEE Press, 1993.
- [29] (2019) Antenna Toolbox for MATLAB (AToM). Czech Technical University in Prague. www.antennatoolbox.com. [Online]. Available: www.antennatoolbox.com

- [30] R. McWeeny, *Symmetry: An Introduction to Group Theory and Its Applications*. London: Pergamon Press, 1963.
- [31] A. Fässler and E. Stiefel, *Group Theoretical Methods and Their Applications*. Birkhäuser Boston, 1992.
- [32] J. F. Cornwell, *Group Theory in Physics: An Introduction*. London: Academic Press, 1997.
- [33] H. Burzlaff and H. Zimmermann, “Point-group symbols,” in *International Tables for Crystallography*, Oct. 2006, vol. A, ch. 12.1, pp. 818–820.
- [34] R. S. Mulliken, “Report on notation for the spectra of polyatomic molecules,” *The Journal of Chemical Physics*, vol. 23, no. 11, pp. 1997–2011, Nov. 1955.
- [35] A. C. Tripp and G. W. Hohmann, “Block diagonalization of the electromagnetic impedance matrix of a symmetric buried body using group theory,” *IEEE Transactions on Geoscience and Remote Sensing*, vol. GE-22, no. 1, pp. 62–69, Jan. 1984.
- [36] J. H. Wilkinson, *The Algebraic Eigenvalue Problem*. Oxford University Press, 1988.
- [37] A. F. Peterson, S. L. Ray, and R. Mittra, *Computational Methods for Electromagnetics*. Wiley – IEEE Press, 1998.
- [38] J. L. Volakis, A. Chatterjee, and L. C. Kempel, *Finite Element Method Electromagnetics: Antennas, Microwave Circuits, and Scattering Applications*. Wiley – IEEE Press, 1998.
- [39] G. E. Shilov, *Linear Algebra*. Dover, 1977.
- [40] Y. Saad, *Numerical Methods for Large Eigenvalue Problems*. Society for Industrial and Applied Mathematics (SIAM), 2001.
- [41] —, *Iterative Methods for Sparse Linear Systems*. Society for Industrial and Applied Mathematics (SIAM), 2003.
- [42] G. H. Golub and C. F. Van Loan, *Matrix Computations*. Johns Hopkins University Press, 2012.
- [43] M. Hamermesh, *Group Theory and Its Application to Physical Problems*. Dover, 1989.
- [44] C. Chisholm, *Group Theoretical Techniques in Quantum Chemistry*. London-New York: Academic Press, 1976.
- [45] M. A. Blanco, M. Flórez, and M. Bermejo, “Evaluation of the rotation matrices in the basis of real spherical harmonics,” *Journal of Molecular Structure: THEOCHEM*, vol. 419, no. 1-3, pp. 19–27, Dec. 1997.
- [46] R. J. Garbacz, “Modal expansions for resonance scattering phenomena,” *Proceedings of the IEEE*, vol. 53, no. 8, pp. 856–864, Aug. 1965.
- [47] —, “A generalized expansion for radiated and scattered fields,” Ph.D. dissertation, The Ohio State Univ., 1968.

- [48] R. F. Harrington and J. R. Mautz, “Computation of characteristic modes for conducting bodies,” *IEEE Transactions on Antennas and Propagation*, vol. 19, no. 5, pp. 629–639, Sept. 1971.
- [49] —, “Theory of characteristic modes for conducting bodies,” *IEEE Transactions on Antennas and Propagation*, vol. 19, no. 5, pp. 622–628, Sept. 1971.
- [50] R. F. Harrington, “Matrix methods for field problems,” *Proceedings of the IEEE*, vol. 55, no. 2, pp. 136–149, Feb. 1967.
- [51] S. M. Rao, D. R. Wilton, and A. W. Glisson, “Electromagnetic scattering by surfaces of arbitrary shape,” *IEEE Transactions on Antennas and Propagation*, vol. 30, no. 3, pp. 409–418, May 1982.
- [52] M. Capek, V. Losenicky, L. Jelinek, and M. Gustafsson, “Validating the characteristic modes solvers,” *IEEE Transactions on Antennas and Propagation*, vol. 65, no. 8, pp. 4134–4145, Aug. 2017.
- [53] D. Tayli, M. Capek, L. Akrou, V. Losenicky, L. Jelinek, and M. Gustafsson, “Accurate and efficient evaluation of characteristic modes,” *IEEE Transactions on Antennas and Propagation*, vol. 66, no. 12, pp. 7066–7075, Dec. 2018.
- [54] E. Newman, “Small antenna location synthesis using characteristic modes,” *IEEE Transactions on Antennas and Propagation*, vol. 27, no. 4, pp. 530–531, July 1979.
- [55] J. Mautz and R. Harrington, “Modal analysis of loaded N-port scatterers,” *IEEE Transactions on Antennas and Propagation*, vol. 21, no. 2, pp. 188–199, Mar. 1973.
- [56] J. B. Knorr, “Consequences of symmetry in the computation of characteristic modes for conducting bodies,” *IEEE Transactions on Antennas and Propagation*, vol. 21, no. 6, pp. 899–902, Nov. 1973.
- [57] K. R. Schab and J. T. Bernhard, “Radiation and energy storage current modes on conducting structures,” *IEEE Transactions on Antennas and Propagation*, vol. 63, no. 12, pp. 5601–5611, Dec. 2015.
- [58] J. Liska, “Fundamental bounds on magnetic levitation and magnetic confinement,” diploma thesis, Czech Technical University in Prague, Czech Republic, 2021. [Online]. Available: <https://dspace.cvut.cz/handle/10467/94783>
- [59] M. Gustafsson, K. R. Schab, L. Jelinek, and M. Capek, “Upper bounds on absorption and scattering,” *New Journal of Physics*, vol. 22, no. 7, p. 073013, Sept. 2020.
- [60] T. Bernabeu-Jiménez, A. Valero-Nogueira, F. Vico-Bondia, and A. A. Kishk, “A comparison between natural resonances and characteristic mode resonances of an infinite circular cylinder,” *IEEE Transactions on Antennas and Propagation*, vol. 65, no. 5, pp. 2759–2763, Feb. 2017.
- [61] L. Jelinek and M. Capek, “Optimal currents on arbitrarily shaped surfaces,” *IEEE Transactions on Antennas and Propagation*, vol. 65, no. 1, pp. 329–341, Jan. 2017.

- [62] M. Gustafsson and M. Capek, “Maximum gain, effective area, and directivity,” *IEEE Transactions on Antennas and Propagation*, vol. 67, no. 8, pp. 5282–5293, Aug. 2019.
- [63] J. L. T. Ethier and D. McNamara, “An interpretation of mode-decoupled MIMO antennas in terms of characteristic port modes,” *IEEE Transactions on Magnetics*, vol. 45, no. 3, pp. 1128–1131, Feb. 2009.
- [64] M. Capek, P. Hazdra, P. Hamouz, and J. Eichler, “A method for tracking characteristic numbers and vectors,” *Progress In Electromagnetics Research B*, vol. 33, pp. 115–134, July 2011.
- [65] D. J. Ludick, U. Jakobus, and M. Vogel, “A tracking algorithm for the eigenvectors calculated with characteristic mode analysis,” in *Proceedings of the 8th European Conference on Antennas and Propagation (EUCAP)*, Hague, Netherlands, Apr. 2014, pp. 569–572.
- [66] B. D. Raines and R. G. Rojas, “Wideband characteristic mode tracking,” *IEEE Transactions on Antennas and Propagation*, vol. 60, no. 7, pp. 3537–3541, July 2012.
- [67] Z. Miers and B. K. Lau, “Wide band characteristic mode tracking utilizing far-field patterns,” *IEEE Antennas and Wireless Propagation Letters*, vol. 14, pp. 1658–1661, 2015.
- [68] E. Safin and D. Manteuffel, “Advanced eigenvalue tracking of characteristic modes,” *IEEE Transactions on Antennas and Propagation*, vol. 64, no. 7, pp. 2628–2636, July 2016.
- [69] Z. Yang, D. Su, Y. Li, and Y. Liu, “An improved method for tracking of characteristic modes,” in *2016 IEEE International Conference on Computational Electromagnetics (ICCEM)*, Guangzhou, China, Feb. 2016.
- [70] X. J. Chen, Y. M. Pan, and G. D. Su, “An advanced eigenvector-correlation-based tracking method for characteristic modes,” *IEEE Transactions on Antennas and Propagation*, vol. 69, no. 5, pp. 2751–2758, May 2021.
- [71] Y. N. Demkov and P. B. Kurasov, “Von Neumann-Wigner theorem: Level repulsion and degenerate eigenvalues,” *Theoretical and Mathematical Physics*, vol. 153, no. 1, pp. 1407–1422, Oct. 2007.
- [72] K. R. Schab and J. T. Bernhard, “A group theory rule for predicting eigenvalue crossings in characteristic mode analyses,” *IEEE Antennas and Wireless Propagation Letters*, no. 16, pp. 944–947, 2017.
- [73] S. Chaudhury, W. Schroeder, and H. Chaloupka, “Multiple antenna concept based on characteristic modes of mobile phone chassis,” in *Proceedings of the 2nd European Conference on Antennas and Propagation (EuCAP)*, Edinburgh, UK, Nov. 2007.
- [74] S. K. Chaudhury, W. L. Schroeder, and H. J. Chaloupka, “MIMO antenna system based on orthogonality of the characteristic modes of a mobile device,” in *2007 2nd International ITG Conference on Antennas*, Munich, Germany, Mar. 2007.

- [75] R. Martens, E. Safin, and D. Manteuffel, "Selective excitation of characteristic modes on small terminals," in *Proceedings of the 5th European Conference on Antennas and Propagation (EuCAP)*, Rome, Italy, Apr. 2011, pp. 2492–2496.
- [76] A. Araghi and G. Dadashzadeh, "Oriented design of an antenna for MIMO applications using theory of characteristic modes," *IEEE Antennas and Wireless Propagation Letters*, vol. 11, pp. 1140–1143, 2012.
- [77] H. Li, Z. Miers, and B. K. Lau, "Design of orthogonal MIMO handset antennas based on characteristic mode manipulation at frequency bands below 1 GHz," *IEEE Transactions on Antennas and Propagation*, vol. 62, no. 5, pp. 2756–2766, May 2014.
- [78] T. Hadamik, R. Martens, and D. Manteuffel, "MIMO antenna concept based on characteristic modes for indoor base stations," in *Proceedings of the 9th European Conference on Antennas and Propagation (EuCAP)*, Lisbon, Portugal, Apr. 2015, pp. 1–2.
- [79] B. Yang and J. J. Adams, "Systematic shape optimization of symmetric MIMO antennas using characteristic modes," *IEEE Transactions on Antennas and Propagation*, vol. 64, no. 7, pp. 2668–2678, July 2016.
- [80] E. Antonino-Daviu, M. Cabedo-Fabrés, M. Sonkki, N. Mohamed Mohamed-Hicho, and M. Ferrando-Bataller, "Design guidelines for the excitation of characteristic modes in slotted planar structures," *IEEE Transactions on Antennas and Propagation*, vol. 64, no. 12, pp. 5020–5029, Dec. 2016.
- [81] F. A. Dicandia, S. Genovesi, and A. Monorchio, "Efficient excitation of characteristic modes for radiation pattern control by using a novel balanced inductive coupling element," *IEEE Transactions on Antennas and Propagation*, vol. 66, no. 3, pp. 1102–1113, Mar. 2018.
- [82] K. Li and Y. Shi, "A pattern reconfigurable MIMO antenna design using characteristic modes," *IEEE Access*, vol. 6, pp. 43 526–43 534, 2018.
- [83] N. Peitzmeier and D. Manteuffel, "Selective excitation of characteristic modes on an electrically large antenna for MIMO applications," in *Proceedings of the 12th European Conference on Antennas and Propagation (EuCAP)*, London, UK, Apr. 2018.
- [84] P. Sumithra and D. Kannadassan, "Characteristic mode analysis of concentric circular ring antenna," in *3rd International Conference on Communication and Electronics Systems (ICCES)*, Coimbatore, India, oct. 2018, pp. 1037–1040.
- [85] D.-W. Kim and S. Nam, "Systematic design of a multiport mimo antenna with bilateral symmetry based on characteristic mode analysis," *IEEE Transactions on Antennas and Propagation*, vol. 66, no. 3, pp. 1076–1085, Mar. 2018.
- [86] N. Peitzmeier and D. Manteuffel, "Upper bounds and design guidelines for realizing uncorrelated ports on multimode antennas based on symmetry analysis of characteristic modes," *IEEE Transactions on Antennas and Propagation*, vol. 67, no. 6, pp. 3902–3914, June 2019.
- [87] T. Beni and H. Arai, "Selective excitation of platform eigenmodes using characteristic mode theory," in *International Workshop on Electromagnetics: Applications and Student Innovation Competition (iWEM)*, Makung, Taiwan, Aug. 2020, pp. 1–2.

- [88] W. Geyi, "Physical limitation of antenna," *IEEE Transactions on Antennas and Propagation*, vol. 51, no. 8, pp. 2116–2123, Aug. 2003.
- [89] M. Capek, L. Jelinek, K. R. Schab, M. Gustafsson, B. L. G. Jonsson, F. Ferrero, and C. Ehrenborg, "Optimal planar electric dipole antennas: Searching for antennas reaching the fundamental bounds on selected metrics," *IEEE Antennas and Propagation Magazine*, vol. 61, no. 4, pp. 19–29, Aug. 2019.
- [90] P. Chao, B. Strekha, R. K. Defo, S. Molesky, and A. W. Rodriguez, "Physical limits on electromagnetic response," 2021, eprint arXiv: 2109.05667. [Online]. Available: <http://arxiv.org/abs/2109.05667v1>
- [91] A. Bloch, R. Medhurst, and S. Pool, "A new approach to the design of superdirective aerial arrays," *Proceedings of the IEE*, vol. 100, no. 67, pp. 303–314, Sept. 1953.
- [92] L. J. Chu, "Physical limitations of omni-directional antennas," *Journal of Applied Physics*, vol. 19, pp. 1163–1175, Dec. 1948.
- [93] H. A. Wheeler, "Fundamental limitations of small antennas," *Proceedings of the IRE*, vol. 35, no. 12, pp. 1479–1484, Dec. 1947.
- [94] R. L. Fante, "Quality factor of general ideal antennas," *IEEE Transactions on Antennas and Propagation*, vol. 17, no. 2, pp. 151–157, Mar. 1969.
- [95] R. E. Collin and S. Rothschild, "Evaluation of antenna Q," *IEEE Transactions on Antennas and Propagation*, vol. 12, no. 1, pp. 23–27, Jan. 1964.
- [96] J. S. McLean, "A re-examination of the fundamental limits on the radiation Q of electrically small antennas," *IEEE Transactions on Antennas and Propagation*, vol. 44, no. 5, pp. 672–675, May 1996.
- [97] R. E. Collin, "Minimum Q of small antennas," *Journal of Electromagnetic Waves and Applications*, vol. 12, no. 10, pp. 1369–1393, Apr. 1998.
- [98] D. M. Grimes and C. A. Grimes, "Minimum Q of electrically small antennas: A critical review," *Microwave and Optical Technology Letters*, vol. 28, no. 3, pp. 172–177, Feb. 2001.
- [99] R. F. Harrington, "Antenna excitation for maximum gain," *IEEE Transactions on Antennas and Propagation*, vol. 13, no. 6, pp. 896–903, Nov. 1965.
- [100] S. Molesky, W. Jin, P. S. Venkataram, and A. W. Rodriguez, "T operator bounds on angle-integrated absorption and thermal radiation for arbitrary objects," *Physical Review Letters*, vol. 123, no. 257401, Dec. 2019.
- [101] H. Shim, H. Chung, and O. D. Miller, "Maximal free-space concentration of electromagnetic waves," *Physical Review Applied*, vol. 14, no. 1, July 2020.
- [102] S. Molesky, P. S. Venkataram, W. Jin, and A. W. Rodriguez, "Fundamental limits to radiative heat transfer: Theory," *Physical Review B*, vol. 101, no. 035408, Jan. 2020.
- [103] S. Molesky, P. Chao, W. Jin, and A. W. Rodriguez, "Global T operator bounds on electromagnetic scattering: Upper bounds on far-field cross sections," *Physical Review Research*, vol. 2, no. 033172, July 2020.

- [104] Z. Kuang and O. D. Miller, “Computational bounds to light-matter interactions via local conservation laws,” *Physical Review Letters*, vol. 125, no. 263607, Dec. 2020.
- [105] R. Trivedi, G. Angeris, L. Su, S. Boyd, S. Fan, and J. Vučković, “Bounds for scattering from absorptionless electromagnetic structures,” *Physical Review Applied*, vol. 14, no. 014025, July 2020.
- [106] S. Boyd and L. Vandenberghe, *Convex Optimization*. Cambridge, Great Britain: Cambridge University Press, 2004.
- [107] M. Capek, M. Gustafsson, and K. R. Schab, “Minimization of antenna quality factor,” *IEEE Transactions on Antennas and Propagation*, vol. 65, no. 8, pp. 4115–4123, Aug. 2017.
- [108] M. Uzsoky and L. Solymár, “Theory of super-directive linear arrays,” *Acta Physica Academiae Scientiarum Hungaricae*, vol. 6, no. 2, pp. 185–205, Dec. 1956.
- [109] M. Capek, L. Jelinek, and M. Masek, “Finding optimal total active reflection coefficient and realized gain for multi-port lossy antennas,” *IEEE Transactions on Antennas and Propagation*, vol. 69, no. 5, pp. 2481–2493, May 2021.
- [110] O. Ergul and L. Gurel, *The Multilevel Fast Multipole Algorithm (MLFMA) for Solving Large-Scale Computational Electromagnetics Problems*. Wiley – IEEE Press, 2014.
- [111] Q. I. Dai, J. W. Wu, H. Gan, Q. S. Liu, W. C. Chew, and W. E. I. Sha, “Large-scale characteristic mode analysis with fast multipole algorithms,” *IEEE Transactions on Antennas and Propagation*, vol. 64, no. 7, pp. 2608–2616, July 2016.
- [112] M. Masek, M. Capek, P. Hazdra, Q. I. Dai, and W. C. Chew, “Characteristic modes of electrically small antennas in the presence of electrically large platforms,” in *Progress In Electromagnetics Research Symposium*, St. Petersburg, Russia, May 2017, pp. 3733–3738.
- [113] M. Capek, V. Neuman, J. Tucek, and L. Jelinek, “Shape regularization and acceleration of topology optimization via point group symmetries,” 2022, accepted to the *16th European Conference on Antennas and Propagation (EuCAP)*, Madrid, Spain, Apr. 2022.
- [114] K. R. Schab, J. M. Outwater Jr., M. W. Young, and J. T. Bernhard, “Eigenvalue crossing avoidance in characteristic modes,” *IEEE Transactions on Antennas and Propagation*, vol. 64, no. 7, pp. 2617–2627, July 2016.
- [115] J. F. Cornwell, *Group Theory in Physics Vol. 1,2*. London: Academic Press, 1984.
- [116] R. F. Harrington, *Time-Harmonic Electromagnetic Fields*, 2nd ed. Wiley – IEEE Press, 2001.
- [117] J. A. De Loera, J. Rambau, and F. Santos, *Triangulations – Structures for Algorithms and Applications*. Berlin, Germany: Springer, 2010.

- [118] M. Masek, M. Capek, L. Jelinek, and K. R. Schab, “Modal tracking based on group theory,” 2018, eprint arXiv: 1812.03006. [Online]. Available: <https://arxiv.org/abs/1812.03006>
- [119] M. Cabedo-Fabres, E. Antonino-Daviu, A. Valero-Nogueira, and M. F. Bataller, “The theory of characteristic modes revisited: A contribution to the design of antennas for modern applications,” *IEEE Antennas and Propagation Magazine*, vol. 49, no. 5, pp. 52–68, Oct. 2007.
- [120] (2016) FEKO. Altair. [Online]. Available: www.feko.info
- [121] A. Nuttall, “Some windows with very good sidelobe behavior,” *IEEE Transactions on Acoustics, Speech, and Signal Processing*, vol. 29, no. 1, pp. 84–91, Feb. 1981.
- [122] M. Giordani, M. Polese, M. Mezzavilla, S. Rangan, and M. Zorzi, “Towards 6G networks: Use cases and technologies,” 2020, eprint arXiv: 1903.12216. [Online]. Available: <https://arxiv.org/abs/1903.12216>
- [123] J. Reed, M. Vassiliou, and S. Shah, “The role of new technologies in solving the spectrum shortage [point of view],” *Proceedings of the IEEE*, vol. 104, no. 6, pp. 1163–1168, June 2016.
- [124] D. Gesbert, M. Shafi, D. shan Shiu, P. Smith, and A. Naguib, “From theory to practice: an overview of MIMO space-time coded wireless systems,” *IEEE Journal on Selected Areas in Communications*, vol. 21, no. 3, pp. 281–302, Apr. 2003.
- [125] J. Winters, “On the capacity of radio communication systems with diversity in a Rayleigh fading environment,” *IEEE Journal on Selected Areas in Communications*, vol. 5, no. 5, pp. 871–878, June 1987.
- [126] M. Jensen and J. Wallace, “A review of antennas and propagation for MIMO wireless communications,” *IEEE Transactions on Antennas and Propagation*, vol. 52, no. 11, pp. 2810–2824, Nov. 2004.
- [127] S. Yang and L. Hanzo, “Fifty years of MIMO detection: The road to large-scale MIMOs,” *IEEE Communications Surveys & Tutorials*, vol. 17, no. 4, pp. 1941–1988, Fourthquarter 2015.
- [128] A. F. Molisch, *Wireless Communications*. Wiley-IEEE Press, 2010.
- [129] J. Andersen and H. Rasmussen, “Decoupling and descattering networks for antennas,” *IEEE Transactions on Antennas and Propagation*, vol. 24, no. 6, pp. 841–846, Nov. 1976.
- [130] P.-S. Kildal and K. Rosengren, “Correlation and capacity of MIMO systems and mutual coupling, radiation efficiency, and diversity gain of their antennas: simulations and measurements in a reverberation chamber,” *IEEE Communications Magazine*, vol. 42, no. 12, pp. 104–112, Dec. 2004.
- [131] E. Antonino-Daviu, M. Cabedo-Fabres, M. Gallo, M. F. Bataller, and M. Bozzetti, “Design of a multimode MIMO antenna using characteristic modes,” in *Proceedings of the 3rd European Conference on Antennas and Propagation (EuCAP)*, Berlin, Germany, Mar. 2009, pp. 1840–1844.

- [132] T. O. Saarinen, J.-M. Hannula, A. Lehtovuori, and V. Viikari, “Combinatory feeding method for mobile applications,” *IEEE Antennas and Wireless Propagation Letters*, vol. 18, no. 7, pp. 1312–1316, July 2019.
- [133] J.-M. Hannula, T. O. Saarinen, J. Holopainen, and V. Viikari, “Frequency reconfigurable multiband handset antenna based on a multichannel transceiver,” *IEEE Transactions on Antennas and Propagation*, vol. 65, no. 9, pp. 4452–4460, Sept. 2017.
- [134] J. C. Coetzee and Y. Yu, “Port decoupling for small arrays by means of an eigenmode feed network,” *IEEE Transactions on Antennas and Propagation*, vol. 56, no. 6, pp. 1587–1593, June 2008.
- [135] R. F. Harrington and J. R. Mautz, “Pattern synthesis for loaded N-port scatterers,” *IEEE Transactions on Antennas and Propagation*, vol. 22, no. 2, pp. 184–190, Mar. 1974.
- [136] W. Su, Q. Zhang, S. Alkaraki, Y. Zhang, X.-Y. Zhang, and Y. Gao, “Radiation energy and mutual coupling evaluation for multimode MIMO antenna based on the theory of characteristic mode,” *IEEE Transactions on Antennas and Propagation*, vol. 67, no. 1, pp. 74–84, Jan. 2019.
- [137] D. Manteuffel and R. Martens, “Compact multimode multielement antenna for indoor UWB massive MIMO,” *IEEE Transactions on Antennas and Propagation*, vol. 64, no. 7, pp. 2689–2697, July 2016.
- [138] H. Jaafar, S. Collardey, and A. Sharaiha, “Optimized manipulation of the network characteristic modes for wideband small antenna matching,” *IEEE Transactions on Antennas and Propagation*, vol. 65, no. 11, pp. 5757–5767, Nov. 2017.
- [139] D. Wen, Y. Hao, H. Wang, and H. Zhou, “Design of a MIMO antenna with high isolation for smartwatch applications using the theory of characteristic modes,” *IEEE Transactions on Antennas and Propagation*, vol. 67, no. 3, pp. 1437–1447, Mar. 2019.
- [140] L. Qu, H. Lee, H. Shin, M.-G. Kim, and H. Kim, “MIMO antennas using controlled orthogonal characteristic modes by metal rims,” *IET Microwaves, Antennas & Propagation*, vol. 11, no. 7, pp. 1009–1015, June 2017.
- [141] Q. Wu, W. Su, Z. Li, and D. Su, “Reduction in out-of-band antenna coupling using characteristic mode analysis,” *IEEE Transactions on Antennas and Propagation*, vol. 64, no. 7, pp. 2732–2742, July 2016.
- [142] J. L. T. Ethier and D. McNamara, “The use of generalized characteristic modes in the design of MIMO antennas,” *IEEE Transactions on Magnetics*, vol. 45, no. 3, pp. 1124–1127, Mar. 2009.
- [143] M. Gustafsson and S. Nordebo, “Characterization of MIMO antennas using spherical vector waves,” *IEEE Transactions on Antennas and Propagation*, vol. 54, no. 9, pp. 2679–2682, Sept. 2006.
- [144] —, “On the spectral efficiency of a sphere,” *Progress In Electromagnetics Research*, vol. 67, pp. 275–296, 2007.

- [145] L. R. Ximenes and A. L. F. de Almeida, "Capacity evaluation of MIMO antenna systems using spherical harmonics expansion," in *2010 IEEE 72nd Vehicular Technology Conference - Fall*, Ottawa, ON, Canada, Sept. 2010.
- [146] A. A. Glazunov, M. Gustafsson, and A. F. Molisch, "On the physical limitations of the interaction of a spherical aperture and a random field," *IEEE Transactions on Antennas and Propagation*, vol. 59, no. 1, pp. 119–128, Jan. 2011.
- [147] C. Ehrenborg and M. Gustafsson, "Fundamental bounds on MIMO antennas," *IEEE Antennas and Wireless Propagation Letters*, vol. 17, no. 1, pp. 21–24, Jan. 2018.
- [148] M. Migliore, "On the role of the number of degrees of freedom of the field in MIMO channels," *IEEE Transactions on Antennas and Propagation*, vol. 54, no. 2, pp. 620–628, Feb. 2006.
- [149] A. A. Glazunov and J. Zhang, "On some optimal MIMO antenna coefficients in multipath channels," *Progress In Electromagnetics Research B*, vol. 35, pp. 87–109, 2011.
- [150] M. D. Migliore, "Horse (electromagnetics) is more important than horseman (information) for wireless transmission," *IEEE Transactions on Antennas and Propagation*, vol. 67, no. 4, pp. 2046–2055, Apr. 2019.
- [151] M. Mohajer, S. Safavi-Naeini, and S. K. Chaudhuri, "Spherical vector wave method for analysis and design of MIMO antenna systems," *IEEE Antennas and Wireless Propagation Letters*, vol. 9, pp. 1267–1270, 2010.
- [152] J. Wallace and M. Jensen, "Mutual coupling in MIMO wireless systems: A rigorous network theory analysis," *IEEE Transactions on Wireless Communications*, vol. 3, no. 4, pp. 1317–1325, July 2004.
- [153] A. Krewski, W. L. Schroeder, and K. Solbach, "Multi-band 2-port MIMO LTE antenna design for laptops using characteristic modes," in *Loughborough Antennas and Propagation Conference (LAPC)*, Loughborough, UK, Nov. 2012, pp. 1–4.
- [154] R. Martens and D. Manteuffel, "Systematic design method of a mobile multiple antenna system using the theory of characteristic modes," *IET Microwaves, Antennas & Propagation*, vol. 8, no. 12, pp. 887–893, Sept. 2014.
- [155] A. Krewski, W. Schroeder, and K. Solbach, "Bandwidth limitations and optimum low-band LTE MIMO antenna placement in mobile terminals using modal analysis," in *Proceedings of the 5th European Conference on Antennas and Propagation (EuCAP)*, Rome, Italy, Apr. 2011, pp. 142–146.
- [156] C. H. Papadimitriou and K. Steiglitz, *Combinatorial Optimization*. Dover Publications Inc., 1998.
- [157] M. Manteghi and Y. Rahmat-Samii, "Multiport characteristics of a wide-band cavity backed annular patch antenna for multipolarization operations," *IEEE Transactions on Antennas and Propagation*, vol. 53, no. 1, pp. 466–474, Jan. 2005.

- [158] M. Gustafsson, D. Tayli, C. Ehrenborg, M. Cismasu, and S. Norbedo, "Antenna current optimization using MATLAB and CVX," *FERMAT*, vol. 15, no. 5, pp. 1–29, May–June 2016. [Online]. Available: <http://www.e-fermat.org/articles/gustafsson-art-2016-vol15-may-jun-005/>
- [159] R. F. Harrington, "Reactively controlled directive arrays," *IEEE Transactions on Antennas and Propagation*, vol. 26, no. 3, pp. 390–395, May 1978.
- [160] M. Capek and L. Jelinek, "Optimal composition of modal currents for minimal quality factor Q," *IEEE Transactions on Antennas and Propagation*, vol. 64, no. 12, pp. 5230–5242, Dec. 2016.
- [161] M. Masek, M. Capek, L. Jelinek, and K. R. Schab, "Modal tracking based on group theory," *IEEE Transactions on Antennas and Propagation*, vol. 68, no. 2, pp. 927–937, Feb. 2020.
- [162] C. A. Balanis, *Advanced Engineering Electromagnetics*. Wiley, 1989.
- [163] K. Rosengren and P.-S. Kildal, "Radiation efficiency, correlation, diversity gain and capacity of a six-monopole antenna array for a MIMO system: theory, simulation and measurement in reverberation chamber," *IEE Proceedings – Microwaves, Antennas and Propagation*, vol. 152, no. 1, p. 7, Feb. 2005.
- [164] C. A. Balanis, *Antenna Theory Analysis and Design*, 3rd ed. Wiley, 2005.
- [165] J. L. Volakis and K. Sertel, *Integral Equation Methods for Electromagnetics*. Scitech Publishing Inc., 2012.
- [166] T. B. A. Senior and J. L. Volakis, *Approximate Boundary Conditions in Electromagnetics*. IEE, 1995.
- [167] G. A. E. Vandenbosch, "Reactive energies, impedance, and Q factor of radiating structures," *IEEE Transactions on Antennas and Propagation*, vol. 58, no. 4, pp. 1112–1127, Apr. 2010.
- [168] M. Cismasu and M. Gustafsson, "Antenna bandwidth optimization with single frequency simulation," *IEEE Transactions on Antennas and Propagation*, vol. 62, no. 3, pp. 1304–1311, Mar. 2014.
- [169] M. Capek, L. Jelinek, and P. Hazdra, "On the functional relation between quality factor and fractional bandwidth," *IEEE Transactions on Antennas and Propagation*, vol. 63, no. 6, pp. 2787–2790, June 2015.
- [170] D. M. Pozar, *Microwave Engineering*, 4th ed. Wiley, 2011.
- [171] H. Raza, J. Yang, and A. Hussain, "Measurement of radiation efficiency of multiport antennas with feeding network corrections," *IEEE Antennas and Wireless Propagation Letters*, vol. 11, pp. 89–92, 2012.
- [172] H. Li, Y. Tan, B. K. Lau, Z. Ying, and S. He, "Characteristic mode based tradeoff analysis of antenna-chassis interactions for multiple antenna terminals," *IEEE Transactions on Antennas and Propagation*, vol. 60, no. 2, pp. 490–502, Feb. 2012.
- [173] R. Luomaniemi, J.-M. Hannula, A. Lehtovuori, and V. Viikari, "Switch-reconfigurable metal rim mimo handset antenna with distributed feeding," *IEEE Access*, vol. 7, pp. 48 971–48 981, 2019.

- [174] M. Manteghi and Y. Rahmat-Samii, "Broadband characterization of the total active reflection coefficient of multiport antennas," in *IEEE International Symposium on Antennas and Propagation and USNC-URSI Radio Science Meeting*, Columbus, OH, USA, June 2003, pp. 20–21.
- [175] N. Jamaly and A. Derneryd, "Efficiency characterisation of multi-port antennas," *Electronic Letters*, vol. 48, pp. 196–198, Feb. 2012.
- [176] D. W. Browne, M. Manteghi, M. P. Fitz, and Y. Rahmat-Samii, "Experiments with compact antenna arrays for MIMO radio communications," *IEEE Transactions on Antennas and Propagation*, vol. 54, pp. 3239–3250, Nov. 2006.
- [177] S. H. Chae, S.-K. Oh, and S.-O. Park, "Analysis of mutual coupling, correlations, and TARC in WiBro MIMO array antenna," *IEEE Antennas and Wireless Propagation Letters*, vol. 6, pp. 122–125, 2007.
- [178] J. R. Costa, E. B. Lima, C. R. Medeiros, and C. A. Fernandes, "Evaluation of a new wideband slot array for MIMO performance enhancement in indoor WLANs," *IEEE Transactions on Antennas and Propagation*, vol. 59, pp. 1200–1206, Apr. 2011.
- [179] J.-M. Hannula, J. Holopainen, and V. Viikari, "Concept for frequency-reconfigurable antenna based on distributed transceivers," *IEEE Antennas and Wireless Propagation Letters*, vol. 16, pp. 764–767, 2016.
- [180] J. Helander, D. Tayli, and D. Sjöberg, "Synthesis of large endfire antenna arrays using convex optimization," *IEEE Transactions on Antennas and Propagation*, vol. 66, no. 2, pp. 712–720, Feb. 2018.
- [181] J.-M. Hannula, T. O. Saarinen, A. Lehtovuori, J. Holopainen, and V. Viikari, "Tunable eight-element mimo antenna based on the antenna cluster concept," *IET Microwaves, Antennas & Propagation*, vol. 13, no. 7, pp. 959–965, 2019.
- [182] M. Wang, T.-H. Loh, Y. Zhao, and Q. Xu, "A closed-form formula of radiation and total efficiency for lossy multiport antennas," *IEEE Antennas and Wireless Propagation Letters*, vol. 18, pp. 2468–2472, Dec. 2019.
- [183] R. F. Harrington and J. R. Mautz, "Control of radar scattering by reactive loading," *IEEE Transactions on Antennas and Propagation*, vol. 20, no. 4, pp. 446–454, July 1972.
- [184] O. Bucci, G. D'Elia, G. Mazzarella, and G. Panariello, "Antenna pattern synthesis: a new general approach," *Proceedings of the IEEE*, vol. 82, no. 3, pp. 358–371, Mar. 1994.
- [185] P. Hazdra, J. Kracek, and T. Lonsky, "On end-fire super directivity of arrays of two elementary dipoles and isotropic radiators," *IET Microwaves, Antennas & Propagation*, vol. 13, no. 14, pp. 2405–2411, 2019.
- [186] M. Masek, L. Jelinek, and M. Capek, "Excitation schemes of uncorrelated channels," 2020, eprint arXiv: 2003.09378. [Online]. Available: <https://arxiv.org/abs/2003.09378>
- [187] G. L. Nemhauser and L. A. Wolsey, *Integer and Combinatorial Optimization*. John Wiley & Sons, 1999.

- [188] J. Nocedal and S. Wright, *Numerical Optimization*. New York, United States: Springer, 2006.
- [189] R. S. Elliott, *Antenna Theory and Design*. Wiley - IEEE Press, 2003.
- [190] M. Capek, L. Jelinek, and M. Gustafsson, "Shape synthesis based on topology sensitivity," *IEEE Transactions on Antennas and Propagation*, vol. 67, no. 6, pp. 3889–3901, June 2019.
- [191] R. F. Harrington, "Effect of antenna size on gain, bandwidth, and efficiency," *Journal of Research of the National Bureau of Standards. Section D: Radio Propagation*, vol. 64-D, pp. 1–12, Jan.–Feb. 1960.
- [192] M. Gustafsson, M. Capek, and K. R. Schab, "Tradeoff between antenna efficiency and Q-factor," *IEEE Transactions on Antennas and Propagation*, vol. 67, no. 4, pp. 2482–2493, Apr. 2019.
- [193] R. Kormilainen, J.-M. Hannula, T. O. Saarinen, A. Lehtovuori, and V. Viikari, "Realizing optimal current distributions for radiation efficiency in practical antennas," *IEEE Antennas and Wireless Propagation Letters*, vol. 19, no. 5, pp. 731–735, May 2020.
- [194] L. Jelinek and M. Capek, "On the stored and radiated energy density," in *Proceedings of the 9th European Conference on Antennas and Propagation (EUCAP)*, Lisbon, Portugal, July 2015.
- [195] S. R. Best and D. L. Hanna, "A performance comparison of fundamental small-antenna designs," *IEEE Antennas and Propagation Magazine*, vol. 52, no. 1, pp. 47–70, Feb. 2010.
- [196] L. Jelinek, K. R. Schab, and M. Capek, "The radiation efficiency cost of resonance tuning," *IEEE Transactions on Antennas and Propagation*, vol. 66, no. 12, pp. 6716–6723, Dec. 2018.
- [197] *145-2013 – IEEE Standard for Definitions of Terms for Antennas*, IEEE Std., Mar. 2014.
- [198] D. A. Dunavant, "High degree efficient symmetrical gaussian quadrature rules for the triangle," *International Journal for Numerical Methods in Engineering*, vol. 21, pp. 1129–1148, 1985.
- [199] J. R. Mautz and R. F. Harrington, "A combined-source solution for radiation and scattering from a perfectly conducting body," *IEEE Transactions on Antennas and Propagation*, vol. 27, no. 4, pp. 445–454, July 1979.
- [200] J. E. Hansen, Ed., *Spherical Near-Field Antenna Measurements*. United Kingdom: The Institution of Engineering and Technology, 2008.
- [201] V. Losenicky, L. Jelinek, M. Capek, and M. Gustafsson, "Dissipation factors of spherical current modes on multiple spherical layers," *IEEE Transactions on Antennas and Propagation*, vol. 66, no. 9, pp. 4948–4952, Sept. 2018.
- [202] K. R. Schab, A. Rothschild, K. Nguyen, M. Capek, L. Jelinek, and M. Gustafsson, "Trade-offs in absorption and scattering by nanophotonic structures," *Optics Express*, vol. 28, pp. 36 584–36 599, Nov. 2020.

- [203] M. De Berg, O. Cheong, M. Van Kreveld, and M. Overmars, *Computational Geometry: Algorithms and Applications*. Springer, 2008.
- [204] M. Masek, J. Rymus, P. Hazdra, and M. Capek, “Implementation of the theory of characteristic modes into antenna modeling tools AToM and Visual Antenna,” in *22nd International Microwave and Radar Conference (MIKON)*, Poznan, Poland, May 2018.
- [205] Y. Chen, K. Schab, M. Capek, M. Masek, B. K. Lau, H. Aliakbari, Y. Haykir, Q. Wu, W. Strydom, N. Peitzmeier, M. Jovicic, S. Genovesi, and F. A. Dicandia, “Benchmark problem definition and cross-validation for characteristic mode solvers,” in *Proceedings of the 12th European Conference on Antennas and Propagation (EuCAP)*, London, UK, Apr. 2018.



List of Figures

2.1	Four symmetry operations applied to four different objects.	4
2.2	Six nodes arranged into an equilateral triangle and their transformations via symmetry operations of point group C_{3v}	5
2.3	An example of matrix representation \mathbf{D} ($R \in G$) of an equilateral triangle.	6
2.4	Real spherical harmonics S_ℓ^m up to degree $\ell = 4$	9
2.5	Dependency of analytically computed characteristic numbers and characteristic angles on electrical size ka of a spherical shell.	10
2.6	Current densities of the six most significant characteristic modes of a bowtie antenna.	12
2.7	Characteristic angles of four-dipoles array.	13
2.8	Tracked characteristic modes by the correlation algorithm and excitation coefficients α_n of a bowtie antenna.	15
2.9	Comparison of lower bounds on radiation Q-factor with realized antennas.	17
3.1	Six different meshes of a square plate.	20
3.2	Four symmetrically placed ports were excited so as to excite currents belonging to different irreps and providing four orthogonal radiation channels on a rectangular rim.	21
3.3	Four ports are considered and their voltage studied to provide the best total active reflection coefficient (TARC).	22
3.4	Example of linear combinations of TM and TE characteristic modes that can eliminate the erroneous duality gap and reach the fundamental bound on the radiation Q-factor.	23
A.1	Raw untracked and correlation tracked traces of characteristic angles.	30
A.2	An illustration of a simple symmetric structure with depicted RWG basis functions $\{\boldsymbol{\psi}_n(\mathbf{r})\}$. The structure belongs to point group C_{2v}	34
A.3	Eigenvectors $[\mathbf{I}]$ computed by (A.5) at $ka = 0.5$ and corresponding matrices \mathbf{D} ($R \in G$) are shown for the structure depicted in Figure A.2.	35
A.4	Matrices $\boldsymbol{\rho}^\alpha$ and symmetry-adapted basis $\boldsymbol{\Gamma}^\alpha$ for each irrep of the structure in Figure A.2.	35
A.5	Tracked characteristic angles of the four-dipole array treated in Figure A.1.	37
A.6	Tracked characteristic angles of an equilateral triangle.	38
A.7	First characteristic modes of each irreducible representation of equilateral triangle at electrical size $ka = 1$	39

A.8	Six bowtie antennas arranged to a cubic array belonging to the T_d point symmetry group.	40
A.9	Tracked characteristic angles of a cubic array depicted in Figure A.8. . .	41
A.10	Enlarged area from Figure A.9.	41
A.11	Original arrangement of an antenna motif above ground plane GND; removal of the ground plane via image theory; and point group C_s with symmetry operator σ_h	41
A.12	The first odd and even characteristic modes in the vicinity of their resonance of same-length dipoles and dipoles of slightly different lengths. . .	43
A.13	The influence of improper modal tracking on time domain characteristics. . . .	44
A.14	Two most significant modes at every frequency sample of irrep $\alpha = E$ of an equilateral triangle. Panels show raw unsorted data, sorted with respect to their eigenvalues, and data after the removal of vertical shifts. . . .	46
B.1	An example of symmetry operations—a square—the structure belonging to point group C_{4v}	51
B.2	Examples of various point groups with highlighted generator of the structure.	52
B.3	Port locations on a rectangular plate.	53
B.4	The structure of the rectangular rim.	56
B.5	TARC values of four orthogonal states $(\alpha, 1)$ for the rectangular rim from Figure B.4 evaluated for different positions of port in the generator of the structure ξ at $ka = 10.19$	59
B.6	Far-field cuts with polarization along direction $\hat{\varphi}$ computed at $ka = 1$ for excitation vectors $\mathbf{V}^{(\alpha,i)}$ for $\xi = 7$	59
B.7	The best position of the port in the generator of the structure ξ with respect to TARC value t_{RMS} evaluated at each frequency sample.	60
B.8	TARC values evaluated by (B.19) for different positions ξ of the sole ($N_\xi = 1$) feeder which was symmetry-adapted.	60
B.9	TARC values of four orthogonal states $(\alpha, 1)$ for a rectangular rim depicted in Figure B.4, the best position $\xi = 7$ is considered.	61
B.10	Voltage amplitudes $\kappa^{(\alpha,1)}$ for a configuration with a combination of $N_\xi = 2$ positions at $\xi \in \{12, 14\}$	62
B.11	TARC values of four orthogonal states for the rectangular rim depicted in Figure B.4 and a combination of two positions at $\xi \in \{12, 14\}$	63
B.12	Five basis functions and their orientation on a star structure. An excitation vector was symmetry-adapted to four irreps.	65
C.1	Multi-port antenna system.	71
C.2	TARC for a thin-strip dipole of length ℓ and width $\ell/100$. Various characteristic impedances $R_{0,1}$ and surface resistivities were used.	74
C.3	Optimal placement of a delta-gap feeder along the thin-strip dipole made of copper.	75
C.4	A metallic rim with parasitic ground plane with four possible ports. . . .	75
C.5	TARC for the metallic rim with parasitic ground plane, depicted in Figure C.4.	76
C.6	Current density of a port-mode excited at 500 MHz by a unit voltage impressed at port P_2	77
C.7	Comparison of TARC for optimal excitation and uniform excitation. . . .	78

C.8	Comparison of radiation efficiency for optimal excitation and uniform excitation.	78
C.9	Optimal excitation for configurations from Figures C.7 and C.8.	79
C.10	Comparison of TARC for optimal excitation and uniform excitation depending on the value of characteristic impedance $R_{0,p}$	80
C.11	The same metallic rim and parasitic ground plane as in Figure C.4 with the regions for optimal ports' placement.	81
C.12	Results of the feeding synthesis (solution to combinatorial optimization problem) for various approaches of TARC minimization.	82
C.13	An overview of the optimal placement of the ports and their performance in TARC and radiation efficiency. Various approaches found in this paper are utilized.	82
C.14	Current density associated with the fundamental bound on radiation efficiency at frequency $f = 676$ MHz for copper cladding, $\sigma = \sigma_{\text{Cu}}$, under the condition that only the current on the rim is controllable.	83
C.15	TARC as a function of characteristic impedance R_0 and tuning susceptance B_L . The realization with the lowest TARC, <i>i.e.</i> , the one depicted in Figure C.13d, is studied.	85
C.16	The values of characteristic impedances and tuning elements required to reach TARC performance from Figure C.12.	85
C.17	Results of TARC for several realizations from Figure C.15.	86
C.18	Current density induced by the feeding scheme from Figure C.13d at $f = 676$ MHz.	87
C.19	Radiation pattern generated by a current from Figure C.18.	87
C.20	Results of the feeding synthesis (solution to the optimization problem for angle φ) for various approaches of realized gain maximization. The uniform array of four metallic dipoles, separated by distance $d = \lambda/2$ is considered.	89
C.21	Sensitivity of the realized gain G^t in the broad-side direction to the value of characteristic impedance R_0	90
C.22	The optimal excitation of the uniform metallic dipole array with separation distance $d = \lambda/2$	91
C.23	Results of the feeding synthesis (solution to the optimization problem for angle φ) for various approaches of realized gain minimization. The nonuniform array of four metallic dipoles, separated by distance $d = \{\lambda/20, \lambda/10, \lambda/4\}$ is considered.	91
D.1	Various source quantities \mathbf{x} to be optimized.	97
D.2	Shapes and their discretization utilized to solve the optimization problem (D.13).	100
D.3	Eigenvalues (Lagrange's multipliers) λ_1 from (D.16) as functions of Lagrange's multiplier λ_2 (bottom panes) and the corresponding Q-factors (D.17).	101
D.4	Current densities associated with the first two modes of the eigenvalue problem (D.16) evaluated for the rectangular shape depicted in Figure D.2b at $\lambda_2 = \lambda_2^*$	104
D.5	Optimization setting and coordinate system used for the optimization of maximal antenna gain with a self-resonant constraint.	105
D.6	Solution to the dual problem (D.27) for a rectangular plate of electrical size $ka = 1/2$ made of lossy material equivalent to copper at 1 GHz.	106

D.7	Study of an erroneous duality gap expressed in terms of $Q(\lambda_2^*)$ for an optimization of self-resonant Q-factor. Two symmetric objects are considered, a square plate (C_{4v} point group) and a rectangular plate (C_{2v} points group). The parameter ξ distorts the mesh grid both in horizontal and in vertical directions.	107
D.8	Investigation of the close vicinity of the eigenvalue crossing/crossing avoidances for three particular cases from Figure D.7.	108
D.9	A metallic rim with parasitic ground plane with four discrete ports. . .	109
D.10	Eigenvalue (Lagrange's multipliers) λ_1 from (D.41) as functions of Lagrange's multiplier λ_2	111
D.11	Solution to the eigenvalue problem (D.16) for a rectangular rim of electrical size $ka = 1$ of the original problem (D.16), and of the modified problem (D.47) with reactance matrix $\tilde{\mathbf{X}}_0$ defined so as to manipulate B_1 irrep only.	113
D.12	Dependence of the dominant eigenvalues $\lambda_{1,1}$, $\lambda_{1,2}$, and $\lambda_{1,3}$, from irreps B_2 , A_2 , and B_1 , respectively, on the tuning parameter $X_{L,i}$	114
D.13	Three combinations (D.21) of modes generated by (D.47). Due to the additionally introduced degeneracy in Figure D.11, not one, but three solutions are possible.	114
D.14	Flowchart of a general algorithm dealing with degenerated eigenvalues. .	116
E.1	Locations where AToM was downloaded or purchased.	124



List of Tables

2.1	Multiplication table for point group C_{2v}	5
2.2	Character table for point group C_{3v}	7
A.1	Current distribution of the first two modes of each irrep of the four-dipole array.	37
A.2	Character table for point group C_{3v}	38
A.3	Character table for point group T_d	38
A.4	Character table for point group C_s and characterization of modes and physical symmetries with respect to the modes belonging to irreps A' and A''	39
A.5	Reduction of computational time of characteristic mode decomposition for the <i>a priori</i> tracking scheme.	44
A.6	A physical realization of irreps generated by the C_{2v} point group.	45
B.1	Three examples of system states \mathbf{q}_m and associated operators \mathcal{A} preserving orthogonality in the sense of (B.3).	49
B.2	Orthogonal excitation states for a plate from Figure B.3.	53
B.3	Maximum number of symmetry-based orthogonal states N_s / minimal number of ports N_p needed to excite all of them for a given point group.	55
B.4	A symmetry-adapted delta gap number five from Figure B.3.	55
B.5	The best values of root mean square (RMS) of TARC for various excitation strategies on a rectangular rim depicted in Figure B.4.	62
B.6	Character table for point group C_{2v}	66
D.1	Summary of TARC optimization for rectangular metallic rim with a parasitic ground plane for symmetry placement of four ports.	110
D.2	Maximum number of degenerated eigenvalues depending on the point group of an object.	118
D.3	Character table for point group C_1	121
D.4	Character table for point group C_s	121
D.5	Character table for point group C_{2v}	121
D.6	Character table for point group C_{4v}	121
E.1	Statistics of AToM.	124



List of Acronyms

AToM	Antenna Toolbox for MATLAB
CM	characteristic mode
EFIE	electric field integral equation
FEM	finite element method
GEP	generalized eigenvalue problem
GUI	graphical user interface
MIMO	multiple-input multiple-output
MoM	method of moments
PEC	perfect electric conductor
PMC	perfect magnetic conductor
RMS	root mean square
RWG	Rao-Wilton-Glisson
TARC	total active reflection coefficient
TE	transverse electric
TM	transverse magnetic
QCQP	quadratically constrained quadratic program



List of Symbols

The following tables contain summary of symbols used in the body of the thesis. Symbols used in reprinted papers in [Appendices A–D](#) are explained near their first appearance.

Symbol	Meaning	Units
g	order of point group	—
g^α	order of irreducible representation α	—
ka	electrical size	—
\mathbf{r}, \mathbf{v}	Euclidean vectors	m
\mathbf{v}	vector	—
$\mathbf{v}^{(\alpha,i)}$	symmetry-adapted vector	—
$\mathbf{C}(R)$	mapping matrix	—
$\mathbf{D}(R)$	block-diagonalized matrix representation	—
$\mathbf{A}, \mathbf{B}, \mathbf{V}$	matrices	—
\mathbf{E}	identity matrix	—
G	point group	—
\mathbf{I}_n	eigenvector of current density expansion coefficients	A
$\mathbf{J}_n(\mathbf{r})$	modal current density	A
P_{rad}	radiated power	W
Q_{rad}	radiation Q-factor	—
R	symmetry operation	—
\mathbf{R}_0	radiation part of impedance matrix	Ω
\mathbf{R}_ρ	loss part of impedance matrix	Ω
\mathbf{U}	matrix operator of radiation intensity	$\text{W sr}^{-1} \text{A}^{-2}$
V	vector space	—
\mathbf{V}^{inc}	excitation vector	V m
\mathbf{W}	matrix operator of stored energy	J A^{-2}
W_e, W_m	stored electric/magnetic energy	J
\mathbf{X}_0	imaginary part of impedance matrix	Ω
$\mathbf{X}_e, \mathbf{X}_m$	matrix operator of stored electric/magnetic energy	J A^{-2}
\mathbf{Z}	impedance matrix	Ω

Symbol	Meaning	Units
α	irreducible representation (irrep)	—
α_n	modal excitation coefficient	—
(α, i)	species (i -th dimension of irrep α)	—
δ_n	characteristic angle	—
λ_n	eigenvalues (characteristic numbers)	—
$\rho^{(\alpha, i)}$	projection operator	—
$\chi^\alpha(R)$	group character	—
$\psi(\mathbf{r})$	basis function	—
ω	angular frequency	rad s ⁻¹
Γ	symmetry-adapted basis	—
Ω	object's region	—

© 2022 Michal Mašek

Department of Electromagnetic Field
Faculty of Electrical Engineering
Czech Technical University in Prague
Technická 2
166 27, Prague 6
the Czech Republic

Abstract—The thesis focuses on the role of symmetries in computational electromagnetics. The presence of point symmetries—geometric similarities with respect to a fixed point—is studied within the realm of the method of moments, revealing the simultaneous block-diagonalization of matrix operators as the key instrument. The theory and an effective procedure to acquire this so-called irreducible representation are devised and implemented over a set of piece-wise basis functions. The von Neumann-Wigner theorem and its interpretation of avoided crossing are shown to be a remedy of problems associated with parametrized modal analysis. This includes the identification of crossings/crossing avoidances in modal tracking or an erroneous duality gap appearing in the dual formulation of quadratic programs. The orthogonality between irreducible representations is utilized to simultaneously excite independent radiation states, a method that can find its use in multiple-input multiple-output devices. Lastly, it is shown that the block-diagonal description of symmetrical systems can lead to a remarkable increase in the speed of computations.

